CAPITAL UNIVERSITY OF SCIENCE AND TECHNOLOGY, ISLAMABAD

Investigation of Enhanced Tubes and Bends for Heat Transfer and Momentum Transport

by

Rizwan Sabir

A thesis submitted in partial fulfillment for the degree of Doctor of Philosophy

in the

Faculty of Engineering
Department of Mechanical Engineering

2023

Investigation of Enhanced Tubes and Bends for Heat Transfer and Momentum Transport

By

Rizwan Sabir

(DME 163002)

Dr. Aqiang Lin, Associate Professor

Northwestern Polytechnical University, China

(Foreign Evaluator 1)

Dr. Pascal H., Biwole, Professor

Universite Clermont Auvergne, France

(Foreign Evaluator 2)

Dr. Muhammad Mahabat Khan

(Thesis Supervisor)

Dr. Nadeem Ahmed Sheikh

(Thesis Co-Supervisor)

Dr. Muhammad Mahabat Khan

(Head, Department of Mechanical Engineering)

Dr. Imtiaz Ahmad Taj

(Dean, Faculty of Engineering)

DEPARTMENT OF MECHANICAL ENGINEERING

CAPITAL UNIVERSITY OF SCIENCE AND TECHNOLOGY

ISLAMABAD

2023

Dedicated to Syed Irshad Hussain shah (Late),

Haji Ali Asghar

My Wife, & My Children

Haider, Hafsa, & Hoorain

Without whom none of my success would be possible

CAPITAL UNIVERSITY OF SCIENCE & TECHNOLOGY
ISLAMABAD

Expressway, Kahuta Road, Zone-V, Islamabad
Phone:+92-51-111-555-666 Fax: +92-51-4486705
Email: info@cust.edu.pk Website: https://www.cust.edu.pk

CERTIFICATE OF APPROVAL

This is to certify that the research work presented in the thesis, entitled "**Investigation of Enhanced Tubes and Bends for Heat Transfer and Momentum Transport**" was conducted under the supervision of **Dr. Muhammad Mahabat Khan**. No part of this thesis has been submitted anywhere else for any other degree. This thesis is submitted to the **Department of Mechanical Engineering, Capital University of Science and Technology** in partial fulfillment of the requirements for the degree of Doctor in Philosophy in the field of **Mechanical Engineering**. The open defence of the thesis was conducted on **June 01, 2023**.

Student Name : Rizwan Sabir (DME163002)

The Examining Committee unanimously agrees to award PhD degree in the mentioned field.

Examination Committee :

(a) External Examiner 1: Dr. Taqi Ahmed Cheema
Associate Professor
GIKI, Topi, Swabi

(b) External Examiner 2: Dr. Emad ud Din
Associate Professor
SMME, NUST, Islamabad

(c) Internal Examiner : Dr. Waqas Akbar Lughmani
Associate Professor
CUST, Islamabad

Supervisor Name : Dr. Muhammad Mahabat Khan
Associate Professor
CUST, Islamabad

Name of HoD : Dr. Muhammad Mahabat Khan
Associate Professor
CUST, Islamabad

Name of Dean : Dr. Imtiaz Ahmed Taj
Professor
CUST, Islamabad

AUTHOR'S DECLARATION

I, **Rizwan Sabir (Registration No. DME163002)**, hereby state that my PhD thesis entitled, '**Investigation of Enhanced Tubes and Bends for Heat Transfer and Momentum Transport**' is my own work and has not been submitted previously by me for taking any degree from Capital University of Science and Technology, Islamabad or anywhere else in the country/ world.

At any time, if my statement is found to be incorrect even after my graduation, the University has the right to withdraw my PhD Degree.

(Rizwan Sabir)

Dated: 01 June, 2023

Registration No : DME163002

PLAGIARISM UNDERTAKING

I solemnly declare that research work presented in the thesis titled "**Investigation of Enhanced Tubes and Bends for Heat Transfer and Momentum Transport**" is solely my research work with no significant contribution from any other person. Small contribution/ help wherever taken has been duly acknowledged and that complete thesis has been written by me.

I understand the zero-tolerance policy of the HEC and Capital University of Science and Technology towards plagiarism. Therefore, I as an author of the above titled thesis declare that no portion of my thesis has been plagiarized and any material used as reference is properly referred/ cited.

I undertake that if I am found guilty of any formal plagiarism in the above titled thesis even after award of PhD Degree, the University reserves the right to withdraw/ revoke my PhD degree and that HEC and the University have the right to publish my name on the HEC/ University Website on which names of students are placed who submitted plagiarized thesis.

(Rizwan Sabir)

Dated: 01 June, 2023

Registration No : DME163002

List of Publications

It is certified that following publication(s) have been made out of the research work that has been carried out for this thesis:-

1. **R. Sabir**, M. M. Khan, N. A. Sheikh, I. U. Ahad, and D. Brabazon, "Assessment of thermo-hydraulic performance of inward dimpled tubes with variation in angular orientations.", Applied Thermal Engineering, vol. 170, 2020, p. 115040.

2. **R. Sabir**, M. M. Khan, N. A. Sheikh, and I. U. Ahad, "Effect of dimple pitch on thermal-hydraulic performance of tubes enhanced with ellipsoidal and teardrop dimples.", Case Studies in Thermal Engineering, vol. 31, 2022, p. 101835.

3. **R. Sabir**, M. M. Khan and N. A. Sheikh, "Numerical Investigation of Thermal-Hydraulic Performance of U-Tubes Enhanced With Ellipsoidal 45 deg Dimples.", Journal of Heat Transfer, vol. 144(8), 2022, p. 082001.

4. **R. Sabir**, M. M. Khan, M. Imran, N. A. Sheikh and M. Irfan, "Role of transverse dimples in thermal-hydraulic performance of dimpled enhanced tubes.", International Communications in Heat and Mass Transfer, vol. 139, 2022, p. 106435.

(Rizwan Sabir)

Registration No: DME 163002

Acknowledgement

First of all, I would like to thank Allah Almighty, whose benediction bestowed upon me talented teachers, provided me wonderful opportunities and enabled me to undertake and execute this research work. I offer countless Darood and Salaams to my beloved Holy Prophet Hazrat Muhammad (PBUH), for Whom this universe has been manifested. My heartfelt appreciation goes to my affectionate, sincere, kind and most respected supervisor Dr. Muhammad Mahabat Khan and my co-supervisor Dr. Nadeem Ahmed Sheikh for patiently bearing, guiding and continuously encouraging me to complete this thesis. They have been very kind in extending all possible help to make this work a success. I am grateful to all my professors for guiding sincerely and honestly throughout my Ph.D. course work as well. It is a little sad that I could not spare time for my old parents; though their long-lasting prayers have opened new horizons for my success. I pay special thanks and tribute to my beloved Grandmother, Grandfather, mother, father, and uncles who loved me a lot and have been taking since my childhood and I cannot pay the reward for such kind and care. I wish to thank my wife, who has stood by me through all my travails, my absences and impatience. She gave me support and help, discussed ideas and prevented several wrong turns. I am very thankful to her for her support and help in writing this thesis. I am also mentioning the name of my lovely son (Haider) and my daughters (Hafsa and Hoorain), because I have not given much attention to them due to this thesis. I pay regards to my sisters, my brothers, whose sincere prayers and best wishes always would make me courageous. I am also grateful to teachers, friends and colleagues for their guidance. This research work is funded by Capital University of Sciences and Technology (CUST), Islamabad.

(Rizwan Sabir)

Abstract

Heat transfer tubes are the most critical part of any heat exchange system. The size of a heat exchange system depends on the heat and fluid flow performance of these tubes. In this context, dimpled enhanced tubes can play a vital role in improving the performance of heat transfer systems. Therefore, the current thesis deals with the flow and heat transfer characteristics of dimpled enhanced tubes using numerical simulations. A detailed numerical study based on Reynolds Averaged Naiver stokes ($RANS$) is conducted to compare the overall performances of dimpled enhanced tubes. Large Eddy Simulation (LES) of flow in dimpled tube has also been performed to study the complex flow patterns generated by the wakes of the dimples. The straight tube sections in the heat exchange systems are mostly accompanied by 180° bends (U-bends). Hence, fluid flow interaction of dimple enhanced tubes with U-bends of different radii of curvatures are also investigated in this work. The numerical setup has been validated by comparing the current results of Nusselt numbers and friction factors, for both smooth and dimpled tubes, to the published results from the literature. The validated numerical model has been used to investigate the thermal and hydraulic performance of dimpled tubes, subjected to constant heat flux $10kW/m^2$, of varying dimple topologies, pitch (axial dimple to dimple distance) and Star (number of dimples in transverse direction) for a wide range of Reynolds numbers 2300 to 40000. First of all, the performance of enhanced tubes consisting of conical, spherical and ellipsoidal dimples, of equivalent dimple volumes, have been compared. An ellipsoidal dimple 45° inclination angle, from its major axis, increased the thermo-hydraulic performance of the tube by 58.1% and 20.2% in comparison to the smooth tube and 0° ellipsoidal dimpled tube, respectively. LES results revealed a flow channel of connected wakes maximized fluid-surface contact and thus led to the enhancement of the thermal and hydraulic performance of the tube. Furthermore, the ellipsoidal 45° and teardrop dimpled tubes have been found to have an optimum pitch of 3.166 mm with suitable working Re ranges of 9000 to 30000 and 14000 to 40000 yielding performance enhancement ranges of 45.7%-9.0% and 31.2%-3.3%, respectively. The analysis also shows that the thermal-hydraulic performance of

the ellipsoidal 45° dimpled tube with Star 6 is superior to other dimpled tubes for the *Re* range of 5000 to 18000. The ellipsoidal 0° dimpled tube with Star 6 is found to a suitable choice for *Re* range of 18000 to 40000. In the end, the numerical investigation of U-tubes embedded the optimum ellipsoidal 0° and 45° dimpled tubes configurations under favorable *Re* ranges is carried out. The impact of dimples on flow separation, reattachment and the heat transfer of the tubes with different U-bend curvatures are studied in detail. In addition, correlations for Nusselt number and friction factor that cover all angular topologies, pitch, Star and U-tube curvatures of ellipsoidal dimpled tube have been proposed.

Contents

List of Figures

List of Tables

Abbreviations

PEC	Performance evaluating criteria
PEC_S	Performance evaluating criteria of smooth tube

Symbols

A	Surface area of heat transfer, m^2
c_p	Specific heat, J $kg^{-1}K^{-1}$
D_h	Hydraulic diameter, m
fr	Friction factor
fr_S	The friction factor of smooth tube
h_i	Convective heat transfer coefficient, $Wm^{-2}K^{-1}$
H	Dimple height, m
L	Length, m
Nu	Nusselt number
Nu_S	Nusselt number of smooth tube
p	Pressure, Pa
Pr	Prandtl number
Pr_t	Turbulent Prandtl number
P	Dimple pitch, mm
H	Dimple height, mm
D_P	Dimple diameter, mm
De	Dean number
∇p	Pressure drop, Pa
q''	Heat flux, Wm^{-2}
r	Distance from the centerline, m
Re	Reynolds number
R	Tube radius, m
R_c	U-tube curvature radius, m

U	Velocity, ms^{-1}
U_C	Velocity at centerline, ms^{-1}
y	Wall distance, m
y^+	Near wall distance, m
v	Kinematic viscosity, m^2s^{-1}
ϵ	Energy dissipation rate
μ	Dynamic viscosity, Pa.s
ρ	Density,kgm^{-3}
k	Thermal conductivity, $Wm^{-1}K^{-1}$
μ_t	Turbulent viscosity, Pa.s
T	Temperature, K
T_m	Mean bulk temperature of the the fluid, K
T_{wall}	Temperature of the tube wall, K
G_k	Kinetic energy of turbulence for k, JK^{-1}
G_ω	Kinetic energy of turbulence for ω, JK^{-1}
Y_k	Turbulence dissipation of k
Y_ω	Turbulence dissipation of ω
F_1, F_2	Blending functions
S_{ij}	Strain rate tensor
L_S	Combining length of sub grid-scale
Γ_ϕ	diffusion coefficient of ϕ
ϕ_f	Scalar of face f
D_ω	Cross diffusion
∇_{cell}	Cutoff top hat filter, m
$\mathbf{u}$	velocity vector, m
$\mathbf{U}$	Mean steady component of velocity, m
u'	Fluctuating component of velocity, m
Δ	Computational cell volume, m
$Star$	Number of dimples in circumferential direction
C_P	Pressure coefficient
C_f	Skin friction coefficient

c_P	Form drag coefficient
c_F	Friction drag coefficient
St	Stanton number
j_H	Colburn j factor

Subscripts

C	center
c	curvature
exp	experimental
h	hydraulic
i	horizontal direction
j	vertical direction
max	maximum
min	minimum
s	smooth
ref	reference

Chapter 1

Introduction

1.1 Background and Motivation

Heat exchangers are designed for heat transfer between two mediums using liquid or gas. Heat exchangers are of many different types based on fluid flow, its construction and contact type and its applications etc., [1]. For instance, shell and tube heat exchangers are indirect contact type which works as condensers according to classification of process function and mainly deal with process industry, power industry (surface condenser, feedwater heater etc.). They (with single or double tubes) can be configured as parallel flow, counter flow, single phase crossflow and multiphase cross flow etc., according to the flow path configuration [1, 2]. On the other hand, the applications of heat transfer through the tubes can be extended to areas like air conditioning, refrigeration, gas turbines, cooling in manufacturing systems, electronic devices, heat transfer in food and chemical industry, aviation department [3] etc. The performance and economic design of process plants are also dictated by efficient heat utilization [4]. These methods are commonly employed in areas like, process industries, heat exchangers, radiators and internal heat exchangers in vehicles, refrigeration, flow boiling [5] and [6] etc. They have drawn the attention of industry since their inception due to their critical importance in numerous areas. However, there is a need to improve the heat

transfer of thermal systems for energy conservation. Classical heat exchangers barely fulfill the requirements of current industry. The method of improving the heat transfer rate is recognized as heat transfer enhancement/augmentation [7]. Wang *et al.* [8] has stated that augmentation techniques in heat exchangers lead to compactness in size and reduced capital cost.

There are a number of augmentation techniques for the application of heat exchanger system in effective heat extraction, recovery, utilization and conversion [9], [10]. Enhancement or augmentation methods can be categorized as active and passive [11], [12]. In active techniques, external inputs in the systems for enhancing the heat transfer are required, for example surface vibration, mechanical aids, electromagnetic field, etc. These external inputs make the system more complicated and requires supplementary power as well. Therefore this method has a limited scope leading to very few applications. In passive methods, changes within the duct flow are introduced like twisted tapes additions, coils, displaced augmentation devices or surface/geometric modifications (rough surfaces, extended surfaces, dimples etc.,). Heat transfer can be augmented by incorporating the changes in the fluid flow in order to disturb the thermal and viscous boundary layers. It can be achieved by two modes: Enhancing the heat transfer coefficient, as discussed by Lane *etal.* [5] and Liao and Xin [13], or by augmenting the surface area, as reported by Bergles *et al.* [4]. It is a common practice in the industry to opt for the passive methods to augment the heat transfer rate. Ribs, corrugation, grooves, flutes and dimples are commonly used passive techniques [14]. However, all these have a relatively higher friction factor in comparison with the latter most i.e. dimple [15]. Similarly, few other examples of passive method like baffles, fins, turbulizers etc., also produced hydraulic loss and fouling (dirty fuels) in the tubes. Fouling is the formation of unwanted deposition of impurities of the fluid at the corner, edge, or surface of the heat exchange devices. For example, the precipitation of sparingly soluble salts, cake or gel formation, dust pockets, and pore blockage which degrades the heat transfer process. Both these factors are highly undesirable for the efficiency of heat exchangers system. Contrary to these

methods, dimple produced relatively less friction factor with no fouling phenomena, therefore, convective sections of major industries have shifted towards the dimpled surfaces/tubes [16]. However, some examples of relatively less inspired passive methods are also addressed here, in order to understand the limitations, pro and cons of these techniques. Taiwo [17] has investigated the twisted tape inside the tube for laminar, transitional as well as turbulent flows with water as a working fluid. He considered constant heat flux at the tube wall and has discovered that the tube having alternate-axis triangular cut twisted tape (TATCT) provided better performance. He also showed that Nu and performance index of this tube in comparison with plain tube were considerably higher lying in the range of 124.57% and 103.23%, respectively. He also analyzed the TATCT for turbulent flow and showed that Nu and fr were 118.4% and 215.8% higher than those of plane twisted tape. The definitions of Nu and fr are given in section 1.2. Similarly, another comparison was carried out at the Re up to 4610 and it was noticed that TATCT gave better performance. While this study was conducted at the relatively low Re with higher fr. Kumar *et al.* [18] have performed the comparative experimental study of smooth and dimpled helical coiled tube for different mass fluxes (75, 115, 156, 191 $kgm^{-2}s^{-1}$. He used the vapor quality of 0.1-0.8 and saturation temperature of 35°c and 45°c. The results showed that dimpled helical coiled tube gave better heat transfer coefficient in the percentage of 18-32% and 51-61% in comparison with smooth coiled and straight tube, respectively. On the other hand, the frictional loss of dimpled helical coil turned out to be 2.57-4.01 and 1.35-1.75 times the smooth coil and smooth tube respectively. They also proposed the correlations of Nu and fr for mass flux range of 75-191 $kgm^{-2}s^{-1}$. It is pertinent to mention that the mutual comparison of heat transfer coefficient and frictional loss suggest that the latter is considerably higher, which limits the individual application of this technique. Further to passive techniques, explained above, pin fin belongs to the same category, used at low Re and consequently limited in its application i.e. heat sink for micro devices (especially electronic equipment) [19, 20]. Finally, wealth of literature has shown that dimpled surfaces can provide heat transfer rate either by merits (outer surface look) [21] or by

giving relatively low hydraulic loss compared to other heat transfer enhancement techniques Ming Li *et al.* [22] and Ayub *et al.* [23], and Hassan cheraghi *et al.* [24] etc.

It is pertinent to mention that the current dissertation deals with the thermal-hydraulic performance of the dimple enhanced tubes which can be used in any kind of heat exchange device. Therefore, in this study, the heat exchange systems, on the whole, are not focused on. The fluid flow inside the enhanced tube with or without U-bends is multifaceted and it greatly affects the thermal and hydraulic characteristics of the flow. The fluid flow in the vicinity of the dimples is perturbed and separated, creating complex wake structures. Similarly, when the flow sharply turns in the bend sections of the tube secondary flow is produced which leads to flow separation in the post-bend section of the tube. Now if the flow is already agitated by the dimpled tubes before entering the bend section of the U-tube then flow complexity will further be increased. Therefore, in-depth and careful flow analysis is required to investigate the thermal and hydraulic performance of the enhanced tubes. Furthermore, important parameters and non-dimensional numbers used to characterize the thermal and hydraulic performance of augmented tubes are discussed in the subsequent section.

1.2 Important Non-dimensional Numbers and Parameters

Since there are several non-dimensional numbers and parameters including h, fr, C_f, C_p, c_P, c_F, Pr, Re, Nu, PEC, St, j_H and De which are used in the thesis. Therefore it is pertinent to highlight the important parameters here, before we proceed further. Convective heat transfer coefficient (h) is the ratio of heat flux to temperature difference between wall and the fluid. The relationship of h is presented in the following equation.

$$h = \frac{q''}{T_{wall} - T_m} \tag{1.1}$$

where q'' indicates the heat flux, T_m is the mean bulk temperature of the fluid i.e. mass weighted average temperature of the fluid inside the tube, and T_{wall} is the wall local temperature.

Darcy friction factor is used to determine hydraulic loss of the tube flow, as shown in following expression:

$$fr = \frac{2\Delta p D_h}{\rho U^2 L} \tag{1.2}$$

where Δp represents the pressure difference between inlet and outlet of a tube, ρ is the density of the fluid and U is the velocity at the tube inlet. The skin friction coefficient (C_f) is defines as:

$$C_f = \frac{\tau_w}{1/2\rho U^2} \tag{1.3}$$

Where τ_w is wall shear stress, ρ is the density of the fluid and U is the velocity or velocity at the tube inlet. The pressure coefficient (C_p) is defined as:

$$C_p = \frac{p - p_c}{1/2\rho U^2} \tag{1.4}$$

Where p is the static pressure, p_c is the static pressure at the center line or reference pressure at the inlet, ρ is the density of the fluid and U is the velocity or velocity at the tube inlet.

The pressure drag or form drag coefficient is given by:

$$c_P = \frac{1}{1/2\rho U^2 A} \int_{S_w} dS_w (p - p_o)(\hat{n} \cdot \hat{i}) \tag{1.5}$$

Where A is the area of the body, S_w is the wet surface of the body, p is the pressure on the surface dS_w, p_o is the pressure away from the body, $\hat{n}$ is the unit vector

perpendicular to the wet surface dS_w indicating from fluid to solid and $\hat{i}$ is the unit vector in the flow direction.

$$c_F = \frac{1}{1/2\rho U^2 A} \int_{S_w} dS_w(\hat{t} \cdot \hat{i}) T_w \tag{1.6}$$

Where A is the area of the body, S_w is the wet surface of the body, $\hat{t}$ is the unit vector in the direction of shear stress acting on the surface dS_w, and $\hat{i}$ is the unit vector in the flow direction and T_w is the magnitude of shear stress acting on the surface dS_w.

The representation of the Prandtl number Pr is given here:

$$Pr = \frac{\mu c_p}{k} \tag{1.7}$$

Where μ is the dynamic viscosity, c_p is the specific heat and k is the thermal conductivity of the fluid.

The definition of Re is given as:

$$Re = \frac{\rho U D_h}{\mu} \tag{1.8}$$

where U is velocity and D_h is the hydraulic diameter of the tube which is 4 times the cross-sectional area of tube or channel divided by the wetted perimeter of the cross-section. However, in our case, it is the geometric diameter of the tube.

The ratio of convective heat transfer to the conductive heat transfer at a boundary in a fluid is represented by a non-dimensional Nusselt number (Nu), which is locally determined [25] as:

$$Nu = \frac{hD_h}{k} \tag{1.9}$$

where k is thermal conductivity of the fluid. Performance Evaluation Criteria (PEC) [26] is the ratio of heat transfer enhancement to the hydraulic losses. The heat transfer enhancement is associated to the ratio of Nusselt number of enhanced

tube (Nu) and Nusselt number of smooth tube (Nu_s) while the hydraulic losses are associated to the ratio of friction factor of enhanced tube fr and smooth tube fr_s. Therefore, this criterion embeds both traditional indicators for the heat transfer assessment and hydraulic performance estimators.

$$PEC = \frac{Nu/Nu_s}{(fr/fr_s)^{1/3}} \tag{1.10}$$

The mathematical relationships of Stanton number (St) and Colburn j factor (j_H) are presented in the following equations.

$$St = Nu(RePr)^{-1} \tag{1.11}$$

$$j_H = StPr^{2/3} \tag{1.12}$$

The value of Pr for current study is provided in section 4.2.2.

The Dean number De is representative of secondary flow in the curved pipes [27], which can be determined as given below:

$$De = Re\sqrt{R_N}; \text{where } R_N = R/R_C \tag{1.13}$$

Here, the R is the tube radius while the R_C is the radius of curvature of the path of the channel.

1.3 Problem Statement

Augmenting the engineering piping network with inward dimples has shown the favorable possibility of improving overall performance in terms of heat transfer with reduction of size, however, the selection of appropriate shapes, orientations as well as placements of these dimples is challenging especially in complex plumbing configurations such as u-tube/bend.

1.4 Research Objectives

The main objectives of carrying out this study are given below:

- Development of numerical framework for the assessment of heat transfer characteristics in the tubes. This includes using validation with the experimental data to propose correlation of heat transfer for different orientations of ellipsoidal typed dimpled tubes.
- Assessment of varying geometrical parameters, including dimple pitch and circumferential distribution (Star), on the fluid flow and heat transfer characteristics of dimpled tubes.
- Assessment of dimpled tube in a U-shaped arrangement along with prediction of correlation as a function of U-tube curvature variation.

1.5 Layout of the Dissertation

The dimpled tubes, as compared to other augmentation methods, have been found to increase the heat transfer rate without large penalty on hydraulic losses. Therefore, this thesis focuses on the thermal and hydraulic performance augmentation of the dimpled enhanced tubes. This thesis consists of seven chapters. **Chapter 2** gives the literature overview of the development of dimpled enhanced tubes, with their heat transfer and friction factor characteristics as well as the dimple's geometric improvements. **Chapter 3** presents the numerical methodology used in current study for steady and unsteady simulations. It puts forward the $RANS$ model and LES modeling framework along with different discretization schemes and solution methods.

Chapter 4 describes the validation of adopted numerical methodology for the smooth and dimpled enhanced tubes. The numerical results consisting of heat transfer and friction factor of the tubes are compared to empirical correlations

and published results, respectively. The thermal-hydraulic performance of different geometric shapes and orientations of the dimples are analyzed and the optimum topology of the dimple (ellipsoidal 45°) is selected for further investigation. The flow dynamics and the fluid-dimple interactions of the tube with optimum dimple shape and orientation are studied and new correlations of Nusselt number and friction factor are proposed.

Chapter 5 further compares the optimum dimple tube (ellipsoidal 45°), obtained in Chapter 4, to the teardrop dimpled tube configuration under different dimple pitches (dimple to dimple distances) for the constant tube length to dimple pitch ratio (L/P). The overall performances of respective pitches are established for wide range of Re while the best performances of each dimple shape are indicated along with their favorable Re regimes. Local characterization (i.e. heat transfer and hydraulic loss) of best pitched tubes are depicted and the Reynolds analogy is drawn between the heat transfer and hydraulic loss to further characterized dimple configurations. In the end, heat transfer and friction factor correlations are proposed for the optimum tube configurations and working ranges.

Chapter 6 presents the effects of the variation in number of circumferential dimples (Star) for optimum ellipsoidal 0°, ellipsoidal 45° and teardrop dimpled tubes configurations. The optimal Star configuration is identified and analyzed for different configurations. The correlations of heat transfer and friction factor of tubes with formation of Star are proposed.

chapter 7 presents the overall performances of the most suitable dimple tube design with optimal geometric parameters is further embedded in U-tubes configuration. The U-tube curvatures are varied in order to draw the comparative study between their performances. The flow physics and local heat transfer characteristics of optimal U-tube is prescribed. In the end of chapter, the correlations of heat transfer and friction factor of U-tubes are proposed. In the end, numerical investigation of best pitched enhanced tubes is performed with the best-chosen Star formation in conjunction with best U-tube curvature radii U-tubes for practical

prospective. These tubes with two different geometric configurations and Pitch formations are analyzed for two different Re regimes.

1.6 Summary of chapter 1

In this chapter, motivation of this research and background are presented which provides the base to define the problem statement with research objectives. In the end, layout of this dissertation having the role towards the research objectives is presented.

Chapter 2

Literature Overview

One of the most widely used component in several heat exchangers/heat transfer devices is a tube through which fluid transmission occurs while gaining /dissipating heat [28]. Thermo-hydraulics of the transport phenomena involved in the tube flow has been extensively studied, both experimentally and numerically. The compactness of thermal devices along with thermo-hydraulic performance enhancement demands more efficient, innovative, economical and reliable solutions. With the reduction in the size of heat exchangers, the importance of understanding, designing and usage of tubes is getting more attention.

2.1 Importance of Boundary Layer

The developing nature of the flow, especially in terms of hydraulic and thermal boundary layers, is significant from the perspective of tubes. Currently, fully developed velocity boundary layer with underdeveloped and fully developed thermal boundary layered flows have been analyzed experimentally [29–31] as well as numerically [32]. Some heat transfer applications such as laminar flow over a heated flat plate or in a heated tube utilize solely the thermal boundary layer for heat exchange. However, the rates of heat transfer in such cases are much lower and cannot attain the required thermal energy transfer rates of the most of the real

life applications. Therefore, fluid mixing is induced where the fluid surface interactions are enhanced and the roles of both hydraulic as well as thermal boundary layers become important [33].

2.2 Classification of Heat Transfer Enhancement Methods

To promote heat transfer through enhanced fluid mixing, different augmentation methods are used. These methods can be divided into three distinct categories; active, passive and compound methods [34].

2.2.1 Active Method

Active method deals with external forces to augment the heat transfer rate. Magnetic and electromagnetic fields, reciprocating plungers and usage of flow and surface vibrations are the examples of external forces to disturb the flow, which ultimately enhance the heat transfer rate as demonstrated by El-Maghlany *et al.* [35]. They carried out an experimental investigation of Double Pipe Heat Exchanger ($DPHE$) using the rotating inner tube. The hot and cold fluids were utilized in counter and parallel flow configurations. The effectiveness of heat exchangers along with number of transfer units (NTU) were determined at different inner rotating tube speeds. It was found that NTU, effectiveness and heat transfer rate increased with an increase in rotation speed. Similarly, Zhang *et al.* [36] also used rotor assembled strands in the examination of heat transfer augmentation in double pipe heat exchanger. For strands, they utilized bare blade rotor, blade rotor with ladder and helical blade rotor. They found the highest performance for the case of blade rotor with ladders. Nu increased from 71.5% to 123.1% while fr increased from 37.4% to 74.8%, contrary to smooth tube. The usage of additional energy for the thermal-hydraulic performance of the tubes makes active methods unpopular and thus only a limited amount of literature is available.

2.2.2 Passive Method

In passive method, instead of utilizing the external force for heat transfer augmentation flow perturbations are achieved by using different tube inserts [37, 38], by employing wire coils and turbulators [39–41] and through geometric modifications of the tube surface [42–45].

2.2.2.1 Twisted Tape

Twisted tape insert is an effective method for the heat transfer augmentation because of low cost, simplicity and maintenance ease [46]. Different twisted tapes are shown in the figure 2.1.

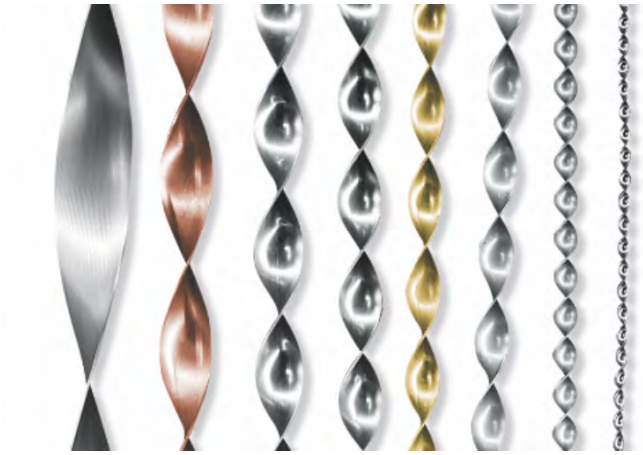

FIGURE 2.1: Twisted tape [46]

In general, twisted tape carries out the swirl generation continuously that leads to the generation of turbulence which ultimately causes the heat transfer augmentation. Significance of half-length twisted tape on the pressure drop and heat transfer of double pipe heat exchanger was investigated by Yadav [47]. In comparison to smooth tube, twisted tape augmented the heat transfer rate by 40% which was mounted at the inner tube of $DPHE$. On the other hand, PEC of smooth tube was 30-50% higher than the augmented tube as frictional loss of augmented tube was much higher than smooth tube. However, according to the literature, twisted tape insert is best for the laminar flow [42].

2.2.2.2 Extended Surface

Extended surface or fin, as displayed in the figure 2.2 is also a geometrical modification which is very famous method and covers the area of conduction and convection. Barga and Saboya [48] numerically and experimentally examined the heat transfer, hydraulic loss and efficiency factor of rectangular fins in the circumferential direction of heat exchanger covering the turbulent flow region.

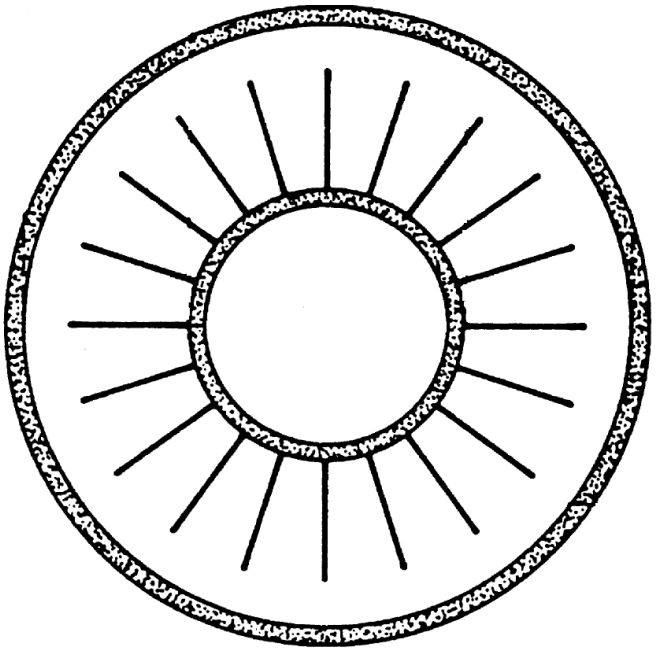

FIGURE 2.2: Extended surface [48]

They used water and air as working fluid in the inner and outer tubes, respectively. They simulated it using 2D model in their analysis and found that fin efficiency was linked with the ratio of internal to external diameter of inner to outer tube of the annulus to the distance of finned tube. They stated that ratio of heat transfer of fined tube to smooth tube was lower than 1 which further decreased as the Re increased. It was revealed that fin negatively affected the heat transfer efficiency.

Kumar *et al.* [49] examined the heat exchanger with longitudinal fins numerically and experimentally whereby they utilized three different fins in triangular, rectangular and parabolic geometries. Based on heat transfer rate, the effectiveness of rectangular fins was better than others however, hydraulic loss of parabolic fins

was lower than other fins. In continuation, they stated that mass flux of cold water should be less than hot water.

Taborek *et al.* [50] examined the multi tube heat exchanger with the rectangular fins numerically and experimentally in their study. They used water as a working fluid and utilized hot water in inner tube and cold water in outer tube. After validation of smooth heat exchanger, they also used fins with different geometries of triangular, rectangular and parabolic shapes. They found the PEC of parabolic fins to be higher than other fins shapes. They also presented the correlations of heat transfer and pressure drop.

Kahalerras and Targui [51] used numerical simulations to study the heat transfer augmentation in heat exchanger with porous fins. They used the Brinkman-Forchheimer Extended Darcy numerical model for the porous media and differential equations of boundary conditions are solved using Finite Volume Method. They found that the results are credible if the working fluid in both tubes are similar and mass fluxes of both fluids are also same.

Similarly, Syed *et al.* [52] numerically examined the heat exchanger with the variable fin tip thickness for the laminar regime. They defined the tip thickness as ratio of fin tip angle to fin base angle which was varying from 0 to 1. They utilized Discontinuous Galerkin Finite Element Method in their numerical simulation. They analyzed the heat transfer, j-factor and effectiveness of heat exchanger and found that heat transfer and j-factor were increased 178% and 89%, respectively, for rectangular fin case, While it was 9.5% and 19% for the triangular fin case, respectively. They also found the link between fin tip angle and height and number of fins.

Furthermore, Iqbal *et al.* [53] conducted the numerical study to analyze the conjugate heat transfer of longitudinal fins with the rectangular, parabolic and trapezoidal shapes of fins. They used Discontinuous Galerkin Finite Element Method in their numerical simulation along-with genetic algorithm (GA) to optimize the fin shape. They carried out the optimization based on the hydraulic and equivalent

diameters. Their results showed that heat transfer rate increased by 70% based on the hydraulic diameter while it was 289% for the case of equivalent diameter.

2.2.2.3 Ribs

Helical rib-roughened tubes are also used to increase the heat transfer rates [54]. Similarly, the use of rib-turbulators has also been found to enhance heat transfer rate [55]. Rectangular ribs in the rectangular channel with heated wall and different specifications are shown in the figure 2.3.

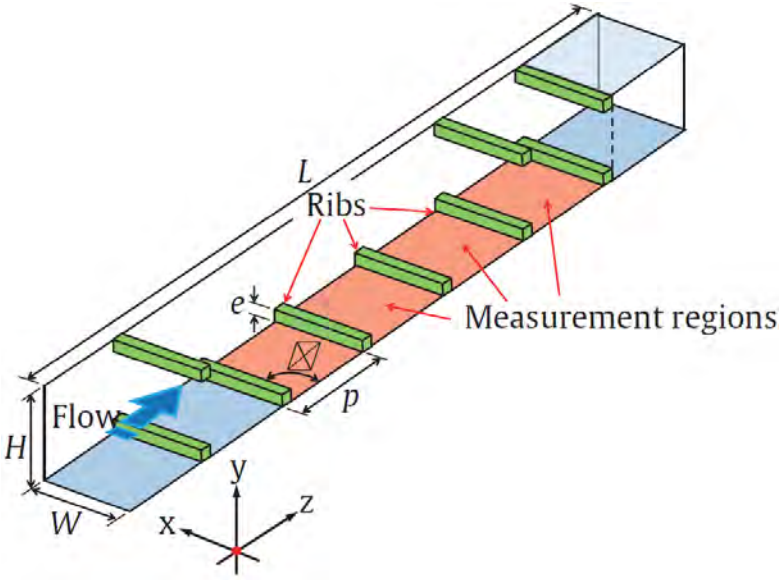

FIGURE 2.3: Rectangular Ribs in channel [56]

The effects of rib angles, ribs spacing, channel aspect ratio, rib height on the heat transfer rate of the tube, at high Reynolds numbers are explored.

2.2.2.4 Wire Coil

Wired coil, as displayed in the figure 2.4, is also very famous in the passive method. In this regard, Garcia *et al.* [57] performed an experimental study by incorporating the helical-wire-coils inside the tubes to improve thermo-hydraulic performance of the tubes for a wide range of Reynolds numbers and Prandtl numbers. In

continuation to their previous study, Garcia *et al.* [58] compared the thermo-hydraulic performance of helical-wire-coils and dimpled tubes.

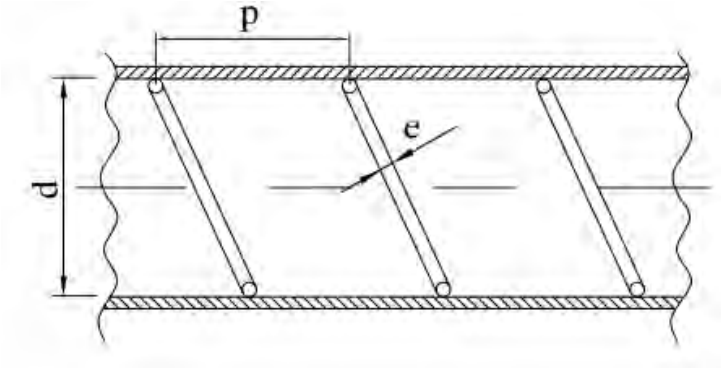

FIGURE 2.4: Wire coil in a tube [57]

It is demonstrated that the performance of dimpled tubes is much superior to the wire-coils, especially encountering turbulent flows. Dimples increase the surface area and disturb the velocity boundary layer of the flow which, in return, increase the heat transfer rate but at the cost of enhanced friction losses. Akpinar *et al.* [59] experimentally analyzed the heat transfer, hydraulic loss and exergy loss in the heat exchanger with the wire-coil inserted in the inner tube. They used hot air in the inner tube and cold water in the annulus of the tube. They found that heat transfer rate increased with the increase in number of helical turns of the wire and decreased with pitch of turn. They concluded that heat transfer, hydraulic and exergy loss were 2.64, 2.74 and 1.16 times higher than the smooth configuration. They also showed the highest heat transfer rate for the helical number of 137 in their study.

2.2.2.5 Dimple Tube

Different heat transfer enhancement methods in the tubes have also been employed in the recent past for the advancement of heat transfer augmentation for dimples. Heat transfer enhancement by increasing surface roughness inside the tubes was achieved by Bergles *et al.* [60]. The boundary layered flow disturbed (or interrupted) by the usage of dimples which increased fluid-surface interaction

and resultant heat transfer. The dimple tube with rough surface is shown in the figure 2.5.

FIGURE 2.5: Dimple tube with rough surface [61]

Experimental study of horizontal dimpled tubes with $R-134a$ as a working fluid performed by Aroonrat *et al.* [62]. In comparison to smooth tube, authors managed to increase the heat transfer coefficient by 70 % by using dimpled tube. Maithani *et al.* [63] achieved a significant increase in the performance of heat exchanger by introducing dimpled tubes. The performance assessment of trapezoidal dimpled tube was performed by Dagdevir *et al.* [64]. They concluded that trapezoidal dimpled tubes improved heat transfer rate considerably in comparison to smooth tubes.

The effect of dimple's depth in enhanced tube was investigated by Cheraghi *et al.* [24]. Authors demonstrated that the heat transfer enhancement of deep dimpled tubes was linked to axially swirling of flow caused by the vortices in the wake of dimples. Numerical studies of different dimpled shaped tubes have been performed recently which show heat transfer improvement through parametric and flow variations [65]. Similarly, Manoram *et al.* [66] investigated the application of spherical dimpled tubes in the solar water heater, experimentally and numerically. A Nusselt number enhancement of 250% was observed for the dimple pitch to diameter ratio of 3 with an 11.1% increment in hydraulic loss, contrary to the plain tube, for the mass flow rate of 2.5 kg/min.

Dagdevir *et al.* [64] carried out the numerical investigation of trapezoidal dimples in the horizontal tube to augment the heat transfer for $Re = 3000 - 8000$ with

water as a working fluid. The heat and fluid flow performance enhancement of the enhanced tube obtained up to 72% for optimum geometry. Jing *et al.*[67] conducted the numerical investigations of teardrop dimples and protrusions in a rectangular channel with carbon dioxide as a working fluid for $Re = 10000 - 90000$. They concluded that internal protrusion of teardrop dimple was favorable for low Re and produced 17% thermal performance while it was 3% for external dimples at the $Re = 90000$.The effect of different patterns of conical dimples on the heat transfer enhancement investigated by Fan *et al.* [68] using three dimensional numerical simulations. The inline dimple pattern showed higher heat transfer rate as compared to staggered dimples.

Li *et al.* [61] conducted three-dimensional steady state numerical simulations of three different tubes with conical, spherical and ellipsoidal dimples. The study recommended inline ellipsoidal dimples in comparison to conical and spherical dimples for heat transfer enhancement in tubes. Authors also studied that the overall performance increases with the decrease in dimple pitches. Liang *et al.* [26] investigated thermal hydraulic performance of ellipsoidal dimpled tubes. They observed that the dimple arrangement significantly affected the heat transfer rate. For $Re < 104$, the ellipsoidal dimples with major axis aligned to the flow direction (i.e., ellipsoidal 0°) resulted in highest heat transfer rate. However, for $Re > 104$, the ellipsoidal dimple with 60° inclination of the major axis with respect to the flow direction (i.e., ellipsoidal 60°) demonstrated highest heat transfer rate. Authors also analyzed the dimple pitches ranging from 10-15 mm. They also observed that 10 mm pitch resulted in better performance at the Re range of 5000 to 25000, while the 12 mm pitch produced better performance at the Re range of 25000 to 30000.

The heat transfer enhancement in a tube with combination of ellipsoidal dimples in vertical and horizontal directions, with respect to flow direction, was studied by Xie *et al.* [69]. It was observed that the heat transfer was increased by decreasing the dimple pitch and also increasing the depth and axis ratio of the dimples. The performance of mini-channels with spherical dimples were compared to channels with cylindrical grooves and fins by Bi *et al.* [70].

Firoozi *et al.* [71] also studied the variety of dimple configurations including dimple pitch and height effect on heat transfer rate. They used Nano fluid as working fluids and numerically analyzed for a Re range of 500-4000. It was discovered that the overall performance increased with a decrease in dimple pitch and an increase in dimple height. They achieved the PEC=2.5 for the water flowing at the Re = 2000, for the minimum pitch of tube and PEC=3.2 for the nano-fluid flow. Similarly, the performance improvement of the cross-combined dimpled tube and innovative dimpled tube, with a decrease in dimple pitch, was numerically studied by Zhang *et al.* [72]. They found that the performance of tube increased by an average of 24.8% than the single ellipsoidal dimple tube. They also varied the Star placements from 2 to 6 and found that overall performance increased approximately from 30% to 88% at the low Re.

2.2.3 Compound Method

In this method, both the active and passive methods are incorporated. An example of this method is the usage of wire coil and simultaneous utilization of fluid vibration in which a number of different experiment have been conducted [73]. Omkar *et al.* [74] also conducted an assessment of heat transfer by using helical fins on the outer surface while the inner surface was rotating. At the annulus, glycol was used as a working fluid and water at the inner tube. They demonstrated that Nu was enhanced by 64% at 100rpm of the inner tube as compared to the static inner tube. It is necessary to mention that such methods are scarcely studied due to the high difficulty level. Therefore, passive methods are preferred.

2.2.4 Why a Dimpled Tube?

Although there are several passive methods for enhancing the heat transfer rate but at the expanse of inducing frictional flow losses. Therefore, thermal and hydraulic performances are important for any passive method. Dimpled enhanced tubes have been found to better than the other enhancement techniques based

on two main advantages. Firstly the dimple tube induce lower pressure losses as compared to other techniques [15, 22, 26, 32, 61, 69] thus reducing pumping power and consequently the cost of the system. Secondly dimpled tubes avoid the fouling [16] which is generally responsible for reducing the fluid surface interaction and thus increasing the resistance to heat transfer [75]. Additionally, the dimples do not have sharp edges therefore the effects of fouling become negligible.

2.2.5 Incorporating the U-Tube

Heat exchange devices carry substantial importance in the energy storage and conversion systems.These devices transmit thermal energy in-between the fluids separated by the solid surface at distinct temperatures. Heat exchangers are utilized in the food industry, chemical and petroleum refineries, refrigeration, air conditioning, transportation, power production, aviation department. However, in most of the engineering applications, compactness of heat exchanger is a basic requirement for the limitations of the work space. Therefore, to limit the heat exchanger size, the tubes are bend in the form of U-shape, L-shape and coils passes [76], as presented in Figure 2.6.

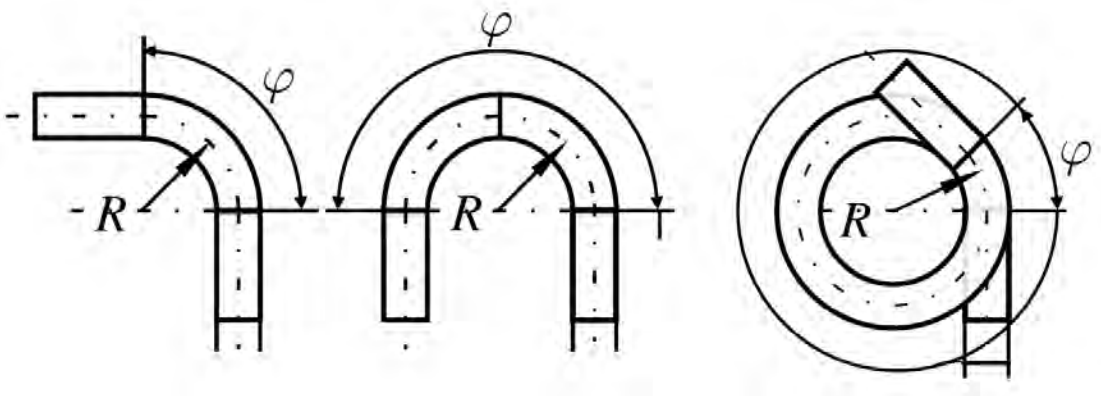

FIGURE 2.6: L shape, U shape and coil

In general, industrial heat exchange devices encompass tubes with 180° return bends (U-bends) for compactness and continuous heat transfer at optimal efficiency [72], [76], [77], [78], [79]. Examples of tubes with U-bends (U-tubes) include

shell and tube heat exchangers [2], refrigeration systems, cooling of electronic devices, heat pipes, cooling channels of fuel cells, and gas turbines blades [80], [81], etc. However, the U-bends generate complicated fluid flow patterns within the tube depending on the sharpness of the bend (bend curvature) which ultimately affects the thermal-hydraulic performance of the overall system. The experimental analysis of Dean [82] showed the generation of counter-rotating vortices (Dean vortices) in the bend section of the tubes under laminar flow conditions. For turbulent flow conditions, more intense Dean vortices were observed in the numerical simulations of Hellstr [83]. The Dean vortices were observed to be responsible for the flow detachment and reattachment in pre-bend and post-bend sections of the U-tubes. Therefore the thermal performance of U-tubes is strongly linked to flow characteristics in the bend sections of the pipes [84].

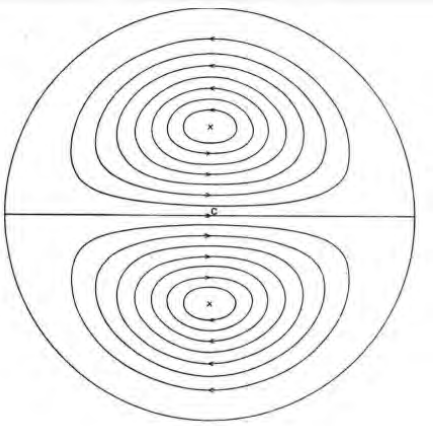

FIGURE 2.7: Schematic of Dean Vortices at low Re [82]

The transition from laminar to turbulent flow was examined by many researchers [85], [86]. For this, the relationship of critical Reynolds number Re_{crit} was presented by the Ward-smith [87] and [88]. Similarly, developing turbulent flows in U-bend was also studied experimentally and numerically by [89] and they presented that the Reynolds stress distributions and mean velocity also denoted two revolving streams, which was also depicted by M. Rowe [90].

In turbulent flow, the experimental demonstration of Dean vortices has not been studied extensively however the numerical simulations ($RANS$ and LES) were recently used as a working tool to investigate the complex vortex structures which

consisted of four to six local minima [83]. The Dey *et al.* [91] also analyzed the secondary flow motion for turbulent flow using the boundary layer approach. He presented his computational results of boundary layer thickness and shear stress for different curvature and Re up to 5×10^5. He showed that the thickness of secondary boundary layer gradually increased along the pipe, however, a rapid growth in secondary boundary layer was observed upon reaching the separation point. Pradhan *et al.* [92] compared the heat transfer characteristics of circular and rectangular U-bend pipes. They have varied the curvature radius and demonstrated that counter-rotating vortices moved toward the inward side of bend to strengthen the flow recirculation, as the aspect ratio of non-circular bend increases. It ultimately enhanced the heat transfer rate. They concluded that rectangular U-bend tube of 1.5 aspect ratio has highest heat transfer rate, in contrary to the square and circular bend tubes.

The cost-effectiveness and thermal efficiency enhancement of different heat exchange devices require thermal-hydraulic design improvement of the tubes. Several methods, regarding the passive technique, have been used in the past to enhance the heat transfer capability of the tubes such as adding surface roughness [93], [94], [95], utilizing ribs [54], [96], introducing corrugations [97], [57] and using helical-wire-coils [58]. Rafal *et al.* [98] investigated the thermal performance enhancement of U-tubes using wire inserts for Re = 800-9000 with water as a working fluid. The heat transfer performance of the enhanced U-tube was improved by 280% with wire inserts, contrary to the plain heat exchanger. Kumar *et al.* [96] enhanced the thermal-hydraulic performance of a double pipe heat exchanger having 180° U-bends by using twisted tape inserts. They used the inner tube of 19 mm diameter, annulus tube of 50 mm diameter, bend radius of 160 mm with a twist ratio of the tape of 10, 15, and 20. The working range of Reynolds number was 16000-32000 for nano-enhanced fluid. They found that heat transfer enhancement was in direct relation with the Re as well as nanoparticle concentration and inverse in relation with the twist ratio. At Re = 30000, for a tape twist ratio of 10, heat transfer increment of 38.7% at a frictional loss penalty of 25.1% was observed.

Similarly, Prasad *et al.* [99] performed experimental investigation of heat transfer enhancement of U-tube by employing twisted tape inserts at Re= 3000-30000. They used tape twist ratios of 5-20 and nano enhanced water with nanoparticle concentrations of 0.01% to 0.03%. They showed that for a tape twist ratio of 5, heat transfer was enhanced by 31.28% by using 0.03% nanofluid as compared to pure water at a hydraulic loss penalty of 23%. Sundar *et al.* [100] performed experimental analysis of thermal performance enhancement of U-tube annular heat exchanger by using wire coil and core-rod as inserts with different pitch ratios. They used Fe_3O_4 as a working nanofluid for Re = 16000-29000. They concluded that heat transfer augmented by 14.76% for nanofluid (0.06%) at Re = 28954 with a hydraulic loss penalty of 10%. Cho *et al.* [101] performed the experimental study of heat transfer for R-22 and R-407C refrigerants-oil mixtures in a U-tube enhanced with micro-fin tube. It was concluded that local heat transfer was maximum at 90° position of the U bend. It also observed that heat transfer in downstream tube section was 33% higher than that in the upstream tube section. In an another study, Sundar *et al.* [102] carried out the experimental study to quantify the effectiveness of U-tube using pure and nano enhanced water. They used wire coil inserts inside the plain tube for a range of $16000 < Re < 30000$. Furthermore, the effects of coil pitch to diameter ratio (p/d) on thermal-hydraulic performance of the U-tube were explored. It was observed that decrease in p/d ratio and increase in Reynolds number lead to augment the heat transfer rate. It was concluded that Nu increased by 32.03% for p/d = 1 at the Re = 28954 and nanofluid (0.06%) with a hydraulic loss penalty of 16.2%.

2.3 Research Gaps and Deliverables

Keeping in view, the immense potential of dimpled enhanced straight tubes in thermal–hydraulic performance augmentation, surprisingly there is no study in the literature exists that investigates the heat and fluid flow performance of dimpled enhanced U-tubes. It is pertinent to note that most of the studies did not keep the dimple volumes constant while comparing different dimple shapes. Consequently,

the comparison of different dimple features on the thermal-hydraulic performance of the enhanced tubes becomes questionable. It is therefore important to keep the total tube volume constant for each topological variation of the dimpled tube. One may argue that the overall Reynolds number should be kept the same, however, it is pertinent to mention that the Reynolds number is generally calculated using the hydraulic diameter, normally taken as base tube diameter, as the characteristic length. With the introduction of dimples, the local Reynolds number will be altered which will in return alter the flow physics and friction factor of the tube. However, a like-for-like case for comparison can only be expected if the tubes deliver or offer the same flow volumes. As noted in the literature, in most previous studies such consideration was not ensured and consequently, the surface area for each dimpled tube was effectively different. Therefore, the role of dimple shape especially when subjected to a comparison considering the thermo-hydraulic performance aspect remains an open question.

Based on the literature review, it can be seen that effect of change in ellipsoidal dimple orientation on the performance enhancement of augmented tube is not properly studied yet. Therefore, in chapter 4, the flow and heat transfer characteristics in dimpled tubes are investigated using numerical simulations. In order to ensure that the available volume for flow of incompressible fluid remain same, the dimple volumes are kept constant. Therefore, equal surface area of the dimples for each shape and orientation is ensured. The influence of the dimple geometry and its arrangement patterns on the heat transfer and flow characteristics are studied for a wide range of Reynolds numbers.

Through a parametric study, identification of the optimum dimple geometry as well as arrangement configuration are investigated using Reynolds Averaged Navier Stokes ($RANS$) under steady flow conditions. The flow physics which results in increase thermo-hydraulic performance of the optimum configuration is further investigated using Large Eddy Simulation (LES) to highlight the transport mechanism of heat and momentum. LES results provide insights on the unsteady dimpled tube flow with high resolution of the wake, elaborating the role of orientation of dimples and their spacing in terms of wake-dimple interaction.

It is also important to note that the distance behind each dimple should be considered while comparing different geometrical features. Moreover, different topological dimples have different axial/major-axis lengths, and the pitch for different geometrical dimpled tubes is expected to have different lengths in between the trailing and leading edges of consecutive dimples. In order to evaluate the influence of geometrical shapes defined as the distance from trailing edge of first dimple geometrical features to the leading edge of second dimple, is kept constant here. This shall provide an account for the effect of vortex formation at the trailing edge of each dimple in a fixed geometrical constraint. It may be argued that the distance behind the trailing edge of dimples is not an important feature.

However, it is pertinent to note that the fluid flow interaction with dimple is only completed when the consideration of both frontal interaction of the fluid with dimple and the formation of tail vortex at the trailing edge of same dimple are considered. If the distance from trailing edge of first dimple to the leading edge of second dimple in axial direction is kept same of each dimpled tube then this approach shall enable one to capture the effect of flow interaction with dimple and the resultant vortex formation. Therefore, a like-for-like case for comparison, can be only expected if the tubes deliver or offer same distance between the dimples while comparing the different shapes of dimples in comparison. It was observed in the literature that most previous studies do not account for such considerations and the concept of equal wake-length was not ensured and thus the resultant analyses may not have same ground for conclusion and reflection. Therefore, the role of wake distance of differently shaped dimples specially when put to a comparison while considering the characteristic of thermo-hydraulic performance remains an open question.

In chapter 5, the flow and heat transfer characteristics in dimpled tubes are investigated using numerical simulations. To ensure that the available distance between dimples, the distance from the leading edge of the upstream dimple to the leading edge of the downstream dimple remains constant for each tube. The influence of the pitch variation and its arrangement patterns on the heat transfer and flow

characteristics have been studied for a wide range of Reynolds numbers in turbulent flow regime. Through a parametric study, identification of the best pitch length with its geometry as well as arrangement configurations are investigated using $RANS$ under steady flow conditions. The thermo-hydraulic performance enhancement for the optimal configuration is investigated and categorized locally. The Literature also highlights that the circumferential spacing between the dimples or the number of dimples in the transverse plane referred to as "Star" is a crucial parameter in improving the thermal-hydraulic efficiency of the dimpled enhanced tubes. The effects of variations of Star on wake dynamics of dimples and the associated heat transfer enhancement along with viscous dissipation have not been investigated. Furthermore, a thorough understanding of the influence of various dimple-Star configurations on the convective heat transfer efficiency of the dimpled tubes is paramount.

Consequently, in chapter 6 for a wide range of turbulent Reynolds numbers, the thermal and hydraulic properties of dimpled tubes consisting of Teardrop (Zero-degree angle with the axial direction of the flow), Ellipsoidal- 0° (Zero-degree angle with the axial direction of the flow) and Ellipsoidal- 45° (45-degree angle with the axial direction of the flow) having various Star configurations are examined numerically. The optimum dimple geometry and Star configurations are identified. The local characterization of dimple-flow interactions and their impact on the overall flow dynamics and convection heat transfer of the tubes are also investigated in detail.

Moreover, the immense potential of dimple enhanced straight tubes in thermal-hydraulic performance augmentation, to the authors' surprise no study in the literature investigates the heat and fluid flow performance of dimpled enhanced U-tubes. Therefore, in the chapter 7, a numerical investigation of ellipsoidal 45° dimpled U-tube subjected to constant heat flux under turbulent flow conditions of $5000 \leq Re \leq 40000$ is carried out. The effects of different U-bend curvatures, of both smooth and dimpled tubes, on fluid flow and heat transfer characteristics, are analyzed in detail. The overall thermal-hydraulic performances of dimple enhanced U-tubes are estimated for different U-tube configurations. The effects of dimples

on the secondary flow vortices in the bend are also analyzed in detail. The local characteristics of heat transfer and each U-tube configuration are also examined.

2.4 Summary of Chapter 2

In this chapter, literature overview regarding the importance of boundary layer, classification and details of heat transfer methods is presented. Selection of dimple enhance tube in passive methods among the other techniques is discussed with the emphasize on the numerical simulation as a working environment. In the end, to address the engineering system regarding the fluid flow and heat transfer characteristics, incorporation of U-tube is discussed with the problems and shortcomings of the study.

Chapter 3

Numerical Methodology

3.1 Introduction

Fluid flow inside the tube is distinguished by the Reynolds number (Re) which provides the pattern of fluid flow. Flow at Low Re is called laminar flow while the flow at high Re is called turbulent flow. Cross flow profiles of fully developed laminar and turbulent flows are completely different especially near the wall and flow at the center of the tube. In laminar flow, the fluid flow is smooth while the fluid layers move over each other in an arranged manner and the boundary layer remains uniform. While in turbulent region, the fluid flow becomes unsteady. However, the region between laminar and turbulent is called transition region which unfolds complex series of events followed by radial change in fluid motion, as shown in the Figure 3.1. This results in chaotic and random state of fluid flow behavior where the pressure and velocity change frequently in fluid flow region. Defining different regions in the tube flows makes Re very essential parameter in the study of tube flows. The Reynolds number is a measure of inertial forces with respect to the viscous forces and is presented in equation (1.8). In the term of Re, laminar region lies at $Re \leq 2300$, transition region exists between the $2300 \leq Re \leq 4000$ and turbulent region stands at $Re \geq 4000$ [103]. To be on

the safer side for a completely turbulent flow we consider $Re = 5000$, since some transitions can be on $Re = 4000$.

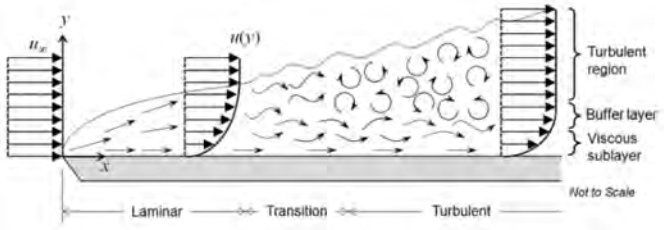

FIGURE 3.1: Schematic of laminar, transition and turbulence regions, [104]

In current study, steady state simulations are performed using $k - \omega$ SST (shear stress transport) model for predicting the turbulent viscosity (μ_t) and coupled scheme is used for pressure velocity coupling. SST $k - \omega$ model showed good results in confined flows where near wall effects were important [61]. The turbulent Prandtl number Pr_t and coupled scheme are detailed in ANSYS Theory Guide [25].

The instantaneous behavior of the flow was modeled using Large Eddy Simulations (LES). The dimples on the surface of the tube can generate secondary flow which consist of different scales of eddies. LES resolves large-scale eddies and models small-scale universal eddies. The accuracy of LES depends on the size of small eddies that are selected through eddy scale separation process. The scale separation of the eddies is performed by filtering out governing equations (in Appendix A) using a cutoff top hat filter Δ_{cell}. The filter size was equal to the cube root of size of computational cell [25], which yielded $\Delta_{cell} = 19.4\mu m$ for the current case. The turbulent viscosity (μ_t) used to account for the turbulent effect of small-scale eddies, was modeled using Smagorinsky Lilly model [105, 106]. The governing equations and LES method are given below while the details of numerical schemes, used in current study, are given in the Appendix A. Moreover, correlations of heat transfer and frictional loss of tubes at the end of each chapter are proposed using the least square method for curve fitting [107]. The basic structure of the Finite Volume Method is also presented in the Appendix A.

3.2 Governing Equations

The fluid flow can be depicted by the Navier stokes equations [108] since the working fluid, water, is supposed to be Newtonian. Therefore, the fluid flow is dictated by the Navier stokes equations whereas heat transfer determined by the energy transport set of equations. In current study, the fluid flow is assumed to be steady state for the transition and turbulent regions with constant fluid properties while viscous dissipation is negligible. These assumptions are successfully applied in many studies, as given in overview section (Passive techniques). ANSYS Fluent software resolved incompressible Navier Stokes equations. The general form of continuity, Navier Stokes equations with energy equation, for the incompressible flow with constant viscosity, are described in equations (3.1), (3.2) and (3.3), respectively [103].

$$\mathrm{div}\mathbf{u} = 0 \tag{3.1}$$

$$\begin{aligned}
\frac{\partial u}{\partial t} + \mathrm{div}(u\mathbf{u}) &= -\frac{1}{\rho}\frac{\partial p}{\partial x} + \nu \mathrm{div}(\mathrm{grad}u) \\
\frac{\partial v}{\partial t} + \mathrm{div}(v\mathbf{u}) &= -\frac{1}{\rho}\frac{\partial p}{\partial y} + \nu \mathrm{div}(\mathrm{grad}v) \\
\frac{\partial w}{\partial t} + \mathrm{div}(w\mathbf{u}) &= -\frac{1}{\rho}\frac{\partial p}{\partial z} + \nu \mathrm{div}(\mathrm{grad}w) \\
\rho c_p \frac{\partial T}{\partial t} &= -p\mathrm{div}u + \mathrm{div}(k\mathrm{grad}T) + \Phi
\end{aligned} \tag{3.2}$$

where

$$\begin{aligned}
\Phi = \mu\Big\{2\Big[\Big(\frac{\partial u}{\partial x}\Big)^2 + \Big(\frac{\partial v}{\partial y}\Big)^2 + \Big(\frac{\partial w}{\partial z}\Big)^2\Big] + \Big(\frac{\partial u}{\partial y} + \frac{\partial v}{\partial x}\Big)^2 + \\
\Big(\frac{\partial u}{\partial z} + \frac{\partial w}{\partial x}\Big)^2 + \Big(\frac{\partial v}{\partial z} + \frac{\partial w}{\partial y}\Big)^2\Big\} + \lambda(\mathrm{div}\mathbf{u})^2
\end{aligned} \tag{3.3}$$

Here ρ, T, μ, ν, k, u denote the density, temperature, dynamic viscosity, kinematic viscosity, thermal conductivity and velocity respectively, while the $\mathbf{u}$ represents the vector representation of velocity with u, v and w components in x, y and z

direction. In equations (3.1), (3.2), and (3.3), the transient term can be neglected, for the steady-state simulations.

The Richardson number is the ratio of Grashof number ($G_r = g\beta(T_w - T_m)D^3/\nu^2$) to the square root of Re determines the buoyancy driven flow which characterizes the flow as natural or force convection [12]. Where g is the gravitational acceleration and β is the coefficient of thermal expansion. The Richardson number at the $Re = 12000$ for the current study is 0.00016944 which is far less than 1. It determines the inertial forces are very high and gravitational forces are weak so that the natural convection and gravitational acceleration can be ignored because it is pure force convection heat transfer. Therefore, in the current study, gravity/body forces is ignored.

3.3 Turbulence Modelling

3.3.1 Reynolds Averaged Navier Stokes (RANS)

Reynolds Average Navior Stokes (RANS) means the averaging of general governing equations to estimate the flow properties. Before going to the modelling of flow properties, turbulence behavior is discussed here, in brief. As given above, the chaotic and random nature of final turbulent state becomes fundamentally unsteady even with steady state enforced boundary condition, a typical measurement of point velocity may display the form as shown below:

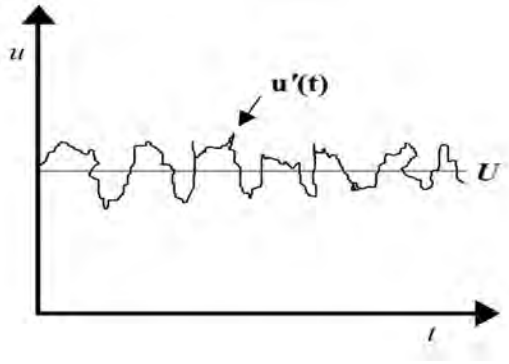

FIGURE 3.2: Point velocity measurement in turbulent flow

Figure 3.2 shows the point velocity measurement for the turbulent flow which can be split into steady mean velocity U with fluctuating component $u'(t)$ placed on it $(u(t) = U + u'(t))$.

Here, it is important to characterize a turbulent fluid flow by the mean values $(U, V, W$ etc.) and the statistical properties of fluctuations $(u', v', w'$ etc.) for the flow properties. In order to do so, let first define the mean Φ of flow property ϕ as given here:

$$\Phi = \frac{1}{\delta t} \int_0^{\delta t} \phi(t) dt \tag{3.4}$$

The flow property ϕ is dependent on time and consider as the sum of fluctuating component ϕ' with the mean value of zero and a steady mean component Φ, therefore $\phi(t) = \Phi + \phi'(t)$. The mean time of ϕ' is, by definition, zero [103]:

$$\overline{\phi'} = \frac{1}{\delta t} \int_0^{\delta t} \phi'(t) dt \equiv 0 \tag{3.5}$$

The root mean square root of the fluctuations can now provide its information, as given here:

$$\phi_{rms} = \sqrt{\overline{(\phi')^2}} = \Big[\frac{1}{\delta t} \int_0^{\delta t} \phi'(t)^2 dt\Big]^{1/2} \tag{3.6}$$

The root mean square values of velocity components are of specific importance as they can be easily measured by the velocity prob sensitive to the turbulence fluctuations and simple electrical circuit.

The kinetic energy and turbulence intensity are directly related with turbulent fluctuation and reference mean flow velocity, respectively. Similarly, the effect of fluctuations on the flow variables ($\mathbf{u} = \mathbf{U} + \mathbf{u}', u = U + u', v = V + v', w = W + w', p = P + p'$) used in Navier-Stokes equations can be changed to measurable values and through some calculations we can get the final form [103], as given here:

Continuity Equation

$$\text{div}\mathbf{U} = 0 \tag{3.7}$$

Reynolds Averaged Navier Stokes Equations

$$\begin{aligned}
\frac{\partial U}{\partial t} + \text{div}U\mathbf{U} &= -\frac{1}{\rho}\frac{\partial P}{\partial x} + \nu\text{div}(\text{grad}U) + \frac{1}{\rho}\Big[\frac{\partial(-\rho\overline{u'^2})}{\partial x} + \frac{\partial(-\rho\overline{u'v'})}{\partial y} + \frac{\partial(-\rho\overline{u'w'})}{\partial z}\Big] \\
\frac{\partial V}{\partial t} + \text{div}V\mathbf{U} &= -\frac{1}{\rho}\frac{\partial P}{\partial y} + \nu\text{div}(\text{grad}V) + \frac{1}{\rho}\Big[\frac{\partial(-\rho\overline{u'v'})}{\partial x} + \frac{\partial(-\rho\overline{v'^2})}{\partial y} + \frac{\partial(-\rho\overline{v'w'})}{\partial z}\Big] \\
\frac{\partial W}{\partial t} + \text{div}W\mathbf{U} &= -\frac{1}{\rho}\frac{\partial P}{\partial z} + \nu\text{div}(\text{grad}W) + \frac{1}{\rho}\Big[\frac{\partial(-\rho\overline{u'w'})}{\partial x} + \frac{\partial(-\rho\overline{v'w'})}{\partial y} + \frac{\partial(-\rho\overline{w'^2})}{\partial z}\Big]
\end{aligned} \tag{3.8}$$

In these equations, eddy viscosity is not considered yet however if the eddy viscosity or turbulent is incorporated from the shear stresses $\tau_{ij} = -\rho(\overline{u_i'u_j'}) = \mu_t(\frac{\partial U_i}{\partial x_j} + \frac{\partial U_j}{\partial x_i})$, then it is computed by the models used in the study while keeping in view that the boundary layer differs in laminar and turbulent flow due to the fluid flow characteristics. In turbulence, instabilities occur in the fluid flow which lead to random vorticity formation [109].

This rotational flow in the turbulence are called eddies which varies from large scale Kolmogorov to smallest scale. The large-scale eddies are mainly dependent on the inertia whereas the smaller eddies are primarily affected by viscosity. The eddies with an extensive span of length and time scale categorize the turbulent flows. Comparatively larger eddies are corresponded in the magnitude of mean flow characteristics length. While, the smallest ones are amenable to the turbulence kinetic energy dissipation.

There are different numerical techniques that are used to capture the turbulence region according to the applications of the system space. For example, $RANS$, LES, and Direct numerical simulation (DNS) numerical simulations are different numerical approaches, as shown in Figure 3.3a. It denotes that the main flow contains the spectrum from larger eddies to very small eddies. DNS resolves the whole spectrum of the turbulence while LES resolves larger eddies and models

the smaller ones. However, *RANS* only models the complete spectrum of eddies. The results of these numerical techniques, in the form of jet flow, are shown in Figure 3.3b. In many cases, only time-averaged values are of interest. Similarly, *LES* resolves the major fluctuations, therefore, it can predict the major portion of the disturbed boundary layer which results in the determination of medium turbulence flow physics [104].

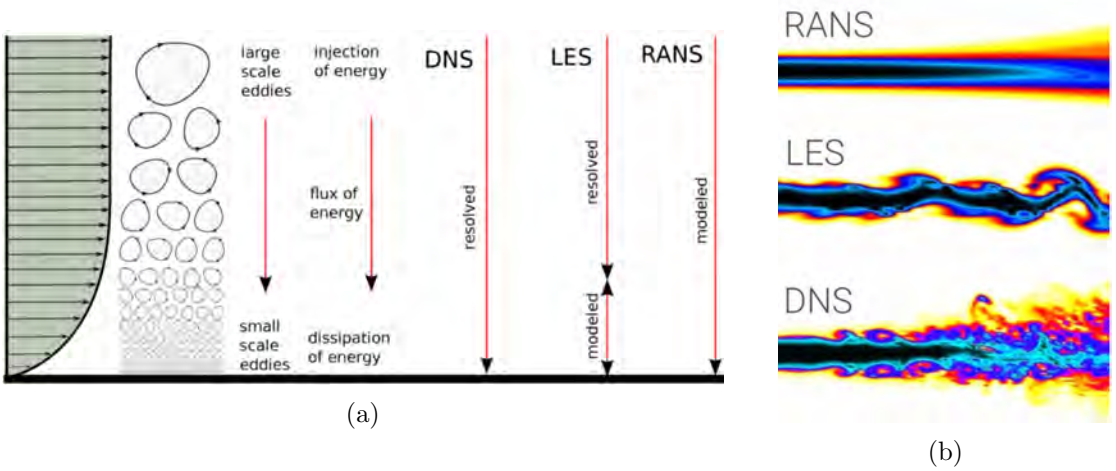

(a) (b)

FIGURE 3.3: Comparison of *RANS*, *LES* and *DNS* techniques (a) Schematic [104] and (b) simulation results [110]

The SST model captures the near boundary layer region using the standard $k-\omega$ model and it uses the blending function for the conversion of $k-\omega$ model to $k-\epsilon$ model which is best for capturing the flow, away from the wall region, is shown in the Figure. 3.4 [104].

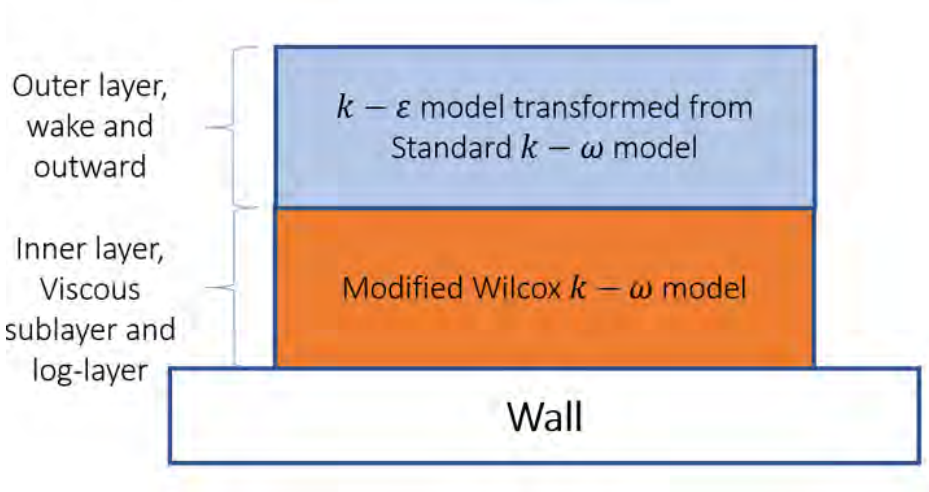

FIGURE 3.4: Schematic of usage of $k-\omega$ SST model, [25]

DNS can be resolved the complete range of turbulence. However, it is computationally very expensive [104]. Therefore, it is not feasible to use the DNS in large range of engineering problems in limited time.

In comparison to DNS, Large eddy simulation LES directly resolve the larger eddies while it model the smallest ones. So, it works between the DNS and $RANS$. The run time for LES to obtain stable statics of the modeled is sufficiently long.

In current study, single phase flow in the enhanced tube will be simulated through the $RANS$ ($k-\omega$ SST model) and LES (Sub-grid-scale model). The $k-\omega$ SST model is given below while the modeling of LES will be explained later, in this chapter.

3.3.2 Transport Equations for (SST) $k-\omega$ Model

The $k-\omega$ turbulence model solves two transported variable equations and interprets for convection and diffusion and known to be two equation model. These two variables are turbulent kinetic energy (k) and Turbulent dissipation rate ω. The definition of k is given below:

$$\mathrm{k} = 3/2(UI)^2 \tag{3.9}$$

where $I = u'/U$ is the turbulent intensity and u' is the root mean square of the turbulence velocity fluctuations or it can be written as $u' = \sqrt{2/3k}$. Similarly, the definition of ω given here:

$$\omega = (C_\mu)^{3/4}(k^{1/2}/l) \tag{3.10}$$

where C_μ is the turbulence model constant with the usual value of 0.09 and l is the turbulence length scale.

As given above, $k-\omega$ model is best for complex boundary layer flow under adverse pressure gradient. SST (shear stress transport) model is established to proficiently blend the effective and distinct expression of $k-\omega$ model nearby wall regime,

whereas it uses $k-\epsilon$ away from the wall. $k-\omega$ SST model has following transport equations for k and ω respectively [25]:

$$\frac{\partial}{\partial t}(\rho k) + \text{div}(\rho k \mathbf{U}) = \text{div}\left(\Gamma_k \text{grad} k\right) + \tilde{G}_k - Y_k + S_k \tag{3.11}$$

and

$$\frac{\partial}{\partial t}(\rho \omega) + \text{div}(\rho \omega \mathbf{U}) = \text{div}\left(\Gamma_\omega \text{grad} \omega\right) + G_\omega - Y_\omega + D_\omega + S_\omega \tag{3.12}$$

Here $\tilde{G}_k$ is the kinetic energy of the turbulence, G_ω is the ω production. While the Γ_k and Γ_ω denote the efficient k and ω dissipation respectively. Similarly, turbulence dissipation of k and ω are denoted by Y_k and Y_ω correspondingly. D_ω represents the cross-diffusion, while the S_k, S_ω are source terms.

3.3.2.1 Effective Diffusivity

$$\Gamma_k = \mu + \frac{\mu_t}{\sigma_k}, \qquad \Gamma_\omega = \mu + \frac{\mu_t}{\sigma_\omega} \tag{3.13}$$

Here σ_k & σ_ω represent turbulent Prandtl numbers of k and and ω respectively. μ_t is the turbulent viscosity and its definition is given here:

$$\mu_t = \frac{\rho k}{\omega} \frac{1}{\max(\frac{1}{a^*}, \frac{SF_2}{a_1 \omega})} \tag{3.14}$$

Here S denotes the strain rate

$\sigma_k = \frac{1}{\frac{F_1}{\sigma_{k,1}} + \frac{1-F_1}{\sigma_{k,2}}} \sigma_\omega = \frac{1}{\frac{F_1}{\sigma_{\omega,1}} + \frac{1-F_1}{\sigma_{\omega,2}}}$, here F_1 and F_2 are blending functions, given as

$$F_1 = \tanh(\Phi_1^4) \tag{3.15}$$

where

$$\Phi_1 = \min\left[\max(\frac{\sqrt{k}}{0.09\omega y}, \frac{4\rho k}{\sigma_{\omega,2} D_\omega^+ y^2})\right] \tag{3.16}$$

in which the D_ω^+ is shown here:

$$D_\omega^+ = \max[2\rho \frac{1}{\sigma_{\omega,2}} \frac{1}{\omega} \frac{\partial k}{\partial x_j} \frac{\partial \omega}{\partial x_j}, 10^{-10}] \tag{3.17}$$

$$F_2 = \tanh(\Phi_2^2) \tag{3.18}$$

where

$$\Phi_2 = \max(\frac{2\sqrt{k}}{0.09\omega y} \frac{500\mu}{\rho\omega y^2}) \tag{3.19}$$

Where y symbolizes surface distance where as D_ω^+ denotes the plus section of cross-diffusion [25].

3.4 Large Eddy Simulation (LES)

In $RANS$, the flow property can be divided into the mean flow and the fluctuating term, while in LES, it is divided into filtered term and modeled term.

Larger eddies are mainly driven by the inertia and the smaller one is driven by viscous forces. In LES spatial filters are used which distinguished the large eddies and the small eddies. Spatial filtering method is given below:

3.4.1 Spatial Filtering Method for the Unsteady Navier-Stokes Equations

The turbulence scale separation is achieved by applying a filtering process to the governing equations. The filtration process is discussed below.

3.4.1.1 Filtering Functions

In *LES*, spatial filtering operations through a filter function $G(x, x', \triangle)$ are defined, as given below:

$$\overline{\phi}(\vec{x}, t) = \iiint_{-\infty}^{\infty} G(\vec{x}, \vec{x}', \triangle)\phi(\vec{x}', t)dx_1^{'}dx_2^{'}dx_3^{'} \tag{3.20}$$

Where, $\phi(\vec{x}', t)$ = unfiltered (original) function $\overline{\phi}(\vec{x}, t)$ = filtered function $\triangle$ = filtered cutoff width

The simplest forms of the function for 3D LES computations are Box filter or top hat:

$$G(\vec{x}, \vec{x}^{'}, \triangle) = \begin{cases} 0, & |\vec{x} - \vec{a}'| > \triangle/2 \\ \frac{1}{\triangle^3}, & |\vec{x} - \vec{a}'| < \triangle/2 \end{cases}$$

Gaussian filter:

$$G(\vec{x}, \vec{x}^{'}, \triangle) = (\frac{\gamma}{\pi\triangle^2})^{3/2} \exp{(-\gamma \frac{|\ \vec{x} - \vec{x}^{'}\ |^2}{\triangle^2})} \tag{3.21}$$

Typical value for parameter $\gamma = 6$ Spectral cutoff:

$$G(\vec{x}, \vec{x}^{'}, \triangle) = \prod_{i=1}^{3} \frac{\sin{([x - x_i^{'}]/\triangle)}}{x - x_i^{'}} \tag{3.22}$$

Box filter or top hat is applied in finite volume employment of **LES** and $\triangle$ is topical grid-scale while it is calculated in coherence with computational cell volume by $\triangle = V^{1/3}$.

3.4.2 Filtered Equations

If the filtering function $G(\vec{x}, \vec{x}^{'}) = G(\vec{x} - \vec{x}^{'})$ is used throughout the computational domain in order to make independence of G from position x, the simplified form of algebric calculation is possible. After incorporating the filtering function, the equations for the LES becomes:

Continuity equation

$$\mathrm{div}(\widetilde{\mathbf{u}}) = 0 \tag{3.23}$$

Reynolds equations

$$\begin{aligned}
\frac{\partial \widetilde{u}}{\partial t} + \mathrm{div}(\widetilde{u}\widetilde{\mathbf{u}}) &= -\frac{1}{\rho}\frac{\partial \widetilde{p}}{\partial x} + \nu \mathrm{div}(\mathrm{grad}(\widetilde{u})) - (\mathrm{div}(\widetilde{u\mathbf{u}}) - \mathrm{div}(\widetilde{u}\widetilde{\mathbf{u}})) \\
\frac{\partial \widetilde{v}}{\partial t} + \mathrm{div}(\widetilde{v}\widetilde{\mathbf{u}}) &= -\frac{1}{\rho}\frac{\partial \widetilde{p}}{\partial y} + \nu \mathrm{div}(\mathrm{grad}(\widetilde{v})) - (\mathrm{div}(\widetilde{v\mathbf{u}}) - \mathrm{div}(\widetilde{v}\widetilde{\mathbf{u}})) \\
\frac{\partial \widetilde{w}}{\partial t} + \mathrm{div}(\widetilde{w}\widetilde{\mathbf{u}}) &= -\frac{1}{\rho}\frac{\partial \widetilde{p}}{\partial z} + \nu \mathrm{div}(\mathrm{grad}(\widetilde{w})) - (\mathrm{div}(\widetilde{w\mathbf{u}}) - \mathrm{div}(\widetilde{w}\widetilde{\mathbf{u}}))
\end{aligned} \tag{3.24}$$

Where $\mathrm{div}(\widetilde{w\mathbf{u}}) - \mathrm{div}(\widetilde{w}\widetilde{\mathbf{u}}) = \frac{\partial \tau_{ij}}{\partial x_j}$, and τ_{ij} is refer to convection momentum equation due to interaction between the unresolved eddies, which are called sub-grid-scale (SGS) stresses, [103].

3.4.3 Selection of the Model

Several models have been developed in recent few decades which use the Boussinesq hypothesis to compute eddy viscosity. However, for engineering problems, the models can be divided into two categories namely Smagorinsky and dynamic models. Smagorinsky uses constant eddy viscosity coefficient for the entire flow domain and is not valid for the complex engineering flows. While the dynamic model varies the constant value through out the domain directs by local flow characteristics [111] which is suitable for the complex flow problems. For example, the authors of [112] and [113] used model in the straight and curved flow pipes while Yang *et al.* [114] used Smagorinsky for the rotating pipe flow.

Tutar *et al.* [115] utilized the Smagorinsky Lilly Model in the LES simulation of flow around the circular cylinder. He observed that results of turbulence model based on the Smagorinsky Lilly Model produced more reasonable results than the two equation model or RSM. Gong *et al.* [116] used the Smagorinsky Lilly Model to capture the wake characteristics around the valve. They presented the evolution of vortices around the valve to illustrate the formation of the single

vortex propagating downstream. Smagorinsky [117] developed the Smagorinsky model which is further developed by the Lilly [105, 106] and it is discussed in the coming section.

3.4.4 Smagorinsky Lilly Model

This model utilized the boussinesq hypothesis for calculating the sub-grid turbulence stresses. These stresses compute from:

$$\tau_{\mathbf{ij}} - 1/3\tau_{\mathbf{kk}}\triangle_{\mathbf{ij}} = -2\mu_{\mathbf{t}}\mathbf{S_{ij}} \tag{3.25}$$

Here μ_t is the turbulent viscosity of the sub-grid-scale. Furthermore, the τ_{kk} is not demonstrated here, though contributed to the filtrated static-pressure expression. $\overline{S}_{ij}$ is the strain-rate tensor for the calculated scale defined by:

$$\overline{\mathbf{S}}_{ij} = \frac{1}{2}\Big(\frac{\partial \mathbf{u_i}}{\partial \mathbf{x_j}} + \frac{\partial \mathbf{u_j}}{\partial \mathbf{x_i}}\Big) \tag{3.26}$$

Eddy viscosity is utilized in this model as follows:

$$\mu_t = \rho L_s^2 |\overline{S}| \tag{3.27}$$

And L_s is combining length for subgrid-scales while $|\overline{S}| = \sqrt{2\overline{S}_{ij}\overline{S}_{ij}}$. Similarly, L_s is calculated:

$$L_s = \text{minimum}(kd, C_s\triangle)$$

where k is constant of Von-Karman, d is the near-wall distance, C_s is constant value of Smagorinsky and $\triangle$, as given above, is topical grid-scale while it is calculated in coherence with computational cell volume by $\triangle = V^{(1/3)}$. Furthermore, C_s is the Smagorinsky constant and its value is selected to be 0.1, [25].

Chapter 4

Role of Dimple Topologies in Thermal-Hydraulic Performance Enhancement of Tubes

4.1 Introduction

In this chapter, the flow and heat transfer characteristics of dimpled tubes are investigated using numerical simulations. At first, the numerical outcomes (Nu) and (fr) of smooth tube are compared with the empirical correlation. Afterwards, the conical, spherical and ellipsoidal dimpled tubes are analyzed and their heat transfer and hydraulic losses are compared. To ensure that the available volume for flow of incompressible fluid remained same, the dimple volumes are kept constant. Therefore, equal surface area of the dimples for each shape and orientation is ensured. The ellipsoidal dimpled tube is provided better heat transfer characteristics with relatively less friction. Afterwards, the orientation of ellipsoidal dimple with tube axis has been varied from 0° to 90° and the influence of the dimple geometry and its arrangement patterns on the heat transfer and flow characteristics are studied for a wide range of Reynolds numbers.

Through a parametric study, identification of the optimum dimple geometry as well as arrangement configuration are investigated using Reynolds Averaged Navier Stokes ($RANS$) under steady flow conditions. The flow physics which resulted in increased thermo-hydraulic performance of the optimum configuration is further investigated using Large Eddy Simulation (LES) to highlight the transport mechanism of heat and momentum. LES results provided insights on the unsteady dimpled tube flow with high resolution of the wake, elaborating the role of orientation of dimples and their spacing in terms of wake-dimple interaction. In addition, correlations for Nusselt number and friction factor that cover all angular topologies of ellipsoidal dimpled tube are proposed.

4.2 Computational Domain

4.2.1 Geometry and Boundary Conditions

The computational domain is a tube of diameter D_h with dimple diameter D_p, dimple depth H and center to center distance, as shown in Figure 4.1a-4.1c. The length of the tube is 120 mm; however, the effective enhanced tube length is selected to be 100 mm in order to eliminate any spurious effects of inlet and outlet boundary conditions. The inward facing dimples in the tube are positioned in the in-line and staggered arrangements, as presented in Figure 4.1d. The dimples in the inline configuration are in-phased while in the staggered configuration dimples are out of phase. The number of dimples in circumferential direction is referred in this study as "Star". Ten dimples are used in the axial direction for all configurations. The dimples shape along with other geometrical parameters are presented in Table 4.1. Three different shapes of dimples consisting of conical, spherical and ellipsoidal profiles are used which are shown in Figure 4.2a-4.2c while the conical, spherical and ellipsoidal dimpled tubes are also shown for the complete view in Figure 4.3a-4.3c, respectively. These tubes are also used in the numerical investigation by Li *et. al.*[22].

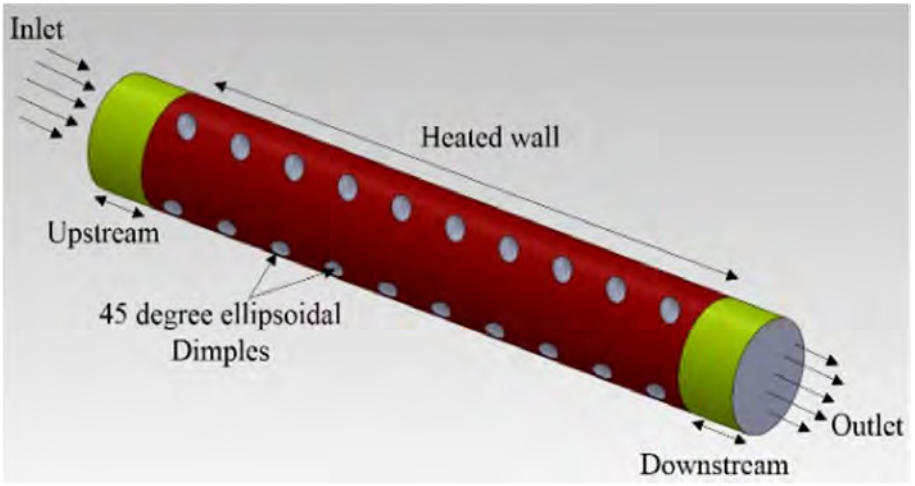

(a)

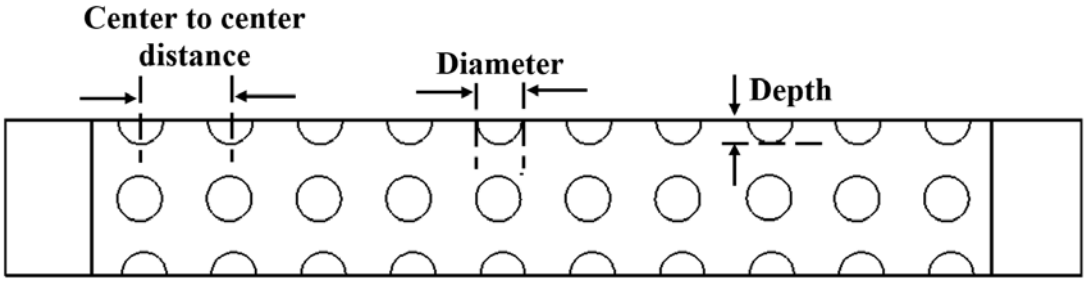

(b)

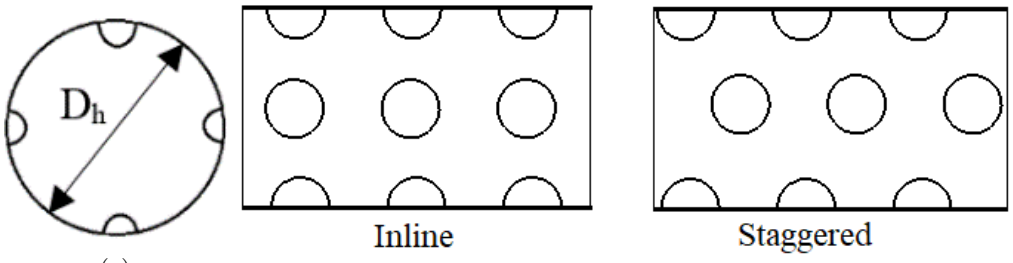

(c) (d)

FIGURE 4.1: (a) Geometry of the ellipsoidal dimpled tube (b) geometric properties of dimple (center to center distance, diameter and depth) (c) cross-section of dimpled tube (d) dimple inline and staggered configurations

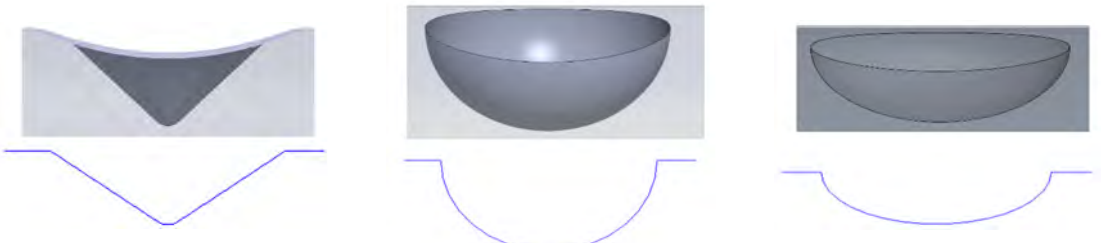

(a) (b) (c)

FIGURE 4.2: Shapes of dimples (a) conical (b) spherical (c) ellipsoidal

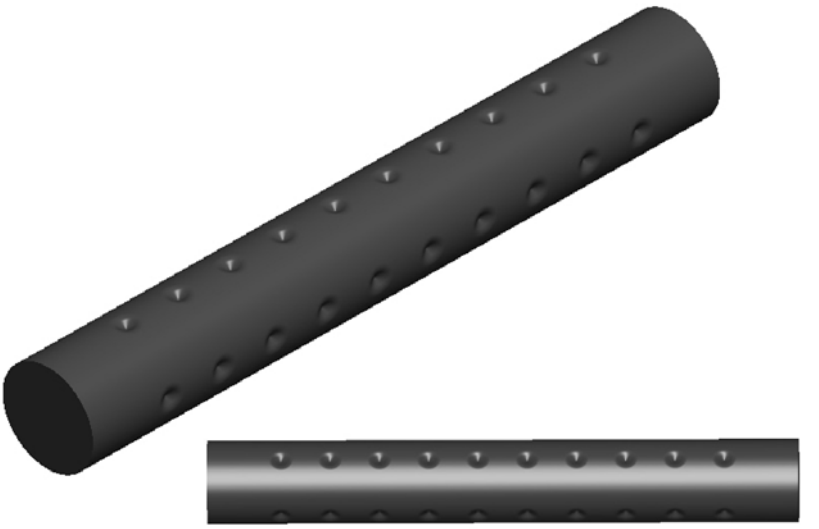

(a)

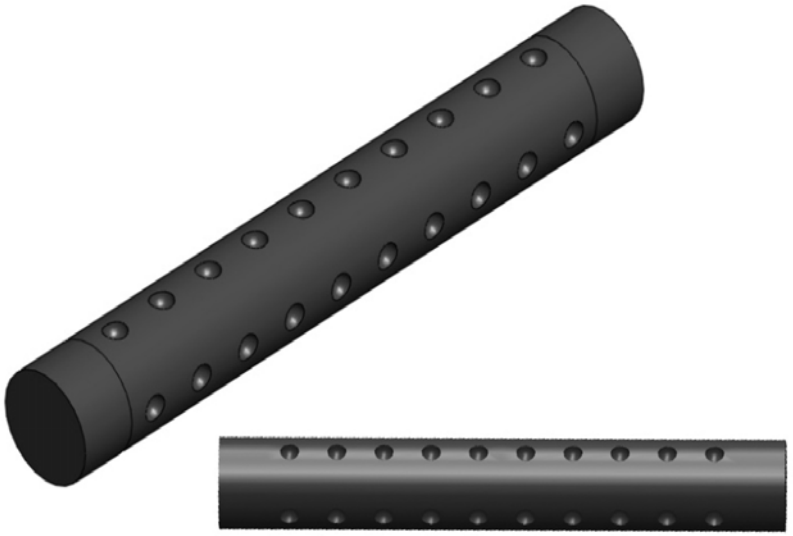

(b)

(c)

FIGURE 4.3: Geometry of enhanced tubes having different dimple shapes: (a) conical (b) spherical (c) ellipsoidal

TABLE 4.1: Parameters of all tubes used for validation

Sr. No.	(D_h) (mm)	Dimple Profile	Depth(H) (mm)	Center to center distance (mm)	(D_p) (mm)	Star	Configuration
tube 1	17.272	conical	1.2	10	5	6	staggered
tube 2	17.272	conical	1.2	10	5	6	inline
tube 3	17.272	conical	1.2	10	5	4	inline
tube 4	17.272	spherical	2.5	10	5	4	inline
tube 5	17.272	ellipsoidal(0°)	1.5	10	5	4	inline

4.2.2 Boundary Conditions

The flow at the inlet of the channel is considered to be fully developed. A turbulent inlet velocity profile, representing the fully developed flow using $1/7^{th}$ power law [118], is imposed as the inlet boundary condition. The velocity profile at the inlet of the tube is presented in following equation (4.1).

$$\frac{U}{U_c} = (1 - \frac{r}{R_h})^{1/7} \tag{4.1}$$

where r denotes the radial distance, R_h is half of the hydraulic diameter of tube. At the outlet, pressure outlet boundary condition is used which considers zero-gauge pressure at outlet while no slip condition boundary condition is used at the wall. The working fluid is water with constant fluid properties. The density of water is $994.57 kg/m^3$, dynamic viscosity is $7.5407 \times 10^{-4} kg/m.s$, thermal conductivity is $0.62215 W/m.K$ and a Prandtl number is 4.8734. The operating temperature range in this work is sufficiently small therefore these properties are considered as constant. Generally, the surface of the tubes can be heated by maintaining three different types of thermal boundary conditions: (i) uniform wall temperature circumferentially and uniform heat flux axially, (ii) uniform wall heat flux in both axial and circumferential direction, and (iii) uniform wall temperature. However, according to [61], the choice of thermal boundary conditions does not effect thermal and hydraulic trends of the enhanced tubes. Therefore, in the current study, a uniform wall heat flux in both axial and circumferential direction is applied. The

value of heat flux is set as $10kW/m^2$, which is uniformly applied along the length of the tube as shown in Figure 4.1a. This heat flux value is selected as the reference value based on the experimental work of Li *et al.* [22]. The adiabatic condition is applied at the upstream and downstream part of the dimpled tube. The collective information of boundary conditions is given in Table 4.2.

TABLE 4.2: Boundary condition (BC) for the tube analysis and modeling

Inlet	Velocity inlet
Inlet(thermal)	305.5K
Outlet	Pressure outlet (0-gauge pressure)
Wall(friction)	No slip
Wall(thermal)	Constant heat flux 10 kW/m^2
Up and downstream	Adiabatic condition
Working fluid	Water, with constant properties

4.2.3 Grid Generation of Dimple Enhanced Tube

The domain discretization is performed by generating a structured mesh with refinement at near plane wall and dimple surface, as presented in Figure 4.4a - 4.4d. For this, ICEM CFD is used to generate the structured blocking for multi region which helps to generate the high resolution grid at the area of interest [103]. In order to do it, the original block is sliced in axial and radial direction along with the generation of "O-grid" around the dimples, as shown in Figure 4.4a.

In current study, the dimple is the area of high resolution, therefore, a high-quality mesh around the dimples is imperative since the flow separation, attachment, vortex formation and flow mixing take place in the vicinity of the dimple. Therefore, additional care is taken while generating the mesh around the dimples. On the other hand, minimum mesh density is used away from the dimple in order to avoid extra mesh size.

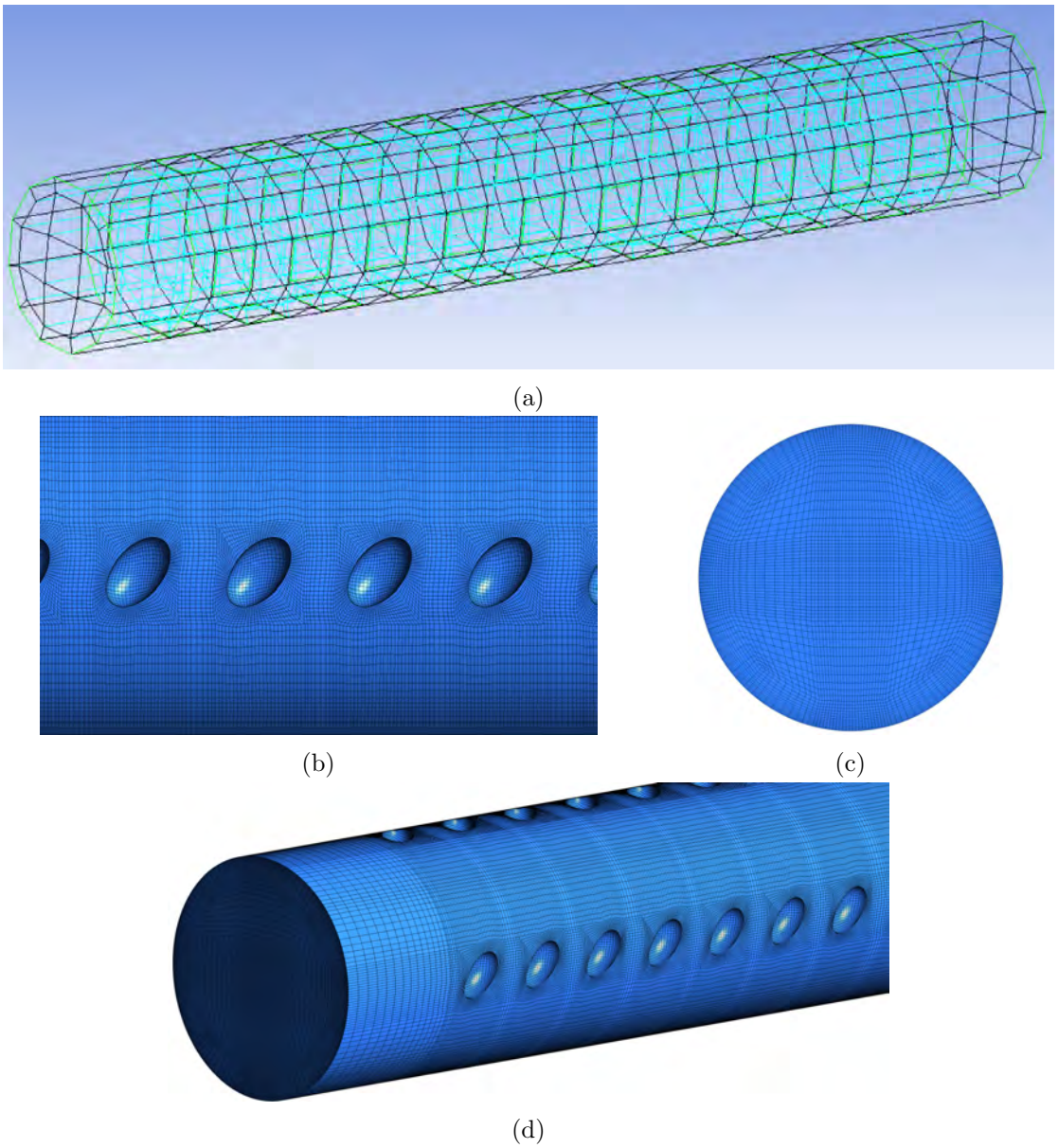

FIGURE 4.4: (a) Structured Blocking of dimpled tube, (b-d) Orientations of structured grid of ellipsoidal 45° dimpled tube

4.2.4 Grid Independence Study

A thorough mesh independence study is conducted and results for the case of tube 3 at Re=5000 and 9000 are presented below. The resultant Nu and fr are presented in Table 4.3 for different mesh sizes for the selected cases. The number of cells, for different mesh sizes, are varied from 0.28 million (Coarse mesh) to 6.5 million (Fine Mesh). The percentage difference in Nu and fr is increased as the

mesh size is reducing, however, it becomes constant at a 2.0 million mesh size. In order to ensure that the mesh dependent variations are taken care of, a 3.0 million mesh is selected for all computational analyses presented in this paper. Moreover, the accuracy of the solution of turbulent flow depends on the resolution of the mesh in boundary layer region. In the selected mesh of 3.0 million elements, the resultant $y^+ \approx 0.51$ is noted which ensures that the mesh size is adequate to resolve the near wall effects.

TABLE 4.3: Grid independence study of conical staggered enhanced tube (tube 3)

Grid	Re = 5000		Re = 9000	
(Millions)	Nu	fr	Nu	fr
0.28	74.8	0.0820	112.0275	0.0761
1	69.36	0.0780	112.2322	0.0701
2	68.33	0.07815	11.9493	0.0679
3	68.31	0.0783	112.9873	0.06592
6.5	68.30	0.07835	112.9879	0.0650

4.3 Results and Discussion

4.3.1 Validation

The validation of numerical methodology is performed by comparing the results of smooth tubes with empirical correlations and the dimpled tubes with experimental results from literature. Typically, the most appropriate correlation to compare the numerical Nu would be the Gnielinski correlation [119] as shown in equation (4.2). The numerical friction factor is compared with the correlation presented by Petukhov [120] in for smooth tube, as given in equation (4.3).

$$Nu = \frac{(fr/8)(Re - 1000)Pr}{1 + 12.7(fr/8)^{1/2}(Pr^{2/3} - 1)} \tag{4.2}$$

$$fr = (0.79lnRe - 1.64)^{-2} \tag{4.3}$$

The equation (4.2) is valid for a large range of Pr; $0.5 \leq Pr \leq 2000$. The equation (4.2) and (4.3) are valid for $3000 \leq Re \leq 5 \times 10^6$.

Figure 4.5a - 4.5b shows comparison between numerical results and experimental correlations of smooth tubes. Typically, in smooth tubes, Nu is directly proportional to the Re while fr is inversely proportional to the Re. This trend can be observed in Figure 4.5a which shows that the numerical simulations also predict increase in Nu with increasing Re and a decrease in fr with increase in Re. The percentage difference between the numerical results and correlations results of Nu and fr is well with the range of 15%. The maximum difference is in transition region.

The numerical results are also validated for the enhanced tubes and here some of the results with conical dimples are presented. The Nu and fr of tube 1 and tube 2 (referred to Table 4.1) are compared with experimental results of Li *et al.* [22]. They have used thermocouples for their experimental apparatus for heat transfer measurement. Initially, they have validated the smooth tube results (Nu and fr) with the empirical correlation following the generation of conical tube results. And these results are validated and compared in current study. The results from the present numerical study have shown a reasonably accurate comparison to the experimental and numerical results, as depicted in Figure 4.6a - 4.6b. It can be observed from Figure 4.6a - 4.6b that Nu increases and fr decreases for both tube 1 and tube 2 with increasing Re. A maximum deviation of 24.4% is observed for Nu and 18.34% for fr predictions. It is also observed that root mean square error ($RMSE$) is 11.635 for the Nu while it is 0.016523 for fr.

It is pertinent to mention that the turbulence models in $RANS$ are known to over predict the hydraulic losses and heat transfer coefficient in the transition region [68] and [61]. Therefore, the discrepancies between the experimental and numerical results are expected in the transition region and reasonably matches well with the previously reported trends. It can be noted that the maximum difference

between the experimental and numerical results is observed in the transition Re region. However, as the flow becomes fully turbulent, the turbulence closure model improves the accuracy of the results by reducing the percentage difference to less than 4% for Nu and 10% for fr.

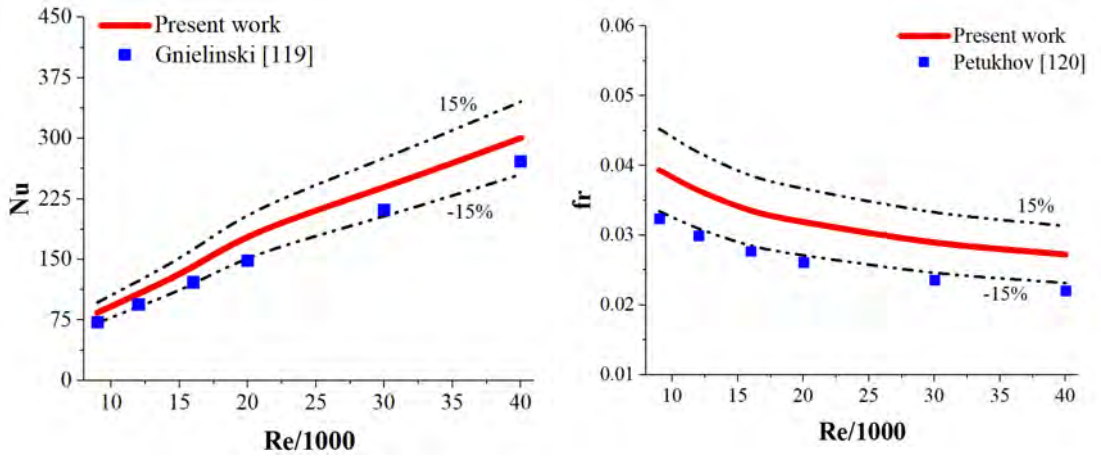

(a) (b)

FIGURE 4.5: Comparison of predicted results with empirical correlations (i.e. Gnielnski [119]) (a) Nu and (Filonieko [120]) (b) fr

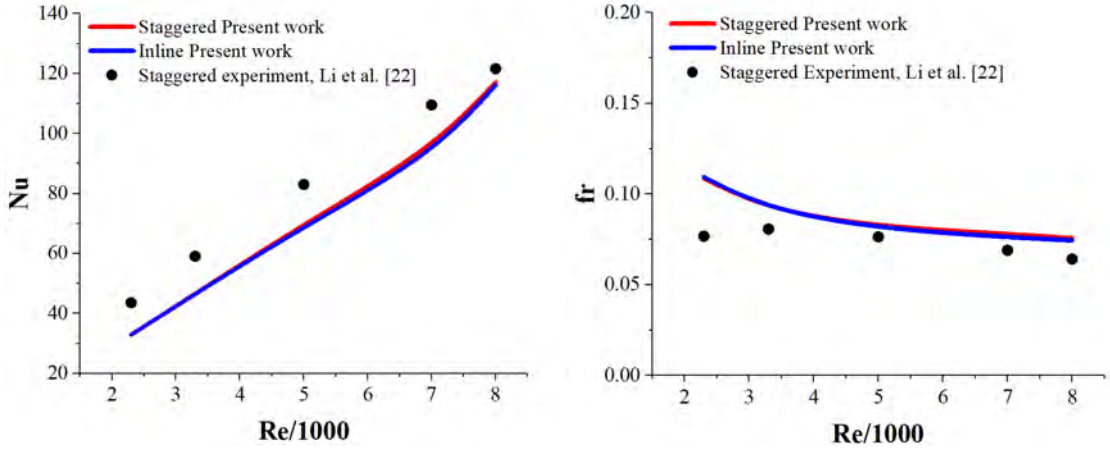

(a) (b)

FIGURE 4.6: Comparison of present work of tubes 1 and 2 with experimental results of Li et al., [22], (a) Nu and (b) fr

The validations with the numerical results of Li *et al.* [61] are also performed for tube 3, tube 4 and tube 5. The Nu and fr are compared in Figure 4.7a - 4.7b for $2300 \leq Re \leq 15000$. It can be noted in Figure 4.7a that the spherical dimple demonstrates highest heat transfer rate in comparison to ellipsoidal and conical

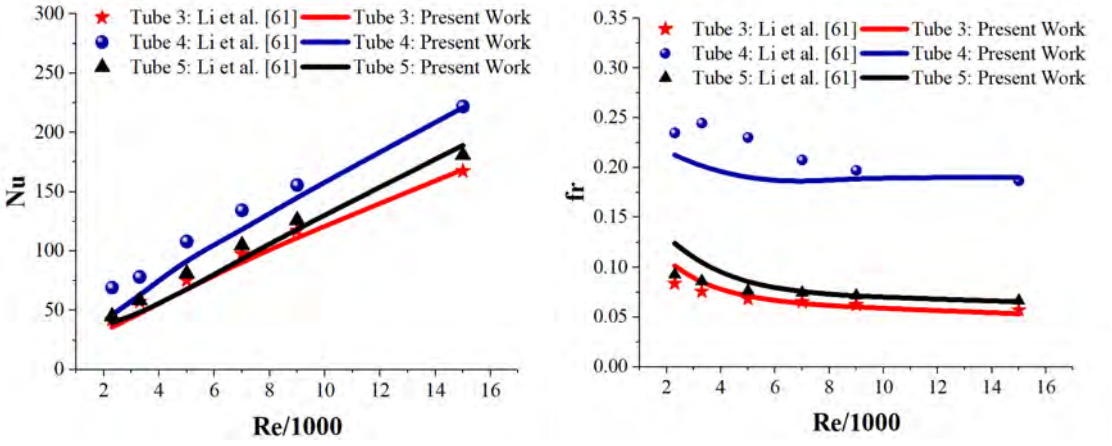

(a) (b)

FIGURE 4.7: Comparison between the numerical results of Li et al., [61] and the present work of the tubes (3-5), (a) Nu and (b) fr

dimpled tubes. Spherical dimpled tube shows 33.34% higher Nu than the conical dimpled tube and 27.7% higher than the ellipsoidal dimpled tube. The presented numerical results of Nu have shown a very good agreement to the results of Li *et al.* [61]. It can also be noted from Figure 4.7b that the spherical dimple also offered a relatively higher hydraulic loss in comparison to the other dimpled tubes. Again, a maximum deviation of 15.35% occurs in the transition Reynolds numbers range as compared to the results reported by Li *et al.* [61]. However, in the fully turbulent region a very good agreement is observed between the present study results and the results of Li *et al.* [61].

4.3.2 Selection of Dimple Shape and size for Further Detailed Analysis

Figure 4.7a - 4.7b shows the heat transfer and friction factors of conical, ellipsoidal and spherical dimple tubes. Spherical dimple plays important role in enhancing the heat transfer and it also produces highest hydraulic loss. These three dimple shapes are taken from the literature Li *et al.* [61]. The comparison needs discussion of some critical points for further work.

In comparison within three dimple shapes, the spherical dimple has highest geometric volume while the conical dimple has lowest volume. Geometric volume of dimple is one of the important factor which dominates in generating the heat transfer characteristics and some times it surpasses the geometric shape, if the volume of the dimple shape is comparatively very small. It means the shape is irrelevant. It directly makes the spherical dimple to generate highest heat transfer rate as well as highest frictional loss. If the volume of each dimple shape is same, the results would be slightly different. On the other hand, conical and spherical dimples are symmetric in its own axis of revolution. In contrary to, ellipsoidal dimple has asymmetric shape where the lengths of major and minor axis are different. It gives the ellipsoidal dimple a significant role if orientation is changed. These are the reasons for selecting the ellipsoidal dimple shape for further detailed analysis.

It is important to mention that the volume of the ellipsoidal dimple is also selected along with the ellipsoidal shape, and it is kept constant onward, throughout the study. In any case of upcoming dimple shape or orientation of the enhanced tube, the volume of the dimple is kept constant and is same as the volume of the conical dimple which is 5.3040 mm^3.

4.3.3 Thermal and Hydraulic Characterization of Enhanced Tubes

The topologies of ellipsoidal dimples could play an important role in the thermal and hydraulic performance enhancement of the tubes [26]. A variation in the orientation of ellipsoidal dimple can offer ways of controlling heat transfer rate by altering the flow characteristics.

However, according to authors' knowledge, none of the previous studies have performed a systematic investigation of thermal hydraulic characteristics of ellipsoidal dimple tubes, based on the orientations of the dimples. Therefore, the present study includes all possible variations of the orientations of ellipsoidal dimples and

identifies the optimum geometry based on the Performance Evaluation Criteria (PEC) [26], presented in equation (1.10).

The orientation of ellipsoidal dimples depends on the angles and patterns of the dimple. The angle of ellipsoidal dimple, as presented in Figure 4.8, is an angle between major axis of the dimple and tube axis.

From here onward in this study, the angle of the ellipsoidal dimple is referred as placement angle (α). The placement angle of the dimples is varied from 0° to 90°. The tubes with placement angles of 0° and 90° are presented in Figure 4.9a - 4.9b.

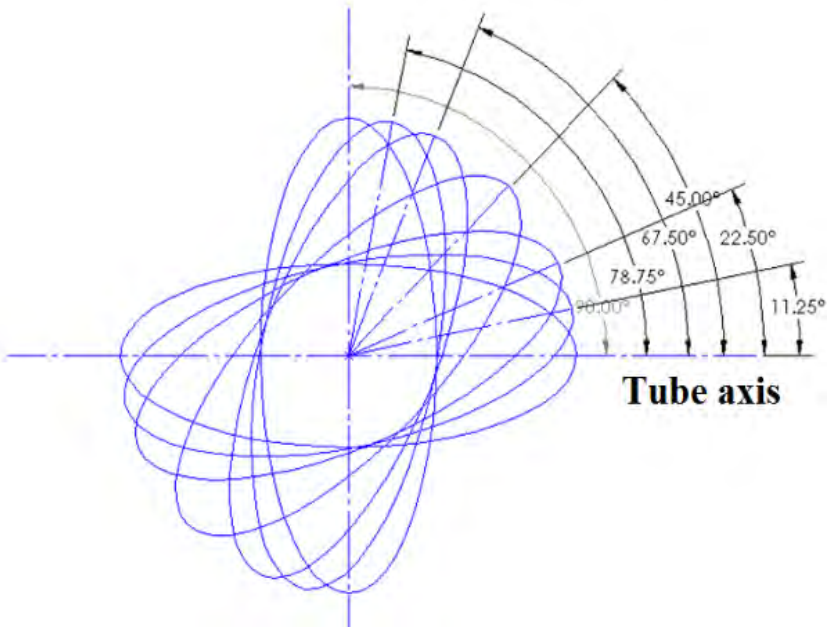

FIGURE 4.8: Ellipsoidal placement angle

Two type of dimple patterns are used in this study i.e. parallel and perpendicular as shown in Figure 4.9c - 4.9d. In the parallel dimple pattern, the placement angles of dimple rows are measured opposite to flow direction. Whereas, in perpendicular pattern, the placement angles of the first dimples row are measured opposite to flow direction.

In the adjacent row, the placement angles are measured in the flow direction. Therefore, in the perpendicular pattern, the circumferentially adjacent dimple has an additional 90° angle. Table 4.4 and Table 4.5 shows different tube parameters and configurations based on the placement angle and dimple patterns respectively.

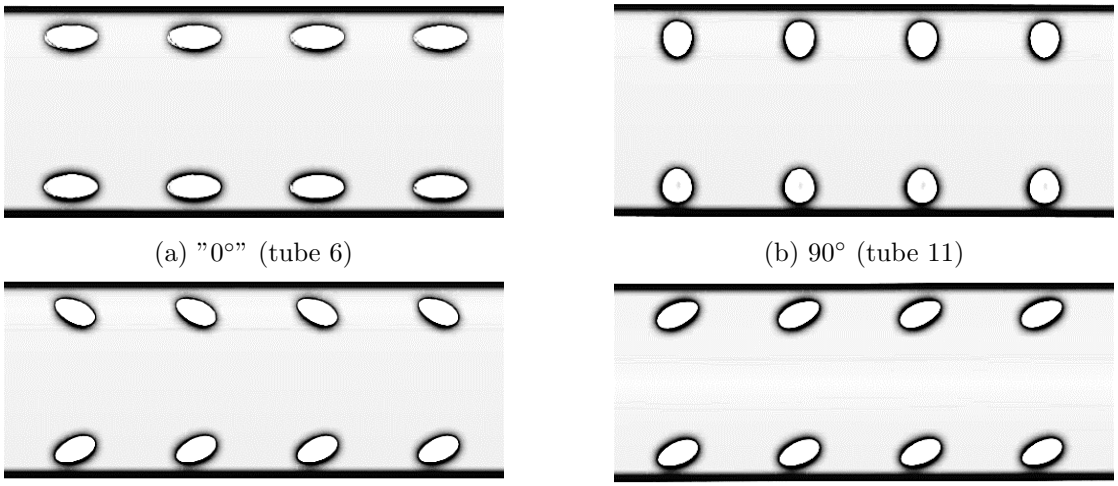

(a) "0°" (tube 6)

(b) 90° (tube 11)

(c) 45° perpendicular pattern (tube 7)

(d) 45° parallel pattern (tube 8)

FIGURE 4.9: Geometry of ellipsoidal dimple tubes

TABLE 4.4: Shape parameters of ellipsoidal dimple used in the tubes 6 to 15

D_h (mm)	H(Depth or height) (mm)	P (mm)	D_p (mm)	Star	Tube Configuration
17.272	1.1686	10	3.89506	4	Inline

4.3.4 Average Flow and Heat Transfer Characterization

The effects of the topologies of dimples on the thermal and hydraulic performance of the enhanced tubes are presented in Figure 4.10a - 4.10c. The ellipsoidal 45° parallel dimpled tube (tube 8) shows the highest heat transfer rate in comparison to all the other tubes. The ellipsoidal 45° perpendicular dimpled tube (tube 7) and ellipsoidal 22.5° parallel (tube 12) have demonstrated enhanced thermal heat transfer rate in comparison to both 0° and 90° dimpled tubes (tube 6 and tube 11). This is shown that the heat transfer rate is greatly modified by the inclination of dimpled tube. It is important to mention that the tube 6 is shown lowest value for Nu in most of the Re as observed in Figure 4.10a.

Interestingly, the heat transfer rate of each tube increases as the placement angles increases from 0° to 45° but decreases as the placement angle is increased from

45° to 90°. Tube 7 and Tube 8 which refer to ellipsoidal 45° perpendicular and parallel dimple orientations have shown better thermal performance than all other tube configurations.

TABLE 4.5: Orientations of all tubes used in current study

Sr. No.	Dimple Placement angle (α)
Tube 6	0°
Tube 7	45° Perpendicular
Tube 8	45° Parallel
Tube 9	22.5° Perpendicular
Tube 10	67.5° Perpendicular
Tube 11	90°
Tube 12	22.5° Parallel
Tube 13	67.5° Parallel
Tube 14	11.25° Parallel
Tube 15	78.75° Parallel

However, the thermal performance cannot be the only performance criteria to identify the optimum configuration of the enhanced tube. Hydraulic performance of the tubes is also a crucial factor in the design of the dimpled tubes. For all the tubes, fr presents a decreasing trend with respect to the Re. The relative ranking of the tubes in Figure 4.10b resembles the ranking observed in Figure 4.10a. Ellipsoidal 45° parallel tube is experienced the higher-pressure loss and the ellipsoidal 0° dimpled tube has the lowest hydraulic loss. The fr values of the rest of the tubes are between the fr values of these two limiting tubes arrangements.

Figure 4.10c shows the PEC of tube 6 to tube 15 for different Reynolds numbers. The results have shown that initially PEC of all tubes increases for $2300 \leq Re \leq 3200$ and decreases for $Re > 3200$. This trend was a result of flow transition from laminar to turbulent. In the pure laminar region, flow inside the tube remains attached to the surface and therefore high friction factor values could be observed.

However, during the transition from laminar to turbulent flow, the friction factors reduces rapidly owing to the onset of flow detachment across the dimples. The enhanced fluid-surface interactions also increases the heat transfer in the tubes. Therefore, PEC increases rapidly in flow transition regime.

However afterwards in fully turbulent regime this effect become gradually decreasing as the flow detached resulted in persistent pressure loss in the dimpled tubes. A significant variation in the value of PEC is observed as the placement angle increases from 0° to 45°. The PEC of the 90° ellipsoidal dimpled tube (tube 11) shows average performance. The tube 8 shows highest PEC value whereas tube 7 has a slightly lower PEC. Moreover, tubes parallel patterns demonstrate higher PEC than tubes with perpendicular patterns.

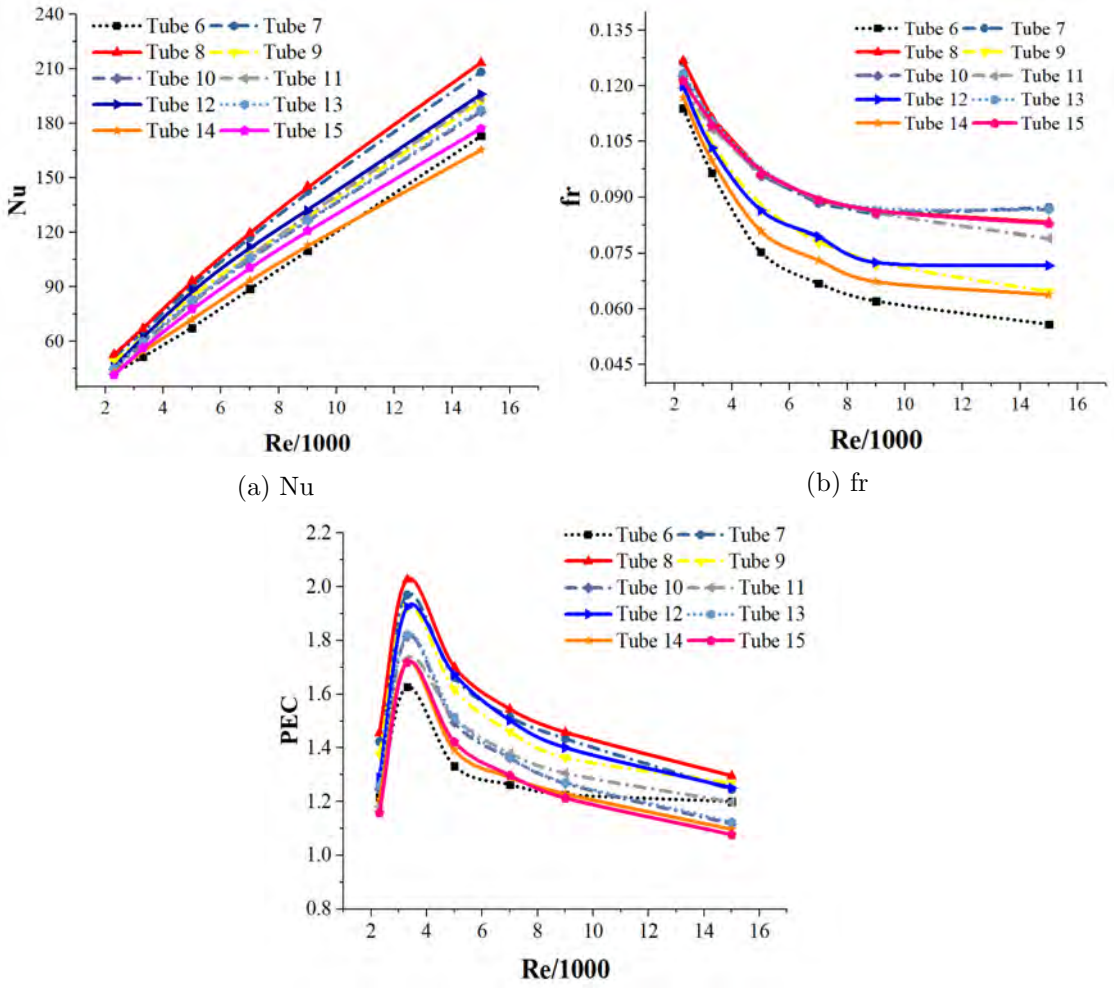

(a) Nu

(b) fr

(c) PEC

FIGURE 4.10: Comparison between the tubes with equivalent dimples volumes of the tubes (6-15) of the characteristics of (a) Nu, (b) fr and (c) PEC

Thermo-hydraulic performance enhancement of 45° dimpled tube in comparison to the other tubes can be associated to the flow dynamics. In this regard, Figure 4.11a presents velocity contours of tube 6, tube8 and tube 11 in axial and circumferential directions. The velocity profile evolution is observed to be completely different in all three tubes. In Figure 4.11a, it can be observed that initially the tube 6 which is an ellipsoidal 0° dimpled tube has a very thin velocity core in comparison to tube 8 (ellipsoidal 45°) and tube 11 (ellipsoidal 45°). The velocity core of the tube 11 appears to remain constant throughout the tube. The velocity core of tube 8 comparing to tube 11 is also thinner in the beginning but it quickly grown up and become thicker than the tube 11. The flow patterns in the velocity boundary layer of tube 6 and tube 11 shows that the flow is completely detached from the wall and the dimple surface whereas in case of tube 8, the flow remains attached to the wall and interacts with the dimple. This could be the reason that the fr of tube 8 is higher. However, this could be also due to the fact that the enhancement in fluid contact with the surface enhances the heat transfer rate. The temperature distributions are presented in Figure 4.11b which show that tube 8 has much thicker thermal boundary layer than the tube 6 and tube 11. The heat transfer rate of the tube 6 is the lowest of all due to minimal fluid wall interaction.

The circumferential cross-sections of velocity fields at different axial locations are presented in the Figure 4.11c for tube 6, 8 and 11. It is interesting to note that each tube has a unique shape of the velocity core due to the different orientations of ellipsoidal dimples. The velocity core of the tube 6 is circular in shape while the tube 11 and tube 8 are square and diamond shaped respectively. The core region of the tube 8 is larger than the other two tubes. The velocity profile development affected the heat transfer rate but in order to understand the role of dimple orientation, it is necessary to observe the thermal effects more closely.

For this purpose, the surface temperature and Nu distributions are presented, for tube 6, 8 and 11, in Figure 4.12a and Figure 4.12b, respectively. The temperature and Nu distribution on the surface of the tube and dimple are completely different. However, a common pattern in the flow over the dimples for tube 6 and 11 is observed which highlighted the fact that the flow detached very early from the

surface of the dimples. The flow detachment forces the fluid streams of tube 6 and 11 to minimize the fluid-dimple contact of the proceeding dimples which limits the thermal performance of these tubes. However, in case of tube 8, the fluid-dimple interaction is enhanced and therefore heat transfer is promoted.

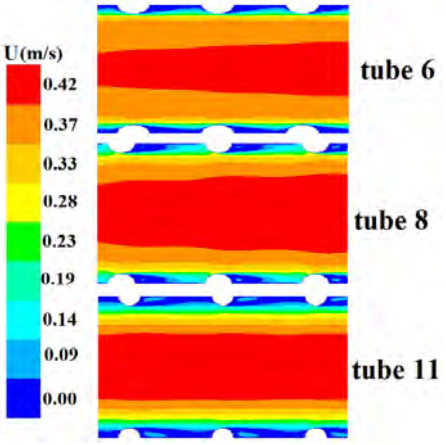

(a) velocity distribution along the flow domination

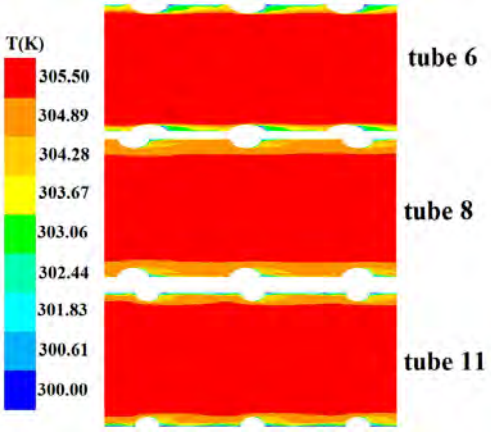

(b) temperature distribution along the axis of tubes

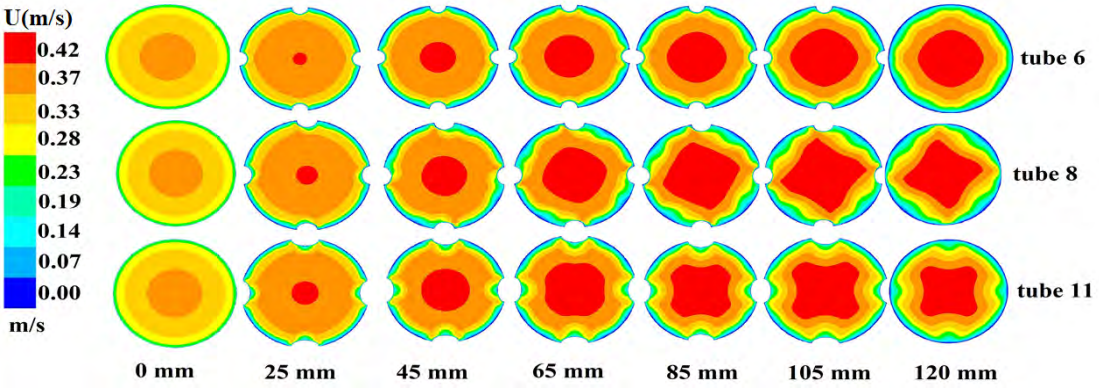

(c) velocity distribution at different cross-sections

FIGURE 4.11: Flow distributions at parallel and cross-flow sections of tubes (6, 8, and 11)

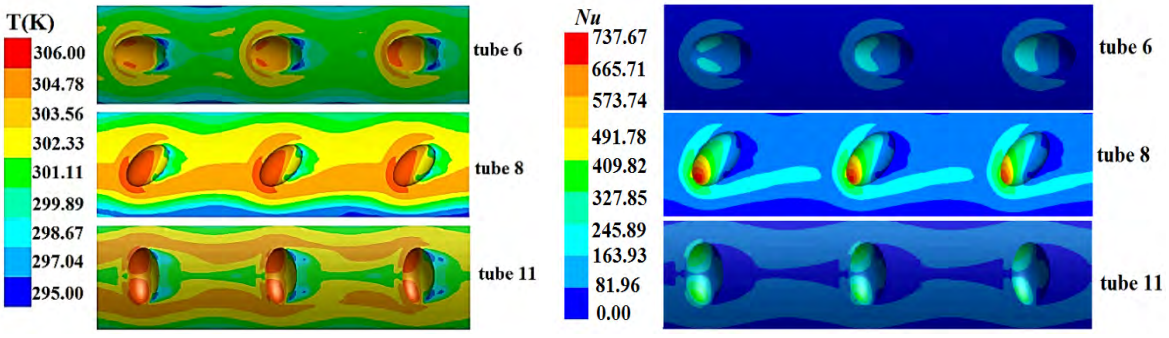

(a) Temperature

(b) Nu

FIGURE 4.12: Contours on the surface of tubes (6, 11 and 8)

Figure 4.13 shows the Nu distribution on the complete surface of tube 8. It is observed that heat transfer is upraised on the fronts of all dimple faces where the axially fluid flow paths exists. All dimple rows in circumferential direction (Star 4) follows same pattern. Although, it is observed that the thermal performance of the tube 8 is superior to the other tubes but the questions regarding the mechanism of heat transfer and associated flow physics remained open. Therefore, it is essential to investigate the instantaneous flow behavior over dimples.

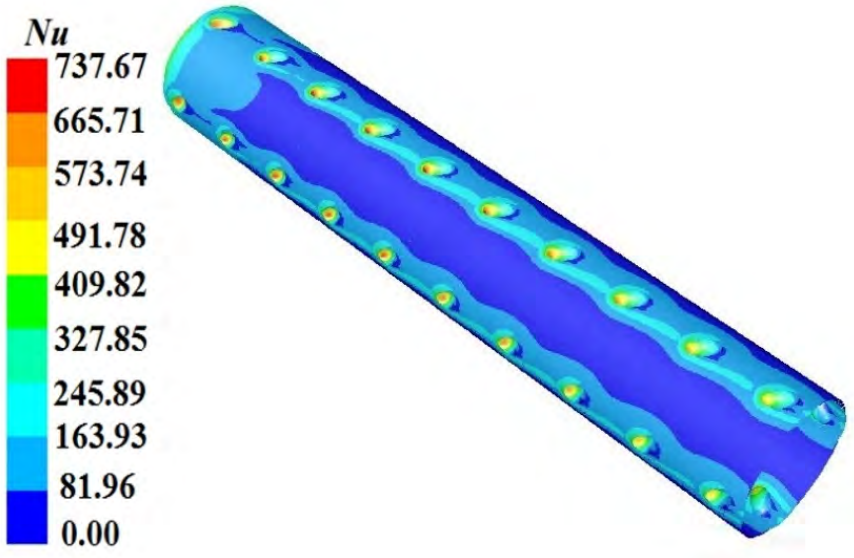

FIGURE 4.13: the Nu distribution on the complete surface of tube 8

4.3.5 Instantaneous Flow and Heat Transfer Characterization

The effects of flow dynamics on the heat transfer enhancement are studied by investigating distribution of Nu and pressure and velocity over the surface of different topologies of ellipsoidal dimples are presented in the Figure 4.14a - 4.14l. It is apparent from the Figure 4.14a - 4.14c that the flow experiences a stagnation point (point A) at the leading edge of the dimples and therefore the fluid velocity reaches local minima. The local Nu is highest at the stagnation point and lowest in the wake of the dimples. After experiencing the stagnation point, the fluid accelerates in the upstream direction of the dimple due to favorable pressure

gradient. The fluid velocity reaches local maxima at the top and bottom of the dimple indicating symmetric flow behavior for tube 6 and tube 11 (0° and 90° dimples). After point C, a combined effect of viscous forces and adverse pressure gradient forces the flow to decelerate rapidly. The flow eventually detaches at point C initiating unstable detached shear layer of the flow producing a large vortex in the wake of the dimple. The shear layers re-attached at point E for tube 6, tube 11, as presented in Figure 4.14g - 4.14i, respectively. The flow re-attachment points of both tube 6 and 11 are at the center-line of the dimples which deflects the flow streams over the top and bottom of the upcoming dimples. This in turn reduces the contact between the fluid and dimples. This flow behavior led to limits thermal enhancement of the tube 6 and tube 11.

The flow and the associated wake dynamics of tube 8 (45° dimples) are fairly different in comparison to the symmetric configurations of tube 6 and tube 11. In case of tube 8, the flow over the inclined ellipsoidal dimple causes asymmetric pressure distribution over the dimple which yields different velocity maxima locations at the top and bottom half of the dimples comparing to tube 6 and tube11. At the bottom half of the inclined dimple, the adverse pressure gradient was not as severe as found in symmetric cases due to the gradual slope of the bottom surface. This allows the fluid to remain attached with the surface and delays its separation at point F.

On the other hand, the separation of the flow over the top half of the dimple at point C occurres almost immediately at the top edge due to severe adverse pressure gradient. As a result, asymmetric flow detachment leads to an asymmetric wake as shown in Figure 4.14e and 4.14h. The flow reattachment point E of ellipsoidal dimple is located well below the centerline of the dimples which helps the flow to interact with frontal area of the next dimple and promotes the heat transfer. It is also confirmed by the plots of local surface Nu along the axial direction of the tubes, at the centerline of the dimples, in Figure 4.14j - 4.14l. The Nu of tube 8 is significantly higher than the tube 6 and tube 11. More over, velocity vector representation of flow around the dimples of tubes 6, 8 and 11 are elaborated in the figure 4.15a - 4.15c. Figure 4.15a - 4.15c denotes the velocity vectors around the

ellipsoidal 0°, 45° and 90° dimples, where stagnation points, increasing velocity, separation points and vortex regions are clearly visible.

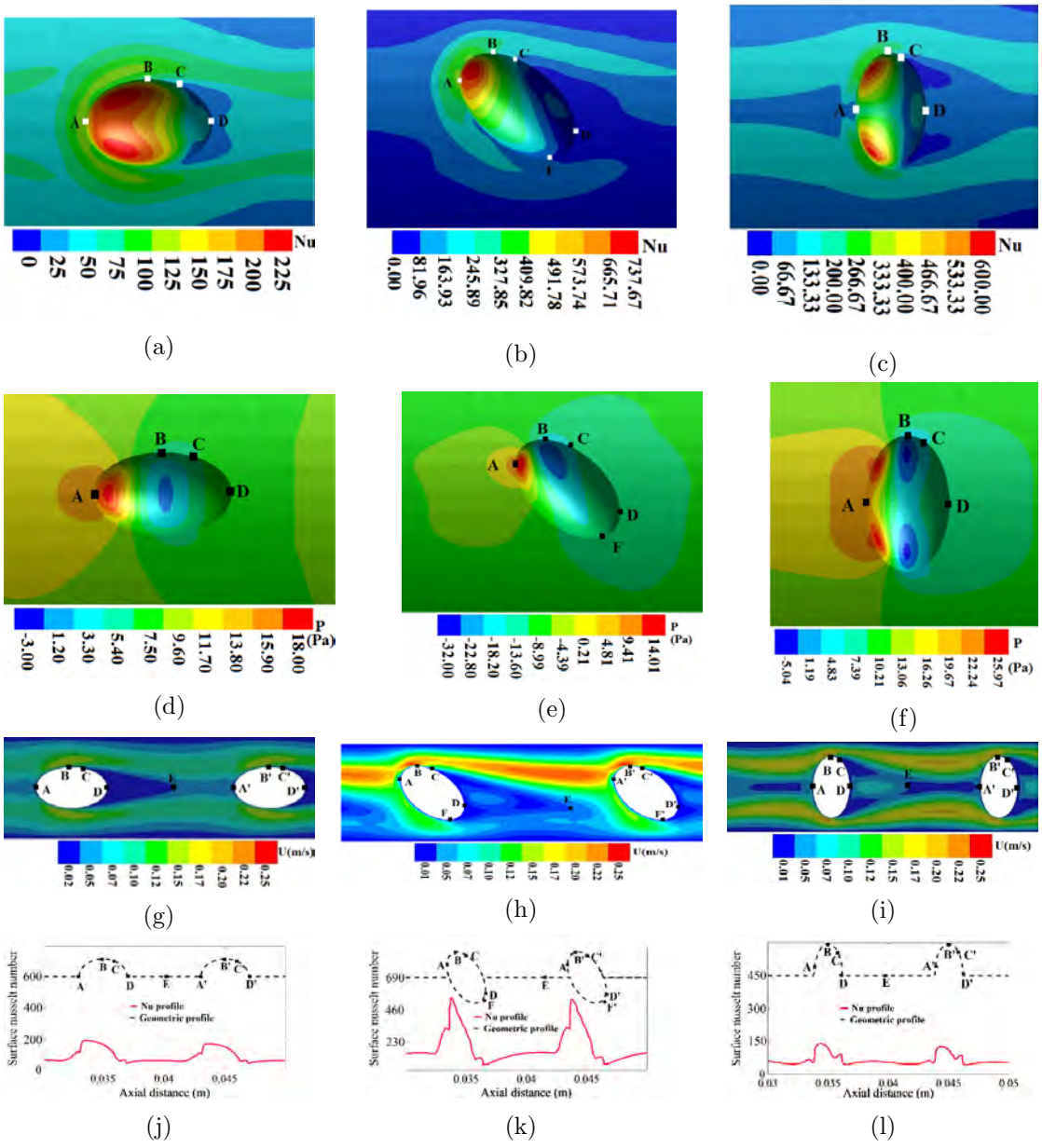

FIGURE 4.14: Assessment of tube 6, 8 and 11, (A): local Nu distribution over a single dimple of tubes; (B-D): pressure distribution;(E-G): velocity distribution at 0.0083m cross-section of tubes ;(H-J): local Nu distribution over two dimples tubes;

In order to further elaborate the heat transfer enhancement, a comparison of local Nu for complete tubes is drawn on the lines having favorable regions of heat transfer enhancement, as shown in the Figure 4.16. Local Nu at the mid line at $z = 0m$ and $z = 0.001m$ are presented in Figure 4.17a and 4.17b. The crest of

local Nu represent dimple location while the flat lines of Nu represent the spacing between the dimples. The Nu are comparable for all three tubes (tube 6, 8 and 11) for first dimples as the flow interacts with the complete frontal area of the dimple.

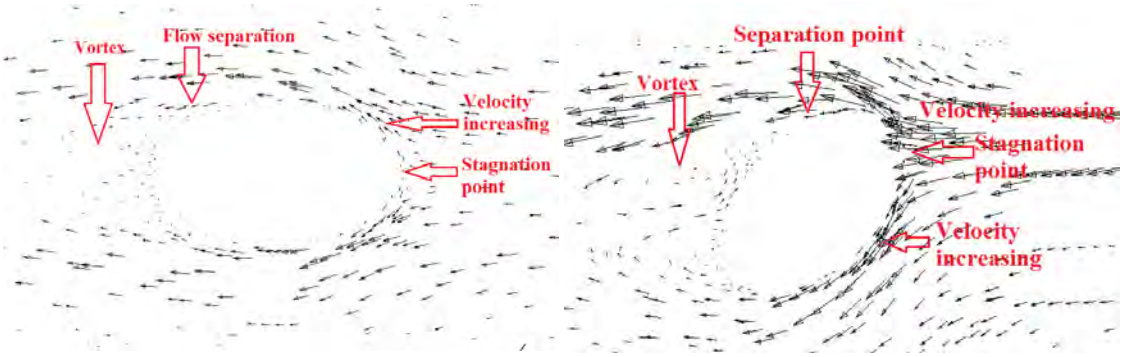

(a) Velocity vector around the dimples of tube 6 (b) Velocity vector around the dimples of tube 8

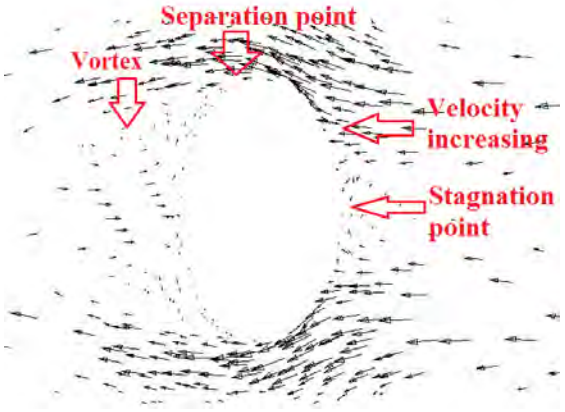

(c) Velocity vector around the dimples of tube 11

FIGURE 4.15: Velocity vector around the dimples of tube 6, 8 and 11

However, the flow separation occurs as soon as the flow crosses over the first dimple and a wake is formed at the back of the dimple. The wake at the back of the dimples dictates the flow interaction with dimples. As explained earlier, the flow is deflected over the upcoming dimples by the symmetric wake of the 0° dimpled tube (tube 6) and 90° dimpled tube (tube 11) which reduces the heat transfer whereas the asymmetric wake of 45° dimpled tube (tube 8) allows the flow to interact with the complete frontal area of the upcoming dimple and therefore enhances the heat transfer rate. This is confirmed by the axial Nu profiles in Figure 4.17a and 4.17b which is shown that tube 8 has much higher Nu values than tube 6 and tube 11.

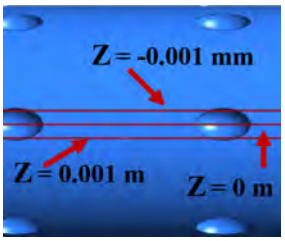

FIGURE 4.16: Schematic of tube 6 with axial lines for local properties on it

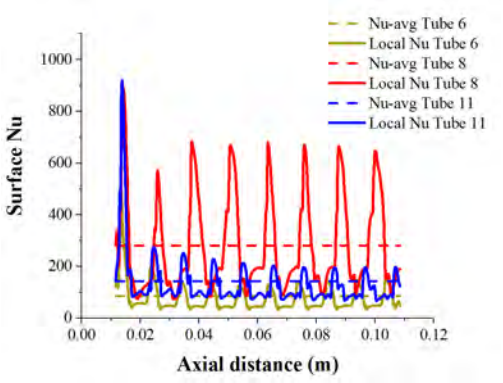

(a) Local Nu of tubes 6, 8 and 11 at the mid line (z=0 m)

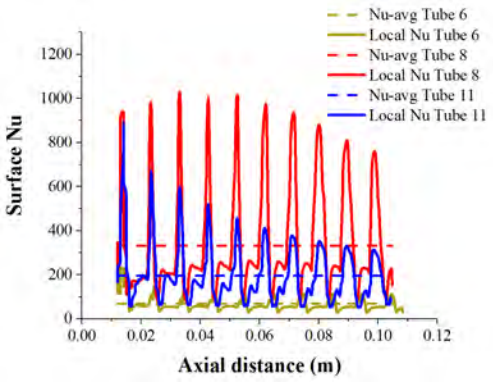

(b) Local Nu of tubes 6, 8 and 11 at the z=0.001m

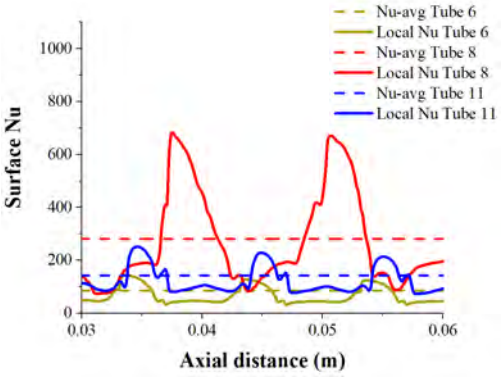

(c) Zoomed portion of Figure 4.17a

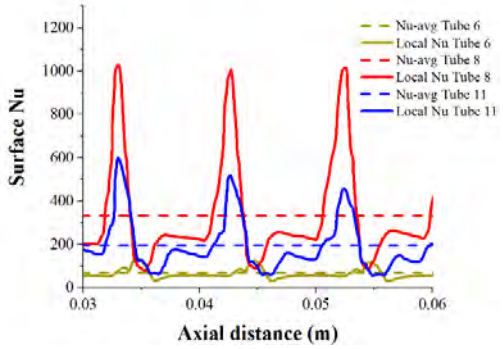

(d) Zoomed portion of Figure 4.17b

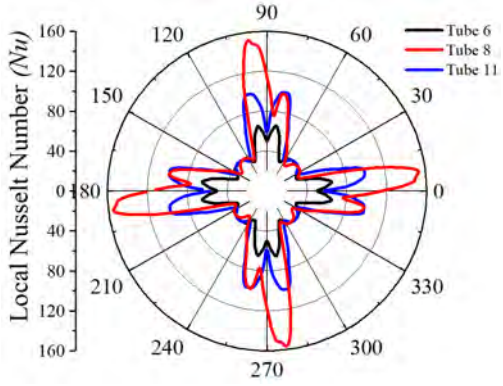

(e) Polar representation of local Nu of tubes 6, 8, and 11 at x=0.06 m of the tube

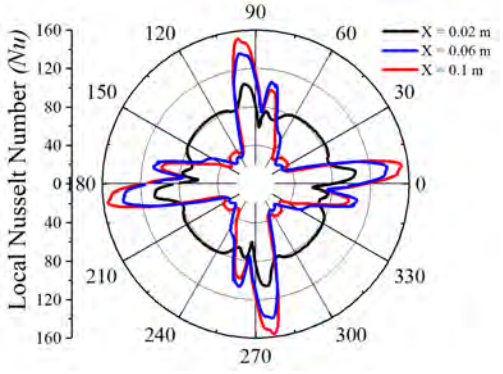

(f) Polar representation of local Nu of tube 8 at various axial locations

FIGURE 4.17: Local Nu of tubes 6, 8, and 11 in axial direction as well as various cross-sections of downstream sections

The average value of Nu of tube 6, 8 and 11 are 85.9, 280 and 142.8 in case of mid line at 0 m and while it is 69.3, 332.3 and 195.2 for the case of mid line at 0.001 m respectively, as shown in Figure 4.17b. Tube 6 has the lowest heat transfer rate in comparison to the other tubes. The role of wake in the thermal performance is further elaborated by investigating the Nu values at circumferential plane in between the two dimples. For this purpose, the distributions of Nu for tubes 6, tube 8 and tube 11 along the circumferential directions at $x = L/2$, which corresponds to a cross-sectional plane at 60 mm from the inlet, are presented in Figure 4.17e. The four peaks of Nu are corresponded to the trailing edges of the dimples of each tube. Tube 8 (45° parallel) is shown higher heat transfer rate, which is 3 times higher than a smooth tube while tube 6 and 11 enhance the heat transfer rate by 1.3 and 1.96 times the smooth tube, respectively. Again, the tube 8 has shown better thermal performance than other tubes.

The Nu along the circumferential direction at different downstream locations of tube 8 are presented in Figure 4.17f. The Nu initially increases in the downstream direction but decreases near the tube outlet. At $20mm$ downstream position, the Nu is two times higher than the Nu of smooth tube and further increases to 3 times at $x = L/2$. At the tube exit ($x = L$), Nu is 2.7 times the Nu_s due to the unsteadiness in the flow field at the tube exit.

4.3.6 Transient Flow and Heat Transfer Characterization using Large Eddy Simulation

The effect of orientation of ellipsoidal dimple changes the flow patterns significantly. Therefore, strong influence of flow dynamics is involved in the heat transfer enhancement. The associated wake dynamics and fluctuating flow are expectedly transient phenomena. For this purpose, Large Eddy Simulation (LES) is performed which resolve integral and inertial sub-range scale eddies in the flow and model the Kolmogorov scale eddies. Minimum volume of the grid, used in current simulation, is $1.07 \times 10^{-14} m^3$ with the smaller edge length of the grid is $2.204 \times 10^{-5} m$. The size of large-scale eddy is generally 7-8% of the characteristic's

length (hydraulic diameter) and it is $0.000121m$ to $0.000138m$ in this simulation. Therefore, it is pertinent to mention that LES in the current simulation resolves the eddies starting from the length $0.000138m$ up to the minimum length of grid $2.204 \times 10^{-5}m$ and below this volume the smaller scale eddies are modeled.

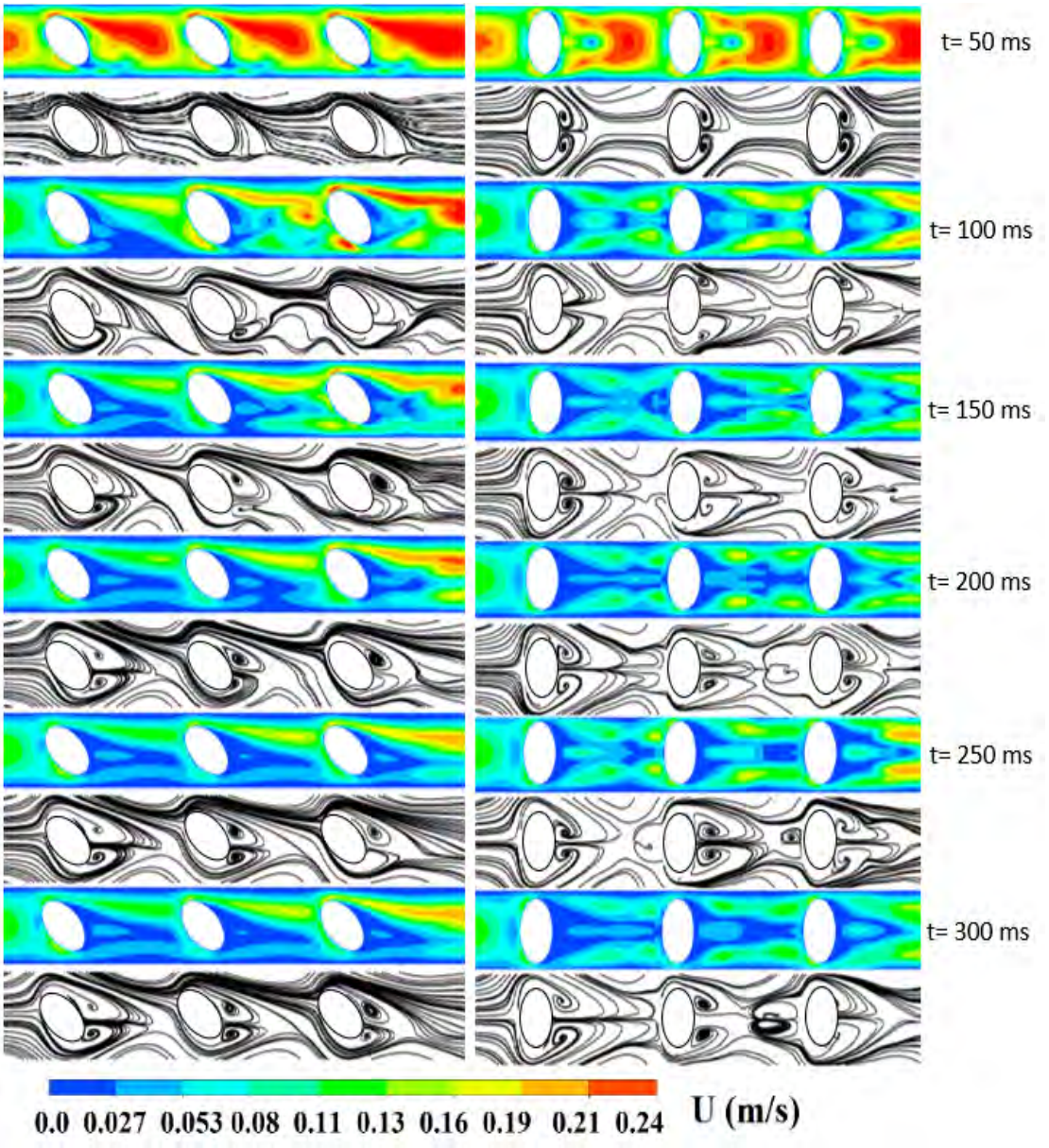

FIGURE 4.18: Velocity contours and streamline plots from LES results of (a) tube 8 (b) tube 11

Since, LES is computationally very expensive, therefore it is used to study only tube 8 and tube 11 at $Re = 5000$ with three dimples in axial direction. A structured mesh with 4.4 million computational cells is used with wall $y^+ < 0.4$. A fixed

time step of $50\mu s$ is employed for both cases for a flow time duration of $300ms$. Temporal distributions of velocity of tube 8 and tube 11 are presented in Figure 4.18. Initially at 50 ms, a vortex pair emerges in the wake of the dimple for tube 11. This vortex is travelled in the downstream direction and eventually interacts with the next dimple. At 100 ms, flow paths are created over the top and bottom half of the dimples. After 150 ms, the tail of the wake of first dimple attaches with the stagnation point of the downstream dimples which forces the fluid streams to travel over the edges of the dimples. It is more elaborated in the streamlines that wake of the tube 11 is symmetric and thick which do not allow the flow to interact with the downstream dimple. Furthermore, in tube 11, as observed in Figure 4.18, the vortex length of second dimple increases and eventually results in vortex shedding. The vortex shedding between the dimples causes additional flow deflection which makes further reduction of heat transfer in tube 11.

However, the wake pattern of tube 8 is different from the tube 11. Figure 4.18 shows that the wake behind the dimples emerges from the bottom half of the dimples which slowly move upwards and attaches to the bottom half of the downstream dimple. The asymmetric wake allows the flow to interact with the downstream dimples and produces a narrow flow path at the bottom half of the dimple. This can also be observed in streamlines which shows that the fluid-dimple interaction is enhanced which in turn increase the heat transfer rate.

4.4 Proposed Correlations for Different Ellipsoidal Dimple Topologies

The correlation of Nu and fr, for all possible topologies of ellipsoidal dimples, are proposed in equations (4.4) and (4.5), respectively. The relationships of Nu and fr are proposed as a function of Re and placement angle α. The Reynolds number is ranged between $2300 \leq Re \leq 15000$, a Prandtl number is 4.8734 while placement angle is varied between $0° \leq \alpha \leq 90°$. The constants a and b of both correlations are linear functions of the placement angle α. The comparisons of

Nu and fr for numerical results and proposed correlations are presented in Figure 4.19a and 4.19b, respectively. These correlations are valid for the fluid properties and boundary conditions, given in section 4.2.2. Moreover, these correlations are proposed using the least square method for curve fitting [107]. A good agreement between the correlation and numerical results is observed. The maximum difference for Nu remained below 5% and below 16% in case of fr, for all placement angles and Reynolds numbers.

$$Nu = aRe^{b(1+0.3\alpha/2\pi)}, a = -0.0006617\alpha + 0.13474 \\ b = 0.00051111\alpha + 0.7412 \tag{4.4}$$

$$fr = [a \ln (Re + \frac{\alpha}{2\pi}) + b]^{-3/2}, a = -0.0079747\alpha + 1.2462 \\ b = 0.059878\alpha - 5.3636 \tag{4.5}$$

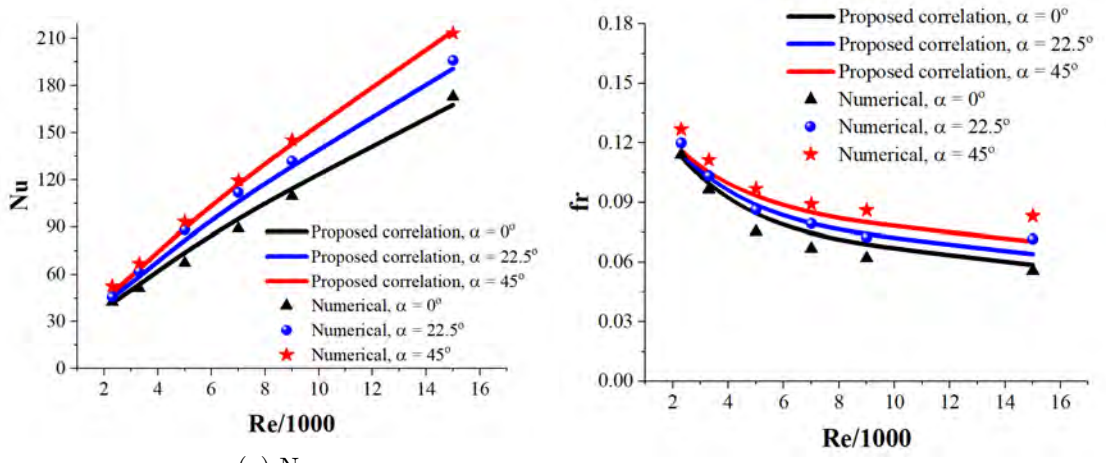

(a) Nu

(b) fr

FIGURE 4.19: Comparison of numerical and correlation results, (a) Nu and (b) fr

4.5 Conclusion

Thermo hydraulic performance of flow through externally heated dimple enhanced tubes with constant surface heat flux was investigated. The tubes were enhanced

by introducing different topologies of ellipsoidal dimples of equivalent volumes. It was observed that in general, in comparison to smooth tubes, all configurations of ellipsoidal dimpled tubes demonstrated improved overall performance of the enhanced tubes. However, the ellipsoidal 45° dimpled tube (tube 8) enhanced the average heat transfer rate, average thermo-hydraulic performance by 119.5% and 58.1% in comparison to the smooth tube, respectively. At low Re, tube 8 achieved the average surface Nu of 52.7 which was 112% higher than that of smooth tube and 25% higher than Nu of tube 6 and tube 11. At high Re, the average surface Nu of tube 8 increased to 213.5 which was 85% higher than Nu of smooth tube while 23% and 10 % higher than tube 6 and tube 11, respectively. The dimple fluid interaction also increased the friction factor of the tube however thermo-hydraulic performance of tube 8 was much higher than that of smooth tubes. The performance evaluation criteria of tube 8 varied between 1.45 and 1.30 for $2300 \leq Re \leq 15000$. The better performance of tube 8 observed in the study is observed to be linked to asymmetric wake behind the dimples which provided a path for the flow to interact with the succeeding dimples. The increased interaction between the flow and dimples promoted heat transfer. Whereas, tube 6 and tube 11 decreased the flow interaction with dimples by deflecting the flow streams over the dimples which subsequently reduced the heat transfer. In the end, correlations for Nu and fr were proposed as a function of Re and dimple placement angle α which covered each configuration of the ellipsoidal dimpled tube. Nu and fr could readily be obtained for different topologies of ellipsoidal dimpled tube with reasonable accuracy for $2300 \leq Re \leq 15000$.

It is pertinent to mention that the study revealed the fluid flow interaction between the dimples causing the performance enhancement. However, fluid flow may exhibit a different behavior when subjected to pitch variation. This may yield lower or higher performance due to flow dissimilarity. This hasn't been numerically analyzed yet. The other aspect is the geometric modification of dimple shape because conical, spherical and ellipsoidal dimples are standard shapes. The shape like ellipsoidal dimple needs to improve for augmentation in heat transfer or reduction in

hydraulic loss, as there is always room for performance enhancement through geometric modification. The innovative dimple like Teardrop dimple which have been claimed to perform better than ellipsoidal 0° dimple [72] and its pitch variation is not included in present numerical analyses. Furthermore, the $Re > 15000$ also affects the performance since it increases the fluid flow interaction with dimples causes more shear on it resulting in better heat transfer. However, the effect of increasing Re may result in significant change in the flow characteristics around the dimple, which may vary along the axial as well as radial directions leading to flow detachment/reattachment. This can significantly influence the frictional losses as well as heat transfer characteristics along the length of the tubes. Moreover, the impact of dimple locations and distributions along the axial as well as radial directions can lead to suppression or enhancement of such flow characteristics. Therefore, in forthcoming chapters, the impact of different flow regimes (in terms of Re) shall be explored for different dimple shapes and geometric arrangements

Chapter 5

Effect of Dimple Pitch on Heat and Flow Dynamics

5.1 Introduction

In previous chapter, orientation of ellipsoidal dimple in enhanced tube from 0° to 90° is numerically analyzed for the heat transfer enhancement. In comparison with all orientations, the 45° orientation is best considered among rest of the orientation, as far as performance augmentation is considered. In this chapter, numerical study is conducted against the pitch variation of ellipsoidal 0°, 45° and innovative teardrop dimpled tubes and comparison is drawn between their overall performances. In order to ensure that the available distance between dimples, the distance from leading edge of the upstream dimple to the leading edge of downstream dimple remains constant for each tube. The influence of the pitch variation and its arrangement patterns on the heat transfer and flow characteristics have been studied for a wide range of Reynolds numbers. Through a parametric study, identification of the best pitch length with its geometry as well as arrangement configuration are investigated using Reynolds Averaged Navier Stokes ($RANS$) under steady flow conditions. The thermo-hydraulic performance enhancement for the optimal configuration is investigated and categorized locally through Nu,

skin friction coefficient. In addition, the effect of variation of the number of dimples in circumferential direction is also analyzed for the optimum tube. At the end, correlations for Nusselt number and friction factor that cover all pitches of ellipsoidal 45° dimpled tube are proposed.

5.2 Computational Domain of Enhanced Tube for Pitch Variation

5.2.1 Introducing the Teardrop Dimple

Ellipsoidal dimple is numerically analyzed and compared with the conical and spherical dimples in the previous chapters. Ellipsoidal dimple has shown the lower hydraulic loss in comparison with spherical dimple. Because ellipsoidal dimple makes its wake behind the trailing edge smoother then the wake of spherical dimple. Teardrop dimple front has spherical in shape while the trailing edge has sharp conical edge, as shown in the Figure 5.1b. This sharp edge has the tendency to reduce the wake size behind it which leads to the reduction in fr, as discussed by Xie *et. al.* [69]. This tendency makes it better than ellipsoidal 0° dimple regarding the overall performance. This is the reason, the authors introduces it in current chapter and make a comparison with ellipsoidal 0° dimple tube.

5.2.2 Geometry of Dimples

Two different geometric shapes of the dimples are considered in this study i.e., ellipsoidal and teardrop dimples. The design parameters of both dimple shapes are provided in Figure 5.1a - 5.1b. These parameters are sensitive, therefore, some numbers are in fourth decimal places.

TABLE 5.1: Geometric parameters for different dimples

Parameters of dimples (mm)			
Ellipsoidal		**Teardrop**	
E_1(major length at the wall)	3.926	T_1(axial length at the wall)	4.996
E_2(minor length at the wall)	2.35	T_2(Width at the wall)	2.491
R_{E1}(major diameter)	1.963	T_3(front nose length)	1.665
R_{E2}(minor diameter)	1.178	T_4(Tail length)	3.532
H(dimple height from wall)	1.1779	R_T(radius of nose sphere)	1.249
		H(dimple height from wall)	1.24886

For example, E_1, E_2, R_{E1}, R_{E2} and H of ellipsoidal dimple are 3.926 mm, 2.35 mm, 1.963 mm, 1.178 mm and 1.1779 mm respectively. Similarly, T_1, T_2, T_3, T_4, R_T and H for the Teardrop dimples are 4.996 mm, 2.491 mm, 1.665 mm, 3.532 mm, 1.249 mm and 1.24886 mm respectively. After rounding off, these parameters are given in Table 5.1.

The ellipsoidal dimples are further divided into categories based on the angle of the major axis and flow direction. The dimples aligned to the flow direction are denoted as ellipsoidal 0° dimples and dimples with the major axis tilted at an angle of 45° to the flow direction are referred to as ellipsoidal 45° dimples. The teardrop dimples are only considered for the aligned arrangement of the dimple axis and flow direction [69].

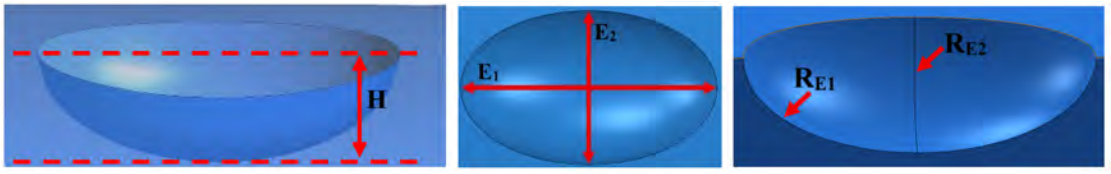

(a) 3D geometry of ellipsoidal dimple with top and side views

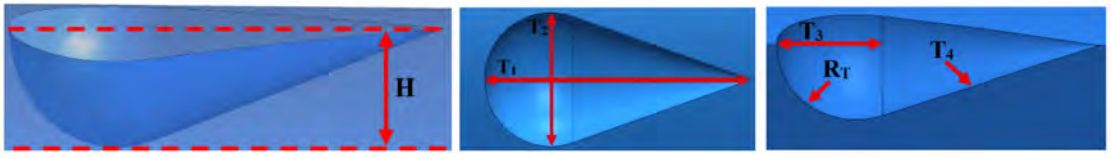

(b) 3D geometry of ellipsoidal dimple with top and side views

FIGURE 5.1: Geometry of ellipsoidal and teardrop dimple

5.2.3 Geometry of Enhanced Tubes with Pitch Variation

Sabir *et. al.* [121] used ellipsoidal dimpled enhanced tube with 10 mm distance from dimple center-to-center in axial direction. They varied the dimple orientation and found the best performance of ellipsoidal 45° dimpled tube contrary to other orientations. The standard definition of pitch for the dimple case is dimple center to center distance, as given by Li *et.al.*[22].

However, in current study, the definition of pitch is slightly changed to account for the distance of vortex formation after the trailing edge in the axial direction. This vortex has influence on the fluid flow and heat transfer characteristics of the enhanced tube. So, the pitch that is the axial distance between the trailing edge and the leading edges of the two consecutive dimples was 7.17 mm.

It is important here to define pitch (P) as the axial distance between leading and trailing edges of the successive dimples for tubes as shown in Figure 5.2a and 5.2b. In current study, the dimple center to center distances of ellipsoidal 45° tubes varies from 6 mm to 16 mm with 2 mm increments.

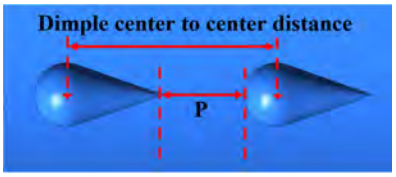

(a) tear drop dimple

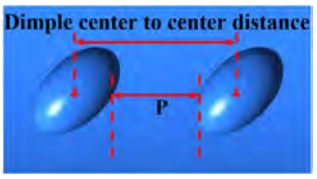

(b) ellipsoidal 45°;

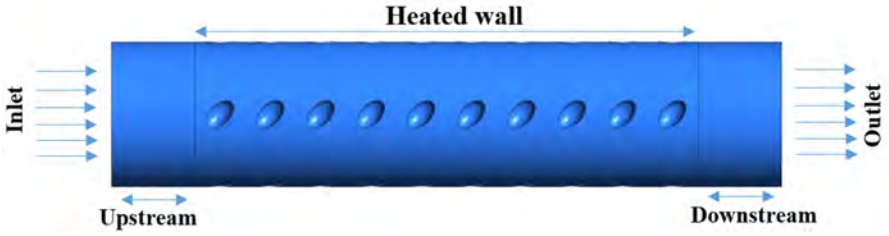

(c) geometric parameters of the dimpled tube displayed on axial cross-section of the tube

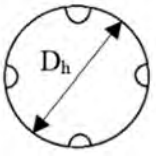

(d) hydraulic diameter of the tube

FIGURE 5.2: Pitch and dimple center to center distance

On the other hand, these center-to-center distances are equivalent to 3.17 mm to 13.17 mm pitches with addition of axial length of dimple shape. As reported in [29], the vortex in the downstream axial direction of the dimple has a significant role

TABLE 5.2: Parameters of all tubes used for current study

Sr no	Tube Names	Diameter of tube (Dh) (mm)	Dimple Profile	Depth (H) (mm)	Pitch (P) (mm)	Star
1	**Tube E0P3**	17.272	Ellipsoidal (0°)	1.175	3.17	4
2	**Tube E0P5**	17.272	Ellipsoidal (0°)	1.175	5.17	4
3	**Tube E0P7**	17.272	Ellipsoidal (0°)	1.175	7.17	4
4	**Tube E0P9**	17.272	Ellipsoidal (0°)	1.175	9.17	4
5	**Tube E0P11**	17.272	Ellipsoidal (0°)	1.175	11.17	4
6	**Tube E0P13**	17.272	Ellipsoidal (0°)	1.175	13.17	4
7	**Tube TDP3**	17.272	Teardrop	1.24886	3.17	4
8	**Tube TDP5**	17.272	Teardrop	1.24886	5.17	4
9	**Tube TDP7**	17.272	Teardrop	1.24886	7.17	4
10	**Tube TDP9**	17.272	Teardrop	1.24886	9.17	4
11	**Tube TDP11**	17.272	Teardrop	1.24886	11.17	4
12	**Tube TDP13**	17.272	Teardrop	1.24886	13.17	4
13	**Tube E45P3**	17.272	Ellipsoidal (45°)	1.175	3.17	4
14	**Tube E45P5**	17.272	Ellipsoidal (45°)	1.175	5.17	4
15	**Tube E45P7**	17.272	Ellipsoidal (45°)	1.175	7.17	4
16	**Tube E45P9**	17.272	Ellipsoidal (45°)	1.175	9.17	4
17	**Tube E45P11**	17.272	Ellipsoidal (45°)	1.175	11.17	4
18	**Tube E45P13**	17.272	Ellipsoidal (45°)	1.175	13.17	4

on the heat transfer. Therefore, for comparative analysis of the effect of different dimple shapes on the heat transfer of the tube, same pitches for all dimple shapes must be considered. This effect of same pitch is considered in current study. The pitch and dimple center to center distances for different dimple configurations are shown in Figure 5.2a and 5.2b.

It is pertinent to mention that the tube lengths, with different geometric shapes of the dimples for a same pitch, are different. In order to avoid this ambiguity, the dimple pitch of each tube configuration are varied from 3.17 mm to 13.17 mm while maintaining the axial length of the tube (L) to dimple pitch (P) ratio (L/P) of 10 as shown in Figure 5.2c and reported in Table 5.2. The constant L/P ratio ensure equal number of dimples in the axial direction of the tube. The hydraulic diameter of the tubes is represented by D_h and it is equal to 17.272 mm while the height of the dimple inside the tube is denoted as H.

Furthermore, to eliminate any spurious effects of inlet and outlet boundary conditions, 20 mm length is used in each "upstream" and "downstream" section of the tube, as shown in Figure 5.2c. The inward dimples in the tube are positioned in inline.

In current study, axial length of each dimple shape is added in the pitch to find out the length of heated section of tube. For example, length of ellipsoidal 0° dimple tube for 3.17 mm pitch = 10 * (3.17+3.926) = 70.92 mm. The numbers of dimples in the axial and radial direction are ten and four, respectively for all tubes. All dimples are of equivalent volume of 5.3040 mm^3. The geometric parameters of the dimpled enhanced tubes are presented in Figure 5.2c and 5.2d and Table 5.2. The tube names are abbreviated from their characteristics, i.e. E0P3 means ellipsoidal 0° dimpled tube with 3.17 mm pitch. Similarly, TDP3 means Teardrop dimpled tube with 3.17 mm pitch and E45P3 means ellipsoidal 45° dimpled tube with 3.17 mm pitch, as shown in Figure 5.3.

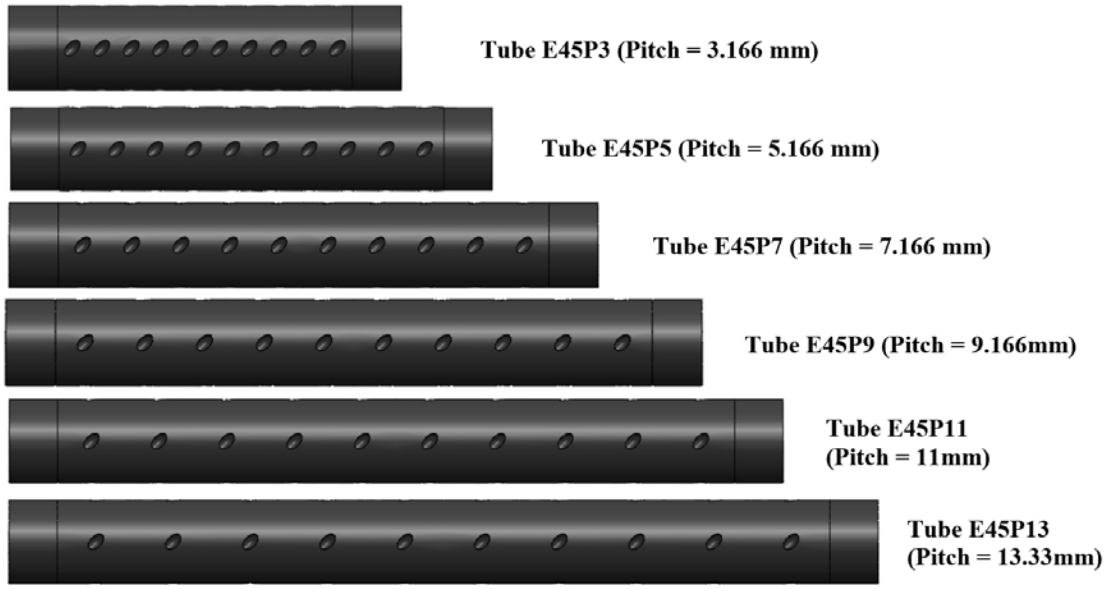

FIGURE 5.3: Schematic of tubes E45P3- E45P13

5.3 Results and Discussion

5.3.1 Effect of Pitch on Heat Transfer and Inertial Loss

As mentioned above, the number of dimples in axial direction are fixed in all the tubes for Re range $9000 \leq Re \leq 40000$. The quantitative analysis of heat transfer and hydraulic loss can be best associated to Nu and fr, respectively.

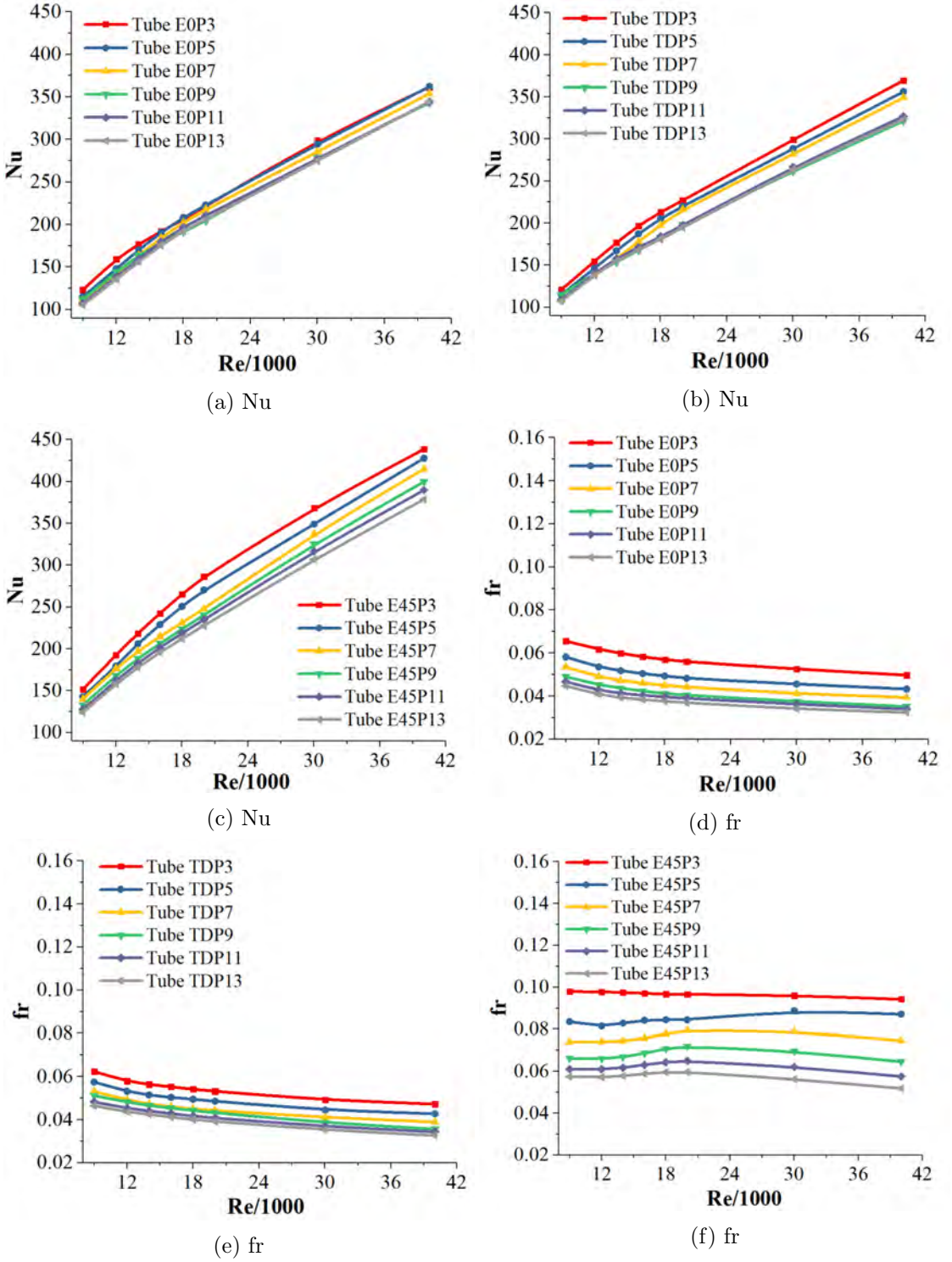

(a) Nu (b) Nu

(c) Nu (d) fr

(e) fr (f) fr

FIGURE 5.4: comparison of Nu and fr (a and d) of Ellipsoidal 0° dimpled tubes: tubes E0P3-E0P13; (b and e) Teardrop dimpled tube: tubes TDP3-TDP13; (c and f) Ellipsoidal 45° dimpled tube: tubes E45P3-E45P13

Therefore, the results of all dimpled tubes for different Re in the form of Nu and fr are presented in Figure 5.4a - 5.4f. Nu varies with respect to Re as well as against

the pitch. It is observed that the Nu increases as the Re increases, however, the Nu decreases as the pitch increases from 3.17 mm (tube E0P3) to 13.17 mm (tube E0P13). The Nu of tube E0P3 ($P = 3.17$ mm, Ellipsoidal 0°) is 16.8% higher than Nu of tube E0P13 ($P = 13.33$ mm of Ellipsoidal 0°) at $Re = 9000$ whereas it is only 4.98% higher at $Re = 40000$.

It is also established from the Figure 5.4a that 3.17 mm pitch of ellipsoidal 0° dimpled tube (tube E0P3) improves the heat transfer rate under all Re. Similarly, the pitches of other dimpled shapes also improve their heat transfer against all Re considered here.

For example, the Nu of the tube TDP3 ($P = 3.17$ mm, Teardrop) is around 14.6% higher than that of tube E0P13 ($P = 13.33$ mm of Ellipsoidal 0°) at the $Re = 9000$, while it is 7.28% at the $Re = 40000$, as shown in Figure 5.4b. Similarly, the Nu of tube E45P3 ($P = 3.17$ mm, Ellipsoidal 45°) is 44% higher than that of tube E0P13 at the $Re = 9000$, and it is 27.38% at the $Re = 40000$, as shown in Figure 5.4c.

It is obvious from the Figure 5.4c that the Nu of dimple tube decreases gradually as the pitches increase from 3.16 mm to 13.16 mm, respectively. This depicts that Nu is inverse in relation with pitch P for all dimple shapes. The friction factors are observed to decrease with an increase in Re.

However, the pattern of increase in fr is same as that of Nu against the variation in pitches i.e. by increasing the dimple pitch P, friction factor reduces, as presented in Figure 5.4d, 5.4e and 5.4f. For example, fr of the tube E0P3 ($P = 3.17$ mm) is 53.07% higher than that of tube E0P13 ($P = 13.17$ mm) at $Re = 9000$, while it is 46.5% at $Re = 40,000$ as observed in Figure 5.4d.

It is also worth noticing that fr of tube E45P3 are considerably higher than tube E0P3 and tube TDP3 under all Reynolds numbers, as presented in Figure 5.4d, 5.4e and 5.4f. It is important to mention from the results that the hydraulic losses of Ellipsoidal 45° dimple tubes are much greater than the other dimple shaped tubes at the same pitch.

5.3.2 Effect of Pitch Variation on the Fluid Flow and Heat Transfer Characteristics of Enhanced Tubes

The fluid flow over different shapes of dimples exhibit distinct patterns which lead to augmentation in heat transfer and hydraulic losses.

These flow patterns are strongly linked to the wakes of the dimples. The streamlines over the Ellipsoidal 0°, Teardrop and Ellipsoidal 45° dimples, in Figure 5.5a - 5.5c, highlight the different wake structures. It can be observed that Ellipsoidal 0° and Teardrop dimples produce large and symmetric wake structures. Whereas, the wake of Ellipsoidal 45° dimple is also large with asymmetric flow detachment. These flow patterns and their effects are further elaborated by pressure, velocity, wall shear stress and temperature distributions at cross-sections of tubes E0P3, TDP3 and E45P3 at a fixed radius of 0.0082 m in Figure 5.6a - 5.6c.

It is apparent from these figures that the flow experiences a stagnation points at the leading edge of the dimples and therefore the fluid velocity reached local minima. Afterwards, the fluid is accelerated in the upstream direction of the dimple due to favorable pressure gradient, however this pressure gradient is different in each dimple due to its specific geometric shape. In other words, dimple shape also dictates this pressure gradient. Generally, the fluid velocity reaches local maxima at the top and bottom of the dimples of each shape. After achieving the local maximum velocities, the flow decelerates rapidly due to combined effect of viscous forces and adverse pressure gradient attenuating unstable detached shear layer of the flow yielding large vortex in the wake of the dimple, also observed in 5.6a - 5.6c.

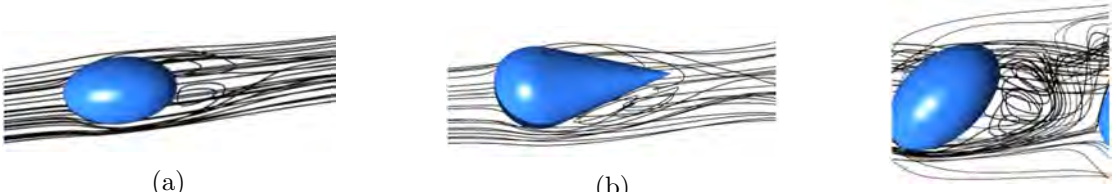

(a) (b) (c)

FIGURE 5.5: Vortex formation ahead of dimple (a) ellipsoidal 0°, (b) teardrop and (c) ellipsoidal 45°

The symmetric local maxima of velocities around the dimples of tube E0P3 (P = 3.17 mm, Ellipsoidal 0°) can be shown on the Figure 5.6a. The local velocity magnitude around the dimples decreases in the rare half of the tube due to homogenous flow distribution and significant pressure drop. For $Re = 12000$, a clear flow path is created around the dimples due to the attachment of the tails of wakes to the frontal stagnation points of the dimples. The wakes of all dimples remain stable and limit the fluid dimple interaction. A similar fluid-dimple interaction can be observed for $Re = 20000$.

Interestingly, the wakes of the first and second dimple are apparently seemed slightly unstable and disturb the flow path initially, as shown in the Figure 5.6a. However, the flow after the third dimple becomes stable and a similar flow pattern appears again as observed in case of $Re = 12000$. Fluid dimple interaction is also shown here using the wall shear distribution which prescribes that how much stress is exerted on the tube wall by the fluid flow.

The scale for the wall shear range is limited from 0 to 25 Pa for both Re cases for both Re all dimple shapes. The front halves of the dimples show higher shear stress and surface temperature in comparison to back halves. This manifests that fluid interaction at the back half of each dimple is minimum due to the flow separation.

Figure 5.6b, for the tube TDP3, also shows a symmetric flow path by generating stable wakes behind the dimples. The detachment of fluid flow around teardrop dimples occurs smoothly due to gradual pressure drop in trailing edge of the dimple. This results in the formation of relatively weak and thin vortex behind the dimples, as observed in Figure 5.5b and Figure 5.6b.

The vortices in the wakes of the dimples are observed to be stretched by the flow streams and consequently are attached to leading edges of the subsequent trailing dimples. As a result, the wall shear increases as flow Reynolds number is increased. Furthermore, the maximum exchange in temperature takes place along the path of wall shear, as depicted in the temperature distribution of tube TDP3 in Figure 5.6b.

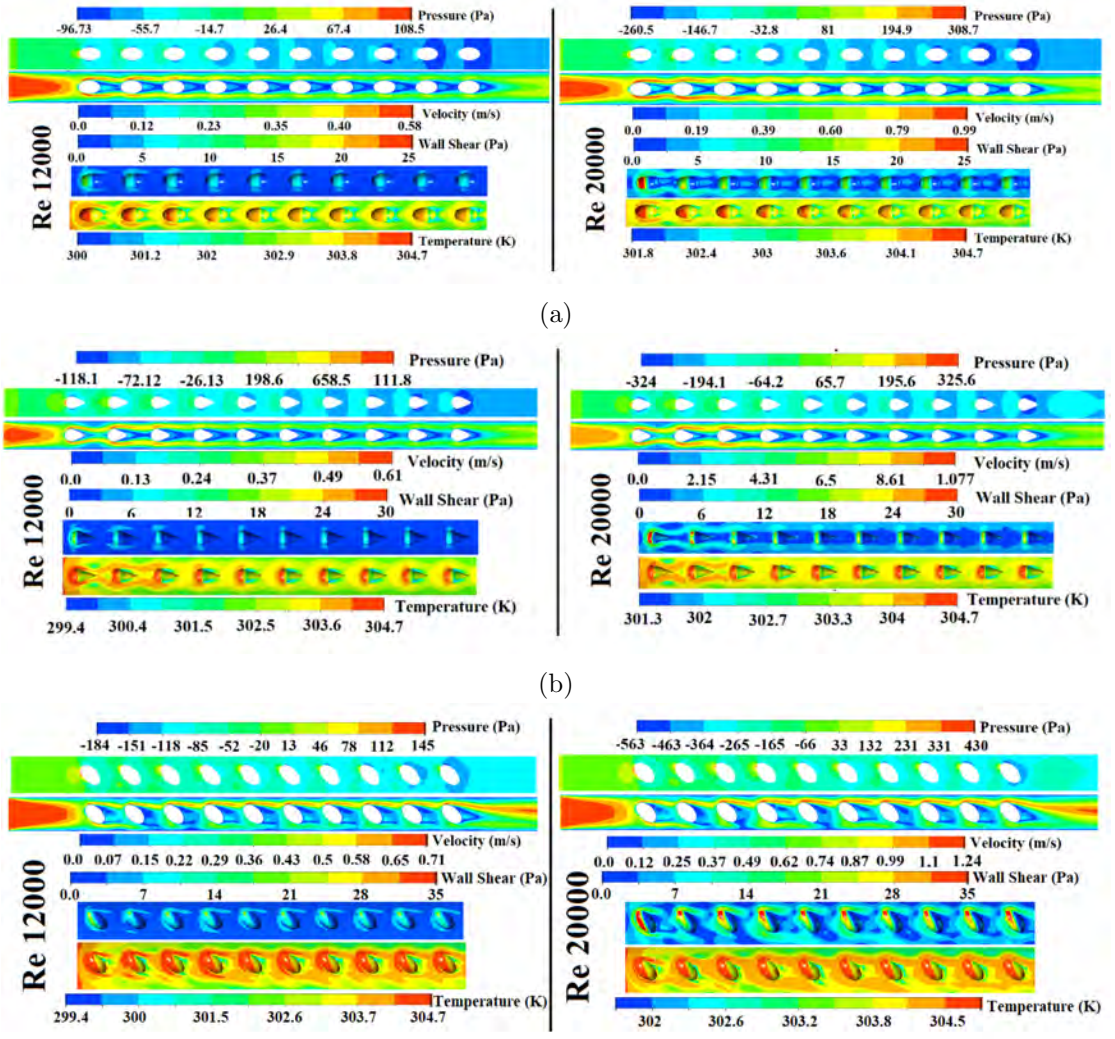

FIGURE 5.6: Pressure, velocity, wall shear stress and temperature contours at radius = 0.0082m for *Re* 12000 and 20000 (a) tube E0P3 (b) tube TDP3 (c) tube E45P3

Figure 5.6c presents the results of tube E45P3 at the $Re = 12000$ and 20000. The angular positions of the dimples modify the flow patterns completely. The stagnation point appears at the top of the dimple and an asymmetric wake structure appears at the back of the first dimple. The asymmetric wakes allow to create a flow path between the dimples and subsequently enhance the fluid surface interactions. This flow pattern exists at all Reynolds numbers. The surface shear stress and temperature contours in Figure 5.6c show the enhancement in frictional effects and heat transfer, respectively. Moreover, Ellipsoidal 45° dimples induce a slight radial flow in the bottom half of the dimples which also promotes fluid-surface

interaction and consequently the heat transfer. This effect is further elaborated by radial cross-sections of velocity for different dimpled tubes at $Re = 12000$ in Figure 5.7.

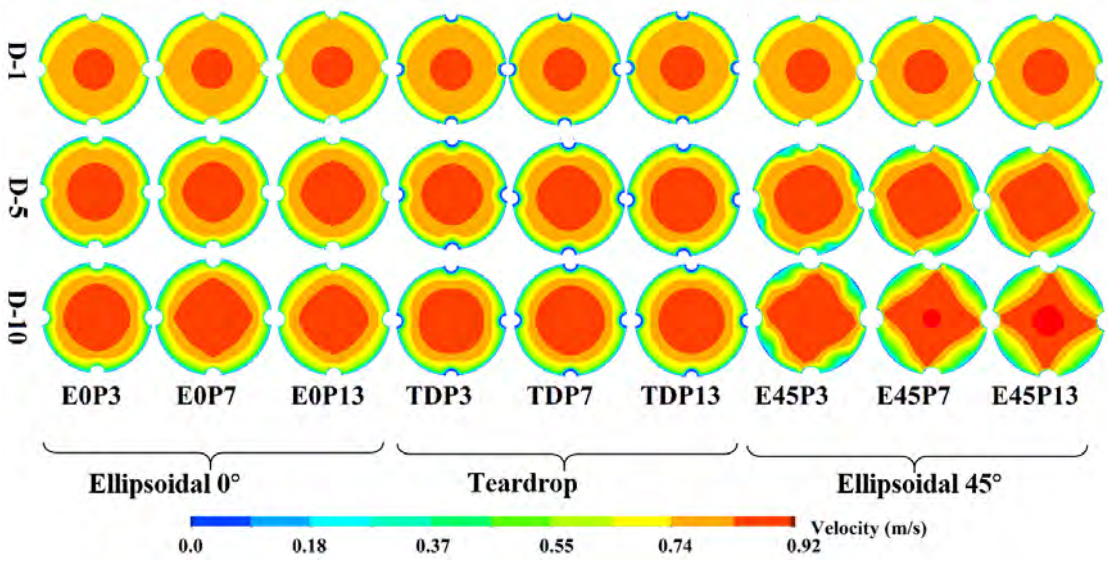

FIGURE 5.7: Velocity distributions for different tubes and dimple locations

The velocity contours are presented across first dimple $(D-1)$, fifth dimple $(D-5)$ and last dimple $(D-10)$. At $D-1$, the velocity core is narrow while the viscous effects are dominant, however, the velocity core plays dominant role at D-10. The velocity core grows wider and approaches approximately double the radius of D-1 core radius. The core of each dimple has its unique shape. The velocity core of Ellipsoidal-0° has tilted square shape, while the Teardrop and Ellipsoidal-45° have circular and diamond shapes respectively. Furthermore, Figure 5.7 also depicts that the boundary layers of Tubes E0P3, TDP3 and E45P3 at their respective dimple locations are more disturbed/perturbed than their other respective pitches.

5.3.3 Influence of Pitch Variation on the Performance Enhancement of Dimple Tubes

The performance enhancement criteria (PEC) for all dimpled tube (18 tubes) are presented in Figure 5.8a - 5.8c. The thermal-hydraulic performance of enhanced

tubes decreases with increase in Re for all pitches. In Figure 5.8a, tube E0P9 (P = 9.17 mm, Ellipsoidal 0°) manifests highest PEC value of 1.35 that is 35% performance improvement in comparison to PEC of smooth tube (i.e. $PEC_s = 1$ at all Re), at $Re = 9000$. The PEC value of tube E0P9 remains greater than 1.3 until $Re = 16000$. At $Re = 20000$, the PEC of tube E0P9 reduces to 1.2 while at $Re = 40000$, PEC diminishes to 1.1.

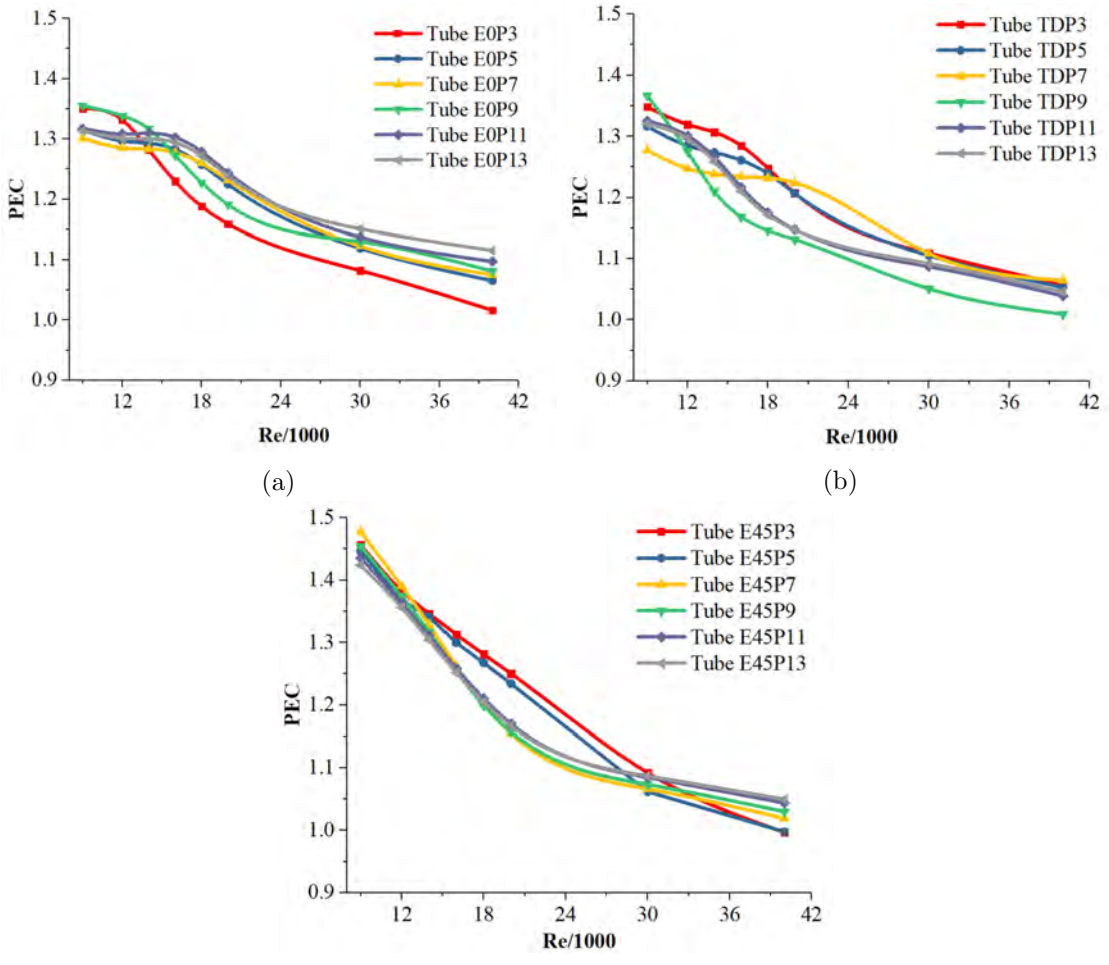

FIGURE 5.8: comparison of PEC of (a) Ellipsoidal 0° dimpled tubes: tubes E0P3-E0P13, (b) Teardrop dimpled tube: tubes TDP3-TDP13 (c) Ellipsoidal 45° dimpled tube: tubes E45P3-E45P13

On the other hand, tube E0P11 (P = 11.17 mm, Ellipsoidal 0°) and tube E0P13 (P = 13.17 mm, Ellipsoidal 0°) demonstrate higher $PECs$ for Re ranges $16000-20000$ and $20000-40000$, respectively. Teardrop dimpled tubes also show similar trends of the PEC curves. In case of teardrop dimpled tube, at $Re = 9000$, tube TDP9

(P = 9.17 mm, Teardrop) shows considerable performance improvement however it diminishes quickly at higher Re.

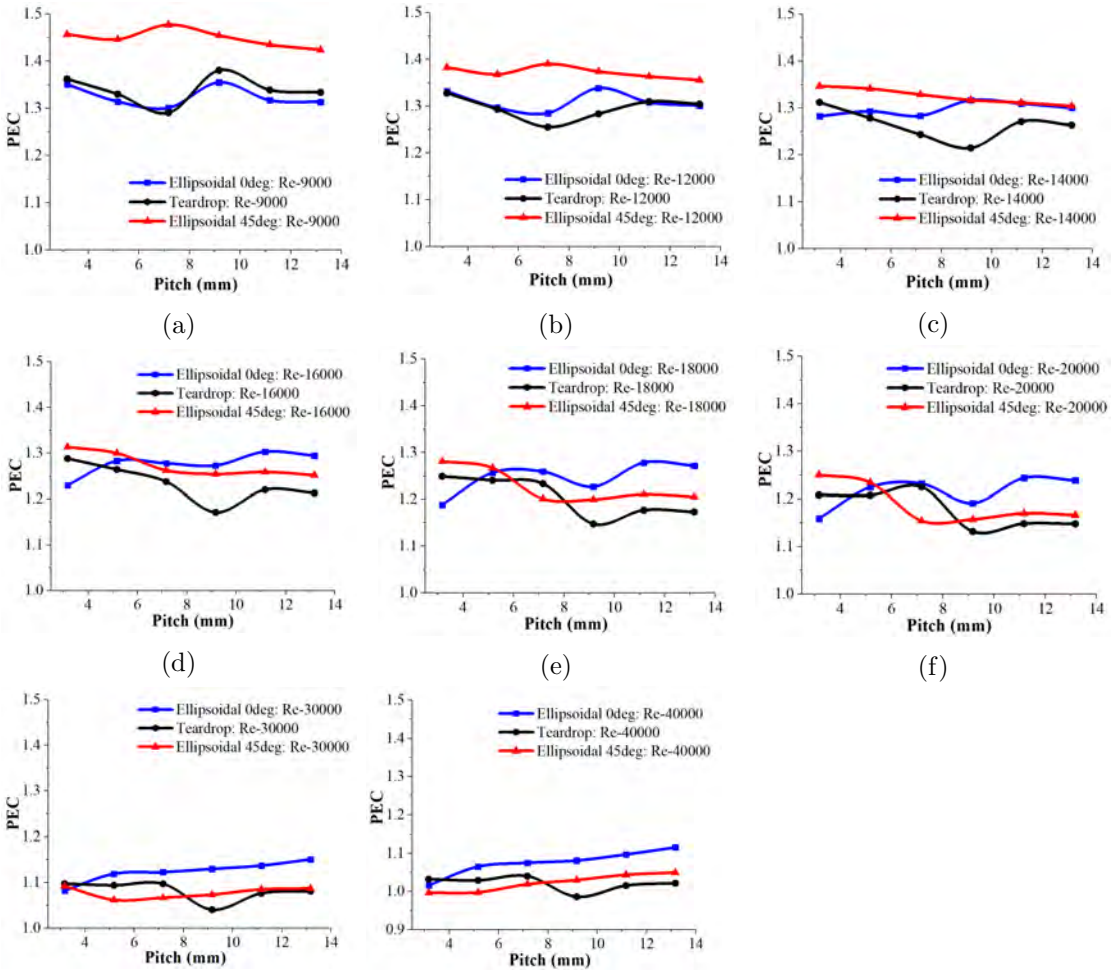

FIGURE 5.9: PEC of all dimple shaped tubes with respect to pitch variation for the Re = 9000 to 40000

Moreover, Figure 5.8c presents a comparison of the performance enhancement for Ellipsoidal 45° dimpled tubes (tubes E45P3-E45P13). The tube E75P7 (P = 7.17 mm) has better performance at the Re = 9000 and 12000 while the Nu of 3.17 mm pitched tube (tube E45P3) is at the peak at the Re = 14000 to 30000. The percentage difference between tube E45P3 and tube E45P13 decreases from 22.2% to 15.85% from Re = 9000 - 40000. This trend makes the tube E45P3 for highest ranking of PEC among 18 tubes from Re = 14000 to 30000 while tube E45P7 depicts the best PEC at the Re =9000 to 12000.

TABLE 5.3: Percentage differences of E-45° dimpled tubes against that of E-0° and Teardrop dimple at same pitches

	Re= 9000		**Re= 12000**		**Re= 14000**		**Re= 16000**		**Re= 18000**		**Re= 20000**		**Re= 30000**		**Re= 40000**	
Pitch (mm)	**E-0° (%)**	**TD (%)**	**E-0° (%)**	**TD (%)**	**E-0° (%)**	**TD (%)**	**E-0° (%)**	**TD (%)**	**E-0° (%)**	**TD (%)**	**E-0° (%)**	**TD (%)**	**E-0° (%)**	**TD (%)**	**E-0° (%)**	**TD (%)**
3.17	7.83	6.94	3.84	4.12	5.0	2.64	6.78	1.95	7.83	1.95	7.86	3.48	0.91	-0.49	-1.94	-3.48
5.17	10.03	8.7	5.51	5.80	3.73	4.89	1.31	2.83	0.82	2.83	0.78	2.19	-5.11	-2.93	-6.34	-3.06
7.17	13.53	14.45	8.61	10.75	3.53	6.86	-1.21	2.0	-4.65	2.0	-6.28	-5.77	-5.01	-2.79	-5.21	-2.04
9.17	7.32	5.32	2.64	7.05	0.02	8.42	-1.46	7.08	-2.28	7.08	-2.85	2.23	-4.99	3.18	-4.75	4.43
11.17	8.93	7.16	4.22	4.11	0.14	3.17	-3.4	3.16	-5.34	3.16	-5.92	1.87	-4.60	0.79	-4.88	2.77
13.17	8.42	6.75	4.19	3.95	0.31	3.32	-3.28	3.19	-5.28	3.19	-5.8	1.59	-5.54	0.53	-5.91	2.71

The performances of the tubes, given in Figure 5.8a - 5.8c, are against the Re. It is worth noticing that different pitches of each dimple shape have exhibited better PEC for their respective Re ranges while the same pitches compromised their performances other than their favorable Re. Therefore, there is need to reconsider the performances of each tube with respect to pitch measurement. For this, performances of all tubes are plotted against the pitch variation, as shown in the Figure 5.9a - 5.9h. Figure 5.9a - 5.9h shows the performance variation concerning the change in pitch for all dimple shapes. It is clear from the Figure 5.9a and 5.9b that the PEC of Ellipsoidal 0° and teardrop are comparable at the Re=9000 to 12000. Beyond Re=12000, only PEC for 3.17 mm pitch of teardrop is higher. Contrary to it, the performance of ellipsoidal 0° remains higher than that of teardrop dimple for rest of the pitches, as shown in Figure 5.9c - 5.9h. Figure 5.9a - 5.9h also shows that the PEC of 3.17 mm and 7.17 mm pitches of ellipsoidal 45° are comparable against the Re =9000 to 12000. Beyond Re = 12000, The PEC of 3.17 mm pitch is distinctly higher than all other $PECs$ up till the Re = 20000, Figure 5.9c - 5.9f.

The percentage differences of PEC at the Re = 9000 for ellipsoidal 45° (3.17 mm pitch) in comparison to ellipsoidal 0° (3.17 mm pitch) and teardrop dimple (3.17 mm pitch) are 7.83% and 6.94% respectively. Similarly, the percentage differences of ellipsoidal 45° (5.17 mm - 13.17 mm pitches) against the same pitches of ellipsoidal 0° and teardrop are 10.03%, 13.53%, 7.32%, 8.93% and 8.42% respectively. The percentage differences of ellipsoidal 45° (3.17 mm - 13.17 mm pitches) against the same pitches of ellipsoidal 0° and Teardrop dimples at all Re are presented in Table 5.3.

TABLE 5.4: Optimum dimpled tube configuration and working ranges

Dimple shape	Optimum tube configuration	Pitch (mm)	Optimum working range of Re	Performance enhancement
Ellipsoidal 45°	E45P3	3.17	9000-30000	45.7% - 9%
Teardrop	TDP3	3.17	14000-40000	31.2% - 3.3%
Ellipsoidal 0°	E0P11	11.17	16000-20000	30% - 24%
Ellipsoidal 0°	E0P13	13.17	30000-40000	15% - 11%

Based on the above comparative study of different pitches, at respective Re, the best PEC ranges of tubes are extracted and subsequently shown in Table 5.4. However, some tubes exhibit remarkably better performances in their favorable Re regimes. For instance, the 3.17 mm pitch of ellipsoidal 45° has significantly higher PEC at Re = 9000 to 16000, contrary to ellipsoidal 0° (11.17 mm pitch) and teardrop (3.17 mm pitch) which are comparable to ellipsoidal 45° at the Re = 18000 to 20000. However, E45P3, E0P11, E0P13 and TDP3 tubes have best performances in their respective Re ranges out of all tubes.

5.3.4 Local Hydraulic Characterization of Dimple Pitched Tubes Having Best Performances

The previous work dealt against the Ellipsoidal 0°, 45° and teardrop dimples shows that the each dimple shaped tubes have better performances against there respective Re ranges. However, in comparison with all dimple tubes, E45P3 has shown the better overall performance in its respective Re. To further elaborate the flow dynamics of these tubes, local characterization of tubes E0P11, TDP3 and E45P3 is of key importance. For this purpose, three positions on the dimple are chosen with respect to its radial height i.e. top section-TS (radial height = 0.0083 m), middle section-MS (radial height = 0.008 m) and lower section-LS (radial height = 0.0077 m), as shown the schematic in Figure 5.10. The values of pressure coefficient, skin friction coefficient and Nu at the specified sections are plotted in Figure 5.11a - 5.11b.

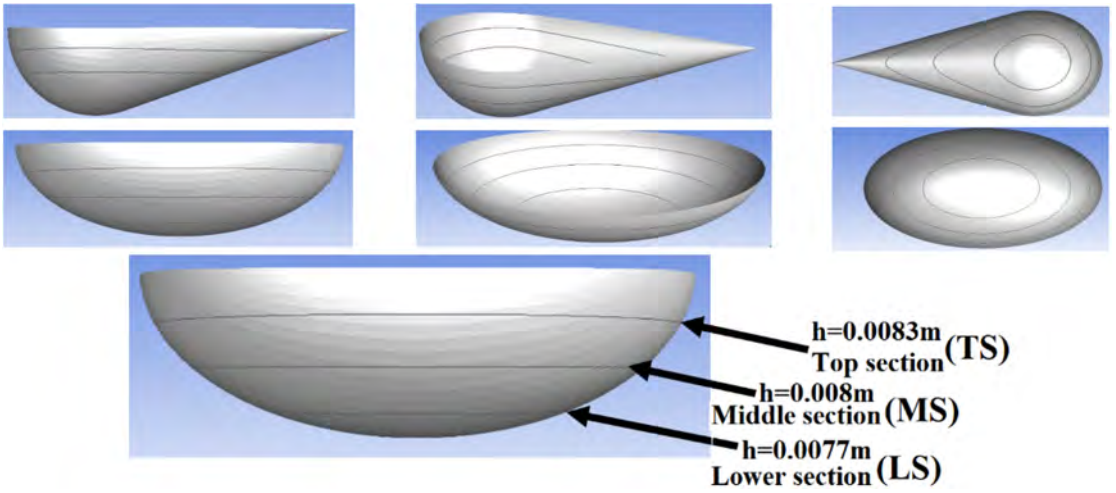

FIGURE 5.10: Three geometric positions on the dimples for characterization

5.3.4.1 Local Hydraulic Characterization:- First Dimple

Figure 5.11a - 5.11b shows the local pressure coefficients (C_p), as provided in equation 1.4, and skin friction coefficients (C_f), as given in equation 1.3 of tubes E0P11, TDP3 and E45P3 at the $Re = 12000$ and these distributions are compared on the polar plots. All sections of 1st dimple for the tubes E45P3, E0P11 and TDP3 are collectively drawn in a graph. Different sections of each dimple shape have various C_p, therefore, in order to understand it in a better way, normalized polar plots (max. magnitude of $C_p = 1$) are presented here. Figure 5.11a shows that the maximum pressure coefficient for tube E0P11 of MS and TS sections lie at the 180° exhibiting the stagnation point, however its magnitude decreases from MS to LS. Contrary to, the pattern of C_p of TS shows the lower values of C_p at the 180° and it also does not has sharp end on it. It reveals that stagnation region just diffuses at the TS. Most of the part of TS exists at the 0° to 90° and 270° to 0° which reveals the detachment of fluid flow. And detachment at TS is more than that at MS and LS.

On the other hand, the magnitude of C_p at MS of tube TDP3 is higher than the TS which shows that the stagnation point lies around the MS, similar to that of Ellipsoidal 0°. The boundary layer is extremely thin at the stagnation point while it gradually starts to thicken afterwards with the increase in fluid

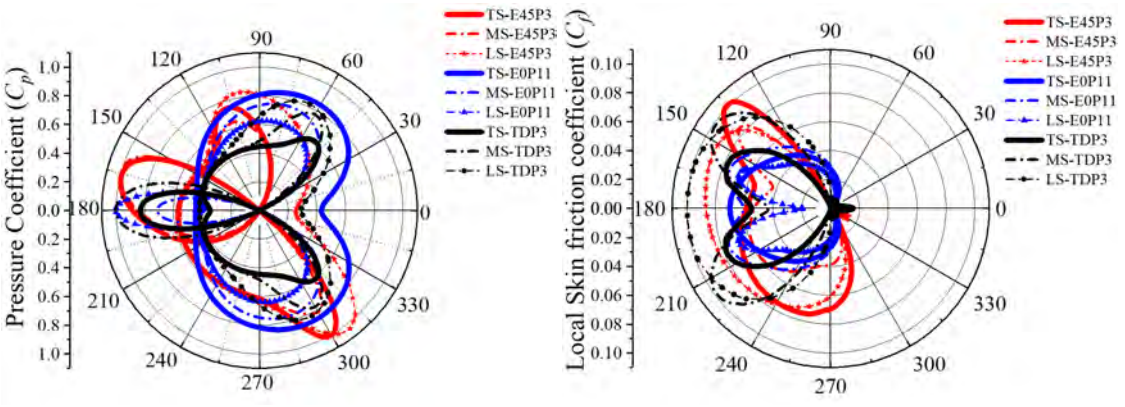

(a) (b)

FIGURE 5.11: Local distributions at TS, MS and LS of first dimple of Ellipsoidal 0°, Teardrop and Ellipsoidal 45° (a) pressure coefficient (b) skin friction coefficient

velocity. This particular behavior can be further understood through skin friction coefficient (C_f). At 180°, the value of C_f is about 0.02 while maximum values are observed from 135° to 180° and onward from 180° to 225°, for the E0P3 and TDP3 dimples. The skin friction of TS of all dimples has close resemblance with the flower petals where two peaks show the fluid flow paths on the either sides of the dimple. Furthermore, the magnitude also decreases from TS to LS. After the crests, as appeared from the Figure 5.11b, that the C_f starts to decreases from the maximum magnitudes up-till the trailing edge where it has minimum values.

Teardrop also has a similar pattern but the curvature radius region is slightly larger than the ellipsoidal 0° as shown in Figure 5.11b. It also shows that the stagnation region lies at the MS section of teardrop contrary to TS of ellipsoidal 0°. The apparent shape of C_f can be attributed as heart-shaped at TS and MS ranging from 120° to 240°. The location of stagnation points in ellipsoidal 0° and teardrop dimple at 180° i.e. frontal side, however, due to change in geometric features, the flow behavior across the dimple is different which causes the deviation in respective C_f. On the other hand, the ellipsoidal 45° is dissimilar from other dimples due to its tilted orientation which exposes maximum frontal area for the incoming fluid flow. As a result, larger area of pressure and skin friction are observed, as shown in Figure 5.11a - 5.11b. Contrary to other dimples, stagnation point of ellipsoidal

45° lies at the 165° with a wide span if about 30° ranging from 150° to 180°. The maximum C_f lies at 135° having a tilted flower shape owing to its orientation.

5.3.5 Local Hydraulic Characterization of Second to Fifth Dimples of Enhanced Tubes

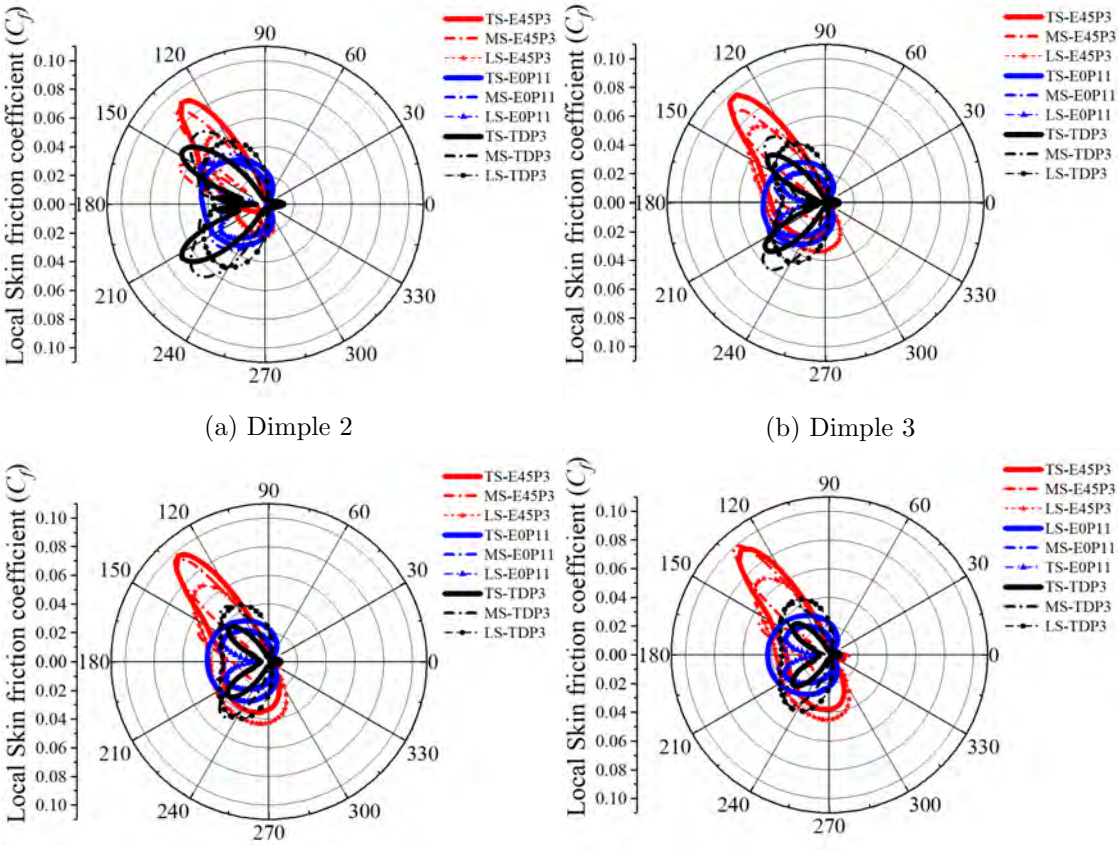

(a) Dimple 2

(b) Dimple 3

(c) Dimple 4

(d) Dimple 5

FIGURE 5.12: Local Skin friction coefficient on the LS, MS and TS of tubes E0P11, TDP3 and E45P3 at dimple 2, 3, 4 and 5

C_p of second to fifth dimples are skipped here in this section to avoid extra information about these dimple and C_f also represents the behavior of fluid dimple interaction in a informative way, especially, when the dimple shapes are different. Figure 5.12a - 5.12d show skin friction coefficient (C_f) distributions for the 2nd to 5th dimple of tubes E0P11, TDP3 and E45P3, at the Re = 12000. The respective magnitudes of C_f for the tubes E0P11 and TDP3 decrease from 2nd to

5th dimple. Contrary to 3rd to 5th dimple of ellipsoidal 0°, the local maxima of C_f for the 2nd dimple lies at 155°. The maxima/minima pattern of teardrop and ellipsoidal 0° from 3rd to 5th dimples remain the same with an overall decrease in magnitude. On the other hand, the magnitude of C_f for the ellipsoidal 45° remains approximately at the 0.1 for the 2nd to 5th dimples. The value of C_f for the 4th to 5th dimples of ellipsoidal 0° (Tube E0P11) and teardrop (Tube TDP3) shapes remains below the 0.05 that is drastically less than C_f of ellipsoidal 45° (Tube E45P3). This depicts that the 2nd to 5th dimples of ellipsoidal 45° (Tube E45P3) contribute much more in regards of C_f, contrary to ellipsoidal 0° (Tube E0P3) and teardrop (Tube TDP3) shapes. C_f depicts the friction by the fluid flow towards the dimple. However, to observe the collective behavior of each dimple towards the formations of friction, the form and friction drag coefficients are discussed in the next section. These drags also differentiate and elaborate the pressure and friction drags.

5.3.6 Form and Friction Drag Coefficients for Different Enhanced Dimples

When the fluid flows having some velocity over an immerse body, the body experiences the resultant force by the the fluid flow. This resultant force in the direction of upstream velocity is called Drag. Drag is affected by geometric shape of the immerse body, velocity and properties of fluid. Drag has been mainly studied for the external flows and it provide the numerous quantitative measure for aerodynamic industry to improve and upgrade it for the next generation challenges [118]. Similarly, drag is also becoming the favorite topic for the internal flows as far as the dimples are concerned because it directs to upgrade the dimple geometric shape which ultimately leads to improve the overall performance [122, 123].

Drag coefficient consists of two major components namely form drag coefficient(c_P), as given in equation 1.5, and friction drag coefficient (c_F), as provided in equation 1.6. As far as the enhanced tubes are concerned, dimples are main source of resistance against fluid flow, therefore drags are computed specifically for the dimples,

as shown in Figure 5.13a - 5.13c. First two dimples of teardrop shape have higher form drag coefficient which increases with increase in Re, as shown in Figure 5.13a - 5.13c.

The drags of teardrop and ellipsoidal 45° are comparable for the first dimple while the difference increases considerably as the fluid moves towards the second dimple. As the fluid flow reaches the 3rd to 5th dimple, ellipsoidal 45° faces high form drag while other two dimples face less pressure resistance.

As far as the viscous drag is concerned, ellipsoidal 45° dimple shows the dominant behavior for the first dimple whereas, the ellipsoidal 0° and teardrop dimples are comparable. From 3rd to 5th dimple, viscous drag coefficient of all the shapes are comparable. The drag behavior shows the 3rd to 5th dimples are the major contributors for the ellipsoidal 45° contrary to the ellipsoidal 0° and teardrop shapes.

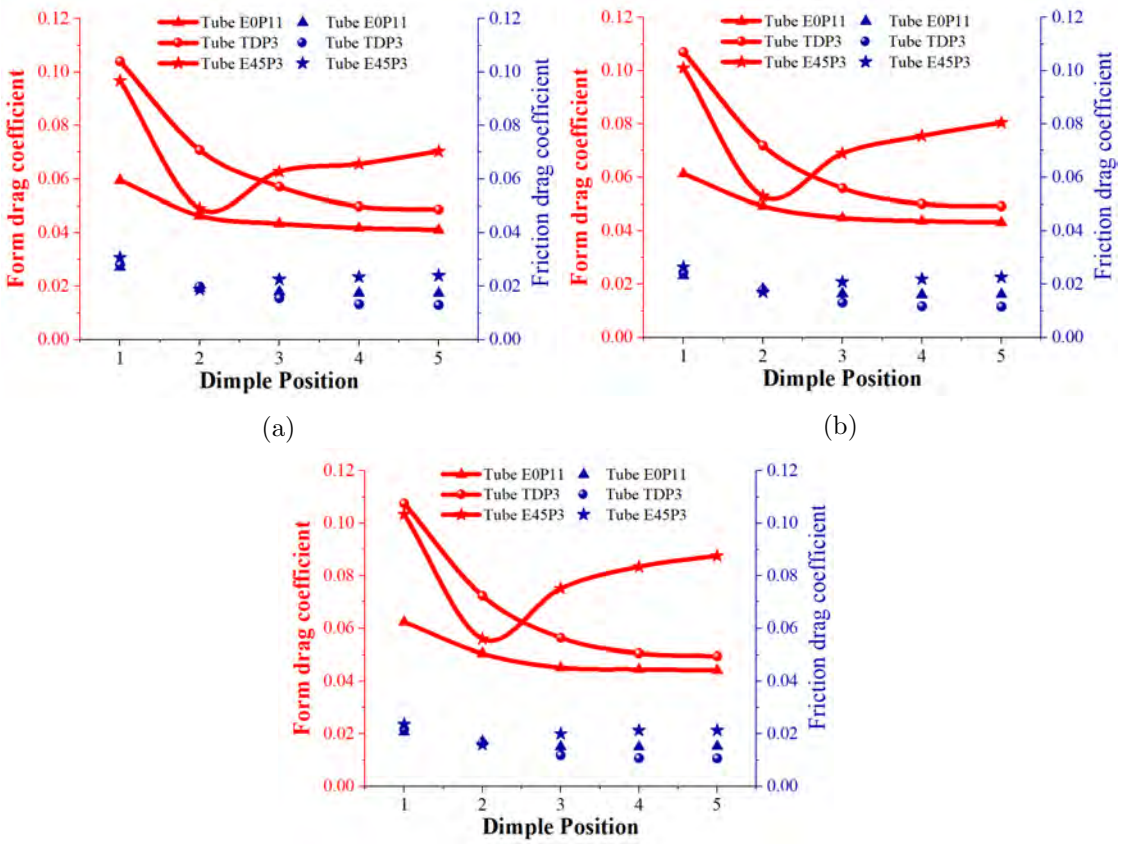

FIGURE 5.13: pressure and viscous drag coefficients of dimples at Re (a) 12000, (b) 16000 and (c) 20000

5.3.7 Local Nu Distributions of First to Fifth Dimple

Figure 5.14a - 5.14e shows the Nu distributions on the lower (LS), middle (MS), and top sections (TS) E0P11, TDP3 and E45P3. The Figure 5.14a apparently shows that, at dimple 1, Nu of ellipsoidal 0° (i.e. in blue color) has maximum value of approximately 1220 at the TS while it decreases from TS to LS. The Nu of teardrop dimple (i.e. in black color) has maximum value of about 1500 which also decreases from TS to LS. Contrary to dimple 1, the disturbed flow interacts with dimple 2 and onward, therefore the maximum value of Nu at the dimple nose front decreases gradually from 2nd to 5th dimple of both configurations. Furthermore, the Nu polar plots of ellipsoidal 0° and teardrop dimples are in circular and heart shapes similar to the patterns of C_f observed in the Figure 5.11b and Figure 5.12a - 5.12d.

In comparison to the ellipsoidal 0° and teardrop dimples, ellipsoidal 45° has a geometric inclination angle that interacts with the fluid first. Afterward, it disperses the flow at 45° inclination angle and establishes the C_p and C_f accordingly, which is shown in Figure 5.11a - 5.11b and Figure 5.12a - 5.12d. As a result, heat transfer also takes place according to its 45° inclination angle, which is shown in Figure 5.14a - 5.14e. The local Nu of ellipsoidal 45° shows the maximum value of 1534 at the TS of dimple 1. However, due to its geometric shape, the stagnation region of ellipsoidal 45° is tilted in shape as compared to ellipsoidal 0° dimple hence producing the effect of the asymmetric wake in the downstream direction. Therefore, Nu has trapezoidal shape with the maximum value of 1534 at the first dimple. Contrary to it, the Nu of MS and LS has circular in shapes, which denotes that stagnation region diffuses towards the top to bottom side of the dimple. In downstream, the Nu maxima of ellipsoidal 0° (Tube E0P11) and teardrop (Tube TDP3) dimples have the range between 400-700, contrary to ellipsoidal 45° (Tube E45P3) which has the Nu range of 1000 to 1250, owing to the pattern of C_f, Figure 5.12a - 5.12d. This depicts that 3rd to 5th dimple of ellipsoidal 45° has a considerable share in heat transfer rate.

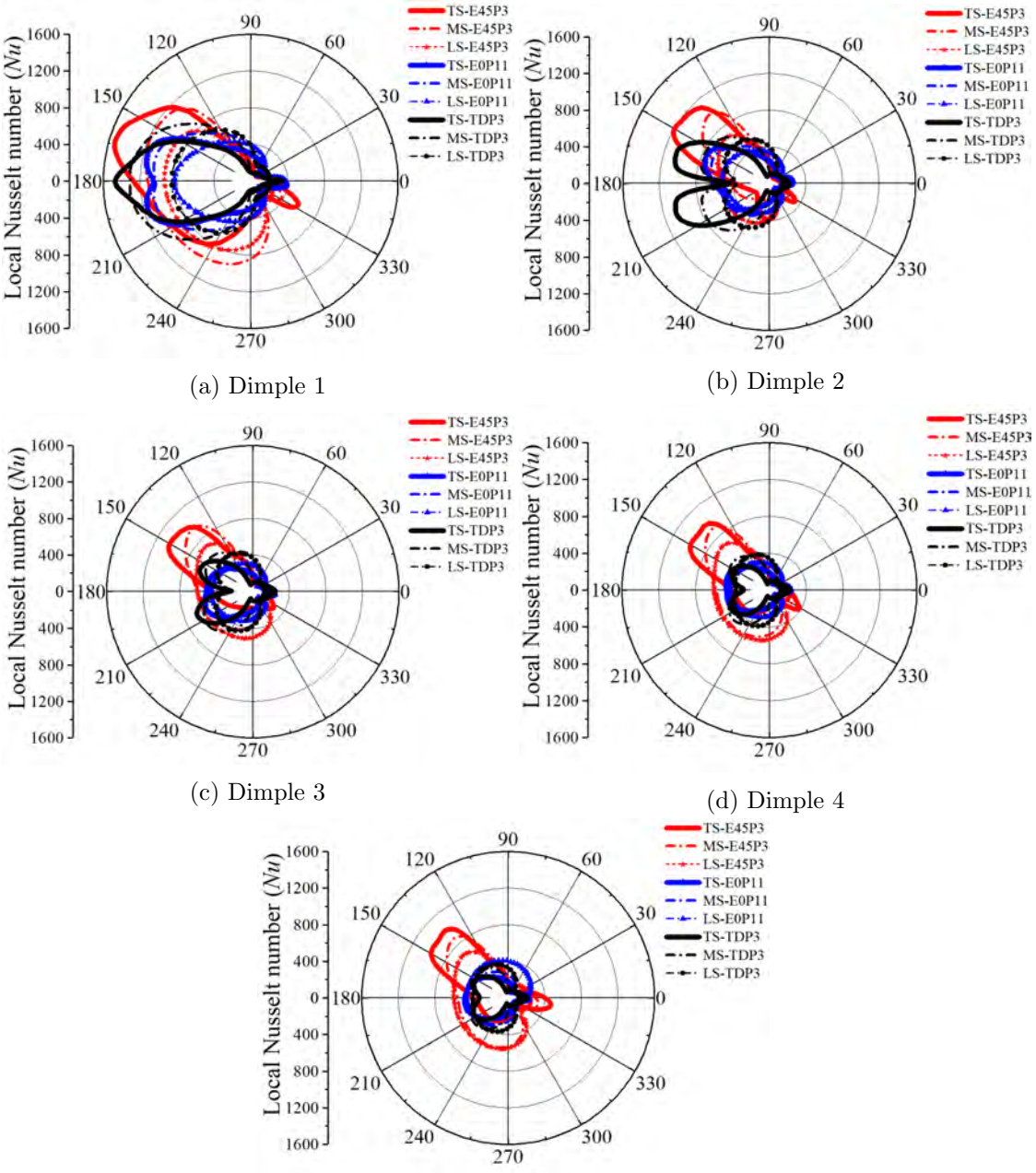

(a) Dimple 1

(b) Dimple 2

(c) Dimple 3

(d) Dimple 4

(e) Dimple 5

FIGURE 5.14: Nu distributions on the LS, MS and TS of tubes E0P11, TDP3 and E45P3 at dimple 1, 2, 3, 4 and 5

5.3.8 Stanton No. and Colburn j Factor of First to Fifth Dimples

Since the fluid inside the tube is the same and only the dimple shape influences the heat transfer, therefore the thermal-hydraulic performance of these tubes can be

compared in patches. The patch is defined as the portion of the tube consisting of dimple and smooth surface as shown in Figure 5.15. Stanton number (St) as given in equation 1.11, a dimensionless number that relates the transfer of heat into the fluid to the thermal capacity of the fluid, and Colburn j factor (j_H) as given in equation 1.12 that draws an analogy between momentum and heat transfer, are used to investigate the performance of these patches. The Prandtl is for the St is given in section 4.2.2. The plots of Stanton number and Colburn j factor versus different patches of the tubes for Re = 12000, 16000 and 20000 are presented in Figure 5.16a to 5.16c, respectively.

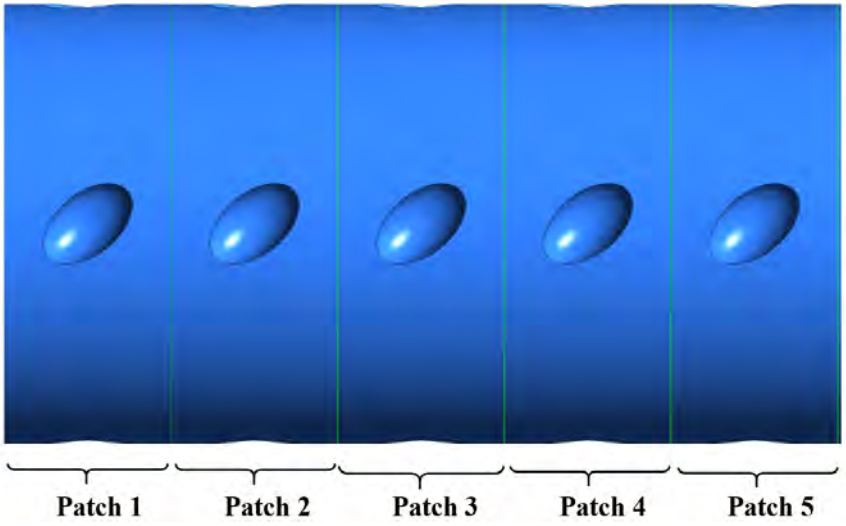

FIGURE 5.15: Schematic of patch 1 to patch 5 on the computational domain

The St and j_H of 1st patch for all the shapes are higher which starts decreasing at the downstream sections. After the second dimple, the St and j_H of ellipsoidal 0° and 45° don't exhibit any significant change for the rest of the downstream section, contrary to the teardrop dimple shape which has a decreasing trend. The ellipsoidal 45° has overall higher St and j_H for all the patches, however, after the second dimple, its difference with teardrop dimple increases at the downstream section.

The overall patterns of St and j_H are same for all Re however, the order of magnitude varies in all cases as shown in Figure 5.16a to 5.16c. At Re = 12000, j_H of tube 13 is 47.7% higher than the j_H of tube E0P11 at the patch 1 whereas it

is 60.04% at patch 5. The j_H of tube TDP3 is 32.11% higher than the j_H of tube E0P11 at the patch 1, while it is 9.19% at patch E0P11.

Furthermore, the percentage differences of St between the tubes E45P3 and E0P11 and tubes TDP3 and E0P11 are approximately the same as mentioned for the j_H of all patches. Figure 5.16a to 5.16b also shows that St and j_H is slightly higher at the $Re = 16000$, in comparison with St and j_H for all the patches at $Re = 12000$.

It is also established from Figure 5.16a to 5.16c that the j_H of tube E45P3 at the $Re = 16000$ is 19.64% higher than the j_H of same tube at $Re = 12000$ for the patch 1 while it is 27.43% for the patch 5. Moreover, the percentage difference of tube E45P3 between $Re = 20000 to 12000$ ranges from 36.33% to 51.35% for the patches 1-5. It is also evident that the ellipsoidal 45° (tubes E45P3) has higher St and j_H for all the patches at all Re.

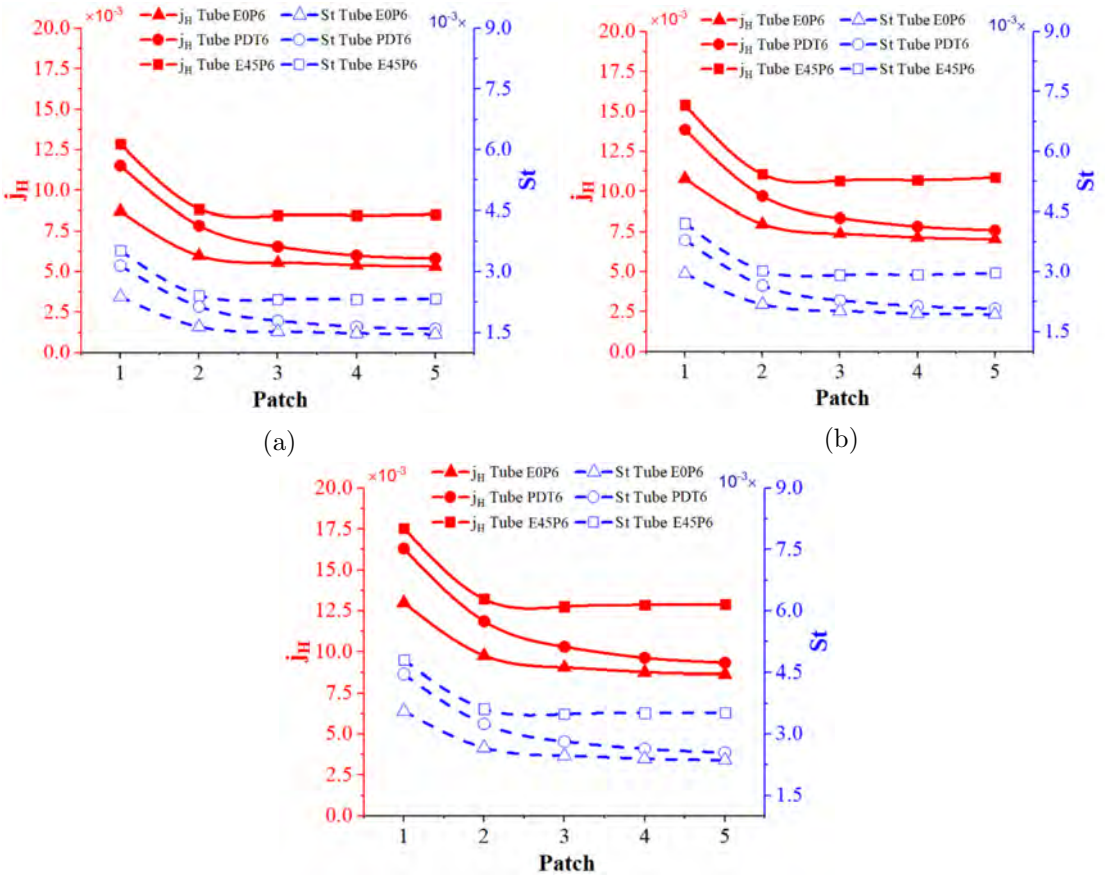

FIGURE 5.16: Colburn j factor and Stanton number for tubes E0P11, TDP3 & E45P3 at the Re (a) 12000, (b) 16000 and (c) 20000

5.4 New Correlations of Nu and fr for Ellipsoidal 45° Dimpled Tube

Since thermal-hydraulic performance of ellipsoidal 45° dimpled tubes is far greater than rest of the dimpled tube configurations. Therefore, it is deemed appropriate to propose correlations of Nu and fr for these enhanced tubes for different pitch configurations for the optimum Re working range. The correlation of Nu and fr, for possible pitches of ellipsoidal 45° dimpled tubes, are proposed in equations (5.1) and (5.2), respectively. The relationships of Nu and fr are proposed as a function of Re and pitch P, where pitch is in millimeters. These correlations are valid for the fluid properties and boundary conditions, given in section 4.2.2. The Reynolds number can be ranged between $9000 \leq Re \leq 30000$, a Prandtl number is 4.8734 while pitch can be varied between 3.17 mm to 13.17 mm.

$$\begin{aligned} Nu &= c_1 Re^{c_2(1+P/1000)} \\ c_1 &= -0.0037866P + 0.19872 \\ c_2 &= -0.00047674P + 0.7367 \end{aligned} \tag{5.1}$$

$$\begin{aligned} fr &= \left[c_3 \log\left(Re + \frac{P}{1000}\right) + c_4\right]^{-3/2} \\ c_3 &= -0.0017367P - 0.11898 \\ c_4 &= 0.20937P + 5.325 \end{aligned} \tag{5.2}$$

The constants a and b of both correlations were linear functions of the pitch P. The comparisons of Nu and fr from numerical results and proposed correlations are presented in Figure 5.17a - 5.17b, respectively. A good agreement between the correlation and numerical results is observed. The maximum difference for Nu remained within 15% while it is 20% in case of fr, for all pitches and Reynolds numbers.

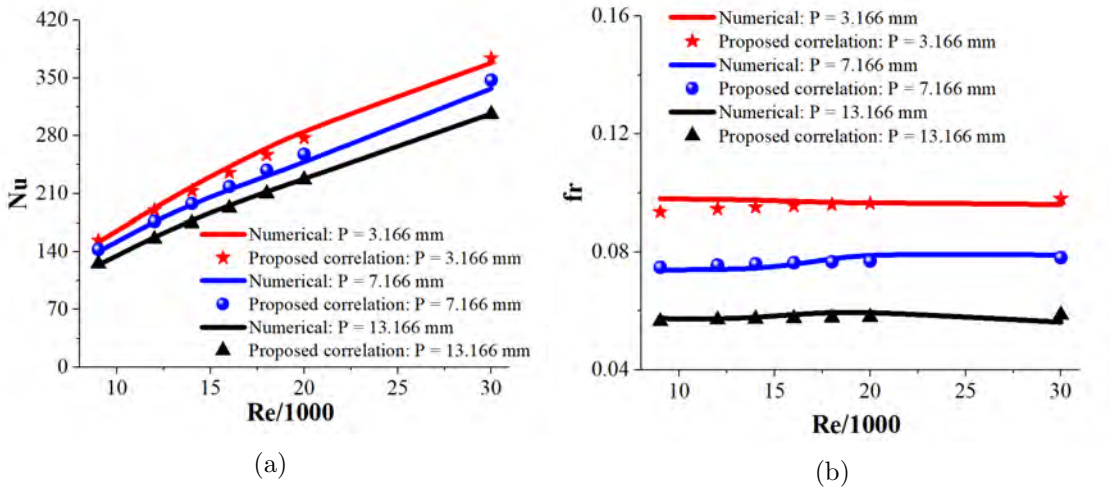

(a) (b)

FIGURE 5.17: Comparison of numerical and correlation results of ellipsoidal 45° dimpled tube (a) Nu and (b) fr

5.5 Conclusion

The numerical investigation of thermal and hydraulic performances of dimpled tubes having various geometric pitches at a constant heat flux of 10 kW/m^2 for a wide range of Reynolds numbers was carried out. Three different dimple shapes of equivalent volume were considered for that purpose i.e., ellipsoidal 0°, Teardrop, and ellipsoidal 45° dimples. The ratio of the tube length to dimple pitch ratio was fixed to 10 to ensure the same number of dimples by accommodating the size of the dimple during the pitch variations for all tube configurations. The dimple pitch played a dominant role in the thermal performance augmentation of the enhanced tubes. The performance of enhanced tubes deteriorated with increasing Reynolds numbers as the friction factors of the tubes increased appreciably. Therefore, optimum dimple pitch along with the best working ranges of Reynolds numbers for all three dimple tube configurations was investigated. The pitch of 3.17 mm was found to be the optimal choice for the teardrop and ellipsoidal 45° dimpled tubes i.e., tube TDP3 and tube E45P3. The thermal-hydraulic performance enhancement of tube E45P3 was found to vary between 45.7% to 9% for the Re range of 9000 to 30000, respectively. Tube TDP3 showed the thermal-hydraulic performance augmentation to alter from 31.2% to 3.3% for the Re range of 14000 to

40000. The best pitch configurations for ellipsoidal 0° dimpled tube were obtained to be 11.17 mm (tube E0P11) and 13.17 mm (tube E0P13) for Re = 16000 to 20000 and Re = 30000 to 40000, respectively. For those ranges of Re, tube E0P11 and tube E0P13 exhibited the performance enhancements of 30% - 24% and 15% - 11%, respectively, as given in Figure 5.18.

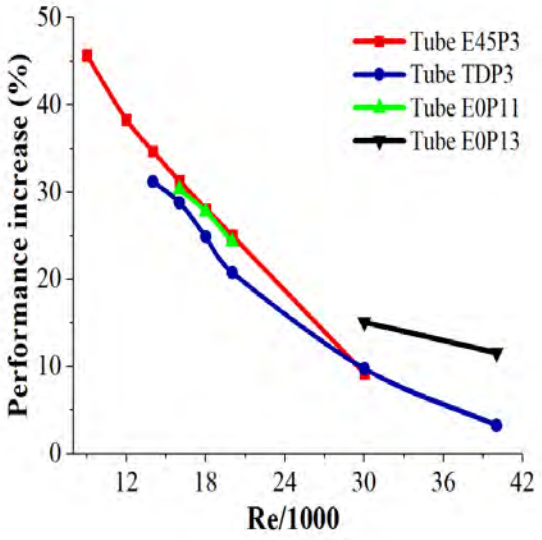

FIGURE 5.18: Best tube configurations with their favorable Re ranges

The performance augmentation of dimpled tubes was found to be strongly linked to flow distribution around the wake and fluid-dimple interactions downstream of the tubes. It is pertinent to mention that the better performance of tube E45P6 was observed to be linked to the asymmetric wake behind the dimples which created a path for the fluid to interact with succeeding dimples which promoted heat transfer. Whereas, tube E0P11 and tube TDP3 generated a stable wake behind the dimples which created channel-like flow with minimal fluid-dimple interaction in the downstream direction and hence yielded a moderate increase in heat transfer rates. Local characterizations of tubes E0P11, TDP3, and E45P3 were presented using skin friction coefficient (C_f), drag coefficient, Nusselt number (Nu), and Colburn j factor (j_H). C_f of tube E45P3 remained constant at 0.1 for the first five dimples while in cases of tube E0P11 and tube TDP3 C_f decreased from 0.1 to 0.04. Local Nu of tube E45P3 decreased from 1534 to 1000 from 1st to 5th dimple however, it was significantly lower for other tubes. As a result, Colburn j factor of

tube E45P3 was 47.7% higher than that of tube E0P11 for the first patch at the $Re = 12000$ and 60.04% at patch 5. Moreover, for tube E45P3, correlations for Nu and fr were also proposed as the functions of Re and P which covered each configuration of the ellipsoidal dimpled tube. The Nusselt numbers and friction factors could readily be obtained for any ellipsoidal dimple tube topology with reasonable accuracy for $9000 \leq Re \leq 30000$.

It is appropriate to mention that the best pitched dimple tubes with Re have been numerically analyzed following with proposed correlations. Up till now, Star (circumferential dimples) configuration in all tubes is fixed, denoting the surface area is not changed yet. It is necessary for the current study to analyze the behavior of fluid flow with the variation in radial orientations of dimple i.e., 'Star of enhanced tube', to evaluate the impact on overall performance. In the next chapter, determination of these characteristics of enhanced tubes with variation in Star is carried out numerically along with the proposed correlations.

Chapter 6

Influence of Transverse Dimples Patterns on Fluid Flow and Heat Transfer Characteristics

6.1 Introduction

In the previous chapter, thermal hydraulic performances of the flow through heated enhanced tubes with best chosen pitches having their favorable Re ranges and constant surface heat flux were investigated for the ellipsoidal 45° dimples. The fluid flow interaction of dimpled tube with Star variation is inevitable for the engineering system design or industrial usages, as discussed in the conclusion of Chapter 5. Therefore, in this chapter, the flow and heat transfer characteristics of ellipsoidal 0°, 45° and Teardrop dimpled tube with variation in Star is numerically analyzed for a wide range of Re. Through a parametric study, identification of the best Star formation is investigated using Reynolds Averaged Navier Stokes ($RANS$) under steady flow conditions for each geometric configuration. The thermo-hydraulic performance enhancement for the optimal configuration is investigated, flow characteristics of the enhanced tube with star variation are discussed and categorized locally through Nu. In addition, the correlations of Nu and fr for the Star variated

enhanced tubes are proposed for the wide range of *Re*. In the end, performance of best pitched tube, along with best Star configuration is presented.

6.2 Computational Domain of Dimple Tube with Star Variation, Boundary Condition and Grid Generation

The effects of dimple pitch on the thermal-hydraulic performance of tubes enhanced with Ellipsoidal 0°, Ellipsoidal 45° and Teardrop dimples have been investigated in the previous chapter. The optimum pitches for each dimple shape have been highlighted while considering only four dimples in the transverse or circumferential direction. The total number of dimples and dimple length to pitch ratios for each tube are fixed to 10. It has been revealed that the thermal performance of the tube is linked to the interruption of the boundary layer flow by the particular axial flow patterns generated by the vortices in the wakes of the dimples. However, the effects of the neighbouring dimples in the transverse dimples were not focused since the dimples were fairly distant. However, the number of dimples in the transverse direction may play a crucial role in the flow patterns generation in dimples wakes and consequently in altering the thermal-hydraulic performance of the augmented tubes.

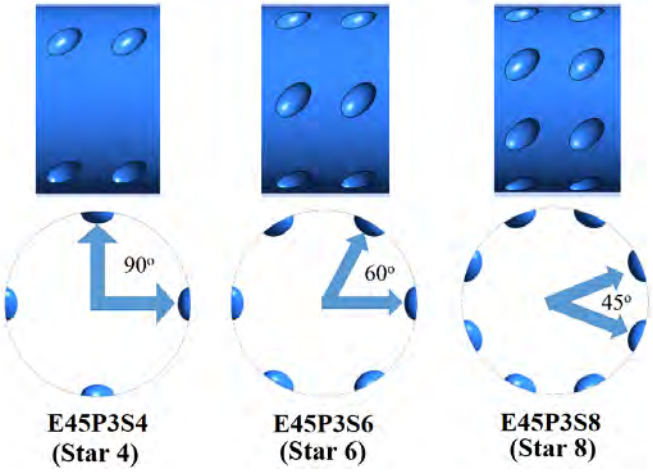

FIGURE 6.1: Geometric configuration of Star

TABLE 6.1: Parameters of all tubes used for the current study

Dimple Pitch (P) (mm)	**Star**				
	4	6	8	**Dimple profile**	**Ratio of Dimple Pitch to height**
3.17	**TDP3S4**	**TDP3S6**	**TDP3S8**	Teardrop	2.54
11.17	**E0P11S4**	**E0P11S6**	**E0P11S8**	Ellipsoidal 0°	9.47
3.17	**E45P3S4**	**E45P3S6**	**E45P3S8**	Ellipsoidal 45°	2.54

Therefore, in current chapter, a detailed investigation of the effects of circumferential dimples on the thermal and hydraulic performance of Ellipsoidal 0°, 45°, and Teardrop dimpled tubes is carried out. The angle between the circumferential dimples is 90°, 60° and 45° for the Star 4, 6 and 8 respectively. Different configurations of Star variation of Ellipsoidal 45° dimple tube along with inside angles are presented in Figure 6.1. And geometries of different tubes are also shown in the Figure 6.2. As given in the previous chapters, the tube numbers are linked with its geometric properties therefore, in current chapter, additional property (i.e. Star) is added in the tube name. For example, TDP3 represents the tear drop dimple tube with 3.17 mm pitch configuration. Here it becomes TDP3S4, which denotes that Teardrop dimpled tube with P=3.17 mm and Star=4. Similarly, all tubes of current chapter having optimum pitches and Star configurations along with tube parameters are given in Table 6.1.

The boundary conditions, used in current chapter, are discussed in the chapter 4. Generation of structured mesh through near-wall refinement is implemented for domain discretization, as presented in Figure 6.3. The number of grid elements are varied from 0.28 million (Coarse mesh) to 6.2 million (Fine Mesh). The difference in Nu and fr increases as the grid size is refined, nevertheless, it becomes constant for 2.0 million grid elements, as given in Table 6.2.

After all, to confirm that the grid dependence disparities are insignificant, 3.0 million mesh cells are favored for all computations in the current study. Since the precision of the solution of turbulent flow depends upon the resolution of the grid in the boundary layer regime, therefore grid size of 3.0 million is preferred which also allows the accurate computation of the near wall effects. In the selected mesh of 3.0 million elements, the resultant $y^+ \approx 0.51$ is noted which ensures that the mesh size is adequate to resolve the near wall effects.

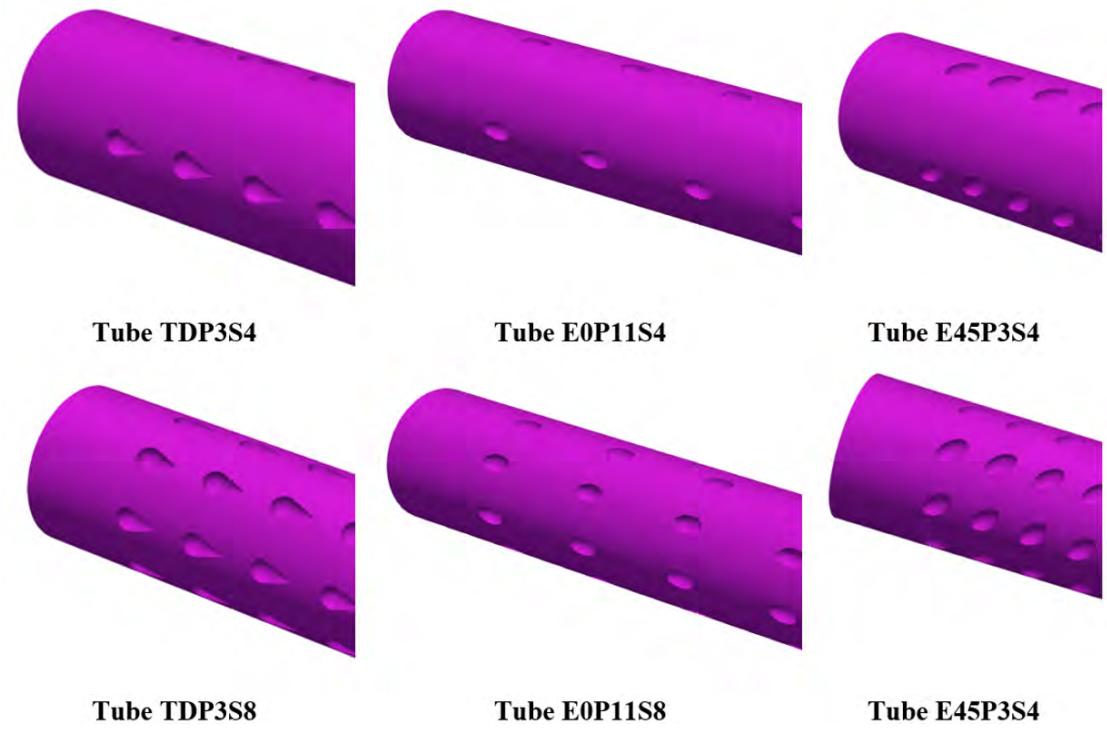

FIGURE 6.2: Geometries of different tubes with Star variation

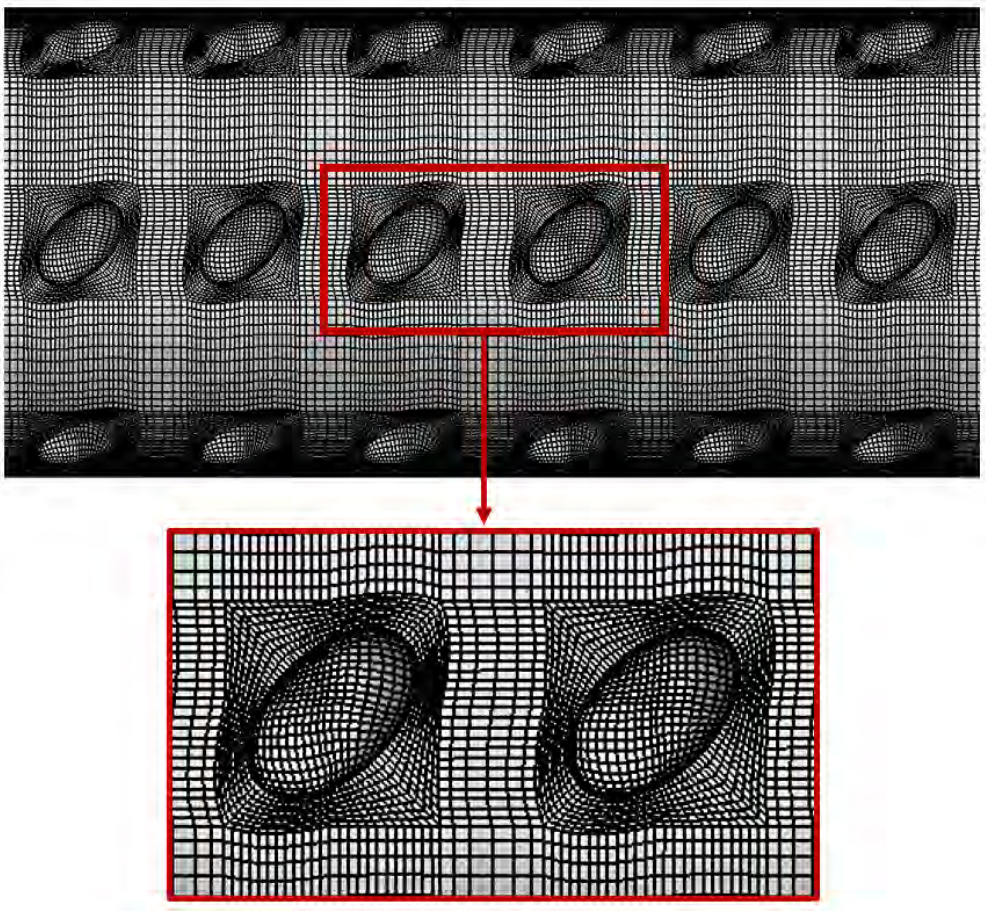

FIGURE 6.3: Structured grid of the computational domain

TABLE 6.2: Grid independence study of Tube E45P3S6

Grid	Re = 9000		Re = 14000	
(in millions)	Nu	fr	Nu	fr
0.28	158.37	0.10864	228.58	0.10951
1	153.58	0.10232	220.69	0.10156
2	152.73	0.09953	219.73	0.09831
3	151.68	0.09797	218.56	0.09754
6.2	151.55	0.09788	218.37	0.09751

6.3 Results and Discussion Section

6.3.1 Influence of Star Variation of Dimpled Enhanced Tubes on the Heat Transfer and Hydraulic Loss

The number of dimples in the circumferential direction varies from 4 to 8, therefore 9 tubes are employed, as presented in Table 6.1. These tubes are analyzed for the Re range $5000 \leq Re \leq 40000$. The quantitative analysis of heat transfer and hydraulic loss can be best associated to Nu and fr, respectively. Therefore, the results of all dimpled tubes for different Re in the form of Nu and fr are presented in Figure 6.4a - 6.4f. It is obvious from Figure 6.4a - 6.4c that Nu increases with increasing Re and the number of circumferential dimples. Tube TDP3S8 shows a higher heat transfer rate for the entire range of Re. It is manifested in Figure 6.4a that the Nu of Tube TDP3S8 is 16.73% higher than Nu of Tube TDP3S4 at the Re=5000 while it is 29.05% at the $Re = 30000$. Similarly, Figure 6.4b depicts that the Nu of Tube E0P11S8 is 14.92% higher in comparison with Nu of Tube E0P11S4 at the $Re = 5000$ while it is 33.49% at the $Re = 40000$. Furthermore, Figure 6.4c also reveals that the Nu of Tube E45P3S8 is 36.94% higher than the Nu of Tube E45P3S4 at the $Re = 5000$, however enhancement reduces to 14.6% at the $Re = 40000$.

Above results shows that the Nu of ellipsoidal 0° and Teardrop dimpled tubes also present the same trend but with lower heat transfer enhancements, particularly at high Re. It is appeared from the Figure 6.4a - 6.4f that the increase in the Star augments the heat transfer rate. In addition, ellipsoidal 45° dimpled tubes have relatively higher Nu.

Figure 6.4d - 6.4f shows the fr of all the tubes which depicts the hydraulic losses of the tubes increase with different Star configurations. To increase the fluid surface interaction, the hydraulic loss is also increased. Figure 6.4d reveals that fr of Tube TDP3S6 is 4.13% higher than the fr of Tube TDP3S4 at the $Re = 5000$ while it is 18.9% at the $Re = 40000$. Similarly, hydraulic loss of Tube TDP3S8 is 22.48% higher than the fr of Tube TDP3S4 at the Re 5000 whereas it is 55.9% at the $Re = 40000$.

It is also established in Figure 6.4f that the hydraulic loss of tubes E45P3S4 to E45P3S8 is much higher in comparison with rest of the tubes. The fr of Tube E45P3S6 is 33.14% higher than the fr of Tube E45P3S4 at the $Re = 5000$ while it is 42.03% at the $Re = 40000$. Likewise, the fr of Tube E45P3S8 is 64.66% higher than fr of Tube E45P3S4 however, it is 72.18% at the $Re = 40000$.

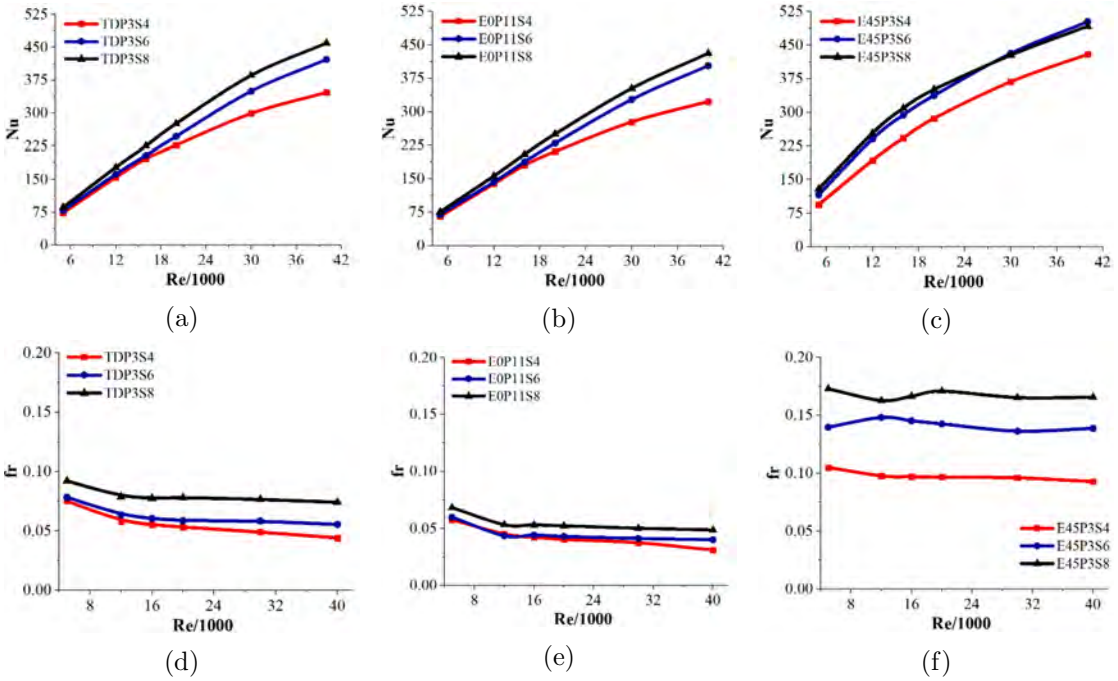

FIGURE 6.4: Comparison of dimpled tubes 1-9 (a, b & c) Nu and (d, e & f) fr

6.3.2 Consequence of Star Variation on the Fluid Flow and Heat Transfer Characteristics

The detailed discussion on the fluid flow and heat transfer characteristics at single Re is not the main objective here as it has already discussed in detail in previous chapters. In the first phase of this subsection, fluid flow property distribution of some of the tubes is shown here for the glance of these distribution. Afterwards, the distribution will on the distinction between the Star variation.

The fluid flow and heat transfer characteristics associated with the trends of Nu and friction factors, as observed in Figure 6.4a - 6.4f are assessed in detail by analyzing the velocity, wall shear, pressure, and Nu distributions of enhanced tubes. Local thermal-hydraulic characteristics are presented in Figure 6.5 at the $Re = 5000$ of tubes TDP3S4, E0P11S4 and E45P3S4. Velocity distributions showing the flow paths around the dimples are drawn at the tube radius of 8 mm. Velocity distributions show the flow paths around the dimples. It depicts that tube TDP3S4 and E0P11S4 dimple tubes have fluid flow paths at the top and bottom sides of the dimples while vortices are between the dimples. Vortices in the wakes of dimples are of different shapes for the different tubes. For example, in the case of TDP3S4 the wake of the upstream dimple attaches to the front stagnation region of the downstream dimples. This forces the fluid to adopt a flow path around the dimples and therefore limits the fluid-dimple interaction. The tube embedded with Ellipsoidal 0° (E0P11S4) also shows a similar flow pattern as observed in Tube TDP3S4 however, due to the larger pitch the wakes of the upstream dimples do not interact with the stagnation points of the downstream dimples and consequently fluid-dimple interaction are not diminished in the front half of the dimples. The heat transfer increases at the front sides of dimples due to the stagnation zone which is also shown in the Nu distributions. The generation of stagnation region already has been discussed at the Ellipsoidal 0°, 45° and 90° dimples in the Chapter 4 in detail. So, there is no need to discuss it again. Now come to the tubes TDP3S4 and E0P11S4. Both tubes have dimples that are symmetric along the axial direction. Axial Pressure distributions of tubes

TDP3S4 and E0P11S4 show front local stagnation pressure of dimples decrease successively in the downstream direction depicting the flow separation, as shown in Figure 6.5. This is also confirmed through the wall shear distributions, Figure 6.5 which illustrate high shear at the upstream section of the tube as compared to the downstream section. On the other hand, the wakes of the Ellipsoidal 45° dimple tube (E45P3S4) are observed to be non-symmetric and the flow pathways around the top and bottom halves of dimples are different. The non-symmetric wakes of the upstream dimples attach to the bottom half of the downstream dimples creating a path for the flow across the front face of the dimples.

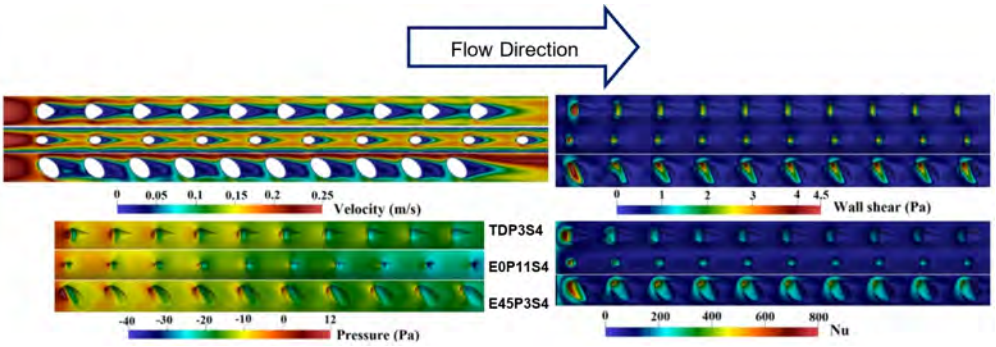

FIGURE 6.5: Thermal and hydraulic property distributions at the Re 5000 of Tubes TDP3S4, E0P11S4 and E45P3S4

Wall shear distributions depict high shear at the upstream section of dimple where the fluid strike at the front side of dimple, as shown in Figure 6.5. As a result, the heat transfer increases at the front sides of dimples, which is shown in the Nu distributions. Both tubes have dimples that are symmetric along axial direction. Contrary to this, Ellipsoidal 45° is asymmetric and produces different results. The velocity distributions depict that the top side of tube E45P3S4 produces a higher velocity magnitude than the bottom side. The vortices are also prolonged between the downstream to the upstream of the next dimple, as shown in Figure 6.5. The pressure gradient location is also inclined, as assist by dimple shape, which causes more experience of pressure for the dimple frontal area. This produces high shear at the dimple frontal area that is aligned at 45°. As a result, Nu increases at these spots, and more dimple areas experience the heat transfer, as shown in Nu distributions in Figure 6.5. Furthermore, the flow in circumferential direction has

major effect on all dimple configurations, especially for the Ellipsoidal 45° dimple shape. This endorses the fluid-dimple contact followed by the advancement of heat transfer. This effect is depicted in the velocity distributions in various cross-flow sections at the $Re = 5000$ in the Figure 6.6. The velocity distributions are drawn on the dimple-1 location '$D-1'$, dimple-5 position '$D-5'$ and dimple-10 place '$D-10'$, respectively. At $D-1$ of Star 4, the velocity core of all tubes is thin as it reflects the dominance of viscous forces. Whereas the core radius develops further at $D-10$ and approaches around double the radius of $D-1$.

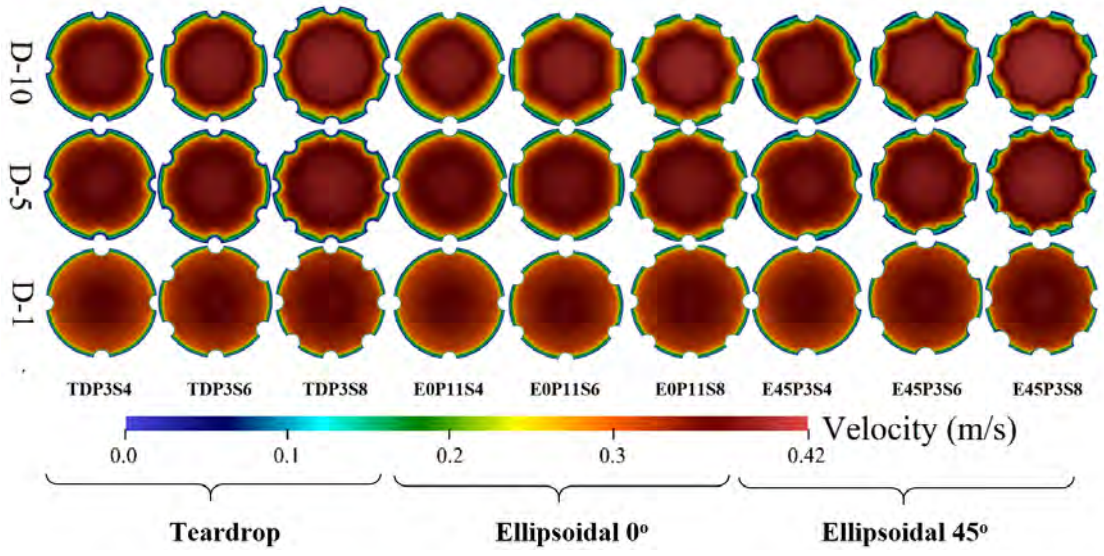

FIGURE 6.6: Velocity distributions of cross-flow sections of tubes TDP3S4-E45P3S4 at different dimple locations D-1, D-5 and D-10

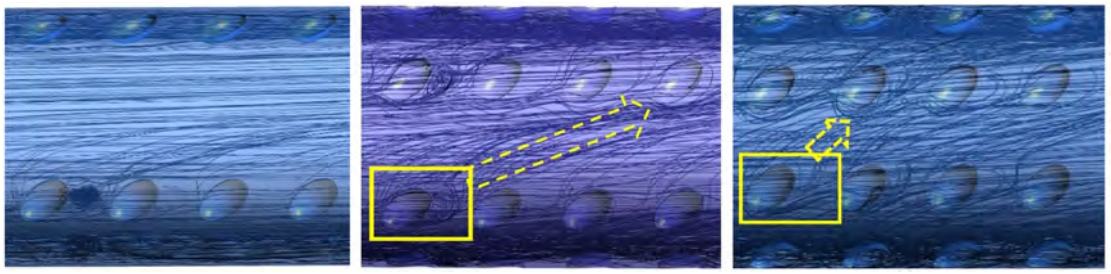

FIGURE 6.7: Velocity Streamlines of tubes E45P3S4, E45P3S6, and E45P3S8, respectively

The velocity core also spreads wider as the Star varies from 4-8. This depicts that central velocity is in direct relation to the Star. There is also unique representation of core shape for each dimple configuration. The velocity core of Teardrop dimple

has almost circular in shape for all Star. The velocity core of Ellipsoidal 0° dimple has tilted square shape for Star 4, while it is hex and octa for the Star 6 and 8, respectively.

The velocity core in Ellipsoidal 45° tube forms a diamond shape for all Star configuration. Moreover, the boundary layer of Ellipsoidal 45° dimple tubes is comparatively thicker and more perturbed. It leads to enhance the fluid-dimple interaction than the other dimple shapes. Therefore, a helical flow pattern is generated in the Ellipsoidal 45° dimpled tube for every star configuration as shown in Figure 6.7.

Figure 6.7 shows the streamlines of fluid flow inside the tubes E45P3S4 to E45P3S8, respectively. Streamlines of tube E45P3S4 show that some of the fluid flow is intercepted by the dimples and the rest of the fluid flow is smooth and it is without any interruption along the axial flow direction. However, the fluid flow of tube E45P3S6 shows stimulating behavior. The fluid flow of tube E45P3S6 also interacts in the circumferential direction. It look like that the flow started rotating and following a helical path. It depicts that the 45° inclination side of the dimple allows the fluid to flow along its side, which tries to interact with the 4th dimple in the next row. This circumstantially directive flow is shown in Figure 6.7. Similarly, the fluid flow interacts with the 2nd dimple in the next row of tube E45P3S8, as shown in Figure 6.7.

6.3.3 Outcomes of Star Variation on the Thermal Hydraulic Performance Enhancement

The performances of dimple tubes are presented in Figure 6.8a - 6.8c, whereas PEC_s denotes the performance evaluation criteria of the smooth tube which is obviously equal to 1. The thermal-hydraulic performance of enhanced tubes decreases with an increase in Re for all pitches. Figure 6.8a - 6.8b shows that for a given value of star, PEC of Teardrop and ellipsoidal 0° dimpled tubes are quasi-identical, particularly at low Re. At higher Re the difference of PEC increases as the Star increases from 4 to 6 but for Star 8 PEC of both dimples once again

becomes quasi similar and therefore limiting the performance. In contrary to, the enhancement in PEC is significantly large at low and moderate Re for Ellipsoidal 45° dimpled tubes. It is established in the Figure 6.8c that the PEC of Tube E45P3S6 is 12.15% higher than the PEC of Tube E45P3S4 at the $Re = 5000$ whereas it is 5.99% at the $Re = 16000$. Similarly, the Tube E0P11S6 is 6.83% higher than the PEC of Tube E0P11S4 at the Re 20000 while it is 14.634% at the $Re = 40000$.

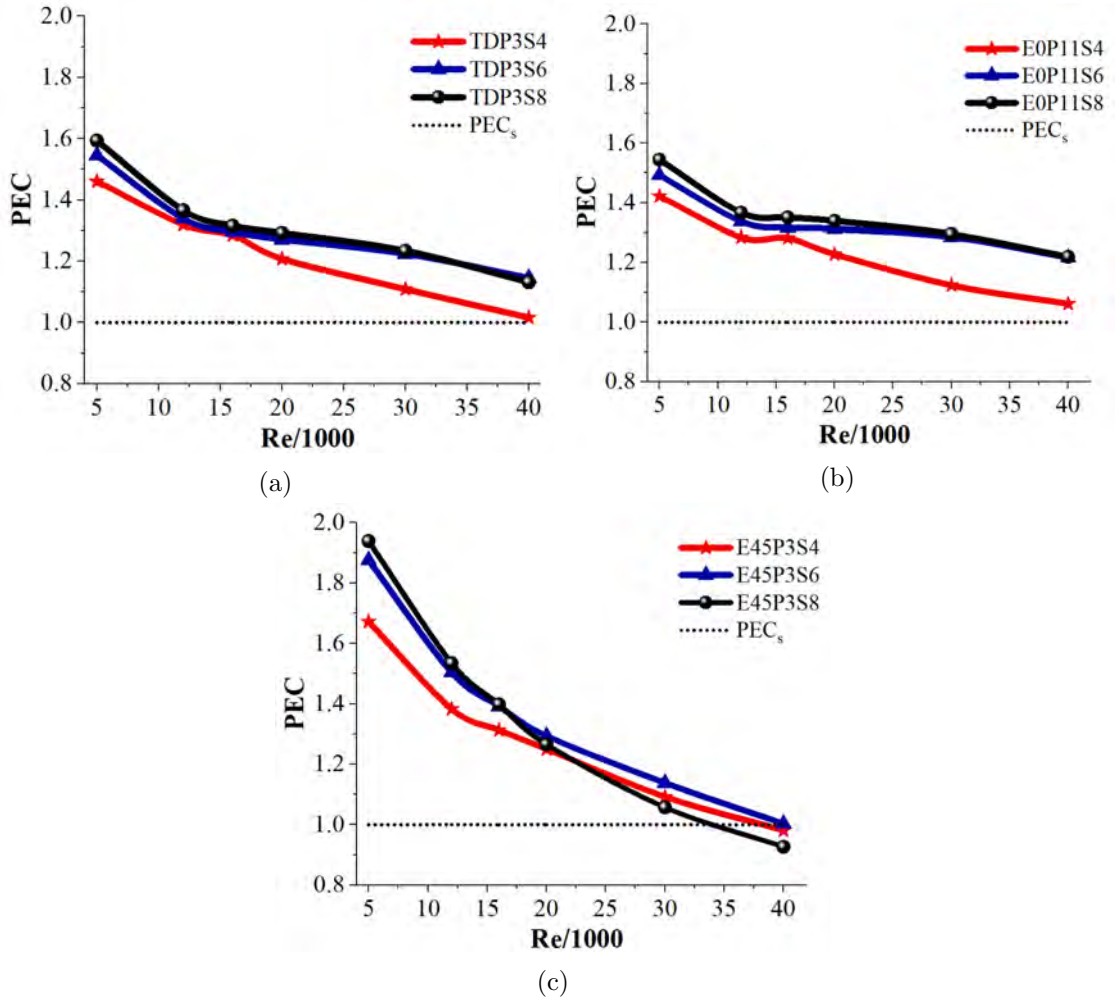

FIGURE 6.8: Thermo-hydraulic performances of: (a) tubes 1-3, (b) tubes 4-6, and (c) tubes 7-9

However, as observed in Figure 6.9a - 6.9f at significantly large Reynolds numbers, i.e. Re greater than the 30000, Ellipsoidal 45° dimpled tubes become ineffective. The reason for the deterioration of the thermal-hydraulic performance of Ellipsoidal 45° dimpled tubes is because at higher Re the flow momentum is

sufficiently large which diminishes the swirl behavior of the tubes and therefore limits the fluid-dimple interaction.

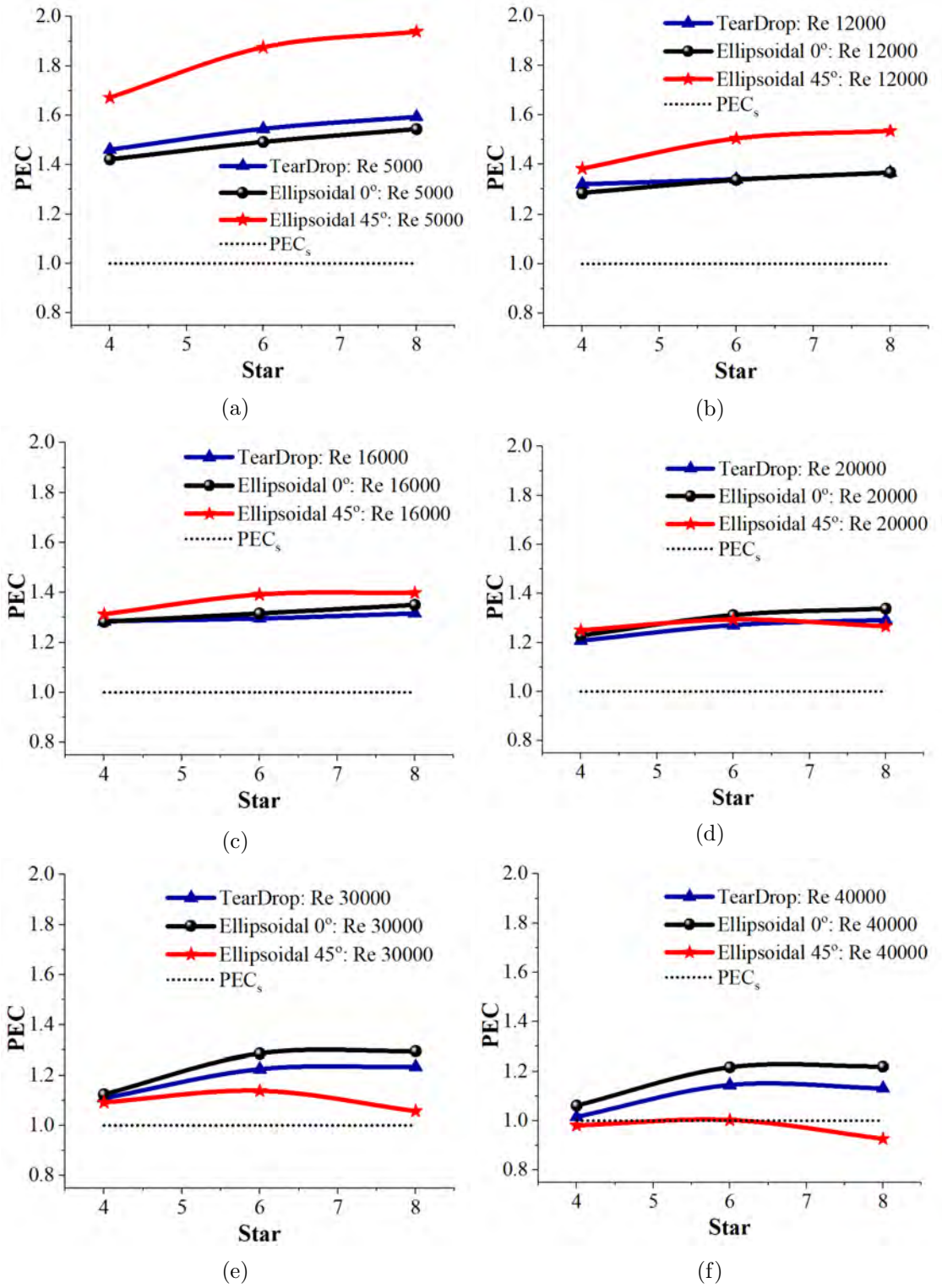

FIGURE 6.9: Performances of Teardrop, Ellipsoidal 0° and Ellipsoidal 45° dimpled tubes at the different Re, (a) $Re = 5000$, (b) $Re = 12000$, (c) $Re = 16000$, (d) $Re = 20000$, (e) $Re = 30000$, (f) $Re = 40000$

Therefore, the optimum configuration of enhanced tubes must be characterized according to the favorable Reynolds number range. It is also pertinent to mention that the thermal-performance enhancement of Star 6 and 8 configurations is indistinguishable. However, the lower manufacturing cost of tubes with Star 6 configuration and high thermal-hydraulic performance gives an edge over the tube with Star 8 configurations. From Figure 6.9a - 6.9f, for Re from $5000 \leq Re \leq 18000$, Tube E45P3S6 (Star 6 Ellipsoidal 45°) is recommended while Tube E0P11S6 (Star 6 Ellipsoidal 0°) should be used for the applications having working range of $20000 \leq Re \leq 40000$.

6.3.4 Local Characterization of Tube E0P11S6 and E45P3S6

Tube E45P3S6 and Tube E0P11S6 are identified as the optimum enhanced configurations for $5000 \leq Re \leq 20000$ and $20000 \leq Re \leq 40000$, respectively. The axial and radial flow and heat transfer characterization of the optimum tube configurations under optimal conditions are also performed. Figure 6.11a - 6.11f shows the distributions of local Nu and skin friction coefficients (C_f) at different locations over the surface of tubes E0P11S6 and E45P3S6, at the Re of 20000 and 12000, respectively. These Reynolds numbers correspond to the optimum flow conditions of the given enhanced tubes. Moreover, the axial distances of the tubes are normalized with their respective dimple pitches. Figure 6.10 shows the specific locations where the Nu and C_f are plotted for the tubes E0P11S6 and E45P3S6. Yr corresponds to the radial displacement representing the dimple at different sections of the dimples i.e., at 1 mm, 0 mm and -1 mm, while each of these lines extends from the inlet to the outlet of the tubes. These different locations on the surface are shown in the schematic of Figure 6.10. Yr is the radial displacement covering the dimple at different locations 1 mm, 0 mm and -1 mm, while each of these lines extends from the inlet to the outlet of the tubes. Figure 6.11a manifests the local Nu at $Yr = 1$ mm which is located in the high-pressure zone that is in the vicinity of the stagnation region for Tube E45P3S6 (Ellipsoidal 45°) while it is located in the low-pressure zone of Tube E0P11S6. The peak values of Nu

depict the location of dimples whereas lower values with flat lines indicate the smooth surfaces in between the dimples. Nu value at first dimple is 1200 for Tube E45P3S6 which almost maintains till 4th dimple. It decreases to 990 at the 5th dimple and decreases further in the downstream direction. At $Yr = 1$ mm, Nu of Tube E45P3S6 is almost two times the Nu that of Tube E0P11S6 even though Re of Tube E0P11S6 is higher than that of Tube E45P3S6. It also denotes that Nu of Tube E0P11S6 from 3rd to 8th dimple remains almost constant at 670 at the $Re = 20000$. The trend of Tube E0P11S6 shows that the fluid-dimple interaction is remained indistinguishable in the downstream direction.

Figure 6.11b represents the Nu at the location $Yr = 0$ mm which is located in the vicinity of the stagnation region for Ellipsoidal 0° dimple. Nu of Tube E0P11S6, at $Re = 20000$, at the location at 1st dimple is approximately 1800 which is approximately 1.7 times higher than that of Tube E45P3S6, at $Re = 12000$, at the first dimple. Afterwards, Nu of Tube E0P11S6 declines to almost 1200 due to flow path development in the axial direction. After the 3rd dimple, the flow path is developed and the Nu becomes constant to a value of approximately 1200.

The local Nu of Tube E0P11S6 at Yr = -1 mm, as presented in Figure 6.11c, decreases from 815 at the first dimple to 630 at last dimple. The trend of Tube E0P11S6 shows that the interaction between fluid and dimple is maintained in the downstream direction. Figure 6.11c also shows the local Nu distribution of Tube E45P3S6 at the position Yr = -1 mm where fluid flow partially detached from the dimpled surface due to the non-symmetric wake of the dimple. The non-symmetric wake allows the flow to form a passage across the dimples and induces a helical flow pattern. This improves the fluid-dimple interaction and generates higher heat transfer rates. The maximum Nu of Tube E45P3S6, for $Re = 12000$, at 1st dimple is approximately 800. Nu declines at the 2nd dimple as flow is unstable but rises quickly to a value of 600 till the 9th dimple. The C_f at the Yr = -1 mm also shows a similar pattern.

The C_f of Tube E0P11S6 at the $Yr = 1$ mm and Yr = -1 mm has magnitudes of range 0.02 to 0.03, as shown in Figure 6.11d and 6.11f. The C_f of Tube E0P11S6

at $Yr = 0$ mm follow the pattern that is different from the pattern of Nu, as shown in Figure 6.11d. The C_f of the 1st dimple at $Yr = 0$ mm is 0.045 which, after the 3rd dimple, slightly decreases to a value of 0.042. It is interesting to note that C_f values of Tube E45P3S6 are typically 1.5 to 3 times higher than those of tube E0P11S6.

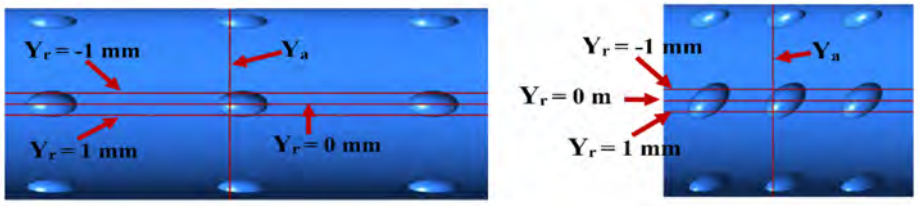

FIGURE 6.10: Schematic of axial and radial locations on the tubes E0P11S6 and E45P3S6, respectively

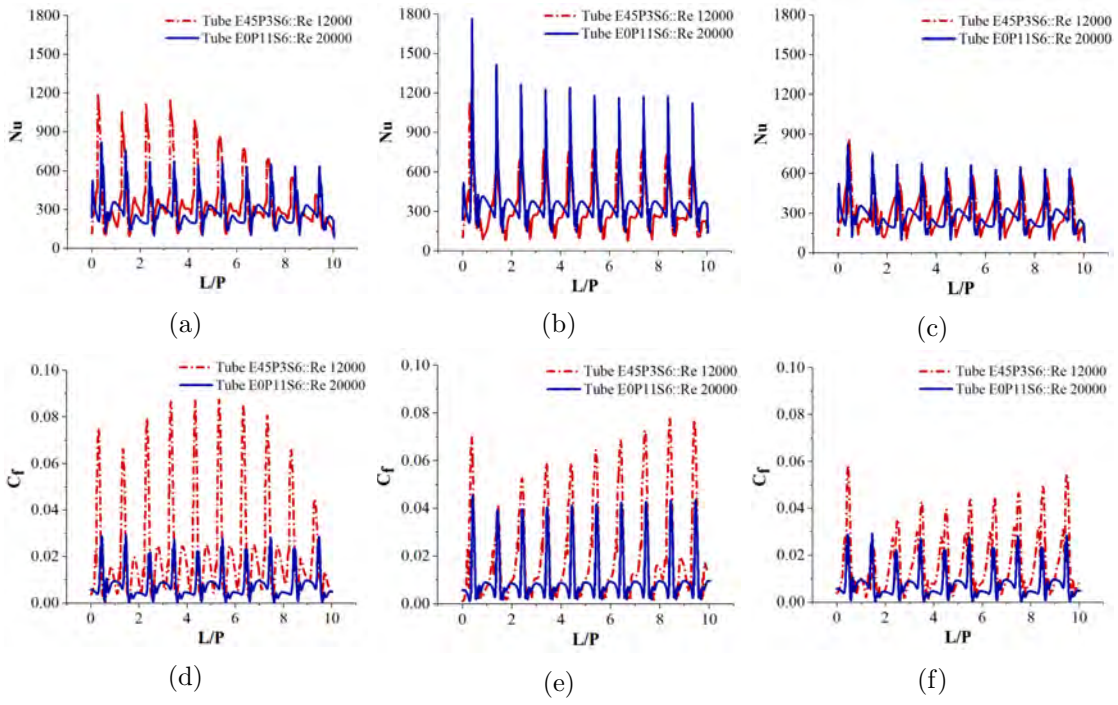

FIGURE 6.11: Local Nu distribution of Tube E0P11S6 at Re=20000 and Tube E45P3S6 at Re=12000 at the locations: (a) Yr =1mm, (b) Yr =0mm, and (c) Yr =-1mm, Local C_f distribution of Tube E0P11S6 at Re=20000 and Tube E45P3S6 at Re=12000 at the locations:(d) Yr =1mm, (e) Yr =0mm, and (f) Yr =-1mm

The local distribution of Nu and C_f are also assessed in the circumferential directions for tubes E0P11S6 and E45P3S6 at Re = 20000 and 12000, by using polar plots at the location of Ya that is 1 mm offset from the center of the dimples in

the upstream direction as shown in Figure 6.12a - 6.12b. These locations represent high heat transfer zones as demonstrated in Figure 6.5.

Figure 6.12a displays Nu distributions over the transverse cross-sections at axial locations of dimple 1, dimple 4, and dimple 8 for both tubes. The magnitude of Nu of Tube E0P11S6 for Re = 20000, in Figure 6.12a, show overall symmetrical behaviour for all axial locations.

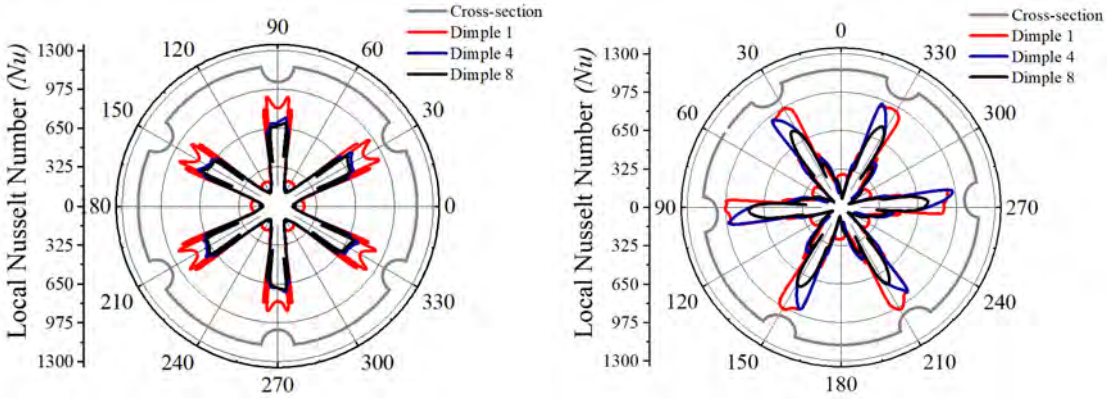

FIGURE 6.12: Polar representations of Nu distributions of tube E0P11S6 and E45P3S6, at (a) Re 20000, (b) Re 12000

Nu maxima at the axial location of dimple 1 is around 935 which decreases to 790 at dimple 4 location while it is 730 for dimple 8 location. It is also observed that all dimples contribute to heat transfer and fluid flow and therefore result in the high thermal-hydraulic performance of the tube, especially at high Re.

Figure 6.12b shows the Nu distribution of Tube E45P3S6 at the Re = 12000. The Nu is approximately 975 at the axial locations of dimples 1 and 4 while it is almost 790 at dimple 8. This shows that even at low Re the Ellipsoidal 45° dimpled enhanced tube demonstrates high heat transfer rates as compared to other tubes.

The peak values of Nusselt numbers do not coincide at any given axial location due to the swirl generation due to non-symmetric wakes of the Ellipsoidal 45° dimples. Moreover, it can also be observed that Tube E45P3S6 has higher Nusselt numbers at smooth surfaces between the dimples as compared to Tube E0P11S6.

6.4 Proposed Correlations for Enhanced Tube with Star Variation

The correlation of Nu and fr, for Tubes E45P3S4-E45P3S8 are proposed in equations (6.1) and (6.2), respectively.

$$\begin{aligned} Nu &= aRe^{b(1+S/1000)} \\ a &= 0.039144S - 0.065709 \\ b &= -0.019147S + 0.88302 \end{aligned} \tag{6.1}$$

$$\begin{aligned} fr &= \left[a \log\Big((Re + S/1000)\Big) + b\right]^{-3/2} \\ a &= -0.031937S + 0.25954 \\ b &= -0.04465S + 3.5019 \end{aligned} \tag{6.2}$$

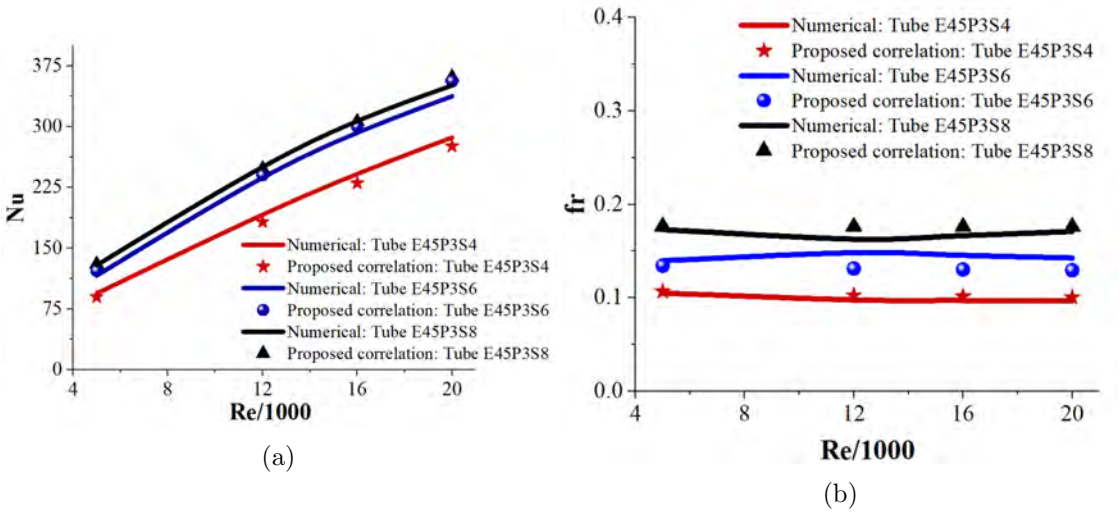

(a) (b)

FIGURE 6.13: Comparison of numerical and correlation results (a) Nu and (b) fr

These tubes are chosen for correlation for having best performance in its favorable Re region. The relationships of Nu and fr are proposed as a function of Re and *Star* - S. The Reynolds number can be ranged between $5000 \leq Re \leq 20000$,

a Prandtl number is 4.8734 while *Star* can be varied between 4 to 8. The constants a and b of both correlations are linear functions of the bent radius S. These correlations are valid for the fluid properties and boundary conditions, given in section 4.2.2. The comparisons of Nu and fr from numerical results and proposed correlations are presented in Figure 6.13a and 6.13b, respectively. A good agreement between the correlation and numerical results is observed. The maximum difference for Nu is limited to 5% and below 11.4% in case of fr, for all Re and *Star* configurations denoted as S in the equations.

6.5 Conclusion

The role of transverse dimple configurations in the augmentation of heat and fluid flow performance of dimpled tubes was investigated numerically in this study. Three different configurations of dimples were considered i.e., Teardrop, Ellipsoidal dimples aligned with flow direction (Ellipsoidal 0°), and ellipsoidal dimples tilted 45° to the flow direction (Ellipsoidal 45°). Each dimpled tube configuration was further modified by employing 4, 6 and 8 dimples in the circumferential directions (Star). Therefore, a total of 9 tubes, subjected to a constant heat flux of ($q'' = 10kW/m^2$), were employed in this study. The total number of dimples and dimple length to pitch ratios for each tube were fixed to 10. A fully developed turbulent flow regime was considered with ($5000 \leq Re \leq 40000$). It was observed that in general for all enhanced tube configurations heat transfer and friction factor increased with increasing transverse dimples. Moreover, Nu increased linearly at low Re but the increasing trend become non-linear at higher Reynolds number. Whereas, friction factors of the tubes decreased with increasing Reynolds numbers. The fluid flow analysis manifested that the increase in Star enhanced fluid and surface interaction and thus resulted in the augmentation of heat transfer rate and pressure losses. However, the rate of heat transfer increase was much greater than hydraulic losses. Thermal-hydraulic performance of Tube E45P3S6 (Ellipsoidal 45° dimpled tube with Star 6) was superior to other dimpled tubes for the Re range $5000 \leq Re \leq 20000$. While Tube E0P11S6 (Ellipsoidal 0° dimpled tube

with Star 6) was found to be the optimum choice for $20000 \leq Re \leq 40000$. Local characterizations of the optimum tubes manifested that Nu of Tube E45P3S6, at $Re = 12000$, was 1200 at 1st dimple which remained quasi-constant until 4th dimple but it was reduced by 50% at 8th dimple. The Ellipsoidal 45° dimples generated swirl in the flow enhancing fluid-surface interaction as demonstrated in friction coefficient. The interaction of fluid and dimple reduced at high Re due to flow separation over the dimples. At high Re, Tube E0P11S6 showed better thermal and hydraulic characteristics due to the creation of a flow path and diminutive flow separation. Therefore, for high Re applications Ellipsoidal 0° tube (Star 6) is recommended while for low Re applications Ellipsoidal 45° (Star 6) tube is suggested. Afterward, correlations for Nu and fr with the function of Re and S were proposed. The maximum difference numerical results and correlations for Nu remained below 5% and below 11.4% in case of fr, for all $Star$ 'S' and Re.

In industrial applications, straight tubes are often used in a series of bends such as U-bend for various applications needing long sections of tubes for transport and heat transfer applications. In such geometric configuration, the conventional U-bend introduces a secondary flow which leads to Dean Vortices. While dimpled straight tubes are showing a promising ability to enhance the overall performance in short length, the u-tube configuration is expected to engage another variational aspect to fluid flow and thus require investigation to ascertain if the dimpled tubes can be arranged in the U-bend arrangements and evaluate resultant flow characteristics. Furthermore, the bend section also introduces additional hydraulic losses, as mentioned previously. And fluid flow interaction of the dimple tube at different radial orientations such as $Star = 4$ or $Star = 6$ with the bend section may alter the frictional losses thus impacting overall performance. This shall be investigated in the next chapter with the detailed comparison and proposing correlation for the U-bend geometry having dimpled tubes along straight portions of the bend.

Chapter 7

Implementation of Optimum Design Parameters of the Dimples in U-Tubes

7.1 Introduction

In the previous chapter, overall performances of flow through heated enhanced tubes with pitch variation and constant surface heat flux were investigated for the ellipsoidal 0°, 45° and teardrop dimples. However, most industrial heat exchange devices encompass tubes with 180° return bends (U-bends) for compactness and continuous heat transfer at optimal efficiency. Examples of tubes with U-bends (U-tubes) include shell and tube heat exchangers, refrigeration systems, cooling of electronic devices, heat pipes, cooling channels of fuel cells, and gas turbines blades, etc.

However, the U-bends generate complicated fluid flow patterns within the tube depending on the sharpness of the bend (bend curvature) which ultimately affects the thermal-hydraulic performance of the overall system. The fluid flow interaction of dimpled tube with U-tubes is inescapable for the engineering system design or industrial usages, as discussed in the conclusion of **Chapter 6**. Therefore, in this

chapter, the flow and heat transfer characteristics of ellipsoidal 45° dimpled tube's interaction with U-tubes are numerically analyzed, for practical perspective.

Because, ellipsoidal-45° dimpled tube has provided the better overall performance at its favorable *Re* region. In the first phase, Star is taken as 4 and curvature variation of U-Tube is considered for the analysis. After finding the U-Tube curvature radius having best performance, best performance tubes of **Chapter 6** having Star = 6, are analyzed in coupled manner.

Because, the number of elements of dimple tube with Star = 6 in conjunction with U-tube are very large and it takes much time for only one simulation. So, In order to save time, initial analysis of dimple tube having Star 4 with U-Tubes are conducted. Afterwards, the final results are drawn of E45P3 and E0P11 with the U-tube having best overall performance.

The effects of different U-bend curvatures, of both smooth and dimpled tubes, on fluid flow and heat transfer characteristics, are analyzed in detail. The effects of dimples on the vortices of secondary flow in the bend are also analyzed in detail. The local characteristics of heat transfer and each U-tube configuration are also examined. In the end, new correlations of Nusselt number and friction factor are presented for dimpled enhanced tube as the functions of Reynolds number and ratio of the radius of U-bend curvature to tube radius.

7.2 Geometry and Boundary Conditions

In the first phase, an ellipsoidal 45° dimpled tube is used with pitch (P) = 3.17 mm or dimple center to center distances of 6 mm having Star = 4, as reported in Chapter 6. The numbers of dimples in the axial and radial direction are ten and four, respectively. All dimples have the same equivalent volume of 5.3040 mm^3. The computational domain of the augmented bend tube is shown in Figure 7.1a.

Three different geometric bend curvatures are used in the bend section. The hydraulic diameter D_h for both smooth and enhanced tubes is fixed to 17.272 mm.

The geometric curvatures are different in bend sections; therefore, the overall tube lengths are also different.

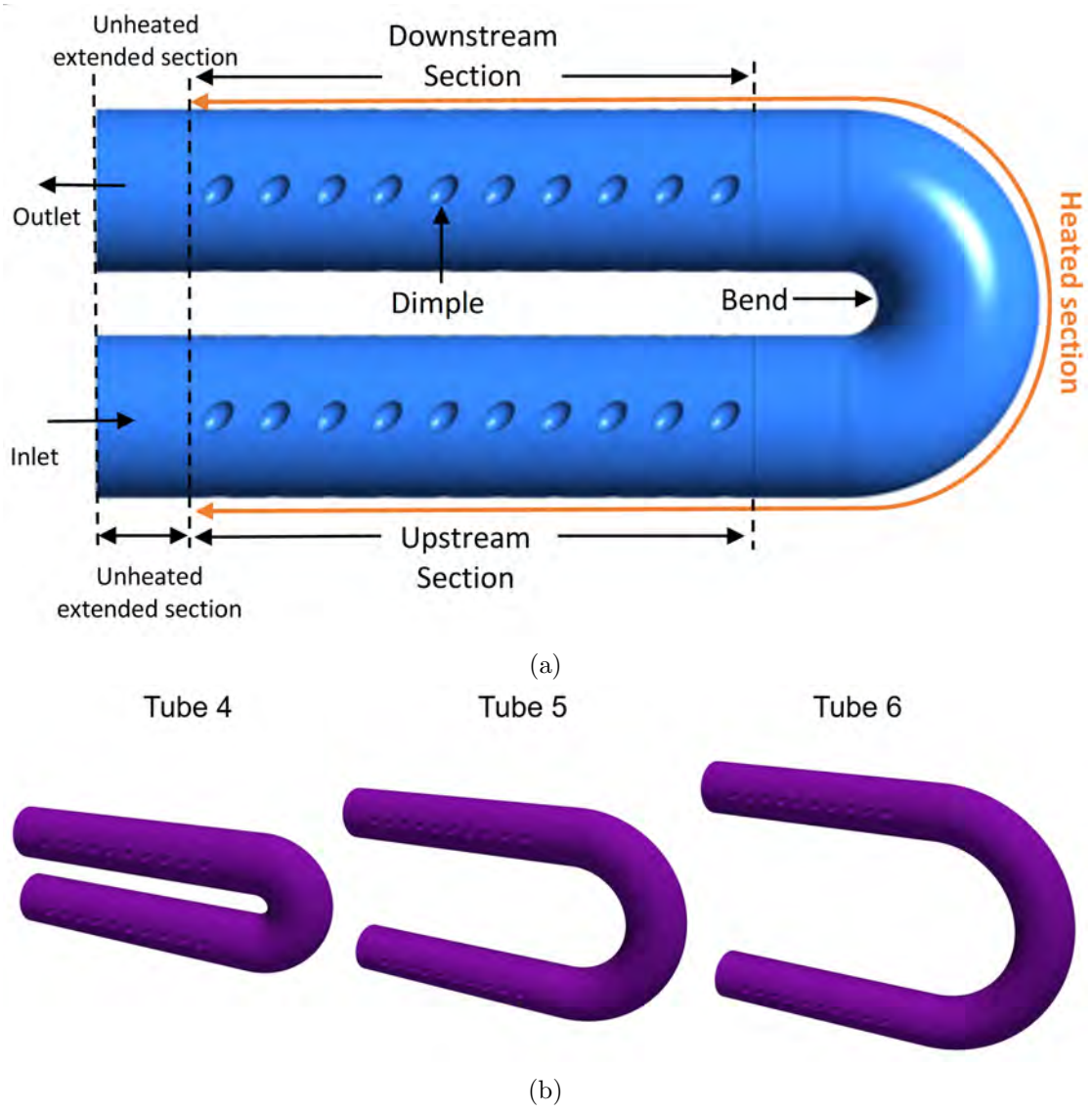

FIGURE 7.1: (a) Ellipsoidal dimple with U-tube with tube characteristics (b) Geometries of U-tube E1 to E3, respectively

The tubes with different bend sections and other design parameters are given in Table 7.1. U-tube S1 denotes the U-tube having radius of $0.6945D_h$ in conjunction with the smooth tube. To eliminate any spurious effects of inlet/outlet and upstream/downstream section of bend, 40 mm length is used. Geometries of different U-tubes are also shown in Figure 7.1b. The inward dimples in the tube are positioned inline.

TABLE 7.1: Parameters of all tubes utilized in the current study

Sr. No	U-tube	Diameter of tube (D_h) (mm)	Dimple Profile	Depth (H) (mm)	Pitch (P) (mm)	U-tube curvature radius (mm)
1	**S1**	17.272	Smooth tube	-	-	$0.6945D_h$
2	**S2**	17.272	Smooth tube	-	-	$1.5D_h$
3	**S3**	17.272	Smooth tube	-	-	$2D_h$
4	**E1**	17.272	Ellipsoidal (45°)	1.175	3.17	$0.6945D_h$
5	**E2**	17.272	Ellipsoidal(45°)	1.175	3.17	$1.5D_h$
6	**E3**	17.272	Ellipsoidal(45°)	1.175	3.17	$2D_h$

7.2.1 Parameter Definition

The De, as given in the equation 1.13, is the representative of only the bend section. Different De for the U-tubes of current section are presented in the Table 7.2.

TABLE 7.2: Dean number of different tubes utilized in current study

		Dean number De		
		U-tube curvature Radius (mm)		
Re		**0.6945** D_h	**1.5** D_h	**2** D_h
	5000	2393.1	1628.7	1410.5
	12000	5743.4	3908.8	3385.1
	20000	9572.4	6514.7	5641.9
	30000	14359	9772.1	8462.8

it is important to mention that the U-tube is a subsection of the whole system in which smooth/dimple tube and U-tube are parts of the system where high Re of turbulent flow is considered.

7.3 Mesh Generation and Grid Independence

The structured mesh with near-wall refinement is implemented for domain discretization, as shown in Figure 7.2. For this, ICEM CFD is used to generate the structured blocking for multi region which helps to generate the high resolution grid at the area of interest [103].

TABLE 7.3: Grid independence study of U-tube E1

Grid (Million)	Re=5000		Re=10000	
	Nu	fr	Nu	fr
0.84	104.53	0.2123	208.467	0.2654
2	101.35	0.1716	205.35	0.2036
4.5	99.4182	0.163	204.0884	0.181777
7	99.4563	0.1627	204.094	0.1812
12.5	99.4566	0.1621	204.0943	0.1808

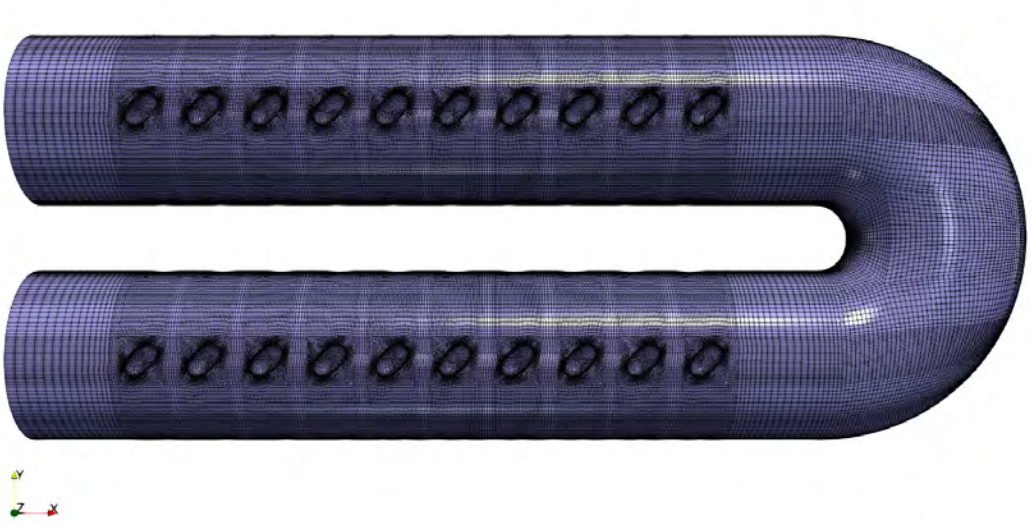

FIGURE 7.2: Grid generation of dimple U-Tube E1

In order to do it, the original block is sliced in axial and radial direction along with the generation of "O-grid" around the dimples, as shown in Figure 7.2. In current study, the dimple is the area of high resolution, therefore, a high-quality mesh around the dimples is imperative since the flow separation, attachment, vortex formation and flow mixing take place in the vicinity of the dimple. Therefore, additional care is taken while generating the mesh around the dimples.

A detailed mesh independence study is performed and solutions for U-tube E1 at the $Re = 5000$ and 12000 are demonstrated. The Nu and fr are shown Table 7.3 for various grid sizes. The grid sizes are varying from 0.84 million (Coarse mesh) to 12.5 million (Fine Mesh). It is observed that initially the difference, between two grid sizes, of Nu and fr is comparatively larger, however, it becomes

TABLE 7.4: U-tube correlations of heat transfer and friction factor

Author	Empirical correlation	Re & De ranges	Eq.
Rogers [124]	$Nu = 0.023Re^{0.85}Pr0.4(d/D)^{0.1}$	$9 \times 10^3 < Re < 10^5$	(7.4.1)
Mori [125]	$Nu = \frac{Pr}{26.2(Pr^{2/3}-0.074)} Re^{0.8}(d/D)^{0.1}\left[\frac{0.098}{[Re(d/D)^2]^{0.2}}\right]$	$10^4 < Re < 2 \times 10^5$	(7.4.2)
Mori [125]	$fr = 0.3(d/D)^{-0.5}[Re(d/D)^2]^{-0.2}[1 + 0.112[Re(d/D)^2]^{-0.2}]$	$Re_{critic} < Re < 6.5 \times 10^5(d/D)^{0.5}$	(7.4.3)
Schmidt [108]	$fr = f_{s,t}[1 + 0.0823(1 + d/D)(d/D)^{0.53}Re^{0.25}]$	$2 \times 10^4 < Re < 1.5 \times 10^5$	(7.4.4)
Mandal[126]	$fr = f_{s,t}[1 + 0.03De^{0.27}]$	$2.5 \times 10^3 < De < 1.5 \times 10^4$	(7.4.5)

almost constant for 4.5 million mesh cells and onwards. To ensure the negligible mesh-dependent variations and accurate results, 5.5 million grids with $y^+ \approx 1.3$ is selected for numerical analysis in the current study.

7.4 Results and Discussion on the U-Tube System

7.4.1 Validation with Empirical Correlations

The numerical methodology is validated by comparing the numerical results of the bend section of U-tube S3, obtained from the current methodology to the empirical correlations documented in the literature. Some of the most appropriate correlations of Nu for smooth bend tubes are presented in Table 7.4. The correlations of Nu consist of Rogers and Mayhew [124], equation (7.4.1) and Mori and Nakayama [125], equation (7.4.2). equation (7.4.1) has a wide Re range of $9 \times 10^3 < Re < 10^5$ equation (7.4.2) is valid for the Re range $10^4 < Re < 2 \times 10^5$. Mori *et al.* [125] also proposed the correlation equation (7.4.3) for fr which is suitable for the comparison in the current study. The relation is valid for $Re_{crit} < Re < 6.5 \times 10^5(d/D)^{0.5}$. Likewise, Schmidt [108] and Mandal [126] have also presented the fr correlations, which are givens in the equation (7.4.4) and equation (7.4.5), respectively. These fr also compare in the present study. Equations (7.4.4) and (7.4.5) are valid for the Re ranges of $2 \times 10^4 < Re < 1.5 \times 10^5$ and $2.5 \times 10^3 < De < 1.5 \times 10^4$ respectively.

7.3a - 7.3b shows the comparison of results from the present methodology and empirical correlations of smooth U-tubes while the empirical correlations of Nu

and fr along with Re and De ranges are presented in Table 7.4. Figure 7.3a - 7.3b shows that Nu is direct in relation to the Re while fr is inverse in relation to the Re. This trend can be observed in Figure 7.3a which illustrations that the numerical simulations also predict the direct relation of Nu with the Re while the relation of fr is inverse with the $Re \leq 12000$. The results of Rogers *et al.* [124] for Nu are comparable in evaluation with the numerical results, as compare to Mori *et al.* [125]. However, both the results are well within ±15% range. Most of the results of fr correlations are also within the ±15% range, since, the magnitudes of fr are very small and a few of the fr correlation results lie outside the ±15% range. Nevertheless, the correlations of Nu and fr validate the numerical methodology of present work.

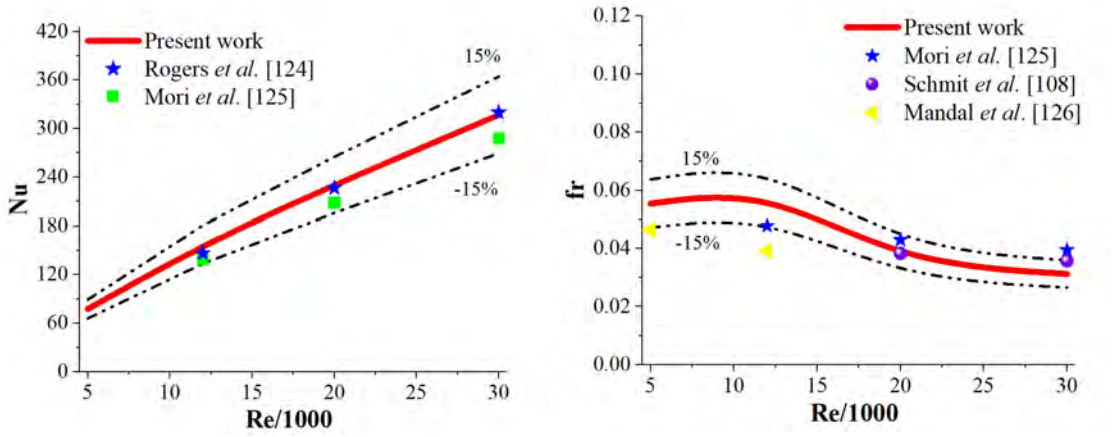

(a) (b)

FIGURE 7.3: Comparison of predicted numerical results of the bent section of U-tube S3 with empirical correlations (a) Nu and (b) fr

7.4.2 Heat Transfer and Hydraulic Loss of U-Tubes

The dimpled enhanced tubes are generally used to increase the heat transfer surface area and alter flow dynamics for thermal-hydraulic augmentation of the heat transfer system [121]. However, the compactness of the system demands the usage of 180° return bends (U-bends) in the tubes. The secondary flow in U-bends, consisting of counter-rotating vortices, is inherently generated due to the sudden change in direction of the fluid. The secondary flow dynamics play an important

role in the flow detachment and reattachment in post bend section. Therefore, it has a significant influence on the thermal-hydraulic performance of the overall system. The presence of dimples in the straight section of the tube alters the secondary flow and heat transfer performance of the system. In current chapter, Ellipsoidal-45° dimples are used in enhanced tubes for three different curvature radii of U-bend. Therefore, a total number of six tube configurations, three each for smooth and dimpled tubes, are studied for Re range of 5000 to 30000.

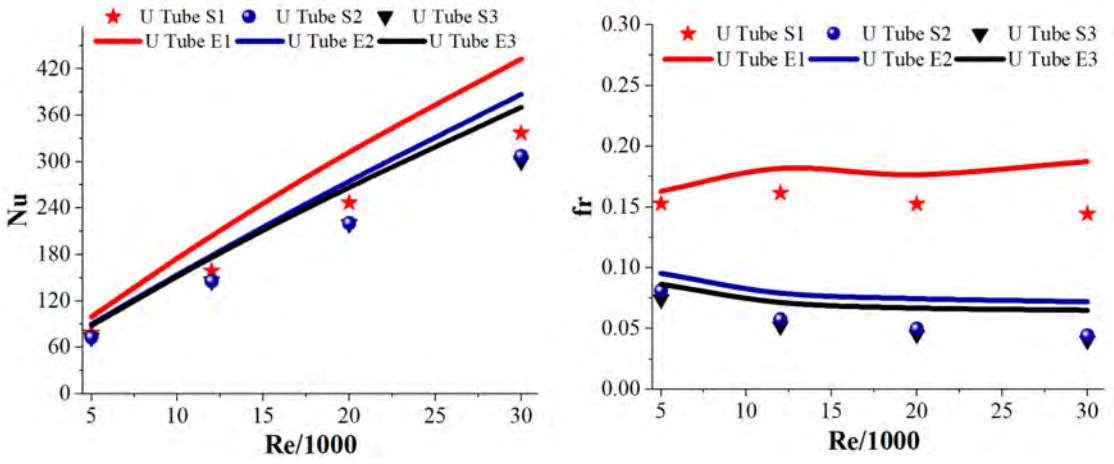

(a) (b)

FIGURE 7.4: Comparison of present work of Tubes 1-6 (a) Nu and (b) fr

In Figure 7.4a, it can be observed that the heat transfer depends on both Re and bend curvature R_c. The Nu increases as the Re increases while it decreases as the R_c increases. However, it is interesting to note from Figure 7.4a that enhanced U-tubes have much higher heat transfer rates than the smooth tube. Figure 7.4a also shows that quantitatively Nu of U-tube E1 is 26.6% higher than the Nu of U-tube S1 at Re=5000, while it is 28.34% higher at Re=30000. Similarly, the Nu of U-tube E3 is 21.4% to 23.29% higher than the Nu of U-tube S3 at the Re = 5000 and 30000, respectively.

Figure 7.4b depicts the rise in hydraulic loss in the enhanced system visa vis smooth system. It also signifies that the fr of U-tube E1 is 6.73% higher than the fr of U-tube S1, at the Re = 5000 whereas it is 29.74% higher at Re = 30000. Similarly, fr of U-tube E2 is 17.29% higher than the fr of U-tube S2 at the Re

= 5000 while at Re = 30000, it is 62.13% higher. Furthermore, fr of U-tube E3 is 16.78% higher than the fr of U-tube S3, at the Re = 5000 whereas at Re = 30000, it is 61.88% higher than the fr of U-tube S3. Moreover, the fr of U-tube E1 is relatively higher than the U-tube E2 and E3.

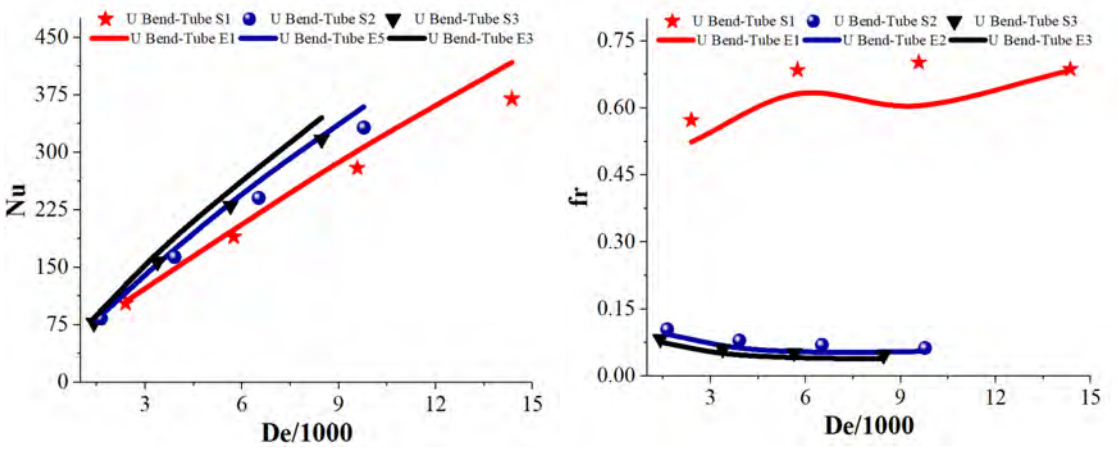

(a) (b)

FIGURE 7.5: Examination of U-bends of present work for Tubes 1-6 against the De (a) Nu and (b) fr

As reported in the introduction section, the De is the representative of secondary flow in the bend section, therefore the heat transfer and frictional losses of bends for tubes U-tubes S1 to E3 are categorized against the De, in Figure 7.5a - 7.5b. It is observed in Figure 7.5a that heat transfer of U-bend is in direct relation with De. On the other hand, the De of lowest bend curvature (i.e. $R_c = 0.695D_h$) denotes higher magnitudes of De representing high centrifugal forces (i.e. Secondary flow) which causes enhancement of heat transfer for both the smooth and the enhanced tube. On the contrary, higher R_c produces lower magnitudes of secondary flow while enhancing the lesser amount of heat transfer. Figure 7.5a shows that the U-bend of the ellipsoidal-45° dimple tube (i.e. $R_c = 0.695D_h$) produces 2.44% higher Nu than the U-bend of smooth tube, at the De = 2393. However, it is 12.85% at the De = 14359. Figure 7.5b denotes the friction factor of the U-bends for the tubes S1 to E3 against the De.

It is mentioned in Figure 7.5b that fr is inverse in relation to the U-bend curvature radius (i.e. R_c). It is also depicted that fr of U-bend of smooth tubes has higher

hydraulic loss than the U-bend with ellipsoidal-45° dimple tube, in comparison with fr of whole U-tube system when it is plotted against the Re. The U-bend of the smooth tube (i.e. $R_c = 0.695D_h$) produces 9.43% higher fr than the U-bend of the ellipsoidal-45° dimple tube at the $De = 2393$, while it is 16.05% at the $De = 9572$. The other tubes having higher R_c experience comparatively lesser hydraulic losses for both tubes. The fr of U-tube with smooth tube has higher hydraulic loss because of the uninterrupted strike of core flow of smooth upstream section to the bend outward side, contrary to dimple interrupted strike of the ellipsoidal-45° dimple tube.

7.4.3 Flow Distributions of U-Tube

The axial cross-sections of all the concerned U-tubes, presented in the Figure 7.6a - 7.6b further highlight the pressure and velocity variation in the tubes at the Re=12000. The pressure distributions depict that the U-tube S1 has higher overall pressure drop demonstrating relative sharp pressure gradients at the U-tube inward section as shown in Figure 7.6a. The outward bend sections of U-tubes S1-S3 denote the high-pressure regions while the upstream and downstream sections represent the smooth pressure drops. However, U-tubes E1-E3 alter the boundary layer of the flow significantly by the fluid-dimple interaction at the upstream and downstream sections. This interaction creates the local stagnation points at the leading edges of the dimples, as shown in Figure 7.6a. The alteration of flow through the dimples wakes onsets a rapid dampening process of the large vortex at the post bend section of the enhanced U-tubes.

The Figure 7.6b shows the velocity distributions of the U-tubes S1-S3 and E1-E3. The smooth pressure drop generates the smooth flow while the U-tube initiates the separation phenomena, having the vortices which elongates in the downstream section. The velocity distribution depicts that flow achieves maximum velocity at the two regions. First region is before the separation phenomena near the inward U-tube side. On the other hand, the second region is the U-tube outlet at the U-tube outward side. Figure 7.6b also emphasis that this local velocity maxima are

also the function of U-tube curvature. It is appeared from the velocity distributions that the velocity maximum magnitudes are inverse in relation with the U-tube curvature radius.

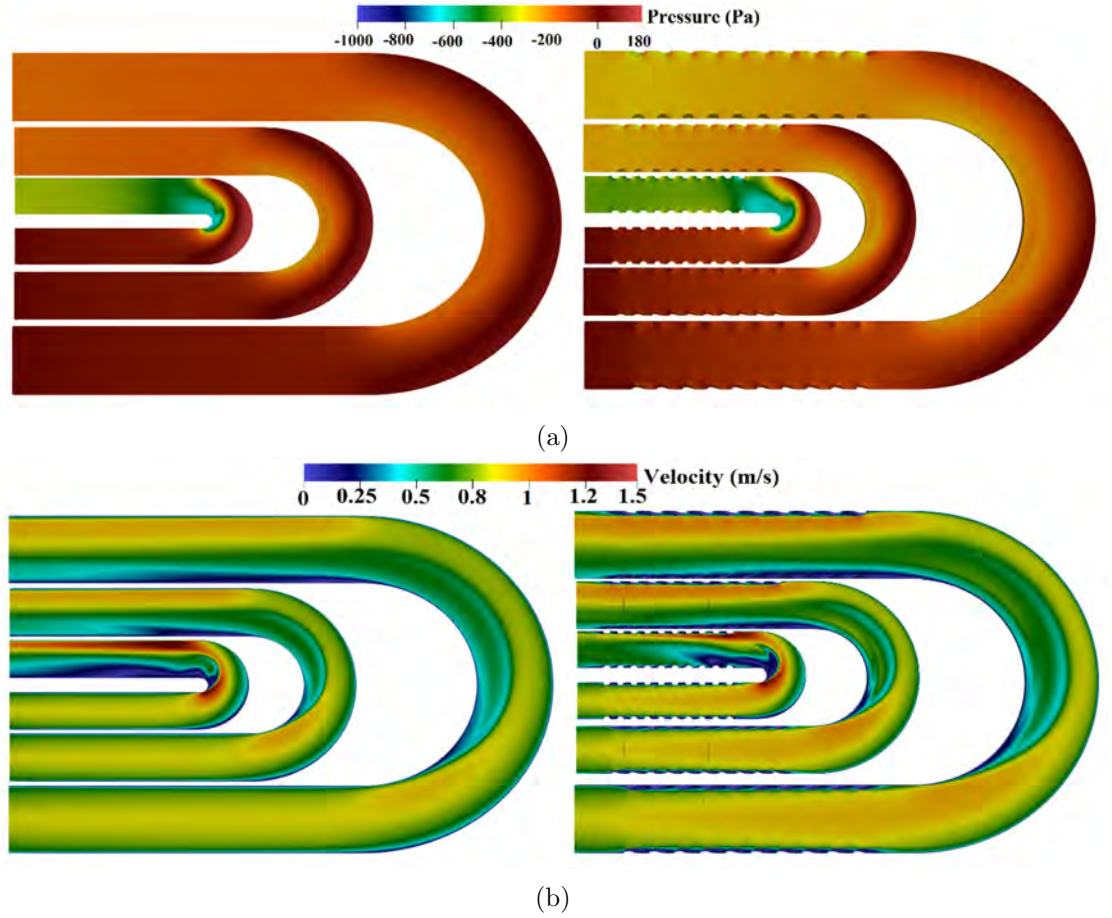

FIGURE 7.6: Property distributions at the cross-sections of U-tubes (a) pressure distribution of U-tubes S1-S3 and E1-E3, (b) velocity distribution of U-tubes S1-S3 and E1-E3

7.4.4 Thermo-Hydraulic Performances of U-Tubes

Figure 7.7 shows the PEC of U-tubes E1-E3 for different Re and PEC_s denotes the performance of smooth tube. It shows that U-tube E1 ($Rc = 0.695D_h$) has a considerable higher PEC at all the Re as compared to the U-tube E2 and E3. PEC of all tubes is inverse in relation with the Re. PEC of U-tube E1 is 7.45% higher than the PEC of U-tube E3 at the $Re = 5000$, while it is 13.07% at the $Re = 20000$. It is pertinent to mention that variation in PEC is marginal amongst

U-tube E2 and E3. Figure 7.7 further implies that bend curvature for tubes is inversely related to PEC.

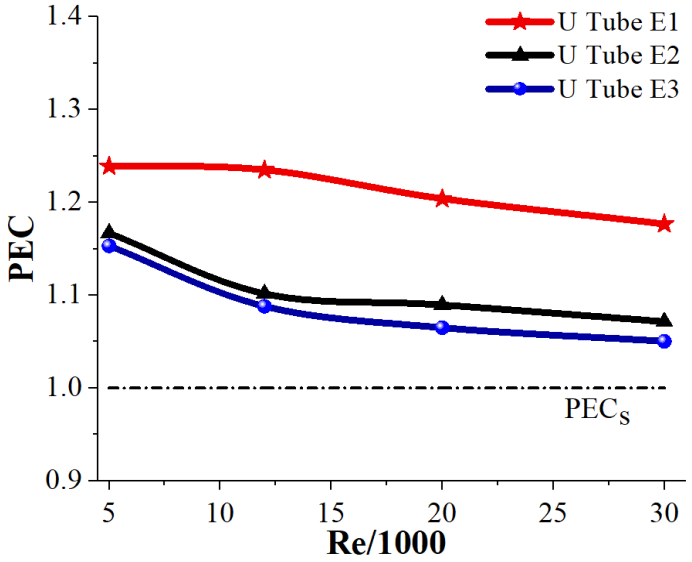

FIGURE 7.7: Thermo-hydraulic performances of U-tubes E1-E3

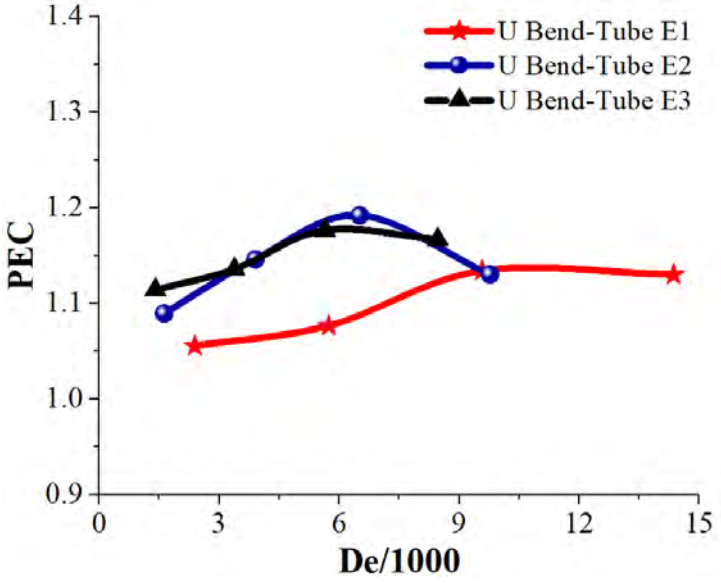

FIGURE 7.8: PEC of the bent sections of U-tubes E1-E3

It is the performances of complete U-tubes; however, the U-bends also introduce the performances. Figure 7.8 shows the PEC of U-bend sections for U-tubes E1 to E3 against the respective De. It is mentioned in Figure 7.8 that the PEC of bent section U-Tube E3 is higher at low De. While the PEC of U bends of Tubes E2

and E3 is approaching each other as the De increases. PEC of U-tube E2 declines as the De approaches 9500. PEC of U-tube E1 remains at 1.13 as $De \leq 9700$.

7.4.5 Flow Characterization in Short Bend Curvature U-Tubes

The enhanced U-tubes with shorter bend curvature demonstrated significant improvement in thermal-hydraulic performance. Therefore, in this section, a detailed flow characterization of U-tube E1 is carried out and the results are compared to U-tube S1. For this purpose, five cross-flow angular sections at U-tube, having 45° apart, are chosen for presenting the property distributions, as given in the Figure 7.9a.

Figure 7.9b shows that there is distinct change in the flow behavior at the U-tube contrary to the smooth flow at different upstream locations of the tube. The fluid flow between 0°-45° in the inward side accelerates which implies the initiation of separation. The flow eventually detaches between the 45°-90° due to geometric curvature, as shown in Figure 7.9b.

On the other hand, pressure distribution suggests the direct hit and mixing of central flow with the boundary layer along U-tube outward side, which ultimately produces the local stagnation zone. At the 135°-180°, the pressure distribution displays the two local minima depicting two vortices, that is also visible in velocity distribution.

This pair of vortices are symmetric in nature, where fluid accelerates outward side and inward side experiences the vortices. After the stagnation region, the pressure decreases which in turn assists the flow to accelerates adjacent to the outward surface. Ultimately, the fluid velocity increases as shown in 180° cross-flow section.

The pair of vortices symbolizes the secondary flow generation, as said by the Dean [82]. Moreover, these two vortices diffuse when the fluid moves in the downstream

section. The flow transforms further in the downstream section and alongside outward surface the accelerated flow compresses the two vortices into one single vortex. However, this single vortex fails to diffuse completely leading to long detachment of flow up-till the exit of the tube.

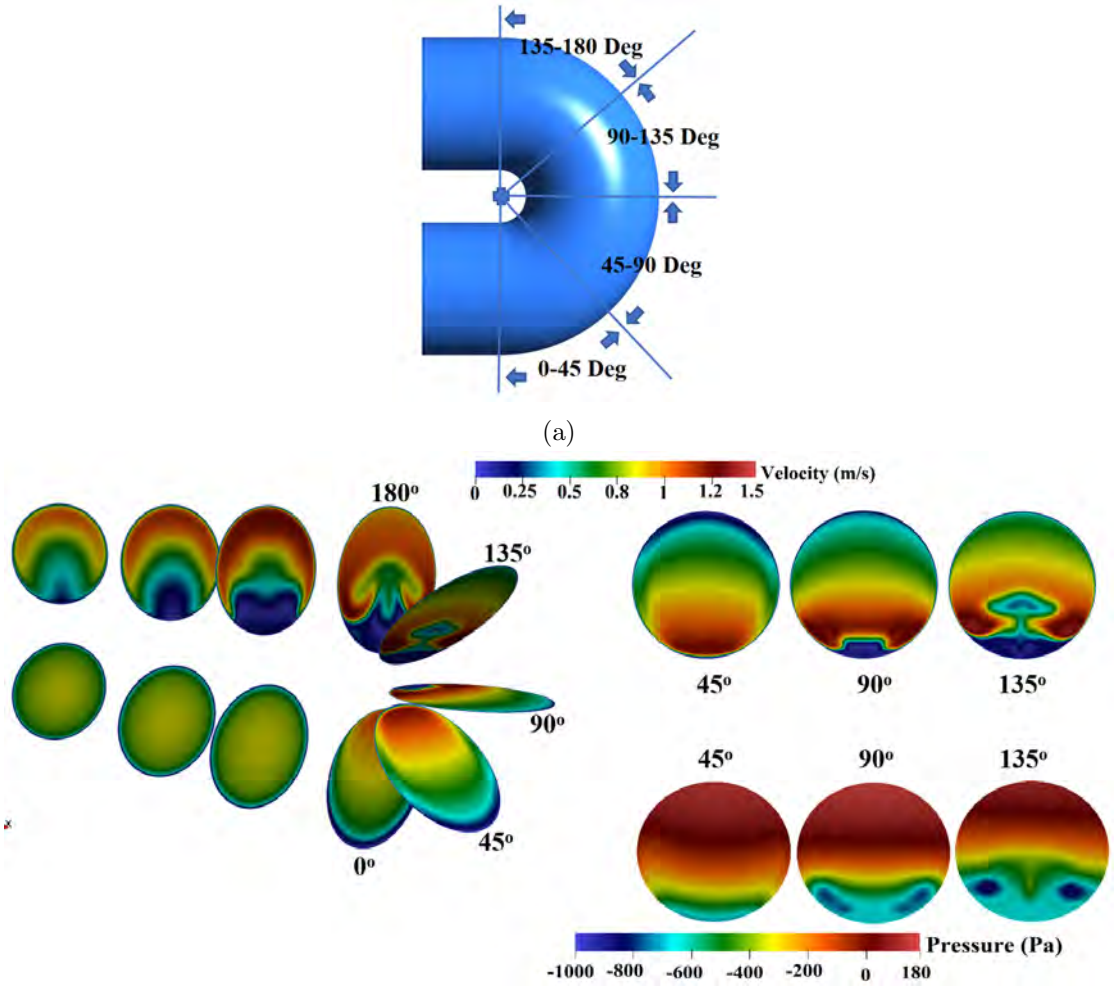

FIGURE 7.9: (a) schematic of angular cross-section for cross-flow distribution, (b) velocity and pressure distributions of U-tube S1 at different cross-sections

Figure 7.10 shows the pressure and velocity distributions at different cross-flow sections of U-tube E1. The fluid flow interaction of the enhanced tubes with smooth bent section is more complex. Because the enhanced tube already propagates the perturbed boundary layer flow due to the Ellipsoidal-45° dimples allowing the center line velocity to increase in magnitude as compared to smooth tube. This phenomenon can also be observed in the Figure 7.10.

The Ellipsoidal-45° dimples assist the near-wall fluid to flow in the 45° direction. Thus, the collective effect of all the dimples is to produce the helicity in the boundary layer flow, while the centerline flow remains undisturbed. This helically swirled boundary layer flow enters the bend section and modifies the behavior of Dean vortices, which is shown in the 135° cross-flow velocity distribution. It is distinguished in the pressure distribution that the two vortices have two different local minima, thereby leading to generate the asymmetric vortices, Figure 7.10 (b-135° cross-flow section).

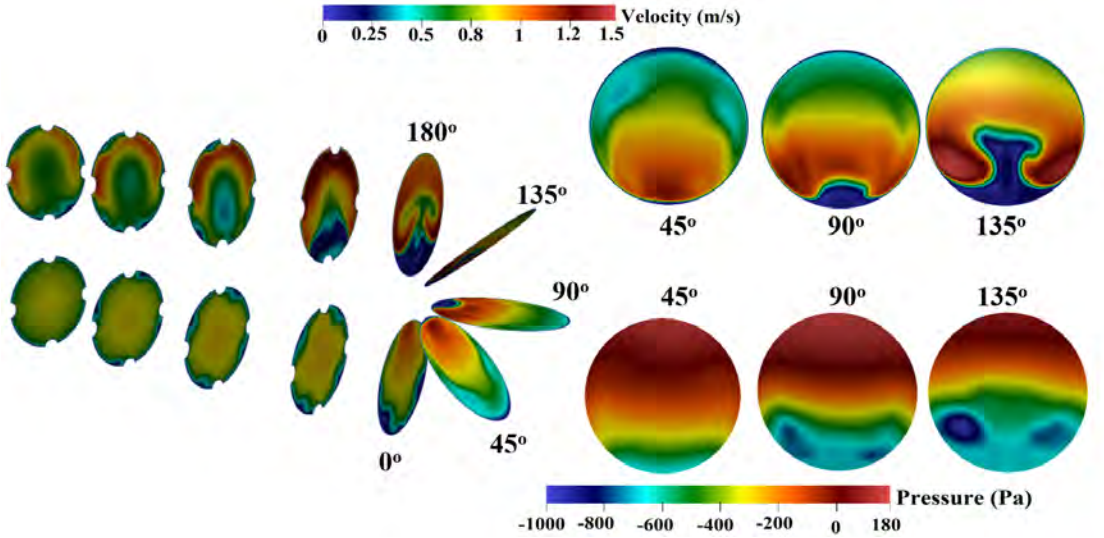

FIGURE 7.10: Velocity and pressure distributions of U-tube E1 at different cross-sections

The fluid moves further, gain acceleration due to pressure gradient and achieve a maximum velocity of approximately 1.5 m/s at the outward side. Upon the interaction of this accelerated flow, an excessive level of disruption is observed at the start of the downstream section. This results in the immediate diffusion of vortices and flow re-attachment with the bottom surface. It is appropriate to mention that this re-attachment occurs upstream of the third bottom dimple, Figure 7.10. Contrary to the flow behavior of U-tube S1, flow separation and reattachment effect are remained intact in the tube center till the flow exits from the tube.

The velocity streamlines of fluid flow inside the U-tube E1 is shown in Figure 7.11. It apparently shows two different types of stream lines which exists inside the tube in a coupled manner. One type shows the high velocity streamlines starting from inlet to the tube exit, which do not interact with the tube wall/dimples and remain smooth inside the tube. Opposite to it, second type of streamlines incorporates in the vortex generation at the inner side of U-tube and it further elongates in post bend tube till the 3rd lower dimple. Figure 7.11 depicts the streamlines near the inner side of the wall of pre-bend tube which further take parts in the generation of secondary flow.

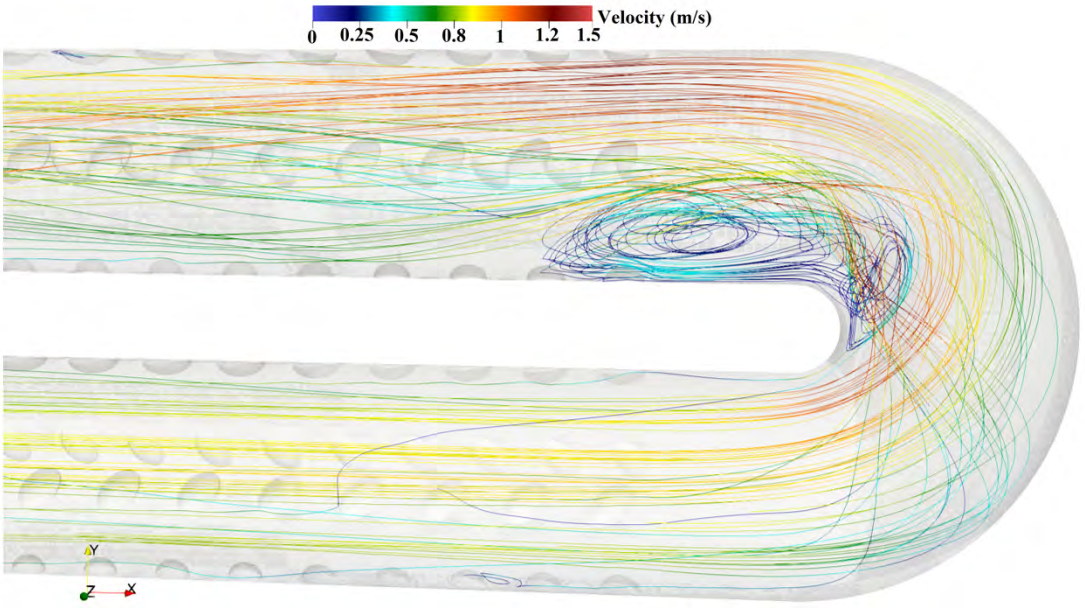

FIGURE 7.11: Velocity streamlines of U-tube E1 at the $Re = 12000$

Figure 7.12a - 7.12b shows the helicity distribution on the Q criterion of tube S1 and Tube E1 at the $Re = 12000$ in order to elaborate the interaction of flow structure between the dimples and the bent. Q criterion characterizes the vortices as the areas where the vorticity magnitude is greater than the magnitude of the rate of strain [25]. The values of the Q criterion of U-tube S1 and E1 are 133.175 s^{-2} and 1344.1 s^{-2} respectively.

As discussed above, Figure 7.12a also shows the same immediate flow separation at the inward side of bend curvature while the bottom tube core flow strikes directly the bend outward frontal area. This fluid strikes and flows along the bend

outward side however the separated flow employs two shears. Firstly, the high-speed separated flow enforces the shear beneath its layer, which tries to stretch the underneath layer and ultimately converted it into a vortex, which remains intact with a bend inward surface. This vortex further elongated its length, as shown in Figure 7.12a.

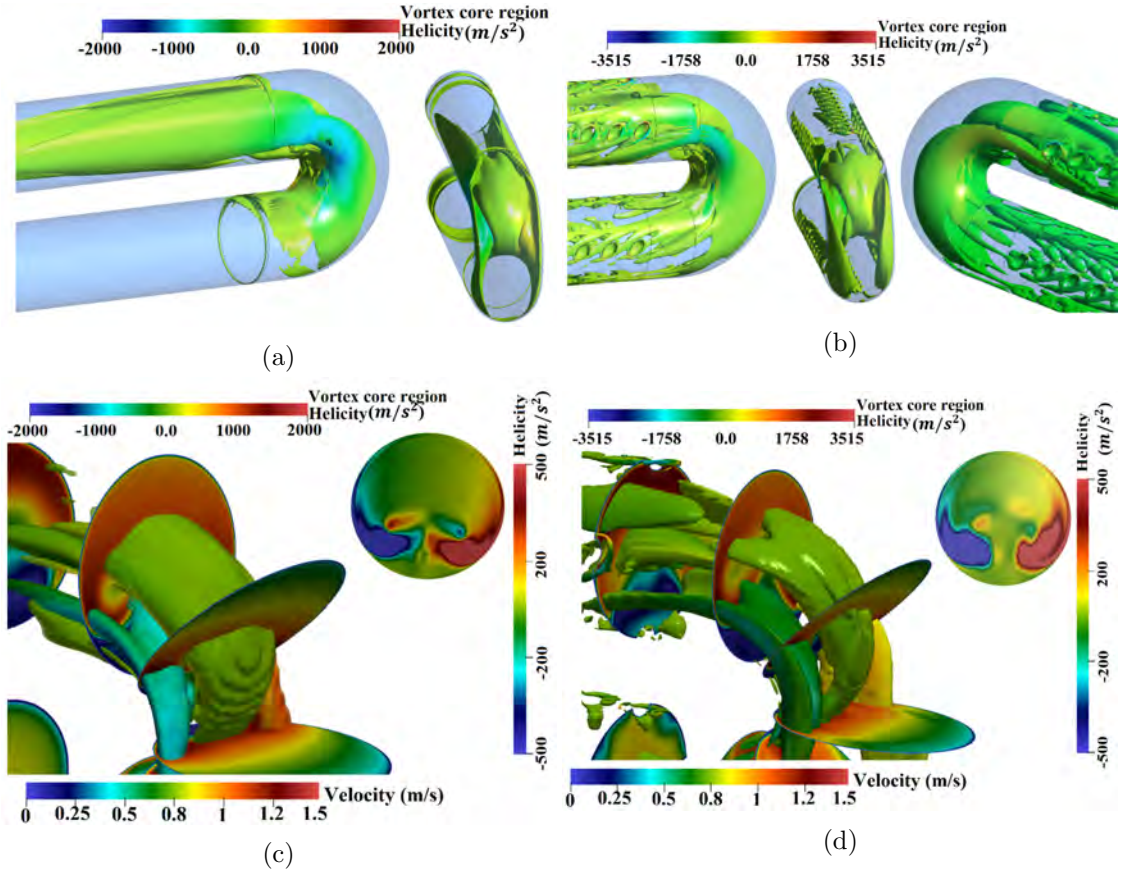

FIGURE 7.12: Q-criterion of U-tube S1, (a) side view, (b) back view, Q-criterion of U-tube E1, (c) side view, (d) back view, Helicity upon Q-criterion, with velocity cross-flow of (e) Tube 1 and (g) U-tube E1, 2D helicity at 135° of (f) U-tube S1 and (h) U-tube E1

Secondly, the separated flow chops and divide the upcoming core flow while employing the shear on the sided flow, which initiates the swirl. Thus, the two shears produce the two vortices, which are represented by the helicity distribution on the cross-flow section, Figure 7.12c. The positive and negative directions of Helicity distributions denote the direction reversal.

One vortex has the clockwise direction while the other has the anti-clockwise direction. The combined effect of two shears produces the Dean vortices which

further elongate at the sides of the tube and diffused near the tube exit, as shown in Figure 7.12a. The overall flow structures of U-tube S1 and E1 are nearly similar except, the wakes of the dimples make a difference by contributing to the bend section.

Figure 7.12b shows that all the dimples of the inlet tube have approximately smaller vortices while the wakes of the last dimples expanded and remain unbroken until they join the origination of the bend's side vortices. Their inputs to the bend initiation of vortices cause the change in the behavior of Dean vortices.

Because the left-sided dimple wake (as shown in Figure 7.12b) is stronger than the right side of the dimple's wake (Figure 7.12b). This causes modification in flow separation and further makes the upcoming left-sided vortex increase in strength. On the other hand, the right-sided dimple's wake remains intact with the bend's vortex, however, this wake is comparatively weak.

This delicate wake won't contribute enough to generate the upcoming vortex with the strength as equal as on the other side. Therefore, the Dean vortices, produce in U-tube E1, are asymmetric, Figure 7.12d. It also particularizes that the central vortex diffuses or divides itself into small vortices having elongated small vortices of different lengths. These vortices of various lengths diffuse further in the core flow, as shown in Figure 6.4 9 7.12c - 7.12d.

In the Q criterion of U-tubes S1 and E1, the velocity distributions are also incorporated which denote the flow magnitudes adjacent to the vortices, as shown in Figure 7.12c - 7.12d. Figure 7.12c - 7.12d interestingly reveals the symmetric and two pairs of vortices, while U-tube E1 shows the three pairs of vortices in which two are relatively small.

It also denotes that direction reversal of pair of large vortices shifts to the opposite direction at the 2nd row of relatively small pair of vortices. Furthermore, U-tube E1 has an additional 3rd row of pair of smaller vortices in which the direction reversal is opposite to the direct reversal of the 2nd row of pair. These additional pairs also elongate in the core flow and diffuse slowly before the exit of the tube.

7.4.6 Local Heat Transfer Characterization

To illustrate the heat transfer mechanism of tubes S1 and E1, an evaluation of local Nu for the complete tube is shown in Figure 7.13a - 7.13c. The local Nu of upstream and downstream sections are presented at the radial deflection = 0.001 m, as this deflection from axis signifies the higher values of Nu, nevertheless, the local Nu of Bend section is drawn at the central line. The crowns of local Nu denote the dimples, whereas, the flat lines of Nu express the smooth spacing between the dimples.

As explained in the **Chapter 4**, the flow is deflected over the proceeding dimple by the asymmetric wake of the 45° dimpled tube (U-tube E1) permitted the fluid flow to interact with the dimple front of the proceeding dimple and therefore augmented the heat transfer rate. This is established by the axial Nu shapes in Figure 7.13a that the top and bottom sides of U-tube E1 transferred around same amount of heat, but it is much higher in contrary to the U-tube S1. The peak value of Nu of first dimple is 1430 while rest of the peak values are around 1000. However, at the axial location of 0.01 m, the Nu of U-tube S1 is 131 and after a while, the Nu remains at the value approximately 105.

Figure 7.13b presents the comparison of Nu plotted at the inward and outward sections of the bends of U-tube S1 and E1. The plots portray that the sudden rise in Nu at the outward section demonstrate the enhanced fluid surface interaction due to the impingement of the separated flow on the outward bend surface. The maximum value of local Nu for U-tube E1 and S1 are approximately 250 and 201 respectively. Afterwards, the Nu of tube U-tubes S1 and E1 becomes constant and uniform at a vertical position of 0.00928 m. This position is adjacently below the 90° cross-flow section depicting similar local flow characteristics and heat transfer characteristics of both tubes until the vertical position of 0.017 m. Afterward, the fluid impingement of U-tube S1 occurs which increases its local heat transfer rate. This shows delayed flow impingement in U-tube S1 as compared to U-tube E1 and highlights the importance of upstream dimples in the straight section of the tube. On the other hand, the local Nu distribution of the inward section of the

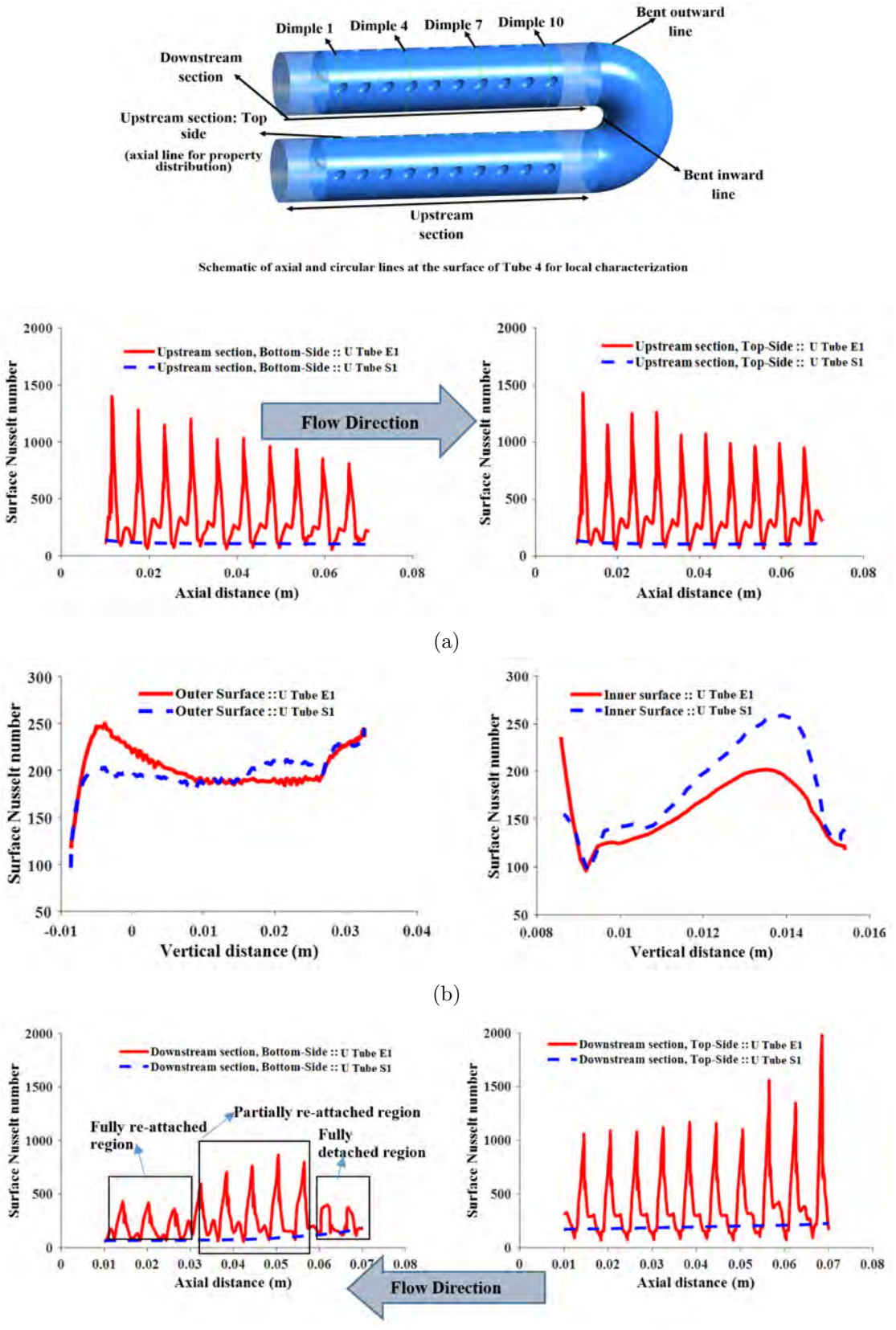

FIGURE 7.13: Local surface Nu distribution of U-tube S1 and E1 at (a) upstream section: bottom side, and upstream section: top side, (b) U-tube outward side, and U-tube inward side, (c) downstream bottom side and downstream top side

downstream tube shows the sudden decrease of Nu, manifesting the flow separation Figure 7.13b. The minimum value of Nu at the detachment point is 95.8. Then Nu of both tubes raises afterwards due to the secondary flow generation. However, the peak value of Nu of U-tube S1 was 259 whereas the U-tube E1 has the Nu of 202. This reveals that the U-tube S1 generated a stronger secondary flow than that of U-tube E1. In the end, the local Nu distribution of the top and bottom side of the downstream section shows axial thermal distribution, Figure 7.13c. The Nu of top section indicates the effective interaction of flow-exiting the bend-section and subsequent dimples at the top side of the post bend section. Figure 7.13c shows that the peak value of Nu at the first dimple is 1980, whereas the Nu of 2nd and 3rd dimples are 1410 and 1525. Afterward, the downstream dimples attain the Nu approximately 1100.

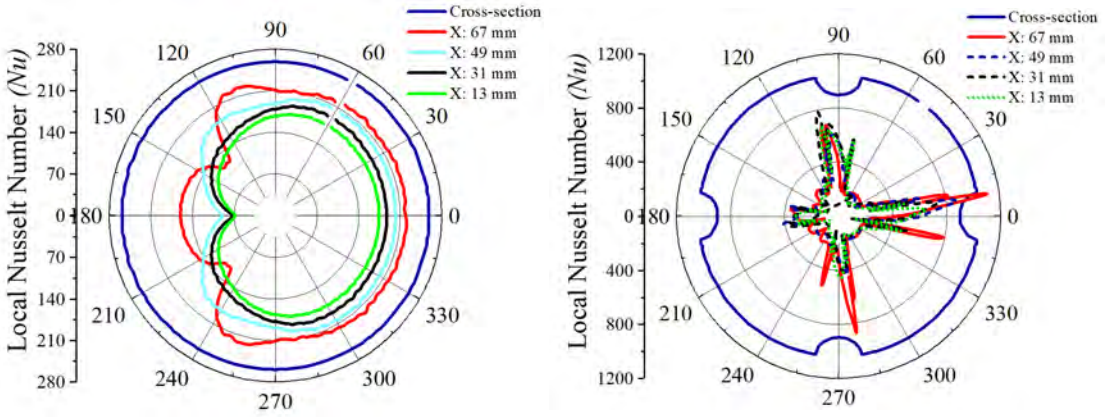

FIGURE 7.14: Polar representation of local Nu of (a) U-tube S1 and (b) U-tube E1

On the contrary, the bottom side of the tube can be segregated in three different heat transfer regions, namely fully detached region, partially re-attached and fully re-attached region. The fully detached region denotes the weak fluid-dimple interaction due to the re-circulation bubble at the bottom of the straight tube immediately after the bend section encompassing 1st and 2nd dimple. Therefore, at this location relatively low heat transfer is obtained yielding $Nu = 380$. The fluid-surface interaction improves in partially reattached region as the main fluid core starts to reattach to the surface resulting in higher Nu values of 803 and 867 at

3rd and 4th dimple, respectively. Interestingly, quickly after the fully re-attached region, the main fluid core diffuses throughout the tube.

The local Nusselt numbers of downstream (post-bend) straight sections of U-tube are further analyzed for both tubes U-tube S1 and E1 through polar plots, presented in Figure 7.14a - Figure 7.14b. For this purpose, cross-sections of both tubes corresponding to the locations of 67 mm, 49 mm, 31 mm, and 13 mm, Figure 7.14a, are selected which cover both detachment and reattachment regions of the tubes. Here, tube exit lies at the 0 mm.

Figure 7.14a - Figure 7.14b both show that the heat transfer rate is much higher in the top halves of the tubes for all given cross-sections. The smooth tube at section 67 mm shows two distinct features in the top and bottom half of the tube. It is observed that in the upper section (90°- 270°) of Tube S1, Nu=200 while in the lower section, at 120° and 240° position Nu=170 which further reduces to 45 at 180°. This manifest that there is flow separation due vertical structures in the bottom half of the post-bend straight section of Tube S1.

A similar pattern is also observed in section 49 mm of Tube S1 demonstrating the same fluid flow behavior. However, sections 31 mm and 13 mm of Tube S1 show the effect of flow reattachment on heat transfer rate as Nusselt numbers values of 170 and 155, respectively, are achieved at the top half of the tube. The heat transfer rate at the bottom half of sections 31 mm and 13 mm of Tube S1 is also increased more than twofold. It is also interesting to note that at section 67 mm two local minima of Nusselt number is observed at 135° and 225° instead of the single minima at 180° of other tube sections.

Figure 7.14b shows the polar plot of local Nu of U-tube E1 (dimpled enhanced U-tube) at sections locations of 67 mm, 49 mm, 31 mm, and 13 mm. The four peaks of Nu correspond to the dimple mid-section, along with schematic of geometric cross-section as shown in Figure 7.14b. The Nusselt number values around the dimples are significantly higher than smooth U-tube. The position at 0° for location 67 mm, represents the top dimple of the tube in the strong fluid-dimple interaction

zone, where it has the local Nu of 1140 while the peak values of Nu at 90° and 270°, representing dimples 2 and 3, respectively, are 650 and 850.

These values significantly reduces in the reattachment zones at sections 31 mm and 13 mm, where Nu attain the values of 700 and 600 for the top dimples, respectively, at 0° positions. The bottom dimples at 180° positions for sections 31 mm and 13 mm achieve Nusselt number values of 405 and 370, respectively. This reiterates the fact that the heat transfer performance of U-tube E1, in both detachment and reattachment regions, is significantly enhanced due to the presence of dimples. Moreover, ellipsoidal 45° dimples induce swirl due to asymmetric wake generation that leads to asymmetric distribution of heat transfer coefficient across the circumference of the tube.

Up till now, U-tubes E1-E3 have provided better overall performances, in comparison with U-tubes S1-S3, as far as $RANS$ is concerned. Before going to the further conclusion, it is mandatory to check the transient behavior behavior of U-tube. The question is, whether the fluid flow behavior inside dimple U-tube will be the same or it will change?. To find out the answer, a transient analysis of U-tube E1 (only one U-tube) is conducted in the coming section.

7.5 Transient Flow and Heat Transfer Characterization of U-Tube E1

The variation of U-tube curvature has strongly influenced on the heat transfer and frictional characteristics, which ultimately effect the overall performance. In order to examine the unsteady behavior of Dean vortices and its impact on post bend dimple tube of U-tube E1, transient analysis is used to configure it. This analysis is conducted for the 300ms and distributions are displayed for different time instances. Figure 7.16 shows the cross-flow velocity contours of U-tube E1 at different times, where D-6 to D-10 denote the 6th to 10th dimple locations, as shown in the Figure 7.15.

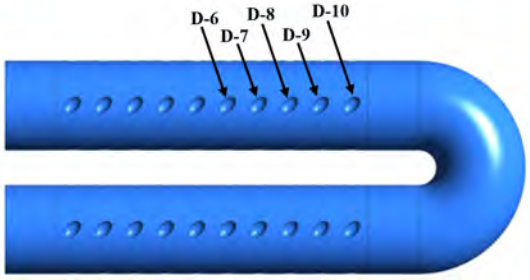

FIGURE 7.15: Schematic of locations for the cross-flow distributions U-tube E1

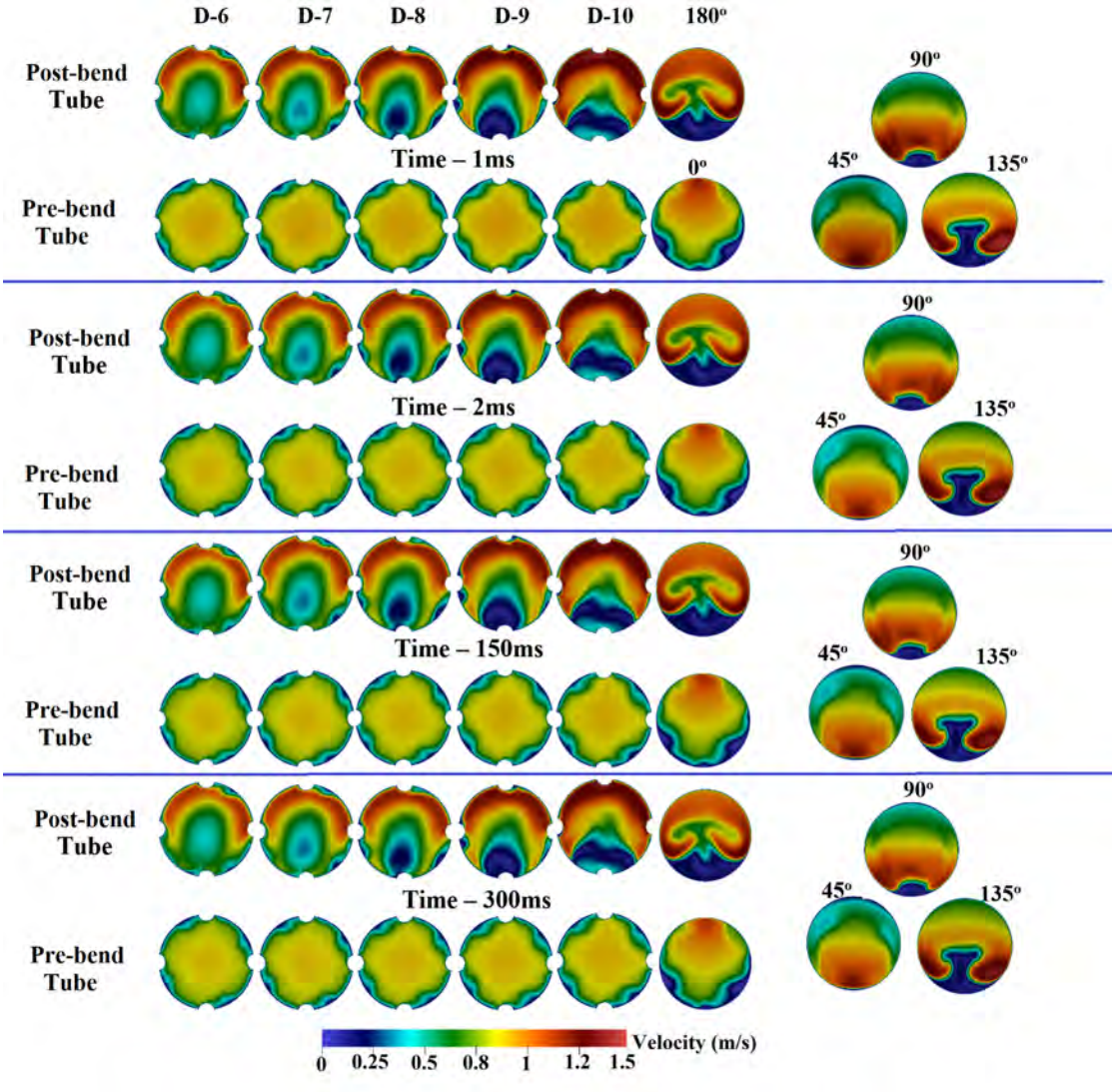

FIGURE 7.16: Cross-flow velocity distributions of U-tube E1 at different locations and bend sections at various time instances

The distributions are shown at different time instances (i.e. 1ms, 2ms, 150 ms and 300ms) for comparative examination. The flow physics is already discussed

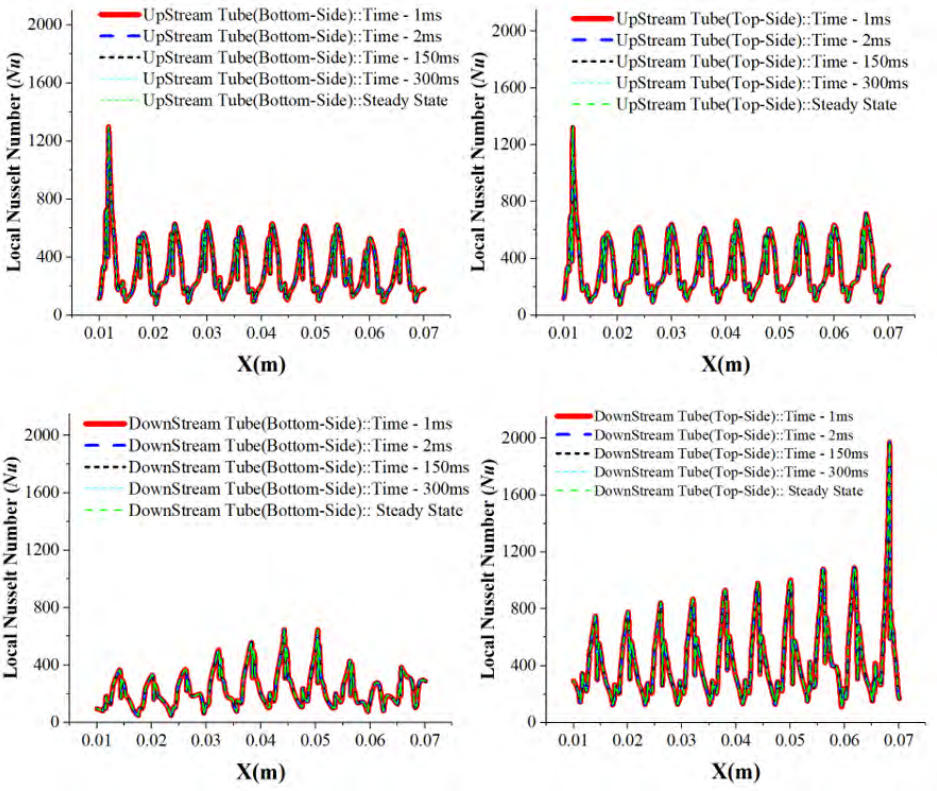

(a)

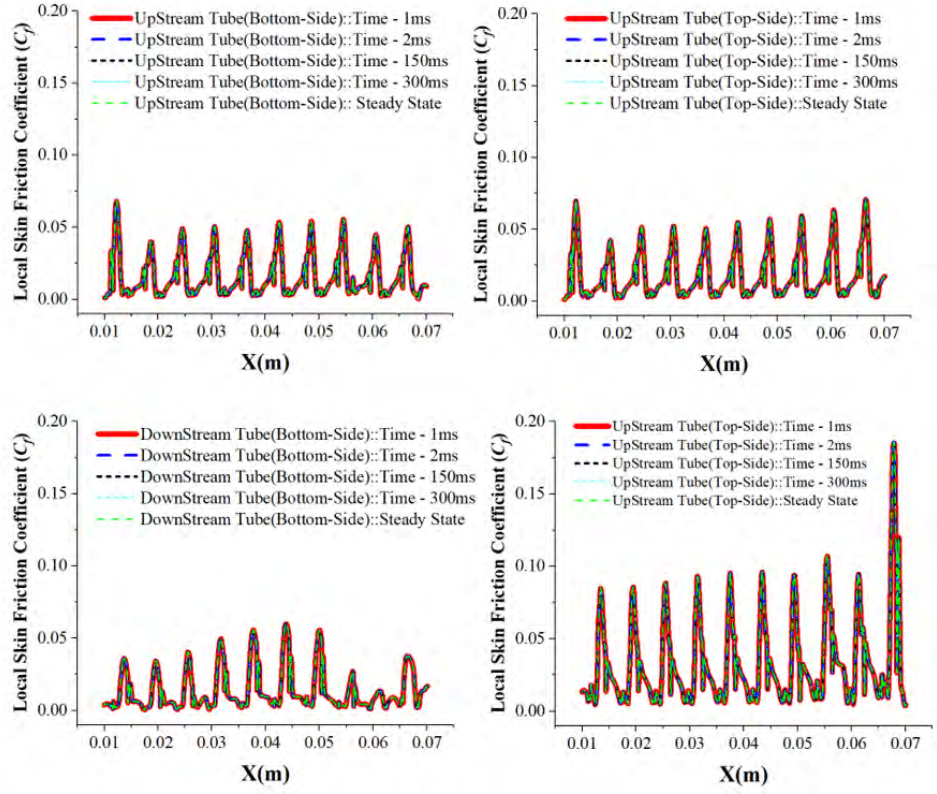

(b)

FIGURE 7.17: Comparison of local property distributions at various time duration (a) Nu and (b) C_f

above in current chapter. It is important to mention here that the velocity distributions at different instances show no major difference in flow physics of Dean vortices and the core flow of pre and post bend sections are also remain unchanged. The developed and disturbed boundary layer at each dimple location (i.e. D-6 to D-10) resembles with the same location of each time duration and the strength of Dean vortices also remain same. These velocity contours have different velocity magnitudes at different flow time. However, the difference of velocity magnitudes is very small and cannot be seen through the distribution as the difference is less than 1%. It is evident through the velocity distribution that overall flow structure is remain unchanged from 1 ms to 300 ms and there is no major difference in flow field between any two time instances. The effect of flow on the local Nu and C_f can be seen on the Figure 7.17a and 7.17b. The behavior of local Nu and C_f is already explained in detail, and the Figure 7.17a and 7.17b show the comparison during different flow time. However, the Nu and C_f show that flow of U-tube E1 has not affected its transient impact on the upstream and downstream dimple tube. For example, the Nu of Pre-bend tube at the top sided location of 48mm is 608 for the steady state, while it is 607, 607, 607 and 606 for time = 1ms, 2ms, 150ms and 300ms respectively. Similarly, the steady state value of Nu of Post-bend tube at the top sided location of 68.2 mm is 1850, while it is 1830, 1822, 1825 and 1823 for the time = 1 ms, 2 ms, 150 ms and 300 ms respectively. The C_f of Post-bend tube at the top sided location of 68.4 mm is 0.0268 for the steady state, while it is 0.0264, 0.0263, 0.0261 and 0.0264 for time = 1 ms, 2 ms, 150 ms and 300 ms respectively. This trend of small difference is not throughout all locations, but it occurs when the peak values come across in the graphs.

7.6 Proposed Correlations for Enhanced Tube with U-Tube Curvature Variation

The correlation of Nu and fr, for U-tubes E1-E3, are proposed in equations (7.2) and (7.3) respectively. The relationships of Nu and fr are proposed as a

function of Re and U-tube radius R_c, where U-tube curvature is in millimeters. The Reynolds number can be ranged between $5000 \leq Re \leq 30000$, a Prandtl number is 4.8734 while bend curvature can be varied between 12 mm to 34.54 mm. There is a linear relationship between the constants a and b of both correlations and the U-tube radius R_c. These correlations are valid for the fluid properties and boundary conditions, given in section 4.2.2. The assessments of Nu and fr from numerical outcomes and suggested correlations are presented in Figure 7.18a - 7.18b, respectively. A appropriate percentage difference between the correlation and present work results is depicted. The maximum percentage difference for Nu is less than $\pm 3\%$ and below $\pm 12\%$ in case of fr, for all R_N and Re.

$$\begin{aligned} Nu &= aRe^{b(1+R_N^{-1}/1000)} \\ \text{where, } a &= -0.00168091R_N^{-1} + 0.086447 \\ b &= -0.0086843R_N^{-1} + 0.8343 \end{aligned} \tag{7.1}$$

$$\begin{aligned} fr &= \left[a \log\left(Re + \frac{R_N^{-1}}{1000}\right) + b\right]^{-3/2} \\ \text{where, } a &= 0.30547R_N^{-1} - 0.51166 \\ b &= -1.8693R_N^{-1} + 6.7584 \end{aligned} \tag{7.2}$$

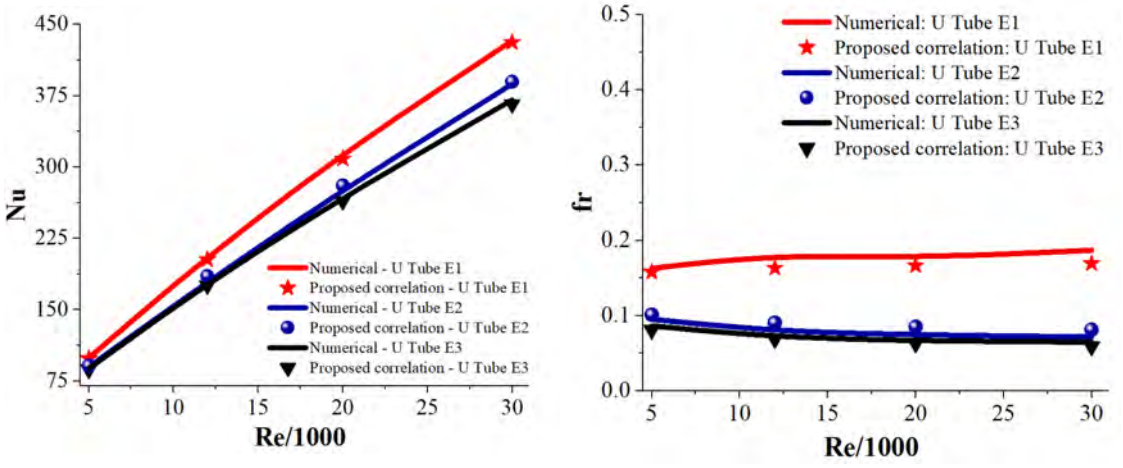

(a) (b)

FIGURE 7.18: Comparison of numerical and correlation results (a) Nu and (b) fr

7.7 Performance of U-Tubes with the Ellipsoidal-0° and 45° Enhanced Tubes

In this section, the performance of various curvature U bends (Curvature radius = $0.6945D_h$, $1.5D_h$, $2D_h$) in contact with the best pitched tubes E45P3S6 and E0P11S6 is evaluated for the Re range of $5000 \leq Re \leq 40000$. U-tubes with dimple tube of Star 4 are analyzed in the above section for the two reason. Firstly, the analysis is performed in order to find out the flow physics inside the U-tube system. Secondly, this is done for the comparison of performances between the U-tubes with Star 4 and Star 6 enhanced. The question is, Whether the performance of U-tube system increased or decreased when it is coupled with enhanced tube having Star 4 and Star 6? So, in this section comparison is made with only the information of Nu, fr and PEC of both U-tube system with different curvatures. All the tubes used in current section are given in Table 7.5. Now, the tube names from the previous chapters incorporates additional term. For example, E45P3S6U12 describes the ellipsoidal 45° dimple tube with P = 3.17 mm, Star = 6 and U-tube curvature radius = 12 mm.

TABLE 7.5: Parameters of all tubes utilized in the current section

Sr. No	Tube names	Dimple profile	Dimple Pitch (mm)	Star	U-tube curvature radius (mm)
7	E45P3S6U12	Ellipsoidal 45°	3.17	6	0.6945Dh
8	E45P3S6U25	Ellipsoidal 45°	3.17	6	1.5Dh
9	E45P3S6U34	Ellipsoidal 45°	3.17	6	2Dh
10	E0P11S6U12	Ellipsoidal 0°	11.17	6	0.6945Dh
11	E0P11S6U25	Ellipsoidal 0°	11.17	6	1.5Dh
12	E0P11S6U34	Ellipsoidal 0°	11.17	6	2Dh

Different geometric configurations of tubes are shown in Figure 7.19a - 7.19b. Since the fluid flow interaction of dimpled enhanced tube with the U bend (i.e. Star 4) is already discussed in the current section, therefore only the Nu, fr and PEC of given tubes are discussed in the following section.

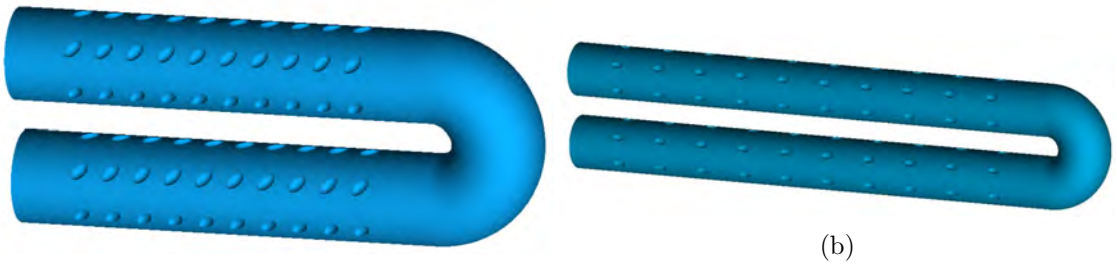

(a) (b)

FIGURE 7.19: Geometries of U-tubes, (a) E45P3S6U12 (b) E0P11S6U12

7.7.1 Heat Transfer and Hydraulic Loss of U-Tubes

Figure 7.20a - 7.20f shows the heat transfer, friction factor characteristics and PEC of U-tubes with the ellipsoidal-45° (P = 3.17 mm) and ellipsoidal-0° (P = 11.17 mm) tubes of Star 6. The characteristics of E45P3S4U12-U34 (i.e. performance of U-tube E1-E3 is also given in the Figure 7.7) tubes are also incorporated in the Figure 7.20e - 7.20f to compare the Star variation (i.e. Star = 4, 6) of U12-34 tube for ellipsoidal 45° dimple tubes for the Re = 5000 to 40000. The fluid flow interaction of these tubes with bend tube shows interesting results. As reported in the section **Performance enhancement of pitched tubes for the straight tubes**, U-tubes also performs the same behavior as the Star increases. Figure 7.20a shows that U-tubes generate better heat transfer with the ellipsoidal-45° dimple shape as the Star increases from 4 to 6 for the lower bent curvature while the tube E45P3S4U34 remains the least at all Re. It also shows that Nu of both tubes increases as the Re increases. Tube E45P3S6U12 produces the Nu 41.54% better than the Nu of E45P3S4U34 at the Re=12000. The Nu of higher curvature of Star 6 U-tube decays and approaches to Nu of Star 4 at the Re = 40000, while the Nu of other tubes remains in-between these tubes.

Figure 7.20b denotes insignificant augmentation of Nu for the ellipsoidal-0° dimple U-tubes as the Star increases from 4-6 while the U34 produces slightly higher Nu at the higher Re. Figure 7.20c depicts that fr of tube E45P3S6U12 increases from Re = 5000 to 12000, afterward, it decreases. The U25-U34 curvature radii faces significantly lower hydraulic loss.

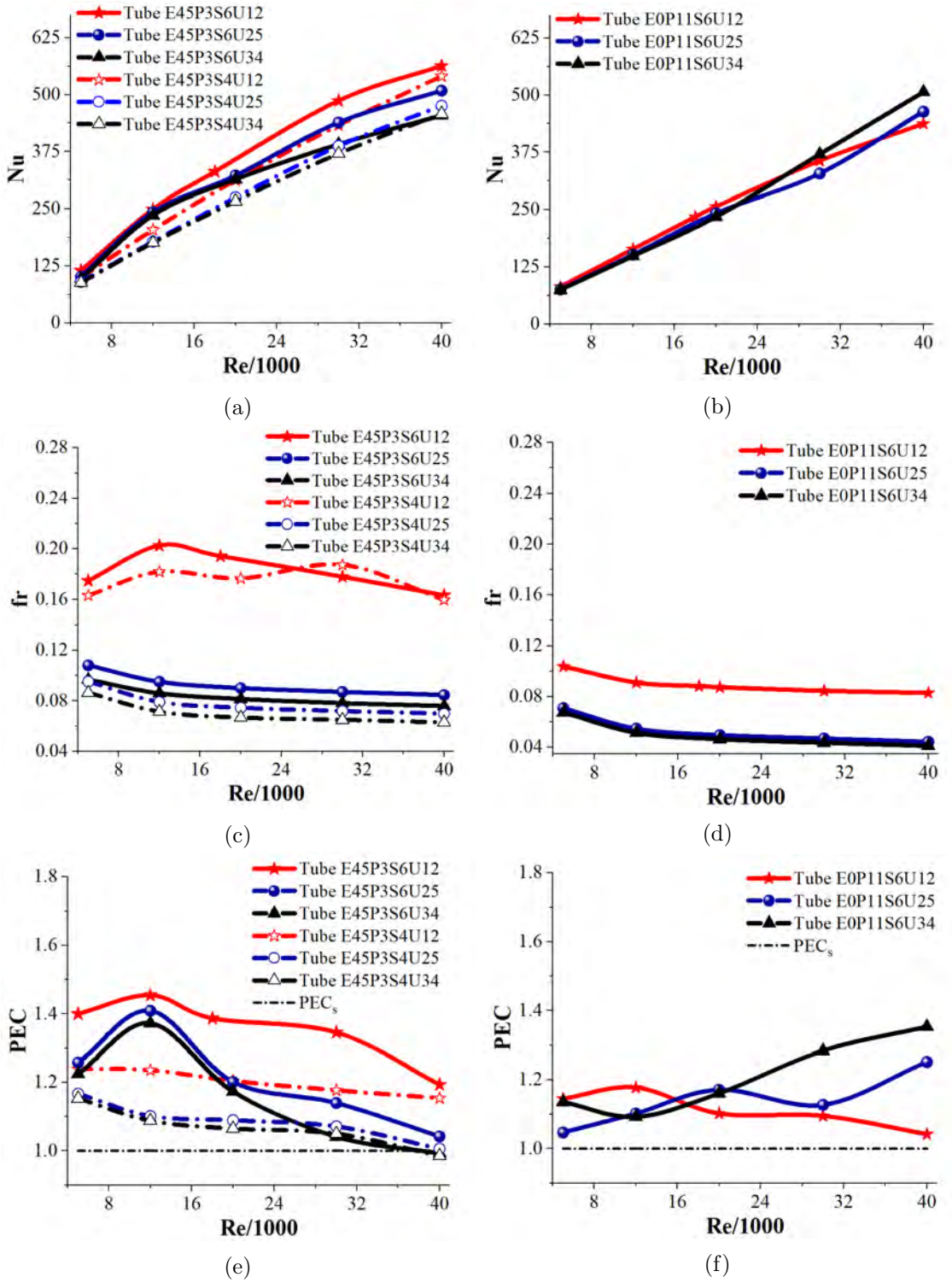

FIGURE 7.20: Characteristics of E45P3S4U12-U34, E0P11S6U12-U34 and E45S6U12-34 Tube E1 tubes, (a) Nu, (b) fr, and (c) PEC

The friction factor of Star 4 with U25-U34 remains the least in the Figure 7.20c - 7.20d. The fr of tubes E0P11S6U12-U34 decreases as the Re increase, however

these tubes faces substantially less fr, contrary to fr of ellipsoidal-45° dimple U-tubes. In Thermo-Hydraulic performances of U-tubes section, ellipsoidal 45° with Star 4 enhanced the performance by 23% at the low Re. On the other hand, Figure 7.20e denotes that E45P3S6U12 (Ellipsoidal 45° dimple) provides the better overall performance against rest of the tubes for Re range of 5000 to 40000. It provides 45.43% performance at the $Re = 12000$. Tubes E45S6U25-U34 generate higher overall performances at the $Re = 12000$, while it remains lower than the performance of tube E45S4U12 at other Re. Tube E0P11S6U34 denotes interesting behavior at higher Re. It provides higher performance at high Re which is 35.3% at the $Re = 40000$. As given in the **Chapter 6**, E0P11S6 provides better performance at high Re. similarly it is appeared from the current analysis that the E0P11S6 also provides better performance in U-tube system but with the higher U-tube curvature radius. Furthermore, all bend tubes provide better performance than the smooth bend (i.e. $PECs$) at all Re.

7.8 Conclusion

Overall performance of flow through heated smooth U-tube in contact with ellipsoidal 45° dimpled enhanced tube with 3.17 mm pitch was numerically carried out. The U-bend curvature of the smooth U-tube was varied from 12 mm to 34.54 mm for the Re range of $5000 \leq Re \leq 30000$. It was found that all the U-tubes/bend tubes have improved the overall performances, however, PEC was increased as the bend curvature decreases. The PEC of U-tubes E1 to E3 was 24% to 15% superior to the smooth tube, at the $Re = 5000$. On the other hand, PEC of Tube E1 was 23% to 17% higher than the smooth tube at the $Re = 5000$ to 30000, respectively. Flow characteristics of tube E1, at the $Re = 12000$, showed the asymmetric pair of vortices as compared to tube S1 (symmetric vortices), because of secondary flow generation. This secondary flow of tube E1 achieved maximum velocity in the bend exit at the outward side and interacted with the upcoming ellipsoidal 45° dimple in the enhanced tube. As a result, high heat transfer was achieved at the upcoming dimple, in the downstream section. Helicity distribution showed

that tube S1 had 2 pairs of vortices at the bend section while it was 3 pairs for tube E1. Furthermore, areas of these vortices at the bend cross-section of tube E1 were larger. Local characterization denoted that the peak value of Nu of the first dimple of the upstream tube was 1430 while the rest of the peak values are around 1000. In the downstream tube, the top and bottom local showed different behavior. The peak value of Nu at the first dimple (Topside) was 1980, whereas the Nu of 2nd and 3rd dimples was around 1500, and afterward, the dimples attained the Nu approximately 1100. However, the bottom side reflected three regions namely the fully detached region, partially re-attached and fully re-attached region. All these regions didn't contribute to the heat transfer augmentation. Polar plots of Nu for the downstream of tubes S1 and E1 were represented at 67 mm, 49 mm, 31 mm, and 13 mm locations. The Nu of 0° located dimple (67 mm-axial location, Topside) of Tube 4 was 442% higher than that of tube S1. Whereas, the Nu of 90°, 180° and 270° located dimples (67 mm-axial location) of tube E1 was 225.2%, 76.2% and 320.5% superior to that of tube S1, respectively. This revealed that 0°, 90°, and 270° located dimples contributed to heat transfer much higher than the 180° (bottom side) located dimples. This pattern of Nu for Tube E1 remained unchanged for the other locations, however, the magnitudes decreased, till the tube exit. The Pre-bend section of tube 4 contributed to heat transfer comparatively lower than the post-bend section.

Transient flow simulation of U-tube E1 showed that there was very little change in property distribution (i.e. Nu and C_f) at different time steps 1 ms, 2 ms, 150 ms and 300 ms. The steady state value of Nu of Post-bend tube at the top sided location of 68.2 mm was 1850, while it was 1830, 1822, 1825 and 1823 for the time = 1 ms, 2 ms, 150 ms and 300 ms respectively. The C_f of Post-bend tube at the top sided location of 68.4 mm was 0.0268 for the steady state, while it was 0.0264, 0.0263, 0.0261 and 0.0264 for time = 1 ms, 2 ms, 150 ms and 300 ms respectively. This showed that fluid flow in the U-tube E1 was steady in nature and negligible deviation at different time steps was observed. Afterwards, correlations for the Nu and fr were proposed for the Re range of $5000 \leq Re \leq 30000$. These correlations were the functions of R_c and Re. An enclosed approximation was observed between

the predicted results and the proposed correlations. In the end, the Nu, fr and PEC of U-tubes with ellipsoidal-0° and 45° dimple tube with Star 6 were also analyzed. The results showed that tube E45S6U12 produced 45.43% performance at the $Re = 12000$. Tubes E45S6U25-U34 generated higher overall performance at the $Re = 12000$, while it remained lower than the performance of tube E45S4U12. Tube E0P11S6U34 denoted interesting behavior at higher Re. It provides higher performance at high Re which is 35.3% at the $Re = 40000$.

Chapter 8

Conclusion and Future Work

In this thesis, the fluid flow and heat transfer characteristics of dimpled enhanced tubes have been investigated using Reynolds Averaged Navier Stokes ($RANS$) for the steady, Unsteady flows and (LES) Large Eddy Simulation for the dynamic flow. Thermal hydraulic performance of flow through externally heated enhanced tubes with constant surface heat flux was investigated subjected to constant external heat flux ($q'' = 10kW/m^2$), for a wide range of Reynolds numbers ($23000 \leq Re \leq 40000$). The tubes were enhanced by introducing different topologies of conical, spherical and ellipsoidal dimples of equivalent volumes. In addition, Pitch and circumferential dimples variation of dimple tubes and ellipsoidal dimple tube with curvature variation of U-tube were investigated to find out the best configuration of enhanced tube.

8.1 Conclusion

Main goal is the development of enhanced tube using dimple in conjunction with the U-tube for heat exchanger depending upon flow physics. This goal is achieved, and conclusions from current investigation have been drawn as given below:

1. While comparing the overall performances in terms of combined performance parameter involving heat and momentum transfer, it can be concluded that

the ellipsoidal dimpled tube is superior compared to conical and spherical dimples. The additional feature of the ellipsoidal dimple allows orientation of the dimple in reference to the tube axis, i.e., varying from 0° to 90°, allows further investigation for better performance. However, in general, dimpled tube (for example tube 8) is superior to smooth tube irrespective of configurations of dimpled tubes by demonstrating enhanced overall performance by 119.5% to 58.1% for $2300 \leq Re \leq 15000$, respectively. At low Re, tube 8 achieved the average surface Nu of 52.7 which was 112% higher than that of smooth tube and 25% higher than Nu of tube 6 and tube 11. At high Re, the average surface Nu of tube 8 increased to 213.5 which was 85% higher than Nu of smooth tube while 23% and 10 % higher than tube 6 and tube 11, respectively. The underline physics is the enhanced dimple fluid interaction which increases the friction factor of the tube however thermo-hydraulic performance of tube 8 was much higher than that of smooth tubes. The performance evaluation criteria of tube 8 varied between 1.45 and 1.30 for $2300 \leq Re \leq 15000$.

2. A detailed investigation involving the effect of enhanced dimple-fluid interaction using LES results showed that the better performance of tube 8 was observed to be linked to asymmetric wake behind the dimples which provided a path for the flow to interact with the succeeding dimples. Whereas, tube 6 and tube 11 decreased the flow interaction with dimples by deflecting the flow streams over the dimples which subsequently reduced the heat transfer. In the end, correlations for Nu and fr were proposed as a function of Re and dimple placement angle α which covered each configuration of the ellipsoidal dimpled tube. The for Nu and fr could readily be obtained for different topologies of ellipsoidal dimpled tube with reasonable accuracy for $2300 \leq Re \leq 15000$. However, the variations in the longitudinal and circumferential placements of dimple seem to be an important parameter.

3. Enhancing the investigation of dimple placements within tube, three different dimple shapes of equivalent volume were considered for pitch variation purpose i.e., ellipsoidal 0°, teardrop, and ellipsoidal 45° dimples. The ratio

of the tube length to dimple pitch ratio was fixed to 10 to ensure the same number of dimples by accommodating the size of the dimple during the pitch variations for all tube configurations. The dimple pitch played a dominant role in the thermal performance augmentation of the enhanced tubes. The performance of enhanced tubes deteriorated with increasing Reynolds numbers as the friction factors of the tubes increased appreciably. Therefore, optimum dimple pitch along with the best working ranges of Reynolds numbers for all three dimple tube configurations was investigated. The pitch of 3.17 mm was found to be the optimal choice for the teardrop and ellipsoidal 45° dimpled tubes i.e., tube TDP3 (P = 3.17 mm, teardrop dimple) and tube E45P3 (P = 3.17 mm, Ellipsoidal 45°). The thermal-hydraulic performance enhancement of tube E45P3 was found to vary between 45.7% to 9% for the Re range of 9000 to 30000, respectively. Tube TDP3 showed the thermal-hydraulic performance augmentation to alter from 31.2% to 3.3% for the Re range of 14000 to 40000. The best pitch configurations for ellipsoidal 0° dimpled tube were obtained to be 11.17 mm (tube E0P11) and 13.17 mm (tube E0P13) for Re = 16000 to 20000 and Re = 30000 to 40000, respectively. For those ranges of Re, tube E0P11 and tube E0P13 exhibited the performance enhancements of 30% - 24% and 15% - 11%, respectively.

4. Local characterizations of tubes E0P11 (P = 11.17 mm, Ellipsoidal 0°), TDP3, and E45P3 were presented using skin friction coefficient (C_f), drag coefficient, Nusselt number (Nu), and Colburn j factor (j_H). C_f of tube E45P3 remained constant at 0.1 for the first five dimples while in cases of tube E0P11 and tube TDP3 C_f decreased from 0.1 to 0.04. Local Nu of tube E45P3 decreased from 1534 to 1000 from 1st to 5th dimple however, it was significantly lower for other tubes. As a result, Colburn j factor of tube E45P3 was 47.7% higher than that of tube E0P11 for the first patch (1st dimple with its smooth surface) at the Re = 12000 and 60.04% at patch 5 (5th dimple with its smooth surface). Moreover, for tube E45P3, correlations for Nu and fr were also proposed as the functions of Re and P which covered each configuration of the ellipsoidal dimpled tube. The Nusselt numbers

and friction factors could readily be obtained for any ellipsoidal dimple tube topology with reasonable accuracy for $9000 \leq Re \leq 30000$.

5. The overall performances of flow, through the selected heated enhanced tubes were numerically carried out with three different dimple configurations, namely teardrop a variant of ellipsoidal dimple, ellipsoidal-0°, and ellipsoidal-45°. The number of dimples in axial direction was 10, and Star (number of dimples in the tangential direction of tube) varied from 4 to 8, subjected to constant external heat flux ($q'' = 10kW/m^2$), for a wide range of Reynolds numbers ($5000 \leq Re \leq 40000$). It was found that overall performance increased as the *Star* increased. A detailed numerical simulation using steady-state Reynolds Averaged Navier Stokes simulations was carried out to compare the flow physics and heat transfer characteristics of dimpled enhanced tubes. The results depicted that the Nu of ellipsoidal 45° dimpled tube with *Star* 8 (Tube E45P3S6 i.e. $P = 3.17$ mm, Star = 6, ellipsoidal 45°) was 36.94% higher in comparison with Nu of tube E45P3S4 ($P = 3.17$ mm, Star = 4, ellipsoidal 45°) at the Re=5000 while it was 14.6% at the $Re = 40000$. The fluid flow analysis prescribed that an increase in the number of *Star* incorporated more dimples in the circumferential direction which introduced more fluid surface interaction. As a result, the heat transfer rate augmented, however, the hydraulic loss was also increased. The hydraulic loss of tube E45P3S8 ($P = 3.17$ mm, Star = 8, ellipsoidal 45°) was 33.14% higher than the friction factor (fr) of tube E45P3S4 at the $Re = 5000$ whereas it was 42.03% at the $Re = 40000$.

6. The comparative analysis against the variation in *Star* showed that thermo-hydraulic performance of the ellipsoidal 45° dimpled tube with *Star* 6 (tube E45P3S6) was superior to other dimpled tubes for the Re range $5000 \leq Re < 18000$. And the overall performance of the ellipsoidal 0° dimpled tube with *Star* 6 (E0P11S6 i.e. $P = 11.17$ mm, Star = 6, ellipsoidal 0°) was better for its favorable Re range $18000 \leq Re \leq 40000$. Local characterization of Tube E0P11S6 presented that centrally located line (i.e. $Yr = 0$ mm) was the major effective line towards the enhancement of Nu and C_f in contrary

to sided lines (i.e. Yr = 1 mm and -1 mm). It denoted that Nu of 1st simple was 600 at the Re = 12000 afterward it decreased gradually. The Nu at the last dimple was approximately 380. The Nu of 1st to 8th dimple was 630 at the Re = 20000, later, it increased to 800 at the last dimple. Opposite to it, Yr = 1 mm location was favorable for the Tube E0P11S6 than the Yr = 0mm and -1mm, regarding the Nu and C_f. Local Nu of E0P11S6 depicted that the first five dimples had Nu greater than 1000 at the Re = 12000 and it was almost 1300 at the Re = 20000. Polar representation of tube E0P11S6 showed that the magnitude of Nu at 150° and 210° located dimples is approximately 1300 while it is 1100 for 30° and 90°, at dimple 1. This denotes that all dimples don't contribute completely to heat transfer augmentation. Afterward, correlations for Nu and fr with the function of Re and S were proposed. The maximum difference numerical results and correlations for Nu remained below 5% and below 11.4% in case of fr, for all *Star* 'S' and Re.

7. Motivated by the utility of the assessment in a straight short tubes, a direct application especially in heat exchangers, is a U-tube tube. Overall performance of flow through heated smooth U-tube in contact with ellipsoidal 45° dimpled enhanced tube with 3.17 mm pitch was numerically carried out. Ellipsoidal 45° dimpled enhanced tube with 3.17 mm pitch with Star = 4 was selected to find out the complex structure of fluid flow physics inside the U-tube before adding the more dimples in the circumferential direction. In doing so, the analysis of curvature variation was conducted in less computational cost. The U-bend curvature of the smooth U-tube was varied from 12 mm to 34.54 mm for the Re range of $5000 \leq Re \leq 30000$. It was found that all the U-tubes/bend tubes have improved the overall performances, however, PEC was increased as the bend curvature decreases. The PEC of U tubes E1 (P = 3.17 mm, Star = 4, ellipsoidal 45°, U-tube radius = 12 mm) to E3 (P = 3.17 mm, Star = 4, ellipsoidal 45°, U-tube radius = 34.54 mm) was 24% to 15% superior to the smooth tube, at the Re = 5000. On

the other hand, PEC of Tube E1 was 23% to 17% higher than the smooth tube at the $Re = 5000$ to 30000, respectively.

8. Flow characteristics of tube E1, at the $Re = 12000$, showed the asymmetric pair of vortices as compared to tube S1 (symmetric vortices), because of secondary flow generation. This secondary flow of tube E1 achieved maximum velocity in the bend exit at the outward side and interacted with the upcoming ellipsoidal 45° dimple in the enhanced tube. As a result, high heat transfer was achieved at the upcoming dimple, in the downstream section. Helicity distribution showed that tube S1 had 2 pairs of vortices at the bend section while it was 3 pairs for tube E1. Furthermore, areas of these vortices at the bend cross-section of tube E1 were larger.

9. Local characterization denoted that the peak value of Nu of the first dimple of the upstream tube was 1430 while the rest of the peak values are around 1000. In the downstream tube, the top and bottom local showed different behavior. The peak value of Nu at the first dimple (Topside) was 1980, whereas the Nu of 2nd and 3rd dimples was around 1500, and afterward, the dimples attained the Nu approximately 1100. However, the bottom side reflected three regions namely the fully detached region, partially re-attached and fully re-attached region. All these regions didn't contribute to the heat transfer augmentation. Polar plots of Nu for the downstream of tubes S1 and E1 were represented at 67 mm, 49 mm, 31 mm, and 13 mm locations. The Nu of 0° located dimple (67 mm-axial location, Topside) of Tube 4 was 442% higher than that of tube S1. Whereas, the Nu of 90°, 180° and 270° located dimples (67 mm-axial location) of tube E1 was 225.2%, 76.2% and 320.5% superior to that of tube S1, respectively. This revealed that 0°, 90°, and 270° located dimples contributed to heat transfer much higher than the 180° (bottom side) located dimples. This pattern of Nu for Tube E1 remained unchanged for the other locations, however, the magnitudes decreased, till the tube exit. The upstream section of tube 4 contributed to heat transfer comparatively lower than the downstream section. In the end, correlations for the Nu and fr were proposed for the Re range of

$5000 \leq Re \leq 30000$. These correlations were the functions of R_c and Re. An enclosed approximation was observed between the predicted results and the proposed correlations.

10. In order to analyze the dynamic behavior of the fluid flow inside the U-tube, transient simulation was performed. The results showed that fluid flow in the U-tube E1 was steady in nature and negligible deviation at different time steps was observed.

11. The Nu, fr and PEC of U-tubes with ellipsoidal-0° and 45° dimple tube for the case of Star 6 were also analyzed. The results showed that tube E45S6U12 (P = 3.17 mm, Star = 6, ellipsoidal 45°, U-tube radius = 12 mm) produced 45.43% performance at the Re = 12000. Tubes E45S6U25 (P = 3.17 mm, Star = 4, ellipsoidal 45°, U-tube radius = 24 mm) - U34 (P = 3.17 mm, Star = 4, ellipsoidal 45°, U-tube radius = 34.54 mm) generated higher overall performance at the Re = 12000, while it remained lower than the performance of tube E45S4U12. Tube E0P11S6U34 denoted interesting behavior at higher Re. It provides higher performance at high Re which is 35.3% at the Re = 40000.

8.2 Future Recommendations

There are some suggestions for the future work, which are given here:

8.2.1 Orientation of Ellipsoidal Dimple in U-tubes

The wakes of ellipsoidal 45° dimples in upstream section of U-tube interact with Dean vortices resulting in asymmetric generation of vortices in the U-tube. Thus, in upstream section one side of the wake is stronger than the other. However, the asymmetric wake pattern may be controlled by changing the dimple orientations on the concerned side of the tube. Therefore, it would be interesting to study this aspect in future.

8.2.2 Incorporation of Dimples in the Bend Sections of U-tubes

In the current study, the dimples were not incorporated in the bend sections of the U-tubes. The inclusion of dimples in the bends would certainly introduce more levels of complexity to the already complex flow field. Therefore, the dimples in the bends may further lead to thermal-hydraulic improvement of U-tubes.

8.2.3 Boiling Heat Transfer in the Dimpled Enhanced Tubes

In this study, the phase change of the working fluid was not studied. In the future, the study of boiling heat transfer in dimpled enhanced tubes can play an important role in the performance augmentation of refrigeration systems.

8.2.4 Investigation of Multiple Bend Section with the Dimple Tube

The investigation of thermal and hydraulic performance of dimpled enhanced tubes with only one bend section was analyzed in this study. The role of dimples may alter in the enhanced tubes with multiple bend sections. Since tubes with multiple bends are commonly used in compact heat exchange devices, therefore, the performance of such tubes may further be explored in the future study.

Bibliography

[1] B. Zohuri, *Compact heat exchangers: Selection, application, design and evaluation.* No. September 2017, 2016.

[2] Thomas, *heat exchanger buying guide.* New york, NY 10001: Thomas for industry.

[3] M. L. Jiji, *Heat Convection.* 2006.

[4] H. Yuncii; A. E. Bergles; F. Mayinger;, *The imperative to enhance heat transfer in heat transfer enhancement of heat exchangers.* 1999.

[5] H. J. Lane and P. J. Heggs, "Extended surface heat transfer — the dovetail fin," *Applied Thermal Engineering*, vol. 25, pp. 2555–2565, 2005.

[6] Y. D. Banekar, S. R. Bhegade, and M. V. Sandbhor, "Dimple tube heat exchanger," *International Journal of Science, Engineering and Technology Research (IJSETR)*, vol. 4, no. 5, pp. 1632–1635, 2015.

[7] J. Chen, H. Müller-Steinhagen, and G. G. Duffy, "Heat transfer enhancement in dimpled tubes," *Applied Thermal Engineering*, vol. 21, no. 5, pp. 535–547, 2001.

[8] L. Wang and B. Sunden, "Performance comparison of some tube inserts," *International Communications in Heat and Mass Transfer*, vol. 29, no. 1, pp. 45–56, 2002.

[9] V. Zimparov, "Enhancement of heat transfer by a combination of three-start spirally corrugated tubes with a twisted tape," *International Journal of Heat and Mass Transfer*, vol. 44, pp. 551–574, 2001.

[10] R. Kumar and A. Mohammadpour, "Effect of twisted tape insert on heat transfer and pressure drop in horizontal evaporators for the flow of R-134a," *International Journal of Refrigeration*, vol. 32, no. 5, pp. 922–930, 2009.

[11] W. M. Rohsenow and J. R. Hartnett, *Handbook of heat transfer*, vol. 36. 1999.

[12] A. Bejan and A. D. Kraus, *Heat Transfer Handbook, Volume 1.* JOHNWILEY & SONS, INC, 2003.

[13] Q. Liao and M. D. Xin, "Augmentation of convective heat transfer inside tubes with three-dimensional internal extended surfaces and twisted-tape inserts," *Chemical Engineering Journal*, vol. 78, no. 2-3, pp. 95–105, 2000.

[14] A. Afzal, M. Samee A. D, A. Javad, A. Shafvan S, P. V. Ajinas, and A. Kabeer K. M, "Heat transfer analysis of plain and dimpled tubes with different spacings," *Heat Transfer - Asian Research*, vol. 47, no. 3, pp. 556–568, 2018.

[15] Liu S; Sakr M;, "Comprehensive review on passive heat transfer enhancements in pipe exchangers," *Renew Sustain Energy Rev.*, vol. 19, pp. 64–81, 2013.

[16] F. Report, "Development and Field Trial of Dimpled-Tube Technology for Chemical Industry Process Heaters," no. September, 2006.

[17] Z. S. Kareem, M. N. Mohd Jaafar, T. M. Lazim, S. Abdullah, A. F. Abdulwahid, and O. T. Oni, "Numerical Investigation of Heat Transfer and Fluid Flow in Tubes Induced with Twisted Tape Inserts," *Experimental Thermal and Fluid Science*, vol. 68, pp. 22–38, 2015.

[18] A. K. Solanki and R. Kumar, "Condensation of R-134a inside dimpled helically coiled tube-in-shell type heat exchanger," *Applied Thermal Engineering*, vol. 129, pp. 535–548, 2018.

[19] A. S. Tijani and N. B. Jaffri, "Thermal analysis of perforated pin-fins heat sink under forced convection condition," *Procedia Manufacturing*, vol. 24, pp. 290–298, 2018.

[20] Y. Peles, A. Koşar, C. Mishra, C. J. Kuo, and B. Schneider, "Forced convective heat transfer across a pin fin micro heat sink," *International Journal of Heat and Mass Transfer*, vol. 48, no. 17, pp. 3615–3627, 2005.

[21] Y. Wang, Y. L. He, Y. G. Lei, and R. Li, "Heat transfer and friction characteristics for turbulent flow of dimpled tubes," *Chemical Engineering and Technology*, vol. 32, no. 6, pp. 956–963, 2009.

[22] M. Li, T. S. Khan, E. Al-Hajri, and Z. H. Ayub, "Single phase heat transfer and pressure drop analysis of a dimpled enhanced tube," *Applied Thermal Engineering*, vol. 101, no. March, pp. 38–46, 2016.

[23] Z. H. Ayub; A. H. Ayub; G. Ribatkshi; T. A. Moreira; T. S. Khan, "Two phase pressure drop and flow boiling heat transfer in an enhanced dimpled tube with a solid round rod insert," *Int journal of heat and mass transfer*, pp. 1–13, 2017.

[24] M. H. Cheraghi, M. Ameri, and M. Shahabadi, "Numerical study on the heat transfer enhancement and pressure drop inside deep dimpled tubes," *International Journal of Heat and Mass Transfer*, vol. 147, p. 118845, 2020.

[25] F. A., *Ansys 16 theory guide*. Ansys Inc., 2013.

[26] Z. Liang, S. Xie, L. Zhang, J. Zhang, Y. Wang, and Y. Yin, "Influence of geometric parameters on the thermal hydraulic performance of an ellipsoidal protruded enhanced tube," *Numerical Heat Transfer; Part A: Applications*, vol. 72, no. 2, pp. 153–170, 2017.

[27] J. Eustice, "Experiments on stream-line motion in curved pipes," *Proceedings of the Royal Society of London. Series A, Containing Papers of a Mathematical and Physical Character*, vol. 85, no. 576, pp. 119–131, 1911.

[28] W. A. J. Smith, "The fluid dynamics of flow in pipes and ducts," *Internal fluid flow*, vol. clarendon, 1980.

[29] N. Cur and E. M. Sparrow, "Measurements of developing and fully developed heat transfer coefficients along a periodically interrupted surface," *Journal of Heat Transfer*, vol. 101, no. 2, pp. 211–216, 1979.

[30] T. Report, "Heat Transfer With Continuous and Discrete Heating in Fully Developed Turbulent Channel Flow: An Application to Convective Cooling of a Waste-Repository Drift," 1981.

[31] O. H. Klepper, "heat transfer performance of short twisted tapes," 1980.

[32] G. Xie and B. Sundén, "Numerical predictions of augmented heat transfer of an internal blade tip-wall by hemispherical dimples," *International Journal of Heat and Mass Transfer*, vol. 53, no. 25-26, pp. 5639–5650, 2010.

[33] A. Bergles, V. Nirmalan, G. Junkhan, and R. Webb, "Bibliography on augmentation of convective heat and mass transfer-ii," tech. rep., Iowa State Univ. of Science and Technology, Ames (USA). Heat Transfer Lab., 1983.

[34] M. Omidi, M. Farhadi, and M. Jafari, "A comprehensive review on double pipe heat exchangers," *Applied Thermal Engineering*, vol. 110, pp. 1075–1090, 2017.

[35] W. El-Maghlany, E. Eid, M. Teamah, and I. Shahrour, "Experimental study for double pipe heat exchanger with rotating inner pipe," *Int J Adv Sci Tech Res*, vol. 4, no. 2, pp. 507–24, 2012.

[36] Z. Zhang, Y. Ding, C. Guan, H. Yan, and W. Yang, "Heat transfer enhancement in double-pipe heat exchanger by means of rotor-assembled strands," *Chemical Engineering and Processing: Process Intensification*, vol. 60, pp. 26–33, 2012.

[37] P. Naphon, "Heat transfer and pressure drop in the horizontal double pipes with and without twisted tape insert," *International Communications in Heat and Mass Transfer*, vol. 33, no. 2, pp. 166–175, 2006.

[38] R. L. Mohanty, S. Bashyam, and D. Das, "Numerical analysis of double pipe heat exchanger using heat transfer augmentation techniques," *International Journal of Plastics Technology*, vol. 18, no. 3, pp. 337–348, 2014.

[39] P. Naphon, "Effect of coil-wire insert on heat transfer enhancement and pressure drop of the horizontal concentric tubes," *International Communications in Heat and Mass Transfer*, vol. 33, no. 6, pp. 753–763, 2006.

[40] S. S. Choudhari and S. Taji, "Experimental studies on effect of coil wire insert on heat transfer enhancement and friction factor of double pipe heat exchanger," *Int. J. Comput. Eng. Res*, vol. 3, pp. 32–39, 2013.

[41] A. Zohir, M. Habib, and M. Nemitallah, "Heat transfer characteristics in a double-pipe heat exchanger equipped with coiled circular wires," *Experimental heat transfer*, vol. 28, no. 6, pp. 531–545, 2015.

[42] P. Bharadwaj, A. Khondge, and A. Date, "Heat transfer and pressure drop in a spirally grooved tube with twisted tape insert," *International Journal of Heat and Mass Transfer*, vol. 52, no. 7-8, pp. 1938–1944, 2009.

[43] S. Eiamsa-Ard, P. Somkleang, C. Nuntadusit, and C. Thianpong, "Heat transfer enhancement in tube by inserting uniform/non-uniform twisted-tapes with alternate axes: Effect of rotated-axis length," *Applied Thermal Engineering*, vol. 54, no. 1, pp. 289–309, 2013.

[44] S. Gunes, V. Ozceyhan, and O. Buyukalaca, "Heat transfer enhancement in a tube with equilateral triangle cross sectioned coiled wire inserts," *Experimental Thermal and Fluid Science*, vol. 34, no. 6, pp. 684–691, 2010.

[45] C. Muthusamy, M. Vivar, I. Skryabin, and K. Srithar, "Effect of conical cut-out turbulators with internal fins in a circular tube on heat transfer and friction factor," *International Communications in Heat and Mass Transfer*, vol. 44, pp. 64–68, 2013.

[46] S. Liu and M. Sakr, "A comprehensive review on passive heat transfer enhancements in pipe exchangers," *Renewable and sustainable energy reviews*, vol. 19, pp. 64–81, 2013.

[47] A. S. Yadav, "Effect of half length twisted-tape turbulators on heat transfer and pressure drop characteristics inside a double pipe u-bend heat exchanger," *JJMIE*, vol. 3, no. 1, pp. 17–22, 2009.

[48] C. Braga and F. Saboya, "Turbulent heat transfer, pressure drop and fin efficiency in annular regions with continuous longitudinal rectangular fins," *Experimental thermal and fluid science*, vol. 20, no. 2, pp. 55–65, 1999.

[49] V. K. Karanth, K. Murthy, *et al.*, "Numerical study of heat transfer in a finned double pipe heat exchanger," *World Journal of Modelling and Simulation*, vol. 11, no. 1, pp. 43–54, 2015.

[50] J. Taborek, "Double-pipe and multitube heat exchangers with plain and longitudinal finned tubes," *Heat Transfer Engineering*, vol. 18, no. 2, pp. 34–45, 1997.

[51] H. Kahalerras and N. Targui, "Numerical analysis of heat transfer enhancement in a double pipe heat exchanger with porous fins," *International Journal of Numerical Methods for Heat & Fluid Flow*, 2008.

[52] K. Syed, M. Ishaq, Z. Iqbal, and A. Hassan, "Numerical study of an innovative design of a finned double-pipe heat exchanger with variable fin-tip thickness," *Energy conversion and management*, vol. 98, pp. 69–80, 2015.

[53] Z. Iqbal, K. Syed, and M. Ishaq, "Fin design for conjugate heat transfer optimization in double pipe," *International Journal of Thermal Sciences*, vol. 94, pp. 242–258, 2015.

[54] D. Gee and R. Webb, "Forced convection heat transfer in helically rib-roughened tubes," *International Journal of Heat and Mass Transfer*, vol. 23, no. 8, pp. 1127–1136, 1980.

[55] J. C. Han and J. S. Park, "Developing heat transfer in rectangular channels with rib turbulators," *International Journal of Heat and Mass Transfer*, vol. 31, no. 1, pp. 183–195, 1988.

[56] N. Kaewchoothong, K. Maliwan, K. Takeishi, and C. Nuntadusit, "Effect of inclined ribs on heat transfer coefficient in stationary square channel," *Theoretical and Applied Mechanics Letters*, vol. 7, no. 6, pp. 344–350, 2017.

[57] A. García, P. G. Vicente, and A. Viedma, "Experimental study of heat transfer enhancement with wire coil inserts in laminar-transition-turbulent regimes at different Prandtl numbers," *International Journal of Heat and Mass Transfer*, vol. 48, no. 21-22, pp. 4640–4651, 2005.

[58] A. Garcia, J. Solano, P. Vicente, and A. Viedma, "The influence of artificial roughness shape on heat transfer enhancement: corrugated tubes, dimpled tubes and wire coils," *Appl. Thermal Eng*, vol. 35, pp. 196–201, 2012.

[59] E. K. Akpinar, "Evaluation of heat transfer and exergy loss in a concentric double pipe exchanger equipped with helical wires," *Energy Conversion and Management*, vol. 47, no. 18-19, pp. 3473–3486, 2006.

[60] A. E. Bergles and R. M. Manglik, "Current progress and new developments in enhanced heat and Mass Transfer," *Enhance Heat transfer*, vol. 20, 2013.

[61] M. Li, T. S. Khan, E. Al Hajri, and Z. H. Ayub, "Geometric optimization for thermal-hydraulic performance of dimpled enhanced tubes for single phase flow," *Applied Thermal Engineering*, vol. 103, no. September, pp. 639–650, 2016.

[62] S. Aroonrat, K.; Ahn, H.S.; Jerng, D.-W.; Asirvatham, L.G.; Dalkılıç, A.S.; Mahian, O.; Wongwises, "Experimental study on evaporation heat transfer and pressure drop of R-134a in a horizontal dimpled tube," *international journal of heat and mass tranfer*, vol. 144, 2019.

[63] R. Maithani and A. Kumar, "Correlations development for Nusselt number and friction factor in a dimpled surface heat exchanger tube," *Experimental Heat Transfer*, vol. 00, no. 00, pp. 1–22, 2019.

[64] T. Dagdevir, O. Keklikcioglu, and V. Ozceyhan, "Heat transfer performance and flow characteristic in enhanced tube with the trapezoidal dimples," *International Communications in Heat and Mass Transfer*, vol. 108, p. 104299, 2019.

[65] X.-s. Lei, J.-j. Shuang, P. Yang, and Y.-w. Liu, "Parametric study and optimization of dimpled tubes based on Response Surface Methodology and desirability approach," *International Journal of Heat and Mass Transfer*, vol. 142, p. 118453, 2019.

[66] R. B. Manoram, R. S. Moorthy, and R. Ragunathan, "Investigation on influence of dimpled surfaces on heat transfer enhancement and friction factor in solar water heater," *Journal of Thermal Analysis and Calorimetry*, vol. 145, no. 2, pp. 541–558, 2021.

[67] Q. Jing, Y. Xie, and D. Zhang, "Thermal-hydraulic performance and entropy generation of supercritical carbon dioxide in heat exchanger channels with teardrop dimple/protrusion," *International Journal of Heat and Mass Transfer*, vol. 135, pp. 1082–1096, 2019.

[68] Fan and X. Yin, "3-D numerical study on the effect of geometrical parameters on thermal behavior of dimple jacket in thin-film evaporator," *Appl. Thermal Eng*, vol. 28, pp. 1875–1881, 2008.

[69] S. Xie, Z. Liang, L. Zhang, and Y. Wang, "A numerical study on heat transfer enhancement and flow structure in enhanced tube with cross ellipsoidal dimples," *International Journal of Heat and Mass Transfer*, vol. 125, pp. 434–444, 2018.

[70] S. Xie, Z. Liang, J. Zhang, L. Zhang, Y. Wang, and H. Ding, "Numerical investigation on flow and heat transfer in dimpled tube with teardrop dimples," *International Journal of Heat and Mass Transfer*, vol. 131, pp. 713–723, 2019.

[71] A. O. Firoozi, S. Majidi, and M. Ameri, "A numerical assessment on heat transfer and flow characteristics of nanofluid in tubes enhanced with a variety of dimple configurations," *Thermal Science and Engineering Progress*, vol. 19, no. April, 2020.

[72] L. Zhang, W. Xiong, J. Zheng, Z. Liang, and S. Xie, "Numerical analysis of heat transfer enhancement and flow characteristics inside cross-combined ellipsoidal dimple tubes," *Case Studies in Thermal Engineering*, vol. 25, no. February, p. 100937, 2021.

[73] W. Duangthongsuk and S. Wongwises, "An experimental investigation of the heat transfer and pressure drop characteristics of a circular tube fitted with rotating turbine-type swirl generators," *Experimental thermal and fluid science*, vol. 45, pp. 8–15, 2013.

[74] M. Shewale Omkar, A. Mane Pravin, A. H. Gazge Sajid, and A. Pasanna Pradeep, "Experimental investigation of double-pipe heat exchanger with helical fins on the inner rotating tube," *International Journal of Research in Engineering and Technology*, vol. 3, no. 07, 2014.

[75] D. J. Kukulka, R. Smith, and K. G. Fuller, "Development and evaluation of enhanced heat transfer tubes," *Applied Thermal Engineering*, vol. 31, no. 13, pp. 2141–2145, 2011.

[76] J. Da, Ricardo, S. Lima, and J. R. Thome, "Two-Phase Flows in U-bends," in *Encyclopedia of Two-Phase Heat Transfer and Flow II*, pp. 141–182, 2015.

[77] F. Xie, X. Li, P. Qian, Z. Huang, and M. Liu, "Effects of geometry and multisource heat input on fl ow and heat transfer in single closed-loop pulsating heat pipe," *Applied Thermal Engineering*, vol. 168, no. December 2019, p. 114856, 2020.

[78] D.-t. Vo, H.-t. Kim, J. Ko, and K.-h. Bang, "An experiment and three-dimensional numerical simulation of pulsating heat pipes," *International Journal of Heat and Mass Transfer*, vol. 150, p. 119317, 2020.

[79] A. García, A. Egea, J. P. Solano, and J. P, "Solar-driven melting dynamics in a shell and tube thermal energy store : An experimental analysis," *Renewalbe energy*, vol. 154, pp. 1044–1052, 2020.

[80] H. Martin, *Heat Exchangers*. Routledge, 1992.

[81] K. C and K. Arul Prakash, "Steady and unsteady numerical investigations of laminar fluid flow and heat transfer in a 180 bend with bypass," *International Journal of Heat and Mass Transfer*, vol. 151, 2020.

[82] W. R. Dean, "Note on the Motion of Fluid in a Curved Pipe," in *Note on the Motion of Fluid in a Curved Pipe*, pp. 208–223, 1911.

[83] F. Hellstr, "Numerical computations of the unsteady flow in turbochargers," no. April, 2010.

[84] H. K. Pradhan, A. K. Sahoo, M. K. Roul, M. M. Awad, and A. K. Barik, "Heat transfer characteristics of an 180 degree bend pipe of different cross sections using nano-enhanced ionic liquids (NEILs)," *SN Applied Sciences*, vol. 2, no. 6, 2020.

[85] H. Itō, "Friction factors for turbulent flow in curved pipes," *Journal of basic engineering*, vol. 81, no. 2, pp. 123–132, 1959.

[86] P. Srinivasan, S. Nandapurkar, and F. Holland, "Friction factors for coils," *Transactions of the Institution of Chemical Engineers and the Chemical Engineer*, vol. 48, no. 4-6, pp. T156–+, 1970.

[87] A. J. Ward-Smith, "Internal fluid flow-the fluid dynamics of flow in pipes and ducts," *Nasa Sti/recon Technical Report A*, vol. 81, p. 38505, 1980.

[88] P. Spedding, E. Bénard, and G. McNally, "Fluid flow through 90 degree bends," *Developments in Chemical Engineering and Mineral Processing*, vol. 12, no. 1-2, pp. 107–128, 2004.

[89] J. Azzola, J. Humphrey, H. Iacovides, and B. Launder, "Developing turbulent flow in a u-bend of circular cross-section: measurement and computation," 1986.

[90] M. Rowe, "Measurements and computations of flow in pipe bends," *Journal of Fluid Mechanics*, vol. 43, no. 4, pp. 771–783, 1970.

[91] S. Dey, "Secondary boundary layer and wall shear for fully developed flow in curved pipes," *Proceedings of the Royal Society of London. Series A: Mathematical, Physical and Engineering Sciences*, vol. 458, no. 2018, pp. 283–298, 2002.

[92] H. K. Pradhan, A. K. Sahoo, M. K. Roul, M. M. Awad, and A. K. Barik, "Heat transfer characteristics of an 180° bend pipe of different cross sections using nano-enhanced ionic liquids (neils)," *SN Applied Sciences*, vol. 2, no. 6, pp. 1–13, 2020.

[93] X. Yuan, Z. Tao, H. Li, and Y. Tian, "Experimental investigation of surface roughness effects on flow behavior and heat transfer characteristics for circular microchannels," *Chinese Journal of Aeronautics*, vol. 29, no. 6, pp. 1575–1581, 2016.

[94] M. J. Tummers and M. Steunebrink, "Effect of surface roughness on heat transfer in Rayleigh-Bénard convection," *International Journal of Heat and Mass Transfer*, vol. 139, pp. 1056–1064, 2019.

[95] J. W. Peeters and N. D. Sandham, "Turbulent heat transfer in channels with irregular roughness," *International Journal of Heat and Mass Transfer*, vol. 138, pp. 454–467, 2019.

[96] R. Kumar, V. Goel, and A. Kumar, "Investigation of heat transfer augmentation and friction factor in triangular duct solar air heater due to forward facing chamfered rectangular ribs: A CFD based analysis," *Renewable Energy*, vol. 115, pp. 824–835, 2018.

[97] H. M. Jaffal, I. A. Ghani, and A. R. Al-Obaidi, "The effect of interruptions on thermal characteristics of corrugated tube," *Case Studies in Thermal Engineering*, vol. 25, 2021.

[98] R. Andrzejczyk, T. Muszynski, and P. Kozak, "Experimental investigation of heat transfer enhancement in straight and U-bend double-pipe heat exchanger with wire insert," *Chemical Engineering and Processing - Process Intensification*, vol. 136, pp. 177–190, 2019.

[99] P. V. Durga Prasad and A. Gupta, "Experimental investigation on enhancement of heat transfer using Al2O3/water nanofluid in a u-tube with twisted tape inserts," *International Communications in Heat and Mass Transfer*, vol. 75, pp. 154–161, 2016.

[100] L. Syam Sundar, N. T. Ravi Kumar, B. M. Addis, P. Bhramara, M. K. Singh, and A. C. Sousa, "Heat transfer and effectiveness experimentally-based analysis of wire coil with core-rod inserted in Fe3O4/water nanofluid flow in a double pipe U-bend heat exchanger," *International Journal of Heat and Mass Transfer*, vol. 134, pp. 405–419, 2019.

[101] K. Cho and S. J. Tae, "Condensation heat transfer for R-22 and R-407C refrigerant-oil mixtures in a microfin tube with a U-bend," *International Journal of Heat and Mass Transfer*, vol. 44, no. 11, pp. 2043–2051, 2001.

[102] L. Syam Sundar, P. Bhramara, N. T. Ravi Kumar, M. K. Singh, and A. C. Sousa, "Experimental heat transfer, friction factor and effectiveness analysis of Fe3O4 nanofluid flow in a horizontal plain tube with return bend and wire coil inserts," *International Journal of Heat and Mass Transfer*, vol. 109, pp. 440–453, 2017.

[103] H. K. Versteeg and W. Malalasekera, *An introduction to computational fluid dynamics: the finite volume method*, vol. M. second edition ed., 1996.

[104] K. Hami, "Turbulence modeling a review for different used methods," *International Journal of Heat and Technology*, vol. 39, no. 1, pp. 227–234, 2021.

[105] D. K. Lilly, "A proposed modification of the German0 closure method h J axi," *Phys. Fluids*, vol. 4, no. 3, pp. 633–635, 1992.

[106] M. Germano, U. Piomelli, P. Moin, and W. H. Cabot, "A dynamic subgrid-scale eddy viscosity model," *Physics of Fluids A*, vol. 3, no. 7, pp. 1760–1765, 1991.

[107] W. Y. Yang, W. Cao, T.-S. Chung, and J. Morris, *Applied Numerical Methods using MATLAB*. JOHN WILEY & SONS, 2005.

[108] D. Warmeiibergang, "Zeitschrift fur Technische Chemie, Verfahrenstechnik und Apparatewesen," pp. 781–789, 1967.

[109] B. Adrian, *CONVECTION HEAT Other books by Adrian Bejan :.* 2013.

[110] K. Velten, W. Lubitz, and A. Hopf, *Simulation of airflow within horticulture high-tunnel greenhouses using open-source CFD software*. PhD thesis, Bachelor thesis, 02 2018.

[111] M. Su, Q. Chen, and C.-M. Chiang, "Comparison of different subgrid-scale models of large eddy simulation for indoor airflow modeling," *J. Fluids Eng.*, vol. 123, no. 3, pp. 628–639, 2001.

[112] F. Unger and R. Friedrich, "Large eddy simulation of fully-developed turbulent pipe flow," in *Proceedings of the 8th Symp. on Turbulent Shear Flows, Sept*, pp. 9–11, 1991.

[113] B. Boersma and F. Nieuwstadt, "Large-eddy simulation of turbulent flow in a curved pipe," 1996.

[114] Z. Yang, "Large eddy simulation of fully developed turbulent flow in a rotating pipe," *International journal for numerical methods in fluids*, vol. 33, no. 5, pp. 681–694, 2000.

[115] M. Tutar, A. Holdo, and A. Lewis, "Comparative performance of various two equation turbulence models and les on simulated flow past a circular cylinder in subcritical flow regime," *Proceedings of ASME Fluids Engineering Summer Meeting on Finite Element Application in Fluid Dynamics*, 1998.

[116] J. Gong, P. Ming, and W. Zhang, "Les of turbulent flows through a butterfly valve," in *AIP Conference Proceedings*, vol. 1376, pp. 457–459, American Institute of Physics, 2011.

[117] J. Smagorinsky, "General circulation experiments with the primitive equations: I. the basic experiment," *Monthly weather review*, vol. 91, no. 3, pp. 99–164, 1963.

[118] B. R. Munson, T. H. Okiishi, W. W. Huebsch, and A. P. Rothmayer, *Fundamentals of Fluid Mechanics, 2013*. John Wiley & Sons, Inc.

[119] V. Gnielnski, "New equation for heat and mass transfer in turbulent pipe and channel flow," *international chemical engineering*, vol. 16, no. 2, pp. 359–368, 1976.

[120] B. S. Petukhov, "Heat transfer and friction in turbulent pipe flow with variable physical properties," in *Advances in heat transfer*, vol. 6, pp. 503–564, Elsevier, 1970.

[121] R. Sabir, M. Khan, N. Sheikh, I. Ahad, and D. Brabazon, "Assessment of thermo-hydraulic performance of inward dimpled tubes with variation in angular orientations," *Applied Thermal Engineering*, vol. 170, apr 2020.

[122] C. Tay, B. Khoo, and Y. Chew, "Mechanics of drag reduction by shallow dimples in channel flow," *Physics of Fluids*, vol. 27, no. 3, p. 035109, 2015.

[123] F. Gattere, A. Chiarini, and M. Quadrio, "Dimples for skin-friction drag reduction: status and perspectives," *Fluids*, vol. 7, no. 7, p. 240, 2022.

[124] G. F. C. Rogers and Y. R. Mayhew, "Coiled and pressure flow," vol. 7, pp. 1207–1216, 1964.

[125] Y. Mori and W. Nakayama, "Study of forced convective heat transfer in curved pipes (2nd report, turbulent region)," *International Journal of Heat and Mass Transfer*, vol. 10, no. 1, pp. 37–59, 1967.

[126] M. M. Mandal and K. D. P. Nigam, "Experimental Study on Pressure Drop and Heat Transfer of Turbulent Flow in Tube in Tube Helical Heat Exchanger," pp. 9318–9324, 2009.

[127] T. J. B. C. Jespersen, "The design and application of upwind schemes on unstructured meshes Moffett Field , CA 27th Aerospace Sciences Meeting," *27th Aerospace Sciences Meeting*, 1989.

[128] A. Ebrahimi and B. Naranjani, "An investigation on thermo-hydraulic performance of a flat-plate channel with pyramidal protrusions," *Applied Thermal Engineering*, vol. 106, pp. 316–324, 2016.

[129] P. Patil and P. Deshmukh, "Numerical Study of Flow and Heat Transfer in Circular Tube With Almond Shape Dimple," vol. 3, no. 8, pp. 21–29, 2014.

[130] W. L. Chow, C. M.; Rhie, "Numerical study of the turbulent flow past an airfoil with tailing edge separation," *AIAA*, vol. 21, no. 11, pp. 1525–1532, 1983.

Appendix A

Numerical Methodology

A.1 Finite Volume Method (FVM)

Finite volume method (FVM) is very popular technique which is implemented in ANSYS Fluent. FVM discretizes the computational domain into finite volumes using grid generation, where scalar quantities are computed at the cell centered and fluxes are computed on the cell faces. This is conducted by the domain decomposition, integration of governing equation in each cell and computation from algebraic equation (linearization of discrete equations). Mainly, two kinds of solvers, in ANSYS Fluent, are used, which are Pressure-based solver (PBS) and Density-based solver (DBS). There are two approaches that are established according to their usages. The PBS is formulated for minimum speed, in-compressible fluid flow while the DBS is purely established for ultra-speed compressible flows. However, two approaches have been re-established further and re-covered of flow development beyond their classical domain. In both methods, momentum-equations are the origin for computing velocity flux. In DBS, the continuity-equation is employed in order to find out the density flux whereas the pressure flux is calculated through the state equation. Furthermore, in the PBS, manipulation of continuity and momentum equation is used to find the pressure/pressure correction equation for

computation of pressure flux. Both methods employ a same grid generation process (FVM), however the method employ to linearize and compute the discretized is dissimilar.

A.1.1 Discretization of Transport Equation

ANSYS Fluent converts the scalar transport equation to algebraic equation in order to compute it numerically using **FVM**. It integrates the transport equation (of scalar ϕ (flow variable, i.e. u, v, w, etc.)) of each cell volume V to figure out the discrete form. For example:

$$\int_V \frac{\partial \rho \Phi}{\partial t} dV + \oint \rho \Phi \vec{v} \cdot dA = \oint \Gamma_\phi \nabla_\phi \cdot dA + \int_V S_\phi dV \tag{A.1}$$

Where $\rho =$ density $\vec{v} =$ velocity $(= u\hat{i} + v\hat{j}$ in 2D) $\vec{A} =$ surface area vector

$\Gamma_\phi =$ diffusion coefficient for ϕ

$\nabla_\phi =$ gradient of $\phi = \frac{\partial \phi}{\partial x}\hat{i} + \frac{\partial \phi}{\partial y}\hat{j}$ in 2D

$S_\phi =$ source of ϕ per unit volume

Equation A.1 is employed to every cell volume. The volume integrals of convective and diffusive fluxes, in equation A.1, are converted to surface integrals while in equation A.2, the surface integrals are converted to semi discretized (summation) form, which can be easily computed in each cell. For example, in the case of following cell volume, the schematic diagram and equation A.2 can be written as:

$$\frac{\partial \rho \phi}{\partial t} dV + \sum_f^{N_{faces}} \rho_f \vec{v_f} \phi_f \cdot \vec{A_f} = \sum_f^{N_{faces}} \Gamma_f \nabla \phi_f \cdot \vec{A_f} + S_\phi V \tag{A.2}$$

Where

$N_{faces} =$ number of faces enclosing cell $\phi_f =$ value of ϕ converted through face f $\rho_f \vec{v_f} \cdot \vec{A_f}$ mass flux through the face $\vec{A_f}$ area of face f ,$|A|$ $(= |A_x\hat{i} + A_y\hat{j}|$

in 2D) ∇_{ϕ_f} = gradient of ϕ at the face f V = cell volume Similar to the 2D triangular element, CFD applies the same procedure in every grid (2D or 3D) of computational domain and calculated it numerically.

A.1.2 Computing the Linear System

As the transport equation A.2 contained the unknown, which needed to be figure out. Generally, the system of equations was non-linear, which was needed to be converted to linear system. Such appearance of equation A.2 can be denoted as:

$$A_p\phi = \sum_{nb} a_{nb}\phi_{nb} + b \tag{A.3}$$

Here the nb denotes the neighbor cells and a_p and a_{nb} are the coefficients of ϕ and ϕ_{nb}. The cell neighbor's quantity dependent on topology of mesh, however it will basically the face numbers be containing the cell. Every cell has the similar equation in the grid which produces a set of algebraic equations for which ANSYS FLUENT resolves the system of linear equation by Gauss seidel incorporation with an algebraic multigrid method.

A.1.2.1 Production of k and ω for (SST)$K-\omega$ Model

$\tilde{G_k} = \min(G_k, 10\rho\beta^* k\omega), G_\omega = \frac{a}{v_t}\tilde{G_k}$ where $\tilde{G_k}$ and G_ω represent the production of turbulence kinetic energy and production of ω respectively. Where G_k is defined likewise the standard $k-\omega$. This expression is different from expression of standard $k-\omega$ model due to the a_∞ term. As the standard $k-\omega$ model used it as constant value of 0.52. while the SST used it as follows:

$$a_\infty = F_1 a_{\infty,1} + (1 - F_1)a_{\infty,2} \tag{A.4}$$

Where

$$a_(\infty, 1) = \frac{\beta_{i,1}}{\beta^*_\infty} - \frac{k^2}{\sigma_{w,1}\sqrt{\beta^*_\infty}}$$

where k is 0.4

A.1.2.2 Model the Turbulence Dissipation for (SST)$K-\omega$ Model

A.1.2.3 k Dissipation

The statement Y_k can be defined like-wise the standard $k-\omega$ model and it denote the dissipation of turbulence kinetic energy. The f_{β^*} is represented as the piece wise-linear function in standard $k-\omega$ while it has constant value of 1 in SST. Therefore,

$$Y_k = \rho\beta^* k\omega \tag{A.5}$$

A.1.2.4 ω Dissipation

Similarly, the statement Y_ω can be defined like-wise the standard $k-\omega$ model and it denotes the ω dissipation. Only difference in SST $k-\omega$ is f_β had a value of 1. Therefore,

$$Y_k = \rho\beta\omega^2 \tag{A.6}$$

Rather a constant value, β_i has the following form

$$\beta_i = F_1\beta_{i,1} + (1-F_1)\beta_{i,2}$$

where F_1 is derived from the Equation

$$F_1 = \tanh(\Phi^4),$$

,

A.1.3 Cross Diffusion Modification

The SST $k-\omega$ is based on standard $k-\omega$ and the standard $k-\epsilon$ models. Therefore, the blending is used between the two models and the cross-diffusion D_ω can be stated as equation follows:

$$D_\omega = 2(1-F_1)\rho\frac{1}{\omega\sigma_{\omega,2}}\frac{\partial k}{\partial x_j}\frac{\partial \omega}{\partial x_j} \tag{A.7}$$

And constants for the model are given here: $\sigma_{k,1} = 1.176, \sigma_{\omega,1} = 2.0, \sigma_{k,2} = 1.0, \sigma_{\omega,2} = 1.168, a_1 = 0.31, \beta_{i,1} = 0.075, \beta_{i,2} = 0.0828$

All supplementary constant $(a^*_\infty, a_\infty, a_0, \beta^*_\infty, R_\beta, R_k, R_\omega, \zeta^*, \text{and} M_{t0})$ has identical values like-wise the standard $k-\omega$.

A.1.3.1 Boundary Conditions (BC) for the Wall

Wall BC has similar treatment to the treatment of k-equation with enhanced wall treatment in $k-\epsilon$ model. This implies the wall BC according to wall function approach. The treatment of wall BC for the k equation in the $k-\omega$ models is same as the treatment of k-equation with enhanced wall treatment in $k-\epsilon$ model. This allowed the wall boundary conditions for the mesh of wall function to discretized according to the wall function, where ω can be written as:

$$\omega_w = \frac{\rho(u^*)^2}{\mu}\omega^+ \tag{A.8}$$

Here the computational solutions may be written as:

$$\omega^+ = \frac{6}{\beta_i(y^+)^2}, \text{ and:} \omega^+ = \frac{1}{\sqrt{\beta^*_\infty}}\frac{du^+_{turb}}{dy^+} \tag{A.9}$$

A.2 Pressure-Based Solver (PBS)

The governing equations are computed sequentially in the currently used solution algorithm (pressure-based solver (PBS)). As the governing equations are coupled and non-linear, the resolution circle should base upon the iterative procedure in order to approach the convergence criteria. Segregated algorithm (SA) solve the governing equations for calculated variables after one another. In the SA, each governing equation for the variables (e.g. u, v, w, p, T, etc) are solve consecutively. Every equation, in computation process, is "decoupled" or "segregated" from rest of the equation, therefore its name is relevant to the solution procedure. The segregated approach was memory economical because in memory, the discretized equations are called one in a time. Therefore, the solution procedure is comparatively slow due to sequential behavior. Segregated algorithm comprises the following steps during each iteration:

- In current iteration, fluid properties (e.g. viscosity, density, turbulent viscosity etc) are modified.
- In each iteration, momentum equations are solved using the upcoming values
- In each iteration, pressure equation is corrected by the current mass and velocity field
- Then, mass fluxes, pressure and velocity fields are adjusted through the information from step 3
- Furthermore, the turbulent quantities, energy and other scalars are solved
- Analyze the convergence criteria These steps, as shown in Figure 3.6 1, are followed until the convergence criteria is fulfilled.

Sequential-algorithm Coupled-algorithm

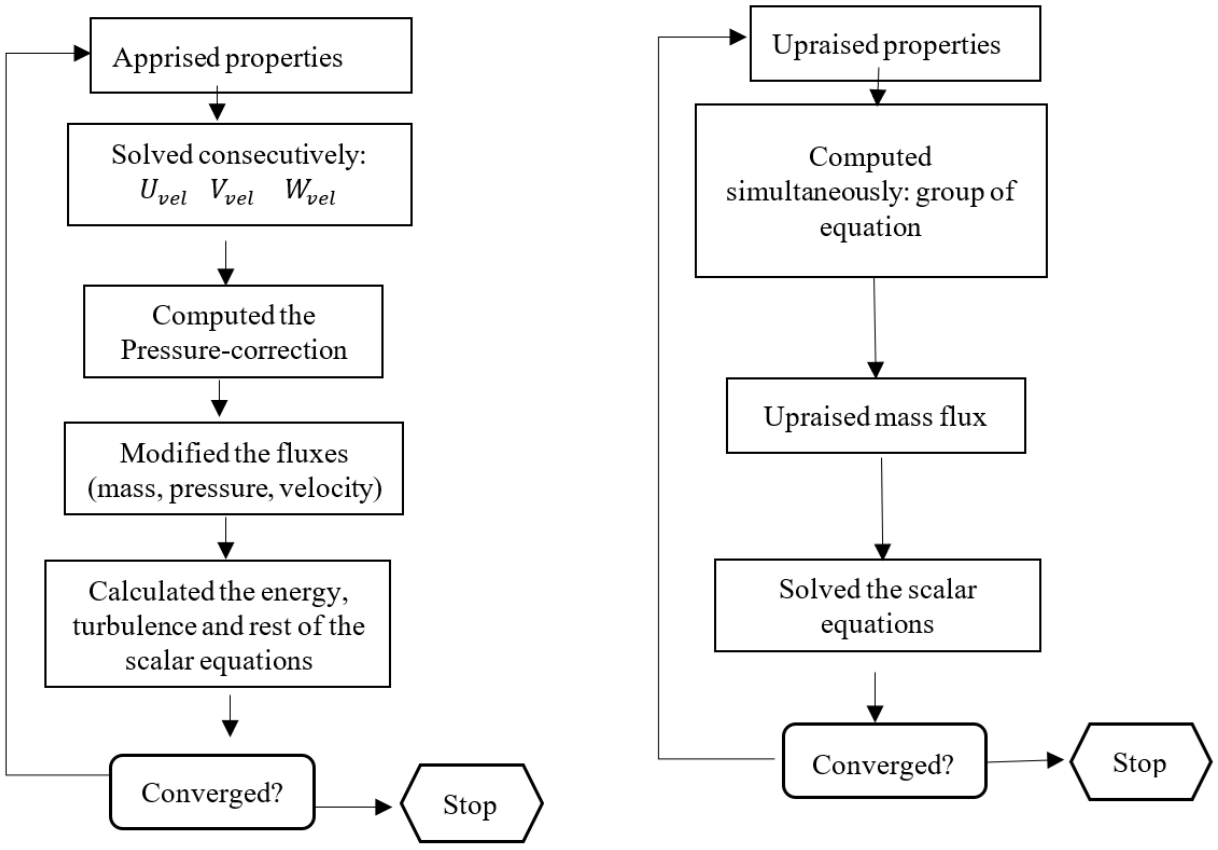

FIGURE A.1: Flow charts for the sequential and coupled algorithm

A.2.1 The Pressure-Based Coupled Algorithm (PBCA)

Opposite to the sequential method, the coupled algorithm resolves the couple system of equations simultaneously. Therefore the 2nd and 3rd steps of sequential method are combined and become one step in coupled method. The other equations are resolved likewise in the sequential method. The coupled algorithm computed the system in less time than the sequential manner, as the continuity and momentum are solved at a time. However, it required more memory to solve the coupled system of equation.

A.2.2 Discretization Schemes

Related content is summarized as follows:

1. Spatial discretization

2. Temporal discretization

3. Assessment of Gradients and derivatives

4. Gradient limiters

A.2.2.1 Spatial Discretization

The cell centers (c_o&c_1) contains the locus of discrete values of cell properties. There is the requirement of face values ϕ_f for the convective term in equation A.2. Moreover, interpolation should be there in the cell middle values. Upwind scheme implies the interpolation. In this scheme ϕ_f is manipulated using the upstream, or "upwind" with respect to v_n in equation A.5. The diffusion terms in equation A.2 are used central-differencing scheme for solution and are consistently correct.

A.2.2.2 Second-Order Upwind Scheme

In this scheme, the scalars at the cell faces are computed using the approach [127]. Taylor series expansion of cell centered computation is employed to attain the higher order accuracy at the faces of cell. Therefore, ϕ_f is calculated as:

$$\phi_{f,SOU} = \phi + \Delta\phi \cdot \vec{r} \tag{A.10}$$

Here ϕ and $\Delta\phi$ are the values at the cell centered while their gradients are in the upstream cell. Similarly, $\vec{r}$ denotes the displacement vector from the upstream cell centroid to the centroid of the face. This is useful to find the solution of the gradient $\nabla\phi$ in each cell. At the end, the gradient $\nabla\phi$ is determined in order to inserted the new maxima.

A.2.2.3 Temporal Discretization

In transient simulations, the discretization of governing equations in space & time must also be applied. The time dependent and steady state equations have same spatial discretization however, for the temporal discretization case, it carries out the integration of each term of differential equation on the Δt. A general expression of time variation of variable ϕ can be written as:

$$\frac{\partial \phi}{\partial t} = F(\phi) \tag{A.11}$$

Here F includes any spatial discretization. If the backward differences are used for the discretization of time derivatives, then second order temporal discretization can be written as:

$$\frac{3\phi^{n+1} - 4\phi^{n} + \phi^{n-1}}{2\Delta t} = F(\phi) \tag{A.12}$$

Here

ϕ = a scalar quantity $n+1$ = next value at the time level $t + \Delta t$ n = value at the current time level t $n-1$ = previous value at the time level, $t - \Delta t$ Afterwards, evaluation of $F(\phi)$ against the ϕ is only remain the question.

A.2.3 Bounded Second Order Implicit Time Integration

The discretization in time for any variable can be written as:

$$\frac{\partial \phi}{\partial t} = \frac{\phi_{n+1/2} - \phi_{n-1/2}}{dt} \tag{A.13}$$

Where

$$\phi_{(n+1/2)} = \phi_n + 1/2\beta_{(n+1/2)}(\phi_n - \phi_{n-1})$$

$$\phi_{(n-1/2)} = \phi_{n-1} + 1/2\beta_{(n-1/2)}(\phi_{n-1} - \phi_{n-2})$$

Here $n, n-1, n-2, n+1/2, n-1/2$ are dissimilar time stages. $\beta_{(n+1/2)}\&\beta_{(n-1/2)}$ are bounding factors for every variable at $n+1/2, n-1/2$ stage.

A.2.4 Assessment of Gradients and Derivatives

There is the requirement of gradients for generating the scalar values at the faces of cell. Secondary, it is also helpful for measuring the secondary diffusion term as well as the derivatives of velocities. The $\Delta\phi$(gradient) is used for discretization of the convective as well as diffusive terms in the conversation of flow equation. CFD solved the $\Delta\phi$using the Green-gauss cell-based (GGCB), Green-gauss node-based (GGNB) and Least squares cell-based (LSCB). However, this study has used the LSCB method because it is superior than others two methods, as given below:

A.2.4.1 LSCB Gradient Evaluation

Here, the linearly variation occurs in solution, which can be denoted as:

$$(\nabla\phi)_{c_0} \cdot \Delta r_i = \phi_{c_i} - \phi_{c_0} \tag{A.14}$$

If similar equations, surrounded by cell c_0, is arranged together, the compact form of system can be denoted as:

$$[J](\nabla\phi)_{c_0} = \Delta\phi \tag{A.15}$$

Where $[J]$ represents the geometry function and it is the coefficient matrix. Furthermore, the $\nabla\phi_0 = \phi_x\hat{i}+\phi_y\hat{j}+\phi_z\hat{k}$ is the main goal here through the minimization of the non-square matrix system. The linear set of equation, as mentioned above, is over-defined which can be computed through the break-downing the coefficient matrix by the process [128]. Here the break-down produces weighted matrix of every individual cell. Here in the cell-centered scheme, it means that the weights $W_{i0}^x, W_{i0}^y, W_{i0}^z$ are made for all faces of the c_0. Thus, the gradient can be calculated

by doing the multiplication of weighted factors and the vector $\Delta\phi = (\phi_{c1} - \phi_{c0})$

$$(\phi_x)_{c0} = \sum_{i=1}^{n} W_{i0}^{x} \cdot (\phi_{c_i} - \phi_{c_0}) \tag{A.16}$$

$$(\phi_y)_{c0} = \sum_{i=1}^{n} W_{i0}^{y} \cdot (\phi_{c_i} - \phi_{c_0}) \tag{A.17}$$

$$(\phi_z)_{c0} = \sum_{i=1}^{n} W_{i0}^{z} \cdot (\phi_{c_i} - \phi_{c_0}) \tag{A.18}$$

A.3 Discretization and Schemes of Pressure-Based Solver (PBS)

The discretization and schemes for the PBS follows the steps leading to discretization of the momentum equation, discretization of the continuity equation, pressure-velocity coupling (PVC), steady-state iterative algorithm and time-advancement algorithm. These steps are easily depicted by considering the integral form of steady-state continuity and momentum equations:

$$\oint \rho\vec{v} \cdot d\vec{A} = 0 \tag{A.19}$$

$$\oint \rho\vec{v}\vec{v} \cdot d\vec{A} = -\oint pl \cdot d\vec{A} + \oint \bar{\bar{t}}\bar{a}ud\vec{A} + \int_V \vec{F}dV \tag{A.20}$$

Here I is the identity matrix, $\vec{F}$ is the force vector, and $\bar{\bar{\tau}}$is the stress tensor.

A.3.1 Discretization of the Momentum Equation

Here discretization pattern of momentum equations is same as for the discretization of scalar transport equations. In the case of x-momentum equation, there is the only adjustment of $\phi = u$;

$$a_{PU} = \sum_{nb} a_{nb}u_{nb} + \sum p_f A \cdot \hat{i} + S \tag{A.21}$$

If the face mass fluxes and pressure field are known, above equation can be solved. The discretization of pressure gradient can be obtained by the interpolation of pressure magnitudes [129, 130] as given below:

$$P_f = \frac{\frac{P_c 0}{a_{p.c_0}} + \frac{P_c 1}{a_{p.c_1}}}{\frac{1}{a_{p.c_0}} + \frac{1}{a_{p.c_1}}} \tag{A.22}$$

This coefficient works good as long as there is smooth pressure variation between cell centers. As the momentum source terms has large gradients, the pressure profiles also have high gradients at the cell faces which cannot be interpolated by this scheme. However, if this method is used, the divergence occurs in overshoots or undershoots of cell velocity. Therefore, it is essential to fill the region of high gradients with larger mesh size to determine the pressure variation effectively. The linear approach evaluates faces pressure through the arithmetic mean of the all terms in the neighboring cells. The second order scheme provides more advancement than the standard or linear schemes. However, if this scheme is used with bad mesh or used at the start of the computation, it will give some trouble.

A.3.1.1 Pressure Velocity Coupling (PVC)

The coupled method has supercity over the segregated solver methods due to its robustness. The pressure based (PB) coupled solver provided another alternative over SIMPLE-type PVC for both the PB and DB segregated solvers. Furthermore, CA is essential in case of transient case, when there is poor mesh quality or time step was larger. The semi implicit computation approach shows slow convergence because the PBSA computes the momentum and pressure correction equation separately. However, the PBCA computes the momentum and pressure-based continuity equation together. In equation A.21, the gradient of pressure for k is:

$$\sum_f p_f A_k = -\sum_j a^{u_k p} p_j \tag{A.23}$$

Here $a^{u_k p}$ is the coefficient obtained from equation A.22, Lastly, for the i^{th} cell, the component u_k, which is the discrete shape of the momentum equation, is written

as followed:

$$\sum_j a_{ij}^{u_k u_k} u_{kj} + \sum_j a_{ij}^{u_k p} p_j = b_i^{u_k} \tag{A.24}$$

In the equation A.33 the equilibrium of fluxes is changed by the flux expression in equation A.34, producing in the discrete form:

$$\sum_k \sum_j a_{ij}^{p u_k} u_{kj} + \sum_j a_{ij}^{pp} p_j = b_i^p \tag{A.25}$$

At the end, the final form of system equation A.24 and A.25. As a consequence, the overall system of equation A.24 as well as A.25, later being converted to the δ form, was written:

$$\sum_j [A]_{ij} \vec{X}_j = \vec{B}_i \tag{A.26}$$

Where the effect of a cell j had the appearance

$$A_{ij} = \begin{pmatrix} a_{ij}^{pp} & a_{ij}^{pu} & a_{ij}^{pv} & a_{ij}^{pw} \\ a_{ij}^{up} & a_{ij}^{uu} & a_{ij}^{uv} & a_{ij}^{uw} \\ a_{ij}^{vp} & a_{ij}^{vu} & a_{ij}^{vv} & a_{ij}^{vw} \\ a_{ij}^{wp} & a_{ij}^{wu} & a_{ij}^{wv} & a_{ij}^{ww} \end{pmatrix} \tag{A.27}$$

Furthermore, the unknown and residual vectors had the following representation

$$\vec{X}_j = \begin{pmatrix} P_i' \\ u_i' \\ v_i' \\ w_i' \end{pmatrix} \tag{A.28}$$

$$\vec{B}_i = \begin{pmatrix} -r_i^p \\ -r_i^u \\ -r_i^v \\ -r_i^w \end{pmatrix} \tag{A.29}$$

A.3.1.2 Under-relaxation (UR) of Variables

It is necessary to regulate the gradient of ϕ which is obtained by the under-relaxation of variables and minimizes the variation of ϕ obtain through-out every iteration. Apparently, the updated value of the variables ϕ, which is contained in a cell, relied on the previous values, ϕ_{old}, the calculated variation in ϕ, $A\phi$, and the UR factor, α, are written as follows:

$$\phi = \phi_{old} + \alpha\Delta\phi \tag{A.30}$$

A.3.1.3 Under-Relaxation (UR) of Equations

The UR of equations is employed in the PBS to regularized the convergence performance by establishing limited amount of ϕ in the system.

$$\frac{a_p\phi}{\alpha} = \sum_{nb} a_{nb}\phi_{nb} + b + \frac{1-\alpha}{\alpha}a_p\phi_{old} \tag{A.31}$$

Furthermore, the CFL number is a factor of solution in the PBCA and it is represented in the form of α:

$$\frac{1-\alpha}{\alpha} = \frac{1}{CFL} \tag{A.32}$$

A.3.2 Discretization of the Continuity Equation

The integration of equation A.19 over the control volume can produced the discretization equation as follows:

$$\sum_{f}^{N_{faces}} J_f A_f = 0 \tag{A.33}$$

Here J_f is the mass flux by faces f,ρv_{ri}. Moreover, it is compulsory to link the velocity face values $\vec{v}_{ri}$ to velocity magnitude obtained at the mid of cells. The linear interpolation of mid cell velocities to the face resulted in unusual checkerboarding of pressure. In order to prevented this, an approach is recommended by

Rhie and Chow [130] is used to prevent board checking. The velocity face value is not averaged linearly, recommended however, it is done using momentum-weighted averaging by applying weighing factors depend upon a_P coefficient from equation A.21 is computed. Following this approach, J_f can be denoted as:

$$J_f = \rho_f \frac{a_{p,c_0} v_{n,c_0} + a_{p,c_1} v_{n,c_1}}{a_{p,c_0} + a_{p,c_1}} + d_f((P_{c_0} + (\nabla P)_{c_0} \cdot \vec{r_0}) - (P_{c1} + (\nabla P)_{c_1} \cdot \vec{r_1})) = j_f + d_f(P_{c0} - P_{c1}) \tag{A.34}$$

Here p_{c0}, p_{c1} and v_{n,c_0}, v_{n,c_1} are the pressures and normal velocities correspondingly, $\hat{J}_f$ has the effect of velocities in corresponding cells. On the other hand, d_f is dependent on $\bar{a}_p$, the mean of the momentum equation a_p coefficients.

A.4 The Energy Equation

In solving the energy equation, other scalars (i.e. pressure, velocity etc.) are used which are computed in momentum and continuity equation, as given above. Then the energy equation can be computed as given below:

$$\frac{\partial}{\partial t}(\rho E) + \nabla \cdot (\vec{v}(\rho E + p)) = \nabla \cdot (k_{eff} \nabla T - \sum_j h_j \vec{J_j} + (\vec{\tau}_{eff} \cdot \vec{v})) + S_h \tag{A.35}$$

Here k_{eff} is the effective conductivity ($k + k_t$, where k_t is the turbulent thermal conductivity, employed corresponding to the used turbulent model), and $\vec{J_j}$ denotes the diffusion flux of j species. Furthermore, E can be denoted as:

$$E = h - \frac{p}{\rho} + \frac{v^2}{2} \tag{A.36}$$

Here the sensible enthalpy h is specified for gases and for incompressible flows respectively, as

$$h = \sum_j Y_j h_j \qquad h = \sum_j Y_j h_j + \frac{p}{\rho} \tag{A.37}$$

Here Y_j is the mass fraction of species

$$h_j = \int_{T_{reff}}^{T} c_{p,j} dT \tag{A.38}$$

Where T_{reff} is reference temperature.